Structure-function relations in mammalian sound localization circuits

Graduate School of
Systemic Neurosciences
LMU Munich

Marc Christopher Ford

Dissertation der Graduate School of Systemic Neurosciences der
Ludwig-Maximilians-Universität München

Munich, October 2014

First reviewer and supervisor: Prof. Dr. Benedikt Grothe

Second reviewer: Dr. Hartmann Harz

External reviewer: Prof. Dr. Henrique von Gersdorff

Date of defense: February 2nd, 2015

Nullius in verba

Motto of the Royal Society

Summary

Animals can detect the location of sound sources in the horizontal plane with remarkable accuracy. In contrast to other sensory systems there is no information of auditory space mapped onto the receptor surface of the cochlea. The auditory system has to compute the location of sound sources from physical cues that result in differences of the movement of the eardrums. The sound localization circuits in the mammalian auditory brainstem, and in particular those processing the microsecond differences in sound arrival time between the two ears through coincidence detection of excitatory and inhibitory inputs, are specialized for high-fidelity temporal processing. The ability of the nervous system to use cues in the microsecond range for localizing low-frequency sound sources is a remarkable performance given that the duration of action potentials are in the millisecond range. To accomplish this, numerous structural and functional specializations have evolved in these circuits which enable them to preserve temporal information and to perform computations with a temporal precision that is in all likelihood the highest in the mammalian brain. The studies presented in this thesis investigate several of these specializations with special focus on structure-function relations.

Study 1:

The calyx of Held is a giant glutamatergic presynaptic terminal in the mammalian auditory brainstem that transmits afferent information from globular bushy cells (GBCs) in the cochlear nucleus to glycinergic principle neurons of the medial nucleus of the trapezoid body (MNTB), thereby converting well-timed excitation into well-timed inhibition. It is an integral part of the neuronal circuits underlying sound localization in the horizontal plane. During postnatal development the calyx undergoes considerable morphological changes. The transformation from a spoon-shaped, closed morphology to a highly fenestrated structure has been proposed to improve high-fidelity synaptic transmission at this synapse. The goal of the first study was to investigate these morphological changes and their impact on temporal fidelity. We were able to demonstrate that the fenestration process does not occur simultaneously in all calyces. Calyces located medially in the MNTB, which are transmitting high-frequency sound information after hearing onset, fenestrate

significantly earlier than calyces located laterally in the MNTB which transmit low-frequency sound information. This finding indicates that a temporary developmental gradient along the mediolateral tonotopic axis is established around the time of hearing onset in Mongolian gerbils. Moreover, we found that the developmental gradient was not present in animals that were unilaterally cochlear ablated or administered ototoxic drugs, which indicates that cochlea-generated activity influences the fenestration process. Immunohistochemical staining revealed that astrocytic processes containing the glutamate transporters GLAST and GLT1 occupy the newly created diffusional exits in the calyx and thus could augment fast reuptake of neurotransmitter. Our physiological data show a faster decay time course of postsynaptic currents as well as a lower amount of residual current accumulating during repetitive synaptic stimulation, suggesting that fenestration of the calyx of Held facilitates glutamate clearance from the synaptic cleft.

Study 2:

In the second study of this thesis we report unexpected structural specializations of myelinated GBC axons that help to preserve temporal information for sound localization. Using anterograde labeling of axons in combination with immunohistochemical staining of nodal and juxtaparanodal marker proteins, we performed a detailed morphometric analysis of bushy cell axons. We found that, on average, the diameter of GBC axons was more than twice the diameter of spherical bushy cell (SBC) axons and the internode length in GBC axons was larger than that found in SBC axons. Moreover, we demonstrate that myelination parameters of GBC axons deviate from the canonically assumed structure and specifically tune axon properties depending on their termination region in their target nucleus, and hence on the sound frequency they are tuned to. Low-frequency axons had a larger diameter than high-frequency axons, but, surprisingly, shorter internodes. This deviation from the generally assumed axonal structure helps to tune the conduction speed and timing of action potentials within the circuit. Moreover, along the distal part of these axons internode length decreases whereas Ranvier node diameter increases progressively. Computer simulations suggest that these gradations ensure precisely-timed depolarization of the giant calyx of Held, and thus contribute to the reliable and precise transmission of temporal information demonstrated experimentally in this circuit.

Study 3:

MSO neurons are highly specialized coincidence detector neurons that can encode interaural time differences (ITDs) in the range of microseconds. These neurons have a remarkably low input resistance of only ~ 5 MOhms and very short time constants of only a few hundred microseconds. While these biophysical specializations help to achieve the temporal precision necessary for binaural coincidence detection, they also constitute a serious problem because the leaky soma might act as a current sink and could thus hamper action potential generation in the axon initial segment, in particular when synaptic conductances are high. In the third study we investigate the mechanisms that enable MSO neurons to generate action potentials at high rates despite their low input resistance. We performed a detailed morphometric analysis of the axon initial segment and proximal axon segments of MSO neurons and found that the axon is less than 1 µm in diameter. Computer simulations show that the thin axons of MSO neurons facilitate action potential initiation in the axon initial segment. Moreover, the model suggests that, under conditions of high synaptic input rates, action potentials are also generated in the nodes of Ranvier. The expansion of the spike initiation area to nodes of Ranvier in the proximal axon is caused by spatial gradient of sodium channel inactivation and a somatic current sink.

Study 4:

The fourth study provides evidence that the ITD sensitivity of MSO neurons is modulated through a $GABA_B$ receptor-dependent mechanism. GABAergic modulation of excitatory and inhibitory MSO inputs has been previously demonstrated *in vitro*, however the functional significance of this modulation for sound source localization *in vivo* and the source providing GABA were unclear. Using anterograde and retrograde fiber tracing we found that a subpopulation of superior paraolivary nucleus (SPN) neurons sends GABAergic projections to the MSO. Moreover, we were able to corroborate the earlier finding that MSO neurons send collateral projections to the SPN in the gerbil. Taken together, our anatomical data strongly indicate that a disynaptic feedback loop via the SPN is involved in GABAergic modulation of MSO inputs.

Table of Contents

1 Introduction

Animals can detect the location of sound sources in the horizontal plane (azimuth) with remarkable accuracy (Carr and Macleod, 2010). The ability to detect sound sources with high spatial acuity has strong evolutionary advantages. The neuronal representation of meaningful changes in the environment is an important requirement to react in an appropriate way, e.g. by initiating the appropriate escape behavior on the approaching of a predator, or for localizing and capturing prey. In contrast to other sensory systems (for instance the visual and somatosensory system) there is no information of auditory space mapped onto the receptor surface of the cochlea. The auditory system has to compute the location of sound sources from physical cues that result in differences of the movement of the eardrums (Grothe et al., 2010).

Acoustic cues for sound source localization in the horizontal plane

There are two binaural physical cues that can be employed for localizing sound sources in the horizontal plane, (1) interaural level differences and (2) interaural time differences (ILDs and ITDs, respectively).

(1) ILDs are sound level differences at the two ears created by the shadowing effect of the head and represent the dominant cue for localizing high-frequency sounds. Sounds with wavelengths smaller than the listener's head are significantly attenuated by the head, which acts as an acoustical obstacle for such frequencies (**Figure 1A**). As a result, if a sound source is located off the midsagittal plane the sound level at the far ear is lower than at the near ear. Maximum ILDs are produced when a sound source is located 90° to the right or left of the listener, while sound sources directly in front produce no ILD. ILDs are frequency-dependent, with higher frequencies producing larger ILDs than lower frequencies. Humans are able to discriminate ILDs of only 1-2 dB (Grothe et al., 2010) .

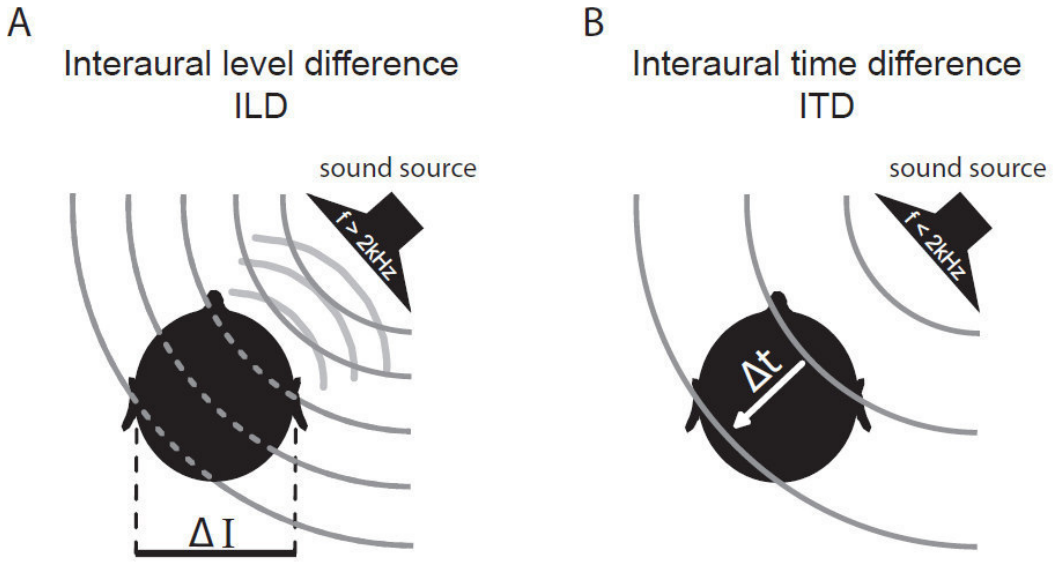

Figure 1: Binaural cues for localizing sound sources in the horizontal plane. (A) Differences in intensity at the two ears created by the shadowing effect of the head can be employed for detecting high-frequency sound sources. (B) Time of arrival differences at the two ears can be used to detect low-frequency sound sources. Modified from (Grothe et al., 2010).

(2) ITDs are the differences in the time of arrival of a sound at the two ears and represent the dominant cue for localizing low-frequency sounds in the azimuth. These time differences, which are in the range of microseconds, are created when sound emitted from a single source arrives first at the near ear and later at the far ear (**Figure 1B**). Thus, ITDs depend on the position of the sound source in the horizontal plane in relation to the head of the listener and the listener's inter-ear distance (Grothe, 2003). Sound emitted from sources directly in front or behind the listener's head creates no ITDs, whereas maximum ITDs are created when the sound source is located 90° to the left or right.

Humans experience ITDs up to roughly 700 µs (this value can be calculated by dividing the inter-ear distance by the speed of airborne sound [~343 m/s]) and are capable of discriminating ITDs of only 10-20 µs (Mills, 1958; Grothe et al., 2010). Mongolian gerbils (*meriones unguiculatus*), which have a smaller inter-ear distance, can detect ITDs up to roughly 135 µs (Maki and Furukawa, 2005) and are able to resolve ITDs as low as ~20 µs (Lesica et al., 2010). Gerbils have been extensively used as model organism for ITD processing because they have a well developed low-frequency hearing, exhibit an audiogram similar to that of humans, and a well

developed neuronal circuitry for ITD processing. Notably, ITDs can also be employed for localizing amplitude modulated high-frequency sounds (Leakey et al., 1958; Henning, 1974; McFadden and Pasanen, 1976; Dreyer and Delgutte, 2006).

ITDs and ILDs enable mammals to localize a sound source with very high spatial accuracy: humans are able to discriminate sound sources that are 1-2 degrees apart (reviewed in Grothe et al., 2010) and the minimal resolvable angle for Mongolian gerbils has been shown to be ~14 degrees (Lesica et al., 2010). The ability of the nervous system to use cues in the microsecond range for localizing sound sources with such high accuracy is a remarkable performance given that the duration of action potentials are in the millisecond range. To accomplish this, the neuronal circuits of the auditory brainstem, which perform the computation of ITDs by comparing binaural cues, have numerous functional specializations that enable them to perform computations with a temporal precision that is arguably the highest in the mammalian brain (Grothe et al., 2010).

Processing of interaural differences by mammalian sound localization circuits

A prerequisite for localizing sound sources with such high accuracy is the precise encoding of the temporal fine structure of sound in the periphery of the auditory system. When sound impinges on the ear it causes vibrations of the tympanum. These vibrations are transmitted via the three middle ear bones to the oval window of the cochlea. The middle ear bones act as an impedance matching device and carry fluctuating pressure changes to the cochlea. There the sound is spectrally decomposed. Pressure fluctuations in the cochlea cause vibrations of the basilar membrane which result in a traveling wave propagating from the base of the cochlea to its apex. Along its length the basilar membrane exhibits systematic variation in width and stiffness. It is narrow and rigid at the base of the cochlea while at its apex the membrane is wide and flexible. As a result of the mechanical tuning, high-frequency signals cause strongest vibrations at the base whereas low-frequency signals cause strongest vibrations at the apex. Thus, sound frequency is systematically represented along the length of the basilar membrane with high

frequencies being represented in the basal part and low frequencies being represented in the apical part.

The basilar membrane bears the sensory epithelium, the organ of Corti. Inner hair cells of the organ of Corti transform the vibrations/deflections of the basilar membrane via a mechanoelectrical transduction process into electrical signals that cause transmitter (glutamate) release from their basolateral pole, which in turn leads to excitation of type 1 spiral ganglion neurons. These are bipolar neurons with cell bodies located in the spiral ganglion and peripheral axons innervating the inner hair cells in the cochlea. Their central axons, which constitute the bulk of auditory nerve fibers, innervate targets in the cochlear nucleus, including the spherical and globular bushy cells (SBCs and GBCs, respectively) which pass on the information to the superior olivary complex for azimuthal sound source localization.

The topographic representation of frequency along the basilar membrane provides the basis for tonotopy, a major organization principle of the auditory system (Kandler et al., 2009; Mann and Kelley, 2011). Tonotopy refers to the systematic representation of best frequency that can be found along the extent of auditory brainstem and midbrain nuclei and areas of the auditory cortex.

A major feature of the auditory nerve and neurons in the sound localization circuits is the ability of time-locking their responses. That is, neurons fire action potentials preferentially at a certain phase angle (phase-locking) of low-frequency tones (Galambos and Davis, 1943; Rose et al., 1967) or the envelope of sinusoidally amplitude-modulated high-frequency sounds (Dreyer and Delgutte, 2006). Notably, individual cells do not necessarily fire at each cycle of the sound stimulus, especially with neurons tuned to higher sound frequencies. Phase locking provides the temporal information about the sound waveform that can be employed for sound source localization.

Numerous morphological and physiological adaptations for time coding have evolved that promote the exquisite temporal processing exhibited by the sound localization circuits (Carr et al., 2001; Carr and Soares, 2002). This includes giant synapses that ensure fast, high-fidelity synaptic transmission with low temporal jitter (Guinan and Li, 1990; von Gersdorff and Borst, 2002) upstream of the neurons that perform the

computation of interaural differences, and biophysical mechanisms that keep action potentials and postsynaptic potentials short and precise (Trussell, 1997, 1999).

The first nuclei in the auditory brainstem that show sensitivity to interaural differences are the medial and lateral superior olive (MSO and LSO, respectively) in the superior olivary complex, where input from both ears converges for the first time (**Figure 2A, C**). From there information is passed on to higher centers of the auditory system.

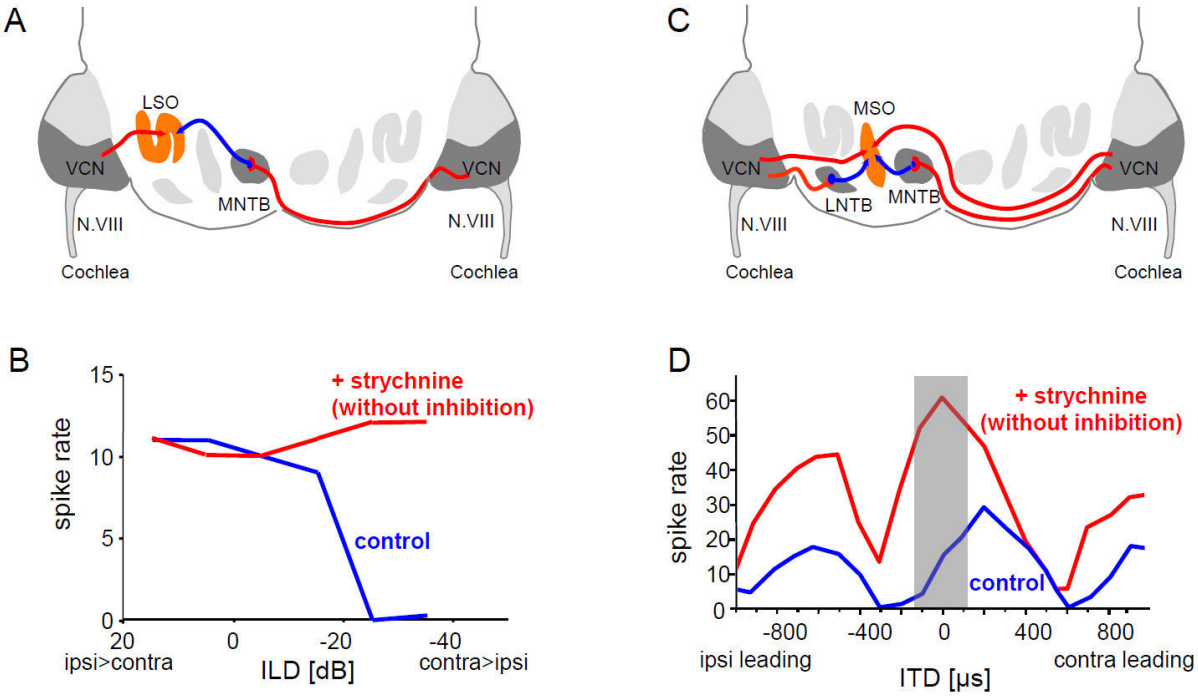

Figure 2: (A) Schematic of the mammalian ILD processing circuit. (B) Typical ILD function of an LSO neuron (blue) and the effect of blocking inhibition by strychnine application (red). (C) Schematic of the mammalian ITD processing circuit. (D) Typical ITD function of an MSO neuron (blue) and the effect of blocking inhibition by strychnine application (red). The grey area indicates the physiological relevant range of ITDs. Modified from (Grothe and Koch, 2011).

ILD processing in the LSO

The first station in the ascending auditory pathway where ILDs are processed is the LSO. Principal cells of the LSO receive well-timed excitatory glutamatergic input from the ipsilateral ear (Cant and Casseday, 1986; Joris et al., 1994) and well timed inhibitory input from the contralateral ear (Moore and Caspary, 1983; Sanes et al., 1987; Wu and Kelly, 1993; Grothe, 2003) (**Figure 2A**). The excitatory inputs originate from spherical bushy cells (SBCs) located in the ipsilateral anteroventral cochlear nucleus (AVCN) and innervate the LSO directly. In contrast, the inhibitory input is indirect: globular bushy cell (GBC) axons originating in the contralateral ventral cochlear nucleus innervate principle cells in the ipsilateral medial nucleus of the trapezoid body (MNTB) via a giant presynaptic terminal, the calyx of Held (Held, 1893). MNTB principal cells convert this well-timed glutamatergic excitation into well timed glycinergic inhibitory projections to the LSO. These specializations enabling the conversion of well-timed excitation into well-timed inhibition will be described in more detail in a later section.

The computation of ILDs in the LSO can simplistically be described as a subtraction process by which contralaterally-driven inhibition is subtracted from ipsilaterally-driven excitation. LSO cells respond maximally when the sound is coming from the ipsilateral side (90 degrees). The firing rate decreases when the sound level is increased at the contralateral ear because this increases the inhibition via the MNTB (**Figure 2B**).

ITD processing in the MSO

ITDs are initially processed in the medial superior olive (MSO) by a binaural coincidence detection mechanism involving excitatory and inhibitory inputs from both ears (**Figure 2C**). The bipolar MSO principal neurons are arranged in a parasagittal plane with their dendrites extending both laterally and medially from the soma. The lateral and medial dendrites receive excitatory inputs as direct projections from the SBCs of the ipsilateral and contralateral cochlear nuclei, respectively (Stotler, 1953; Goldberg and Brown, 1968; Perkins, 1973; Lindsey, 1975; Kiss and Majorossy, 1983; Glendenning et al., 1985; Smith et al., 1993). These afferents provide temporally

precise input to the MSO, and phase locking in SBCs has been reported to be superior to that of auditory nerve fibers. Joris and colleagues suggested that a mechanism of monaural coincidence detection using converging auditory nerve inputs might underlie the improved phase locking (Joris et al., 1994). In addition to these excitatory inputs, MSO neurons also receive temporally-precise glycinergic inhibitory inputs from neurons located in the ipsilateral MNTB and LNTB (Kuwabara and Zook, 1992; Grothe and Sanes, 1993, 1994).

In vivo experiments revealed that a pharmacological blockade of glycinergic inhibition by iontophoretic application of strychnine shifts the ITD sensitivity of the cell (the peak of the ITD function) towards an ITD of 0 (**Figure 2D**) (Brand et al., 2002). This finding suggests that, under physiological conditions, the functional role of glycinergic inhibition consists in shifting the peak of the ITD function out of the physiological relevant range (**Figure 2D**), thereby increasing the dynamic range of the ITD response within the physiological relevant range of ITDs, and indicates that a rate code rather than a peak code may be used by MSO neurons for encoding ITDs (Brand et al., 2002; Pecka et al., 2008). When glycine is tonically applied to MSO neurons *in vivo* during binaural stimulation not only the firing rate is decreased, but also the peak of the ITD function is shifted towards an ITD of 0, arguing for a crucial role of well-timed phasic inhibition in shaping ITD functions (Pecka et al., 2008).

While the exact biophysical mechanisms by which inhibition interacts with excitation in order to shape the ITD sensitivity of MSO neurons are still a matter of debate (Grothe et al., 2010; Portfors and von Gersdorff, 2013; Myoga et al., 2014), it has been shown that inhibition can precede excitation *in vitro* by about 300 µs despite the additional synaptic delay of several hundred microseconds (about 400 µs) at the calyx of Held (Roberts et al., 2013). Earlier evidence for well-timed (and possibly preceding) inhibition via the GBC-MNTB-pathway was presented in an *in vitro* study by Grothe and Sanes (Grothe and Sanes, 1994). Consequently, axons of the inhibitory GBC-MNTB pathway have to be capable of conducting action potentials significantly faster than the excitatory pathway in order to achieve the measured arrival time of inhibition relative to excitation at the MSO.

It has been assumed that the reason for preceding inhibition via the GBC-MNTB-pathway might be the large diameter of GBC axons. However, despite reports that GBCs give rise to the thickest axons of the trapezoid body (Morest, 1968; Spangler et

al., 1985; Spirou et al., 1990), no detailed morphometric analysis has been performed. Moreover, internode length is also an important determinant of axonal conduction velocity in myelinated axons and may be employed for tuning conduction times of GBC fibers (Huxley and Stampfli, 1949; Brill et al., 1977; Waxman, 1980). Indeed, it has been proposed for the analogous ITD detection system in birds that differential regulation of internode length in two axon branches of the same neurons may account for precise matching of arrival times of synaptic input from both ears at postsynaptic coincidence detector neurons (Seidl et al., 2010, 2014).

In addition to glycinergic inhibitory inputs the MSO also receives GABAergic inputs which, using *in vitro* experiments, have been demonstrated to modulate transmitter release from glutamatergic and glycinergic MSO inputs (Hassfurth et al., 2010; Fischl et al., 2012). Surprisingly, despite a very detailed understanding of the anatomy of the sound localization circuits in gerbils, the origin of GABAergic inputs to the MSO was not known.

Specializations for preserving temporal information in the GBC-MNTB pathway

The GBC-MNTB-pathway is an integral part of the sound localization circuits of the mammalian auditory brainstem that provides well-timed glycinergic inhibition to the LSO and MSO. Consistent with its functional role as a fast sign-inverting relay (Moore and Caspary, 1983; von Gersdorff and Borst, 2002; Borst and Soria van Hoeve, 2012) it exhibits numerous specializations for preserving temporal information, including large myelinated axons and giant presynaptic terminals, the calyces of Held. The large calyx forms a glutamatergic axosomatic synapse with principal neurons of the MNTB, enabling fast depolarization of the round, electrically compact postsynaptic neuron with a very short synaptic delay (Taschenberger and von Gersdorff, 2000). The calyx is specialized for fast transmission at high rates with low temporal jitter (Taschenberger and von Gersdorff, 2000). *In vivo* it can sustain high firing rates of several hundred Hz (Spirou et al., 1990; Kopp-Scheinpflug et al., 2008; Lorteije et al., 2009). The presynaptic terminal exhibits an exceptionally large number of active zones (300-700) (Sätzler et al., 2002; Taschenberger et al., 2002; Wimmer

et al., 2006; Dondzillo et al., 2010) which enables it to release more than 100 vesicles in response to a single action potential (Borst and Sakmann, 1996).

Developmental changes at the calyx of Held synapse improve the preservation of temporal information in the GBC-MNTB pathway

During early postnatal development the calyx of Held undergoes considerable morphological and physiological changes (Nakamura and Cramer, 2011) which improve high-fidelity synaptic transmission at this synapse. In P9 rats the spoon or cup-shaped calyx covers roughly 40% of the postsynaptic membrane area of the MNTB principal cell soma (Sätzler et al., 2002). During the following 1-2 weeks it changes to a complex, highly fenestrated (*fenestra* is the Latin word for window) claw-like morphology (Kandler and Friauf, 1993; Kil et al., 1995; Rowland et al., 2000).

It has been proposed that these morphological changes allow faster transmitter clearance and closer contact between astrocytes and presynaptic release sites where glutamate filled vesicles fuse with the presynaptic membrane (Taschenberger et al., 2002), thus promoting more efficient glutamate reuptake via astrocyte-specific glutamate transporters (Gegelashvili and Schousboe, 1998). Fast glutamate clearance from the synaptic cleft contributes to a rapid decay time course for excitatory postsynaptic potentials (Cathala et al., 2005).

The morphological changes that occur during postnatal development of the calyx are paralleled by physiological changes [reviewed in (von Gersdorff and Borst, 2002; Nakamura and Cramer, 2011; Borst and Soria van Hoeve, 2012)]: the half-width of the presynaptic action potential is reduced by approximately two thirds between the first and second postnatal week, while its amplitude does not change significantly (Taschenberger and von Gersdorff, 2000). During development sodium channels show a faster recovery from inactivation, probably due to a switch from $Na_v1.2$ to $Na_v1.6$ subunits in nodes and heminodes (Leão et al., 2005). Moreover, the expression of $Na_v1.6$ subunits increases with age (Leão et al., 2005) and may account for the increased maximum rate of rise in older animals (Taschenberger and

von Gersdorff, 2000). The faster downstroke of the action potential is caused by an upregulation of high-voltage-activated K_v3-type potassium channels (Elezgarai et al., 2003; Nakamura and Takahashi, 2007).

The shape of the presynaptic action potential is an important determinant of the synaptic delay and strength (Sabatini and Regehr, 1999; Boudkkazi et al., 2011) and hence can influence the timing precision of synaptic transmission. At the calyx of Held calcium influx occurs during the downstroke of the action potential (Borst and Sakmann, 1996, 1998), leading to fast transmitter release from the presynaptic terminal. The synaptic delay at the calyx decreases during postnatal development (Taschenberger and von Gersdorff, 2000; Leão et al., 2005), which has been proposed to be related to the developmental changes in the presynaptic action potential duration.

At the calyx of Held synapse glutamate release causes activation of postsynaptic AMPA and NMDA receptors (Forsythe and Barnes-Davies, 1993). While the NMDA receptor-mediated component of the postsynaptic current is strongly reduced during development (Taschenberger and von Gersdorff, 2000), the AMPA receptor-mediated component increases in amplitude (Futai et al., 2001; Joshi and Wang, 2002). Moreover, the decay time constant of the AMPA receptor-mediated component decreases with postnatal maturation (Taschenberger and von Gersdorff, 2000; Joshi and Wang, 2002; Joshi et al., 2004), which is caused by faster deactivation and desensitization rates, probably due to an increase in expression of the *flop* splice variant of the GluA4 AMPA receptor subunit (Caicedo and Eybalin, 1999; Joshi et al., 2004; Koike-Tani et al., 2005). These pre- and postsynaptic changes enable postsynaptic MNTB cell to follow high firing rates and represent important cellular adaptations that contribute to the preservation of temporal information in the sound localization circuits (Trussell, 1997, 1999).

The importance of rapid transmitter clearance from the synaptic cleft

The fast kinetics of AMPA receptors are a prerequisite for temporally precise high-frequency synaptic transmission at the calyx of Held synapse (Taschenberger and

von Gersdorff, 2000; von Gersdorff and Borst, 2002). However, it is also crucial that clearance of glutamate from the synaptic cleft is rapid, in order to avoid re-binding of glutamate to postsynaptic receptors because this can lead to an accumulation of AMPA receptors in a desensitized state (Otis et al., 1996; Attwell and Gibb, 2005) and may decrease temporal fidelity of synaptic transmission (Turecek and Trussell, 2000). Transmitter clearance from the synaptic cleft is dependent on several factors, including passive diffusion of neurotransmitter out of the synaptic cleft and active transport into astrocytes which express high levels of glutamate transporters in their processes. Hence, the time course of transmitter clearance is also influenced by synaptic morphology and the proximity of glial processes with presynaptic active zones, the sites from which transmitter are released into the synaptic cleft (Cathala et al., 2005; Renden et al., 2005). At some synapses alterations of presynaptic structure may account for the developmental acceleration of AMPA receptor mediated currents during development (Cathala et al., 2005; Renden et al., 2005). Moreover, it has been demonstrated recently that astroglial processes can be inserted into synaptic clefts, which represents a mechanism for modulating glutamate reuptake and synaptic strength (Pannasch et al., 2014).

Structure and function of axon initial segments and myelinated axons

In myelinated axons the most proximal, unmyelinated part of the axon is called the axon initial segment (AIS) (Kole and Stuart, 2012). It is usually assumed to be the site where action potentials are initiated (Stuart and Sakmann, 1994; Kole et al., 2008; Foust et al., 2010; Kole and Stuart, 2012). Accordingly, in cortical pyramidal neurons it has been shown to have the lowest threshold for action potential initiation (Kole and Stuart, 2008). In line with these physiological findings, in hippocampal CA1 pyramidal neurons the sodium channel density in the AIS may be ~40 times as high as in the somatodendritic compartment (Lorincz and Nusser, 2010). Moreover, the distribution and composition of voltage-gated ion channels along the AIS can be of functional significance. For instance, it has been shown that two opposed gradients of two types of sodium channels exist in layer 5 pyramidal neurons. This particular arrangement of high- and low-threshold voltage-activated sodium channels promotes

backpropagation of action potentials into the somatodendritic compartment of the cell and thus may play a crucial role in spike-timing-dependent plasticity (Hu et al., 2009). Moreover, it has been demonstrated recently that the length and position (distance from the soma) of the AIS can be tuned to optimize action potential initiation and thus can be of functional importance for information processing (Kuba et al., 2006).

The AIS is followed by the axon proper. In myelinated axons this consists of myelinated segments called internodes which are periodically interrupted by nodes of Ranvier, the sites where sodium channels are clustered at high densities, thus restricting sodium influx to a small unmyelinated fraction of the axon. The concentration of sodium channels at nodes of Ranvier separated by internodes provides the basis for fast saltatory conduction (Huxley and Stampfli, 1949).

Structural determinants of action potential conduction velocity in myelinated axons

Several geometrical factors influence the speed of action potential propagation in myelinated axons. A major determinant of conduction velocity is the axonal diameter, which correlates negatively with the axial resistance of the axon. While in unmyelinated axons the length constant, and hence the conduction velocity, is proportional to the square root of the axonal diameter, in myelinated axons conduction velocity has been reported to be linearly dependent on fiber diameter (Hursh, 1939; Rushton, 1951; Ritchie, 1982) for otherwise structurally similar axons.

Propagation speed along axons of the central nervous system is increased by myelinating axons, thus reducing the effective membrane capacitance and increasing the transverse resistance of the internodal segments (Bakiri et al., 2011). In addition this reduces the axonal energy cost by decreasing the sodium influx needed to produce an action potential because sodium influx is restricted to the unmyelinated parts of the fiber, the nodes of Ranvier. The relative thickness of the myelin sheath is commonly reported as the g-ratio, the ratio of the axon diameter to the outer myelin diameter. In central myelinated axons the g-ratio usually increases slightly with axon diameter, i.e. the relative thickness of the myelin decreases at larger axon diameters (Makinodan et al., 2012).

In addition to the thickness of the myelin sheath, the length of the myelinated internodes is an important determinant of conduction velocity. It has traditionally been assumed to be ~100 times the fiber diameter (outer myelin diameter) (Rushton, 1951). Theoretical studies proposed that the relationship between internode length and conduction velocity can be described by a bell-shaped function with a relatively flat optimum (Huxley and Stampfli, 1949; Goldman and Albus, 1968; Brill et al., 1977). When internode length is short conduction velocity is decreased because a larger fraction of the axonal membrane does not benefit from the capacitance-reducing and insulating effect of the myelin sheath, while at greater internode lengths the conduction speed is reduced because of decreasing transfer of depolarization to the next node. At very long internodes depolarization of the consecutive node is not sufficient anymore for eliciting an action potential and propagation eventually fails.

Finally, it is important to note that conduction velocity of myelinated axons is also dependent on factors other than axon geometry, such as temperature (Paintal, 1965), the number of voltage-gated sodium channels in the nodal membrane, and the ion concentrations inside and outside the axon.

Aim of this thesis

This thesis comprises four independent studies that aimed at gaining a better understanding of the neuronal circuits mediating azimuthal sound localization, with a special focus on structure-function relations.

Study 1:

During postnatal development the calyx of Held undergoes considerable morphological changes (Kandler and Friauf, 1993; Kil et al., 1995). The transformation from a spoon-shaped, closed morphology to a highly fenestrated structure may improve high-fidelity synaptic transmission at this synapse. The creation of diffusional exits has been suggested to facilitate transmitter clearance from the synaptic cleft (Renden et al., 2005). Moreover, it may allow astrocytic processes to invade the newly created diffusional exits, which may result in more

efficient glutamate reuptake via astrocyte-specific glutamate transporters (Taschenberger et al., 2002).

The goal of the first study was to investigate these morphological changes and their impact on temporal fidelity. Firstly, we labelled calyces via tracer injections into the cochlear nucleus and investigated possible differences in fenestration along the mediolateral tonotopic axis of the MNTB at various time points during postnatal development. Secondly, by administrating ototoxic drugs or unilaterally ablating the cochlea before hearing onset, we tested whether the fenestration process is influenced by cochlea-generated activity. Thirdly, using immunohistochemical staining, we determined whether astrocytic processes containing the astrocyte-specific glutamate transporters GLAST and GLT1 occupy the newly created diffusional exits in the calyx. Finally, patch clamp recordings were used to investigate potential differences in glutamate clearance between fenestrated and unfenestrated calyces of Held.

Study 2:

ITDs are first computed in the MSO by coincidence detection of excitatory and inhibitory inputs of both the ipsilateral and contralateral ear. While the excitatory inputs from SBCs innervate MSO neurons directly, the inhibitory pathways include an additional synapse at which the excitatory input arising from GBCs is converted into an inhibitory output. Despite the additional synaptic delay of ~400µs, recent data indicate an earlier arrival time for inhibitory than for excitatory input at the MSO (Grothe and Sanes, 1994; Roberts et al., 2013), suggesting the involvement of functional specializations that tune axonal conduction velocity. Accordingly, GBC axons are reported to have the largest diameter of all fibers of the trapezoid body (Morest, 1968; Spangler et al., 1985; Spirou et al., 1990). However, detailed knowledge of the geometrical parameters determining conduction velocity in GBC and SBC axons was lacking.

The aim of the second study was to perform a detailed morphometric analysis of bushy cell fibers. Using anterograde labeling of axons in combination with immunohistochemical staining of nodal and juxtaparanodal marker proteins, we determined internode length, internodal axon diameter, and node of Ranvier diameter. Using transmission electron microscopy we determined myelin thickness in

GBC fibers. An anatomically constrained computational model of the myelinated axon was used to estimate action potential conduction velocity in bushy cell fibers. Our morphometric analysis revealed that axonal parameters of GBC fibers are graded towards the calyx of Held. Internode length gradations have been reported to exist in motor fibers close to the neuromuscular junction and suggested to aid in depolarizing the large presynaptic terminal (Quick et al., 1979). Therefore, we used computer simulations to test whether the experimentally observed gradations aid action potential propagation into the giant presynaptic terminal and thus contribute to the reliable and precise transmission of temporal information demonstrated experimentally in this circuit.

Study 3:

MSO neurons are highly specialized coincidence detector neurons that can encode ITDs in the range of microseconds. These neurons have a remarkably low input resistance of only ~ 5 MOhms and very short time constants of only a few hundred microseconds (Scott et al., 2005; Couchman et al., 2010). While these biophysical specializations help to achieve the temporal precision necessary for binaural coincidence detection, they also constitute a serious problem because the leaky soma might act as a current sink and could thus hamper action potential generation in the axon initial segment, in particular when synaptic conductances are high.

In the third study we investigated the mechanisms that enable MSO neurons to generate action potentials at high rates despite their low input resistance. Using a combination of retrograde labelling of MSO neurons with immunohistochemical staining of AnkyrinG and Kv1 channels we performed a detailed morphometric analysis of the axon initial segment and proximal axon segments of MSO neurons. The morphometric data was used to create a morphologically constrained computational model of the MSO axon. Computer simulations were used to investigate how the axonal morphology aids MSO neurons in retaining the ability to generate action potentials.

Study 4:

GABAergic modulation of excitatory and inhibitory MSO inputs has been previously demonstrated *in vitro* (Hassfurth et al., 2010; Fischl et al., 2012), however the source providing GABA was unclear. A potential source of GABAergig input to the MSO was

the superior paraolivary nucleus (SPN) which contains a substantial population of GABAergic neurons (Roberts and Ribak, 1987). Moreover, recent data demonstrated that several cell types in the SPN receive collateral projections from MSO neurons (Kuwabara and Zook, 1999), raising the possibility that a disynaptic feedback loop via the SPN is involved in GABAergic modulation of MSO inputs.

In the fourth study we tested this possibility by using anterograde and retrograde fiber tracing in combination with immunohistochemical staining of marker proteins for GABAergic and glutamatergic presynaptic terminals.

2 Results

Study 1

Author contributions:

M.C.F. and A.K. designed the research, M.C.F. performed the experiments; M.C.F. analysed the data [blinded analysis of calyx morphology (assignment of calyces to one of five morphology categories) was performed by two student assistants]. M.C.F. prepared all figures; M.C.F. and A.K. wrote the manuscript; M.C.F., B.G., and A.K. revised the manuscript.

The Journal of Comparative Neurology 514:92–106 (2009)
Research in Systems Neuroscience

Fenestration of the Calyx of Held Occurs Sequentially Along the Tonotopic Axis, Is Influenced by Afferent Activity, and Facilitates Glutamate Clearance

MARC C. FORD,* BENEDIKT GROTHE, AND ACHIM KLUG*
Division of Neurobiology, Ludwig-Maximilians-University Munich, 82152 Martinsried, Germany

ABSTRACT

The calyx of Held is a type of giant glutamatergic presynaptic terminal in the mammalian auditory brainstem that transmits afferent information from the cochlear nucleus to the medial nucleus of the trapezoid body (MNTB). It participates in sound localization, a process that requires very high temporal precision. Consistent with its functional role, the calyx shows a number of specializations for temporal fidelity, one of them being the giant terminal itself with its many release sites. During the first 3 weeks of postnatal development, the calyx transforms from a spoon-shaped, closed morphology to a highly fenestrated open structure.

Calyces in Mongolian gerbils (*Meriones unguiculatus*) were labeled via injection of fluorescent tracers and their morphology was reconstructed at various timepoints during early postnatal development. We show that the fenestration process does not occur simultaneously in all calyces. Calyces transmitting high-frequency sound information fenestrate significantly earlier than those transmitting low-frequency information, such that a temporary developmental gradient along the tonotopic axis is established around the time of hearing onset. Animals that were deprived of afferent activity before hearing onset, either via cochlear removal or administration of ototoxic drugs, do not show this developmental gradient. Glial processes containing glutamate transporters occupy the newly created windows in the calyx and thus could augment the fast clearance of neurotransmitter. The physiological consequences of this faster clearance include a faster decay time course of synaptic currents as well as a lower amount of residual current accumulating during the processing of repeated activity such as stimulus trains. J. Comp. Neurol. 514:92–106, 2009.

Indexing terms: Indexing terms: calyx of Held; synaptic development; activity dependent development; auditory; medial nucleus of the trapezoid body; MNTB; GLAST; GLT1; neuron glia interaction; glutamate reuptake; glutamate clearance

The calyx of Held is a type of giant presynaptic terminal located in the mammalian auditory brainstem (Held, 1891, 1892; Morest, 1968b). The axons that give rise to the calyx originate from globular bushy cells in the anteroventral cochlear nucleus and convey glutamatergic input to principal neurons of the medial nucleus of the trapezoid body (MNTB), which in turn give rise to inhibitory projections to a number of auditory brainstem nuclei (Warr, 1966, 1982; Morest, 1968a,b; Moore and Caspary, 1983; Bledsoe et al., 1990; Kuwabara et al., 1991; Banks and Smith, 1992). One of the hallmarks of this circuit is the extreme temporal precision with which neural activity is processed (Goldberg and Brown, 1969; Forsythe and Barnes-Davies, 1993; Joris et al., 1994; Trussell, 1997, 1999; Smith et al., 1998; Oertel, 1999; Brand et al., 2002; Taschenberger et al., 2002; Grothe, 2003). This fidelity is required since the calyx of Held participates in sound localization, a process during which sound information between the two ears is compared at a microsecond scale (computation of interaural time disparities), and thus very high temporal resolution is mandatory (Moore and Caspary, 1983; Trussell, 1997; Oertel, 1999; Grothe, 2003). Consistent with its functional role, the sound localization circuit and especially the calyx of Held show a number of specializations for temporal fidelity, such as the particularly large size of the synapse and the close proximity of synaptic vesicles to presynaptic calcium channels. Corresponding specializations on the postsynaptic side in-

Grant sponsor: DFG IRTG 1373, the Graduate School of Systemic Neurosciences (GSN-LMU) predoctoral fellowship (to M.C.F.); Grant sponsor: DFG; Grant numbers: KL 1842/1-1 and 1-2 (to A.K.).

*Correspondence to: Achim Klug and Marc C. Ford, Ludwig-Maximilians-University Munich, Biocenter, Division of Neurobiology, Grosshaderner Strasse 2, 82152 Martinsried, Germany. E-mail: achim.klug@lmu.de; ford@bio.lmu.de

Received 30 June 2008; Revised 10 November 2008; Accepted 15 January 2009

DOI 10.1002/cne.21998

Published online in Wiley InterScience (www.interscience.wiley.com).

clude the electrically compact morphology of the postsynaptic cell, and the use of AMPA receptor subunits with very fast decay time constants (Taschenberger and von Gersdorff, 2000; Taschenberger et al., 2002; von Gersdorff and Borst, 2002; Meinrenken et al., 2003; Koike-Tani et al., 2005; Schneggenburger and Forsythe, 2006). The experimental subjects used in this study were Mongolian gerbils (*Meriones unguiculatus*), which are known to localize sound sources well (Heffner and Heffner, 1988), and thus critically depend on the high temporal precision of the involved neural circuits.

Many of the specializations described above are not present at birth but develop during the first few postnatal weeks (Kandler and Friauf, 1993; Kil et al., 1995; Hoffpauir et al., 2006; Rodriguez-Contreras et al., 2006, 2008). Calyx morphology itself also changes during this time. Although the initial contact between the calyx and the postsynaptic neuron is established between postnatal days 0–4 (Kandler and Friauf, 1993; Kil et al., 1995; Rodriguez-Contreras et al., 2008), the synapse subsequently undergoes a number of morphological changes. Just around and after the time of hearing onset, calyces transform from a closed cup- or spoon-shaped morphology to a highly fenestrated and open claw-like structure (Kandler and Friauf, 1993; Kil et al., 1995; Hoffpauir et al., 2006).

The significance of this fenestration process might be the creation of additional diffusional exits for neurotransmitter out of the synaptic cleft, such that the synaptic current can decay faster and more precisely. Additionally, it has been suggested that glial processes with high densities of glutamate transporters might occupy these openings and thus augment the fast decay of synaptic events (Taschenberger et al., 2002; Renden et al., 2005). The observation that fenestration occurs just around and after hearing onset brings up the question whether afferent activity plays a role in this process.

The goal of this study was to investigate the fenestration process in greater detail and determine a possible role of afferent activity. Furthermore, we investigated differences in fenestration along the tonotopic axis of the MNTB. Frequency-based topography is the main organizing principle of the auditory system, including the MNTB. Therefore, we asked the question whether calyx fenestration varies with the location of the terminal within the MNTB, and thus with the sound frequency the neuron responds to. Using immunohistochemistry, we determined whether glial cells, which typically are the major mediators of glutamate reuptake from synaptic clefts, occupy the newly created windows in presynaptic terminals. Finally, we examined potential physiological differences in the clearance of transmitter between fenestrated and unfenestrated calyces.

MATERIALS AND METHODS

All experiments complied with institutional guidelines and were approved by the appropriate government authority (Reg. Oberbayern AZ 55.2-1-54-2531-58-05).

Cochlear ablations

Unilateral cochlear ablations were performed in four Mongolian gerbils (*Meriones unguiculatus)* of both sexes at postnatal days 9 or 10 (P9 and P10). At this age, cochlear ablation-induced cell death is not significant in the cochlear nucleus (Russell and Moore, 1995; Tierney et al., 1997; Vale and Sanes, 2002). Animals were anesthetized with a combination of medetomidin (Dormitor, Pfizer, Germany), midazolam (Midazolam, Ratiopharm, Germany), and fentanyl (Janssen, Netherlands) at 0.4, 4, and 0.04 μg/g body weight (BW), respectively.

A small incision was made $\approx$5 mm caudal to the auditory meatus and the bulla was opened with fine forceps. Under visual control the cochlea was aspirated with a fine glass pipette. The cavity was filled with gel foam and the wound was closed with commercially available cyanoacrylate glue.

When the animals were sacrificed at P14, the cochlea cavity was examined under a surgical microscope to confirm that the cochlea had been aspirated completely. Only animals in which the cochlea was completely absent on the ablated side were used.

Ototoxic drug application

Two gerbils were injected intraperitoneally with kanamycine (Sigma-Aldrich, St. Louis, MO) at P6 or P7 at a concentration of 500 mg/kg BW followed 2 hours later by a systemic injection of ethacrynic acid (Sigma, 50 mg/kg BW) dissolved in physiological NaCl (Izumikawa et al., 2005). Control animals were injected with corresponding volumes of saline.

Tracer injections

A total number of 17 gerbils, age between P10 and P25, were deeply anesthetized with sodium pentobarbital (50 mg/kg BW) and perfused with ice cold Ringer's solution for 2–3 minutes. The brainstems were quickly removed from the skull under ice-cold oxygenated low-calcium artificial cerebrospinal fluid (dissecting ACSF, 125 mM NaCl, 2.5 mM KCl, 1 mM $MgCl_2$, 0.1 mM $CaCl_2$, 25 mM glucose, 1.25 mM NaH_2PO_4, 25 mM $NaHCO_3$, 0.4 mM ascorbic acid, 3 mM myoinositol, 2 mM pyruvic acid; all chemicals from Sigma-Aldrich).

A 10% solution of tetramethylrhodamine dextran, MW 3000 (Invitrogen, La Jolla, CA) was pressure injected into the anterior ventral cochlear nucleus (AVCN) of brainstem explants with 15 PSI using a picospritzer (Picospritzer III, Parker, Cleveland, OH) followed by several electroporation pulse trains (modified from Burger et al., 2005). Pulses (50 ms) had an amplitude of 50V and were applied at a frequency of 10 Hz using an STG 1002 stimulator (Multichannel Systems, Germany) and an IsoFlex stimulation isolation unit (AMPI, Israel). Injections were made in several regions of the AVCN with the goal to fill the entire nucleus with tracer. Subsequently the explants were transferred to a chamber with oxygenated incubating ACSF (125 mM NaCl, 2.5 mM KCl, 1 mM $MgCl_2$, 2 mM $CaCl_2$, 25 mM glucose, 1.25 mM NaH_2PO_4, 25 mM $NaHCO_3$, 0.4 mM ascorbic acid, 3 mM myoinositol, 2 mM pyruvic acid; all chemicals from Sigma-Aldrich) for 4–5 hours to allow for active transport of the tracer. Thereafter, brainstems were immersion-fixed in ice-cold 4% formaldehyde solution for at least 24 hours.

Immunohistochemistry

Brainstems were embedded in agarose and cut into 80-μm thick sections for analysis of calyx morphology, or in 50-μm thick sections for immunohistochemistry using a vibratome (Leica). Unspecific staining of sections was blocked with 1% bovine serum albumin in phosphate-buffered saline (PBS, pH 7.4) with 0.5% Triton X-100 for 1 hour at room temperature. Then sections were incubated for 48 hours at 4°C in the same solution containing primary antibodies (see below). Slices

were washed three times in PBS for 10 minutes and incubated with secondary antibodies (Molecular Probes, Eugene, OR / Invitrogen, A11073 and A21034, 1:400; Chemicon, Temecula, CA AP193C, 1:300; Jackson ImmunoResearch, West Grove, PA Code No. 115076006, 1:200) for 2 hours at room temperature. After washing in PBS (3× 10 minutes), brain slices were counterstained with a NeuroTrace blue fluorescent Nissl stain (Invitrogen).

Antibody characterization

For GLAST a polyclonal guinea pig antiserum (Millipore, Bedford, MA; Cat. No. AB1782, 1:2,000) raised against a synthetic peptide (QLIAQDNEPEKPVADSETKM) from the carboxy-terminus of rat GLAST was used. Preabsorption of the antiserum with the immunogen peptide (Millipore, Cat. No. AG377) completely abolishes the immunostaining (manufacturer's technical information). The antiserum stains a band at ≈65 kDa molecular weight on Western blot of rat brain lysate (manufacturer's technical information).

For GLT1 a polyclonal guinea pig antiserum (Millipore, Cat. No. AB1783, 1:2,000) raised against a synthetic peptide (AANGKSADCSVEEEPWKREK) from the carboxy-terminus of rat GLT1 was used. Preabsorption of the antiserum with the immunogen peptide (Millipore, Cat. No. AG391) completely abolishes the immunostaining (manufacturer's technical information).

For S100β a polyclonal rabbit antiserum (Swant, Bellinzona, Switzerland, Code No. 37, 1:1,000) against purified bovine brain S100β was used. The S100β antiserum recognized the expected band at ≈10 kDa on Western blot of gerbil brain lysate.

For SV2 a monoclonal mouse antibody (Developmental Hybridoma Bank of the University of Iowa, 1:500) raised against highly purified synaptic vesicles from Ommata electric organ was used (Buckley and Kelly, 1985). The appearance of the calyces of Held with antibody staining was similar to that with the tracer injections.

Confocal microscopy and image processing

Image stacks were acquired with a Leica TCS SP or TCS SP5 confocal laser-scanning microscope (Leica Microsystems, Mannheim, Germany). Stacks used for analysis of calyx morphology were obtained with a 63× objective. The distance in z-axis between single optical sections was 0.5 μm. To obtain an improved signal-to-noise ratio, each section was averaged from six successive scans.

Three-dimensional reconstructions of image stacks and single calyces were obtained using the software ImageJ 1.37k (NIH, Bethesda, MD). The 3D reconstructions of single calyces and subsequent evaluations were done as a blind analysis performed by independent observers who were unaware of the age of the animals, the experimental status, and the location within MNTB from which the images were taken. A total of 5,664 calyces was reconstructed, analyzed, and categorized for this study. The five categories for the developmental stages were defined as follows.

Stage 1: Calyces are completely or almost completely closed, appear spoon- or cup-shaped, and are without any openings. Stage 2: Calyces are at an early stage of fenestration, are still mostly closed with some openings and jagged edges. The closed area consists of ≈60–80% of the calyx surface. Stage 3: Calyces are in a stage of intermediate fenestration. The closed surface covers about half of the total synapse surface. Stage 4: Calyces are mostly fenestrated, the closed surface covers ≈10–25% of the total synapse surface. Stage 5: Calyces are completely or almost completely fenestrated. (See also Fig. 3A.)

Images of immunolabeled sections were imported into Adobe Photoshop 8.0.1 (Adobe Systems, San Jose, CA) for optimizing contrast and for labeling and figure layout.

Electrophysiology

Gerbils aged P14 were briefly anesthetized by isoflurane inhalation (Isofluran Curamed, Curamed Pharma, Karlsruhe, Germany) and decapitated. The brain was dissected out under ice-cold low-sodium, high-sucrose artificial cerebrospinal fluid, containing (in mM): 85 NaCl, 2.5 KCl, 1.25 NaH_2PO_4, 25 $NaHCO_3$, 75 sucrose, 25 glucose, 0.5 $CaCl_2$, 4 $MgCl_2$, and 0.5 ascorbic acid (all chemicals from Sigma-Aldrich). Coronal brainstem slices (170–190 μm) containing the MNTB were cut with a vibratome (Leica). Slices were transferred to an incubation chamber containing extracellular solution (ECS) (in mM: 125 NaCl, 2.5 KCl, 1.25 NaH_2PO_4, 26 $NaHCO_3$, 25 glucose, 2 $CaCl_2$, and 1 $MgCl_2$; all chemicals from Sigma-Aldrich) and bubbled with 5% CO_2/95% O_2. Slices were incubated for 20 minutes at 37°C, after which the chamber was brought to room temperature.

Slices were transferred to a recording chamber and perfused (2–5 mL/min) with oxygenated ECS at room temperature. The MNTB principal cells were visualized with an upright BX51WI microscope (Olympus, Oberkochen, Germany) using a 40× water-immersion objective (LUMPlanFI, Olympus) and infrared-differential interference optics equipped with an infrared-sensitive digital camera (Marlin F-046B, Allied Vision Technologies, Ahrensberg, Germany).

Whole-cell voltage-clamp recordings were performed from MNTB principal cells with a Multiclamp 700B amplifier (Axon Instruments, Union City, CA). The signals were filtered with a low-pass Bessel filter at 10 kHz, sampled at 50–100 kHz, and digitized using a Digidata 1440A interface (Axon Instruments). Series resistance (3–7 MΩ) was compensated 10–80% to values below 3 MΩ with a lag time of 10 μs.

Borosilicate glass microelectrodes (GC150F-10, Harvard Apparatus, Edenbridge, UK) were pulled on a DMZ Universal Puller (Zeitz Instruments, Martinsried, Germany), yielding a final tip resistance of 2–4 MΩ.

For voltage-clamp recordings pipettes were filled with cesium gluconate-based internal solution (135 mM Cs-Gluconate, 10 mM Cs-HEPES, 20 mM TEA-Cl, 3.3 mM $MgCl_2$, 2 mM Na_2ATP, 0.3 mM Na_2GTP, 5 mM Cs_2-EGTA; all chemicals from Sigma-Aldrich). Five mM QX-314 (Alomone Labs, Jerusalem, Israel) was added to the pipette to eliminate sodium currents.

Synaptic inputs were elicited by stimulation with a glass electrode filled with ECS. 200-μs-long square pulses with an amplitude of 30–70 V were used as stimuli. Stimulus trains consisted of 15 pulses delivered at 100 Hz.

Evoked AMPA receptor-mediated EPSCs were isolated pharmacologically by adding 500 nM strychnine hydrochloride (Sigma-Aldrich), 20 μM SR95531 hydrobromide (Biotrend, Koln, Germany) and 100 μM DL-AP5 (Biotrend) to the ECS to block glycine, $GABA_A$, and NMDA receptors, respectively. The drug concentrations were identical to those routinely chosen for voltage clamp recordings from MNTB principal cells (Futai

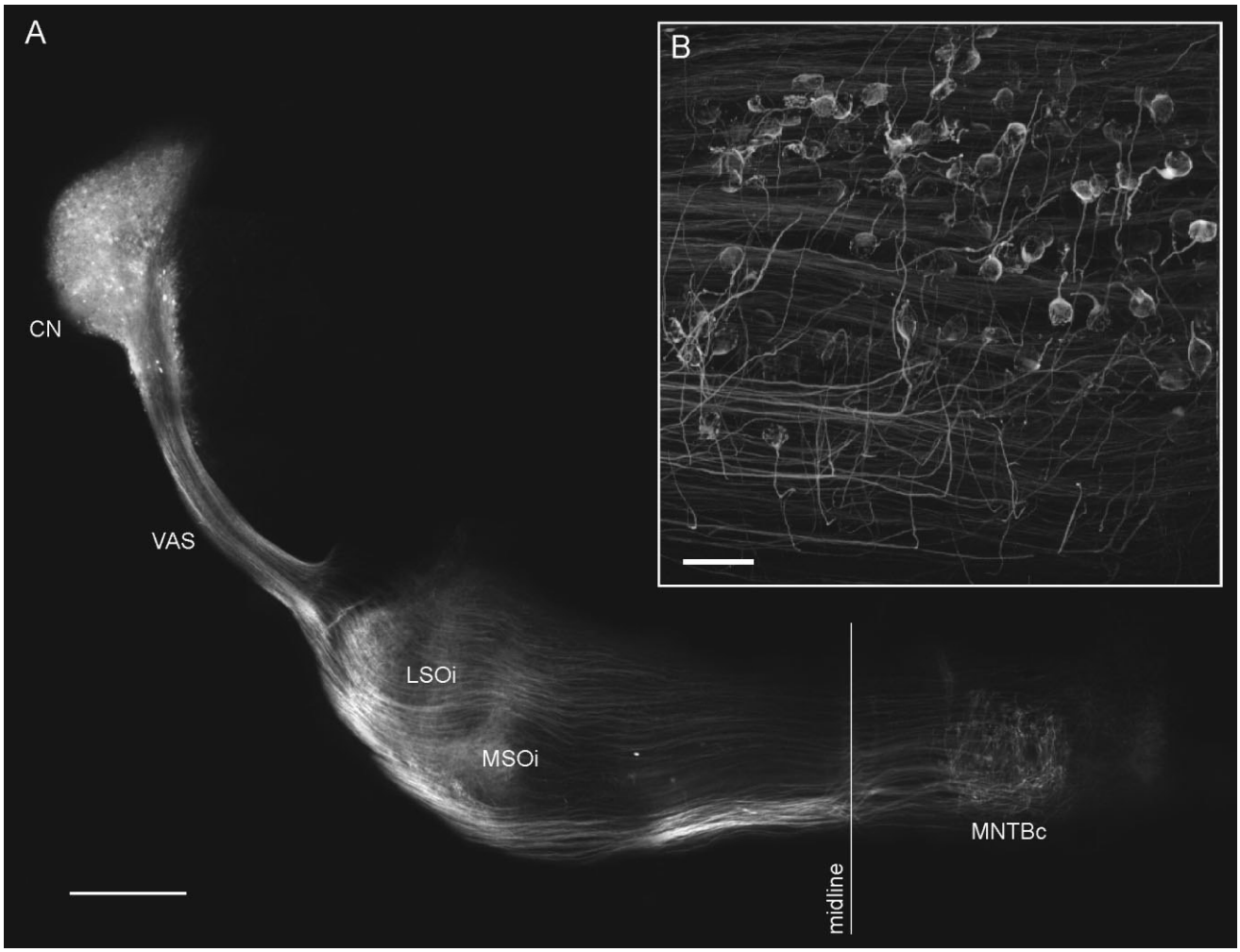

Figure 1.
Labeling of calyces of Held via tracer injections into the cochlear nucleus. **A:** Tetramethylrhodamine dextran-labeled projections from the cochlear nucleus (CN) to several nuclei of the SOC. VAS, ventral acoustic stria; LSOi, ipsilateral lateral superior olive; MSOi, ipsilateral medial superior olive; MNTBc, contralateral medial nucleus of the trapezoid body. **B:** Large portion of the MNTB with afferent axons and calyces of Held, P14. Scale bars = 500 μm in A; 50 μm in B.

et al., 2001; Awatramani et al., 2004, 2005). Desensitization of AMPA receptors was blocked with 100 μM Cyclothiazide (Tocris, St. Louis, MO) (Ishikawa and Takahashi, 2001; Sakaba and Neher, 2001).

Statistical analysis

Data were analyzed in Clampfit 10.1 (Molecular Devices, Palo Alto, CA), IGOR 5 (Wavemetrics), MS Excel 2004 (Microsoft, Redmond, WA), and SigmaStat 3.5 (Systat Software, Point Richmond, CA). Results are reported as mean ± standard error of the mean. Statistical significance was tested with a Student's *t*-test, provided the dataset passed the normality test and equal variance test. Otherwise, significance was tested using the Mann–Whitney Rank Sum Test.

Residual current in trains was calculated by averaging the EPSC amplitude of the last three EPSCs shortly before their onset. Residual currents are reported as percent of initial EPSC amplitude in each train. Decay time courses at the end of each train were fitted with a single exponential using the Chebychev algorithm implemented in Clampfit 10.1.

RESULTS

Visualization of calyx morphology via tracer injections into the cochlear nucleus

The first goal of the study was to document changes in the morphology of the calyx of Held during early postnatal development under control conditions and in response to the elimination of afferent input. In order to visualize calyx morphology, a number of tetramethylrhodamine (TMR) dextran tracer injections were made into the AVCN of explanted gerbil brainstems under visual guidance (see Materials and Methods). Figure 1A shows an overview of a sectioned brainstem that was injected with TMR dextran into the AVCN. Due to the fact that multiple injections were made throughout the AVCN, la-

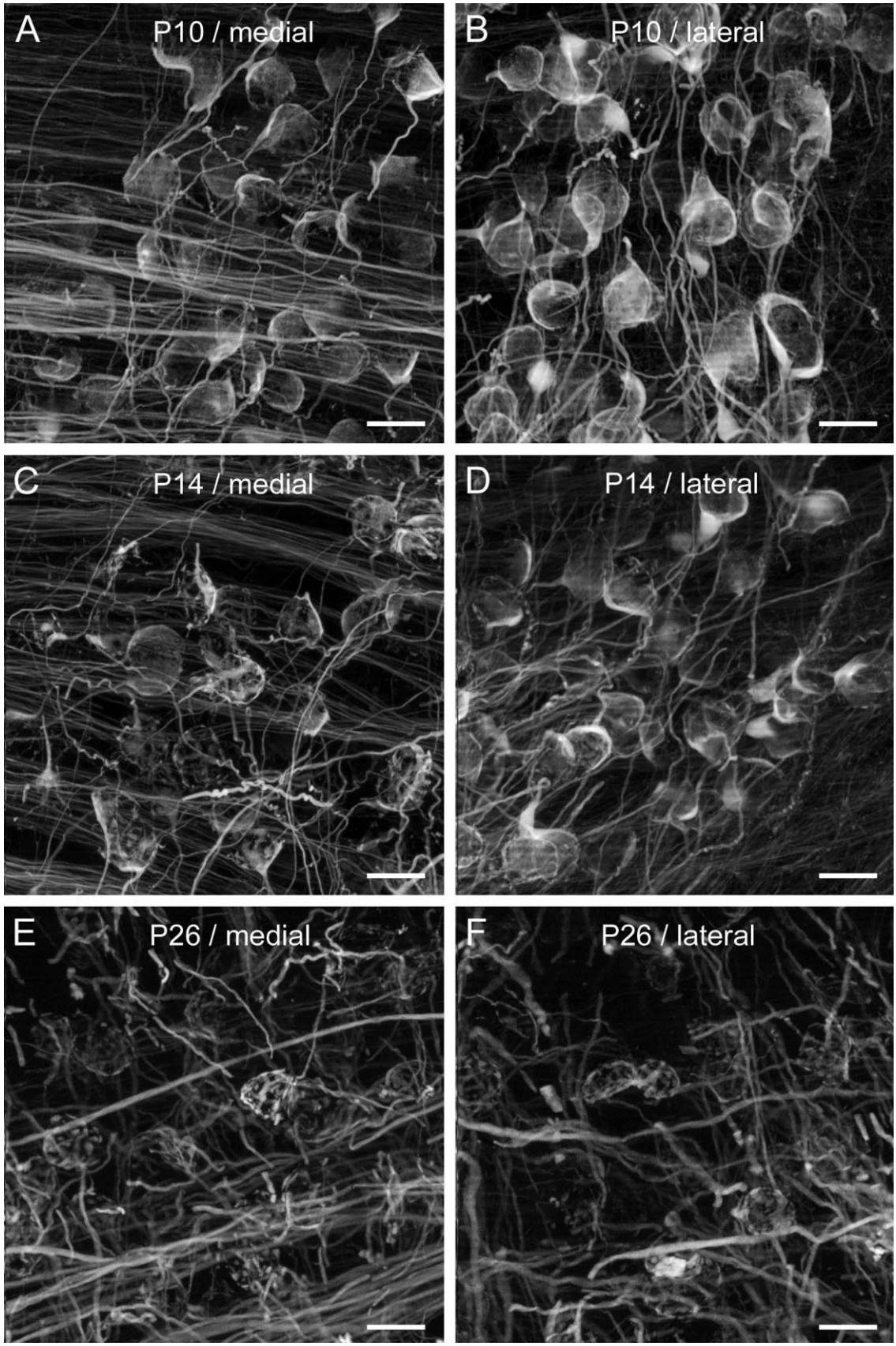

Figure 2.
Comparison of developmental states of calyx morphology between the medial and the lateral part of the MNTB at three different ages **(A,B:** P10; **C,D:** P14; **E,F:** P26). Images show maximum projections of image stacks obtained from the medial (left) and lateral (right) part of the MNTB. Scale bars = 20 μm.

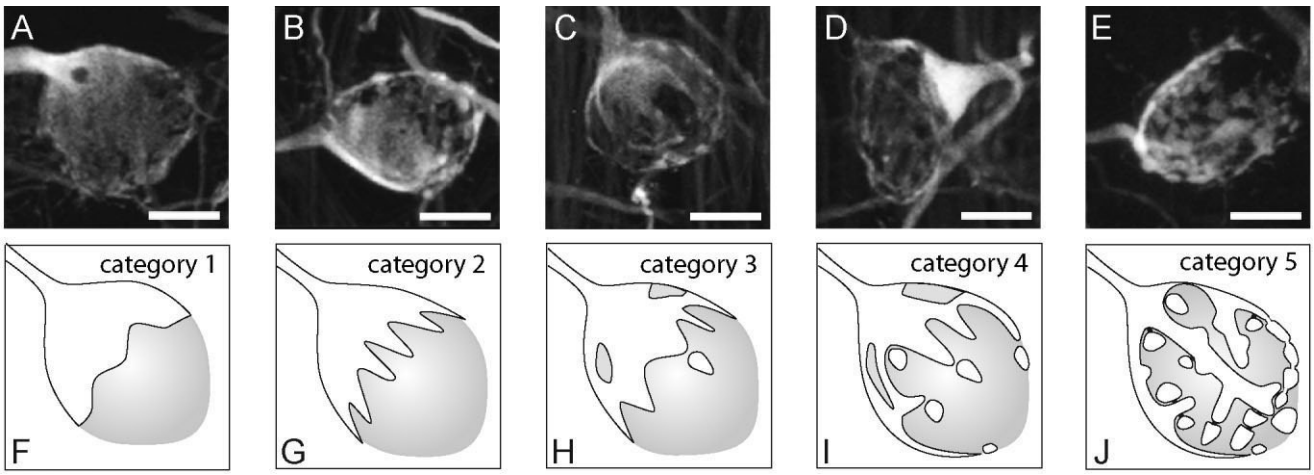

Figure 3.
Categories of calyx morphology. **A–E:** Maximum projections of confocal image stacks of single calyces, representing typical examples of the five developmental stages used in the morphological analysis. **F–J:** Schematic drawings corresponding to the original images shown above. The degree of fenestration increases from category 1 to category 5. Scale bars = 10 μm in A–E.

beling of neurons, presumably including globular and spherical bushy cells, occurred uniformly across the nucleus. Additionally, the efferent fibers of these neurons were labeled. These fibers run along the ventral acoustic stria and project to a number of auditory brainstem nuclei. One of their targets is the contralateral MNTB, where each fiber typically gives rise to one or more calyces of Held (Held, 1892; Hoffpauir et al., 2006; Rodriguez-Contreras et al., 2006).

Figure 1B shows a portion of the MNTB with a number of labeled calyces distributed throughout the nucleus as well as their afferent axons, which enter the nucleus from its ventral and medial aspect. The injections resulted in approximately equal labeling throughout the MNTB.

Changes in calyx morphology during early postnatal development

During the fenestration process, the initially spoon- or cup-shaped presynaptic structure develops into a structure with progressively larger openings in the cup, such that the remaining parts become progressively thinner and finger-like with attached swellings (Kandler and Friauf, 1993; Rowland et al., 2000; Wimmer et al., 2006). This progressive development was also observed in our data and is illustrated in Figure 2. At P10 the majority of calyces are completely or almost completely closed and cup-shaped (Fig. 2A,B). By contrast, in 26-day-old animals virtually all calyces appear completely fenestrated (Fig. 2E,F). At an intermediate age, P14, all developmental stages can be found (Fig. 2C,D), such that both cup-shaped and fenestrated calyces could be observed in the same section, sometimes directly adjacent to each other.

At the intermediate age at P14 there appeared to be systematic differences in calyx morphology between the lateral and the medial aspect of the MNTB, which had not been described previously. This point is illustrated by the two images in Figure 2C,D, which were both taken from the same anatomical section. Figure 2C shows calyces in the medial aspect of the MNTB, which are generally more fenestrated than those shown in Figure 2D, which were obtained from the lateral aspect of the same MNTB.

Classification of fenestration stages and mediolateral developmental gradient

In order to quantify the different stages of fenestration in younger and older animals and between the medial and lateral part of the MNTB, confocal image stacks were obtained from histological sections of the MNTB. One image stack was acquired from the medial part of the MNTB and a corresponding image stack was acquired from the lateral part of the MNTB of the same section. The MNTB is organized tonotopically, such that the neurons located medially process high-frequency sound information, while neurons located laterally process low-frequency sound information (Spirou et al., 1990; Saint Marie et al., 1999; Kopp-Scheinpflug et al., 2008). Maximum projections of such corresponding medial–lateral (or high-frequency / low-frequency) image stacks are shown in Figure 2.

From these confocal stacks, each labeled calyx was reconstructed in three dimensions independently by naïve observers and subsequently classified into one of five developmental categories. These categories ranged from completely closed and cup-shaped to completely fenestrated and mature (Fig. 3) and were: completely closed (stage 1, Fig. 3A,F), early fenestrated (stage 2, Fig. 3B,G), intermediate fenestrated (stage 3, Fig. 3C,H), late fenestrated (stage 4, Fig. 3D,I), completely fenestrated (stage 5, Fig. 3E,J). For the exact definition of each category, see Materials and Methods. Depending on the number of calyces labeled by the tracer injection, between 106 and 656 individual calyces could be reconstructed per animal. The total number of calyces reconstructed and analyzed for this study was 5,664. Figure 4A–C show results from this analysis for three sample animals at the three different ages P10, P14, and P26, respectively. A comparison between the three different ages shows several points: First, consistent with previous studies, calyx fenestration is more advanced at older ages (Kandler and Friauf, 1993; Kil et al., 1995). Second, the most important morphological changes in the fenestration process occur after P10 but before P26, because at P10 most calyces were completely closed (classified as developmental stage 1) while at P26 virtually all calyces were completely

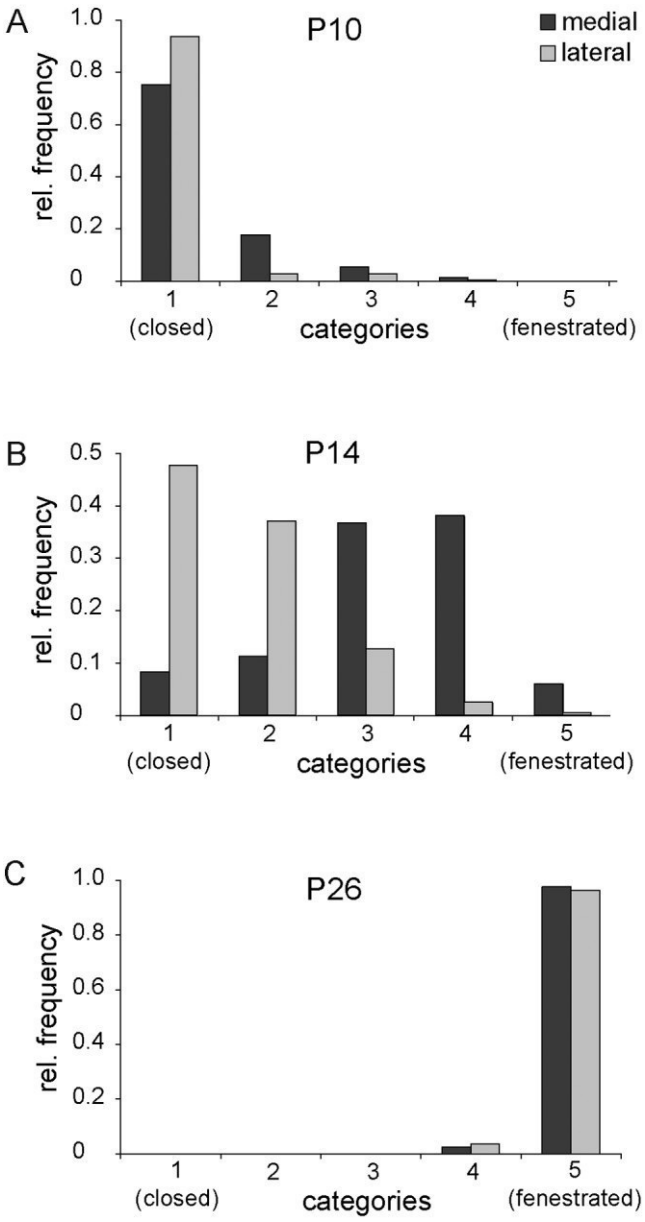

Figure 4.
Frequency distribution of categorized calyces for animals of three different age groups. Categories 1 to 5 are defined in the previous figure. **A:** Frequency distribution in a P10 animal, where the majority of both medially and laterally located calyces were still closed. However, medially located calyces appeared to be further progressed in fenestration. **B:** At P14, clear differences in fenestration could be observed between the medial and lateral part of the MNTB, with medially located calyces showing a higher degree of fenestration. **C:** At P26, the fenestration process appeared to be almost completed for both medially and laterally located calyces.

fenestrated (stage 5). Third, the fenestration process appears to be in full progress at P14, since at this age calyces at any developmental stage could be found in considerable numbers. Fourth and most important, at P14 a substantial difference in fenestration status between the medial and the lateral part of the MNTB could be observed. Among neurons located medially in the MNTB, most calyces were largely fenestrated (stage 4), while among most neurons located laterally the calyces were still completely closed (stage 1). This discrepancy was not observed in the younger (P10) or in the older animals (P26).

Figure 5A shows the results from our sample population of eight animals at age P14. In the lateral part of MNTB (gray bars), the largest proportion of calyces was still completely closed (category 1) and the smallest proportion was fully fenestrated. By contrast, completely closed calyces represented the least frequent category in the medial part of MNTB (black bars), and the proportions of further and further developed terminals increased monotonically, with the exception of category 5. Since the two distributions are largely or even completely monotonic but with opposite directions, the discrepancies in relative frequency with which a certain developmental category occurs medially or laterally is naturally greatest for categories 1 and 5 and smallest for the intermediate category 3. Therefore, differences were statistically significant between medial and lateral for category 1, 2, 4, and 5 (*t*-test or Mann–Whitney Rank Sum Test, *P*-values were 0.002, 0.01, 0.083, 0.01, 0.003, respectively).

A ratio plot of these differences further illustrates this mediolateral difference in fenestration status. The single points of the ratio plot shown in Figure 5C (gray line) were calculated by determining the ratio of the relative frequency of a given developmental category in the medial part of the MNTB and dividing by the relative frequency of the same category in the lateral part of the MNTB. The ratio plot increases monotonically itself, reflecting a mediolateral morphological gradient.

Eliminating afferent activity during early development prevents the establishment of the mediolateral gradient

One developmental milestone that occurs just prior to P14 is the onset of hearing at P12 (Woolf and Ryan, 1984). Before hearing onset, calyx activity is exclusively driven by spontaneous activity, while after hearing onset it is driven by both sound stimulation and spontaneous activity. As a result, neurons tuned to different sound frequencies receive trains of afferent activity with different frequencies and activity patterns. We therefore asked whether afferent nerve activity plays a role in the establishment of the mediolateral developmental gradient of calyx fenestration. The experimental approach was to remove afferent activity from developing calyces before the onset of hearing and determine subsequently whether the developmental gradient was established or not. Two methods were used for removing afferent activity, namely, surgical removal of the inner ear on one side at P9 or P10 (Vale and Sanes, 2002), and alternatively a systemic single dose injection of ototoxic antibiotics administered at P6 or P7 (Izumikawa et al., 2005). The first method removes afferent activity in the auditory nerve immediately after the surgical intervention, such that MNTB neurons located on the side contralateral to the surgical site lose their primary source of afferent input. The second method removes afferent activity from both ears through loss of inner ear hair cells; however, hair cell loss occurs over the course of several days such that the injection of ototoxic drugs has to be performed several days in advance of hearing onset.

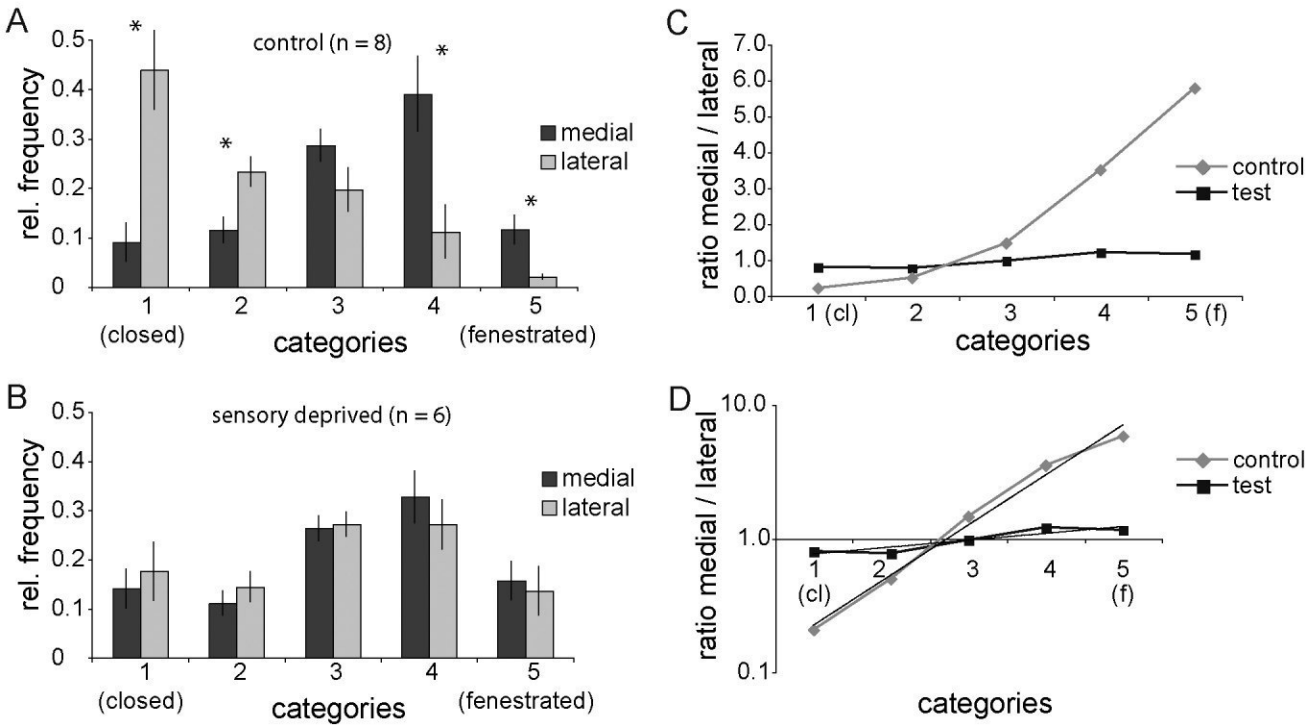

Figure 5.
Establishment of a morphological gradient along the mediolateral (tonotopic) axis is dependent on afferent activity. **A:** Distribution of relative frequency of categorized calyces in the medial and lateral part of the MNTB. The differences in relative frequency between medially and laterally located calyces were statistically significant for each category except category 3 under control conditions, indicating the existence of a morphological gradient between the medial and lateral part of the MNTB. Graph summarizes the data from eight animals. **B:** Distributions for six test animals of the same age, in which afferent activity was removed during development. In these animals none of the five categories showed significant differences in frequency between the medial and lateral part of the MNTB, indicating the absence of such a gradient. **C:** Medial/lateral ratio between relative frequencies of categorized calyces increases monotonically from category 1 to category 5, indicating that medial-lateral ratios are getting monotonically larger under control conditions (gray line). Ratios show values around 1 for animals in which afferent activity was removed during development (black line) **D:** Same data as in C replotted on a logarithmic scale.

Figure 6A,B shows a set of MNTB images taken at P14 from animals in which afferent activity was eliminated by surgically removing the inner ear. The images were obtained from the MNTB contralateral to the removed cochlea, i.e., from the nucleus to which the removed cochlea sends afferent inputs. The figure corresponds to Figure 2C,D and shows a comparison between the lateral and the medial third of the MNTB. While a comparison between the medially and laterally located calyces under control conditions shown in Figure 2C,D, respectively, reveals a clear difference in calyx fenestration, a difference is much less clear in the images shown in Figure 6A,B. Similar results were observed with animals in which afferent activity was removed via an injection of ototoxic drugs (images not shown). Therefore, removal of afferent activity with either one of the two methods seemed to decrease the differences in calyx fenestration between the medial and lateral part of the MNTB.

Labeled calyces from six animals with removed afferent activity (four animals: surgical removal of inner ear; two animals: injection of ototoxic drugs) were reconstructed in three dimensions, categorized, and quantified in the same way as was done for calyces from control animals (Fig. 5B). Although under control conditions significant differences between the medial and lateral part of MNTB were observed in almost all categories (Fig. 5A), these differences were absent in animals in which afferent activity was removed (Fig. 5B). A statistically significant difference between medial and lateral MNTB was not observed in any of the five developmental categories (*t*-test or Mann–Whitney Rank Sum Test, *P*-values 0.64, 0.42, 0.82, 0.46, 0.49, respectively). The corresponding ratio plot is shown in Figure 5C (black line) and contrasted with the data from control animals (gray line). We note that this linear plot visually underrepresents any ratios smaller than 1. In order to represent ratios both smaller and larger than one equally (e.g., 1:3 vs. 3:1), the plot shown in Figure 5C is replotted on a logarithmic scale in Figure 5D. The datasets could be well fitted with single exponentials (shown as straight lines in the logarithmic plots; $R^2 = 0.987$ for control, $R^2 = 0.831$ for test). In summary, the data suggest that the removal of afferent activity before onset of hearing removes developmental differences between the medial and lateral part of the MNTB and, thus, we conclude that afferent activity must play a substantial role in the establishment of these developmental differences. Nevertheless, the fenestration process per se does not appear to be stopped by the removal of afferent activity, since fenestration has progressed between P10 (when cochlea removals were performed) and P14 despite the absence of afferent activity (compare Figs. 4A with 5B).

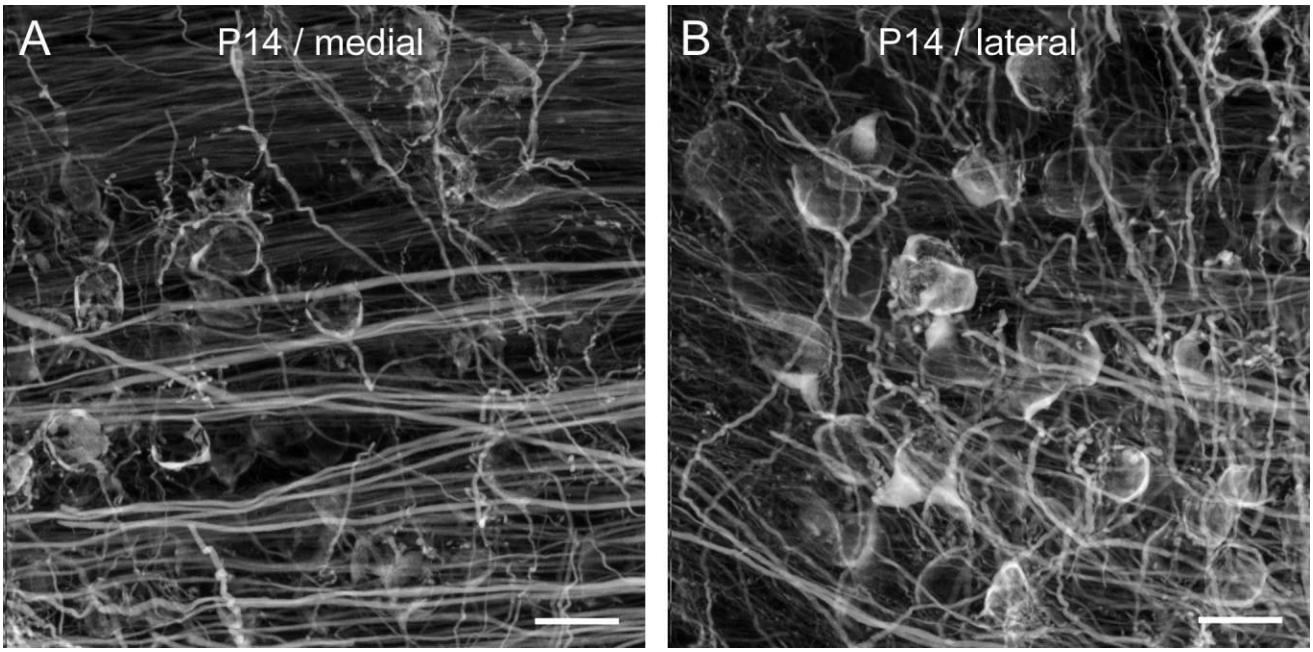

Figure 6.
Labeled calyces of Held in the medial and lateral part of the MNTB of a P14 animal in which afferent activity was removed at P10 by ablating the contralateral cochlea. Images show maximum projections of image stacks obtained from the medial **(A)** and lateral **(B)** part of the MNTB in a P14 animal that underwent unilateral cochlear ablation at P10.

Glial processes with high densities of glutamate transporters in the plasma membrane occupy the windows developing in the presynaptic terminal

Fenestration is one developmental change that the calyx of Held undergoes during the first postnatal weeks. A number of other changes accompany the fenestration and typically result in an increased temporal precision of the transmission process (Taschenberger and von Gersdorff, 2000; Taschenberger et al., 2002; von Gersdorff and Borst, 2002; Meinrenken et al., 2003; Koike-Tani et al., 2005; Schneggenburger and Forsythe, 2006). Calyx fenestration most likely is an important step in improving temporal precision, since the windows in the presynaptic terminal shorten the diffusion pathways for transmitter, in this case glutamate, out of the synaptic cleft. The bulk of glutamate is subsequently taken up by astrocytes, which contain high densities of glutamate transporters (Gegelashvili and Schousboe, 1997). We therefore asked the question whether the open spaces resulting from calyx fenestration would be occupied by glial processes that could facilitate a faster clearance of synaptic transmitter. Of five cloned glutamate transporters, two have been shown to be present predominantly in astrocytes: glutamate aspartate transporter (GLAST) and glutamate transporter 1 (GLT1) (Gegelashvili and Schousboe, 1997; Williams et al., 2005). The localization of GLAST and GLT1 at calyces of Held during different developmental stages as well as potential physiological consequences have not been investigated so far.

We performed antibody staining against GLAST as well as the astrocyte marker S100β (Fig. 7A–F). At lower magnification, S100β and GLAST labeling result in similar staining patterns (Fig. 7A-C), suggesting that S100β and GLAST are expressed in the same cells. At higher magnification, colocalization of the two proteins can be detected in glial processes (Fig. 7D–F). Figure 7G,H shows sections in which calyces had been visualized via tracer injections with tetramethylrhodamine dextran (red) and immunohistochemical stainings had been performed against the glutamate transporter GLAST (green). Figure 7I shows a calyx that had been visualized via tracer injection as well, followed by immunostaining against GLT1 (also green). The image shown in Figure 7G was obtained from the lateral aspect of the MNTB and shows a calyx which is still mostly closed. In cross section, the calyx covers a large portion of the postsynaptic cell (gray) in a relatively uninterrupted way and thus shows only very few openings. Glutamate transporters are restricted to those few openings, and to the area outside the calyx. By contrast, the calyx in Figure 7H, which was located in the medial part of the MNTB, is highly fenestrated and shows a large number of openings in cross section. GLAST-positive immunoreactivity can be detected consistently in these windows, indicating that glial processes with large quantities of the glutamate transporter occupied these openings. The second glial glutamate transporter, GLT1, is also clearly detectable in these openings and has a similar distribution pattern as GLAST (Fig. 7I). Thus, one consequence of calyx fenestration is the occupation of the newly created open spaces by glial processes containing glutamate transporters, presumably to accomplish reuptake of glutamate from the synapse as fast as possible, facilitating the termination of synaptic events.

The same conclusion can be drawn when presynaptic terminals were labeled with an antibody against the synaptic vesicle protein SV2 and glial elements were visualized

with an antibody against the astrocyte marker S100β (Fig. 7J). Glial processes (green) can be detected consistently in the spaces between the presynaptic elements (red) but do not colocalize (see also higher magnification, Fig. 7K,L). As a further control, we obtained images of retrogradely traced MNTB principal neurons (located in the MNTB ipsilateral to the injection site of the tracer) in a section that was immunolabeled against GLAST. The image in Figure 7M shows a labeled principal cell (red) surrounded by astrocytic processes containing GLAST (green). No colocalization can be detected, suggesting the absence of the glutamate transporter in principal neurons. Unlabeled spaces surrounding the postsynaptic cell presumably are occupied by (unlabeled) presynaptic elements.

Taken together, these data suggest that GLAST-positive immunoreactivity can be detected exclusively in astrocytes and is absent in both presynaptic and postsynaptic elements.

Calyx fenestration influences the decay of synaptic currents

To test for physiological consequences of calyx fenestration and occupation of the created windows by glial processes with high densities of glutamate transporters, we performed a series of patch clamp recordings. Slices were prepared from P14 animals, and MNTB postsynaptic neurons were voltage clamped to −60 mV while fibers that give rise to calyces were electrically stimulated to elicit synaptic events. Each calyx action potential resulted in vesicle release, such that excitatory postsynaptic currents (EPSCs) could be recorded from the postsynaptic neuron. AMPA receptor-mediated currents were pharmacologically isolated via the application of glycine, $GABA_A$, and NMDA receptor antagonists. Additionally, the effects of sodium and potassium currents were reduced via blockers in the intracellular solution (see Materials and Methods).

Measurements were taken from principal neurons located in both the medial third of the MNTB and the lateral third. Figure 8A shows a response of a MNTB neuron located in the medial third of the nucleus to a train of 15 pulses, delivered at 100 Hz. This short train is intended to simulate a very simple auditory stimulus such as a tone burst, which is commonly used in auditory research. The black trace in Figure 8A shows the response of the postsynaptic neuron to the stimulus train under control conditions, i.e., a series of EPSCs that progressively depress during the course of the stimulus train. The stimulus frequency of 100 Hz created short interstimulus intervals, which did not allow for complete decay of the postsynaptic current after each single event. This resulted in a build-up of residual current during the course of the stimulus train. This current decayed only after the final stimulus in the train had been presented. When the drug cyclothiazide (CTZ) was washed in to block desensitization of AMPA receptors, the residual current increased even further. In the example shown in Figure 8A, the residual current in CTZ was about 15% of the first EPSC amplitude in the train (indicated by dashed line), a fairly typical value observed for neurons located in the medial region of P14 MNTB neurons (Fig. 8C). By contrast, a sample neuron recorded from the lateral region of the MNTB (Fig. 8B) showed a residual current of about 30%, a typical value observed for neurons located in this region of the MNTB at P14 (Fig. 8C). Consistent with the idea that a higher degree of calyx fenestration results in faster clearance of neurotransmitter, the data from our physiological recordings suggest that calyces with a higher degree of fenestration exhibit less residual current. For our sample of 10 neurons, the residual current observed in lateral neurons was more than twice that observed in medial neurons. This difference was statistically significant (Fig. 8C; mean residual current medial = 12.5 ± 4.65% of initial EPSC amplitude, n = 5; mean residual current lateral = 36.6 ± 4.77% of initial EPSC amplitude, n = 5; *t*-test $P = 0.004$).

The decay time constants of the last EPSCs at the end of the trains were determined by fitting a single exponential. For neurons recorded from the lateral third of the MNTB, this time constant was about twice as long as the decay time constants measured in corresponding medial neurons. This difference was statistically significant (Fig. 8D; mean decay time constant (t) medial = 24.54 ± 1.88 ms, n = 5; mean decay time constant (t) lateral = 48.53 ± 7.27 ms, n = 5; *t*-test $P = 0.013$). These differences were not due to synaptic current amplitude differences between medial and lateral synapses (Fig. 8E; mean values 14.6 ± 0.86 nA and 13.4 ± 0.79 nA; n = 5 in both cases; *t*-test not significant), and suggest that the anatomical changes in calyx fenestration shown above have consequences for synaptic transmission at the calyx of Held. Specifically, higher degrees of fenestration go along with faster decay of synaptic events and lower amounts of residual glutamate in the synaptic cleft.

DISCUSSION

There are four main findings in this study: First, the fenestration of the calyx of Held during early postnatal development does not occur uniformly, but rather sequentially along the tonotopic axis. Specifically, fenestration occurs earlier in neurons tuned to higher sound frequencies compared to neurons tuned to lower sound frequencies such that at postnatal day 14 a large developmental difference between high- and low-frequency neurons can be observed. Second, the time course of calyx fenestration depends at least partially on afferent activity, because the developmental difference in fenestration between low- and high-frequency neurons is absent in animals that were deprived of auditory afferent input during early postnatal development. Nevertheless, the fenestration process continues even in deafferentiated calyces, suggesting that fenestration per se may not be activity dependent. Third, astrocytes extend processes into the openings of the presynaptic terminal that are created during the fenestration process. These processes contain high concentrations of the glial glutamate transporters GLT-1 and GLAST in the plasma membrane. Fourth, calyx fenestration goes along with synaptic currents with faster decay time constants, such that synaptic events become more temporally precise, a feature that is consistent with the functional role of the calyx of Held in the sound localization pathway.

Via the calyx of Held, MNTB neurons receive afferent input from globular bushy cells of the cochlear nucleus and send glycinergic projections to various targets of the auditory brainstem, including the medial and lateral nuclei of the superior olivary complex (Held, 1891; Moore and Caspary, 1983; Spangler et al., 1985; Bledsoe et al., 1990; Kuwabara and Zook, 1991; Smith et al., 1991; Banks and Smith, 1992). Both nuclei are involved in sound localization through the analysis of interaural time- and intensity disparities, respectively (ITDs

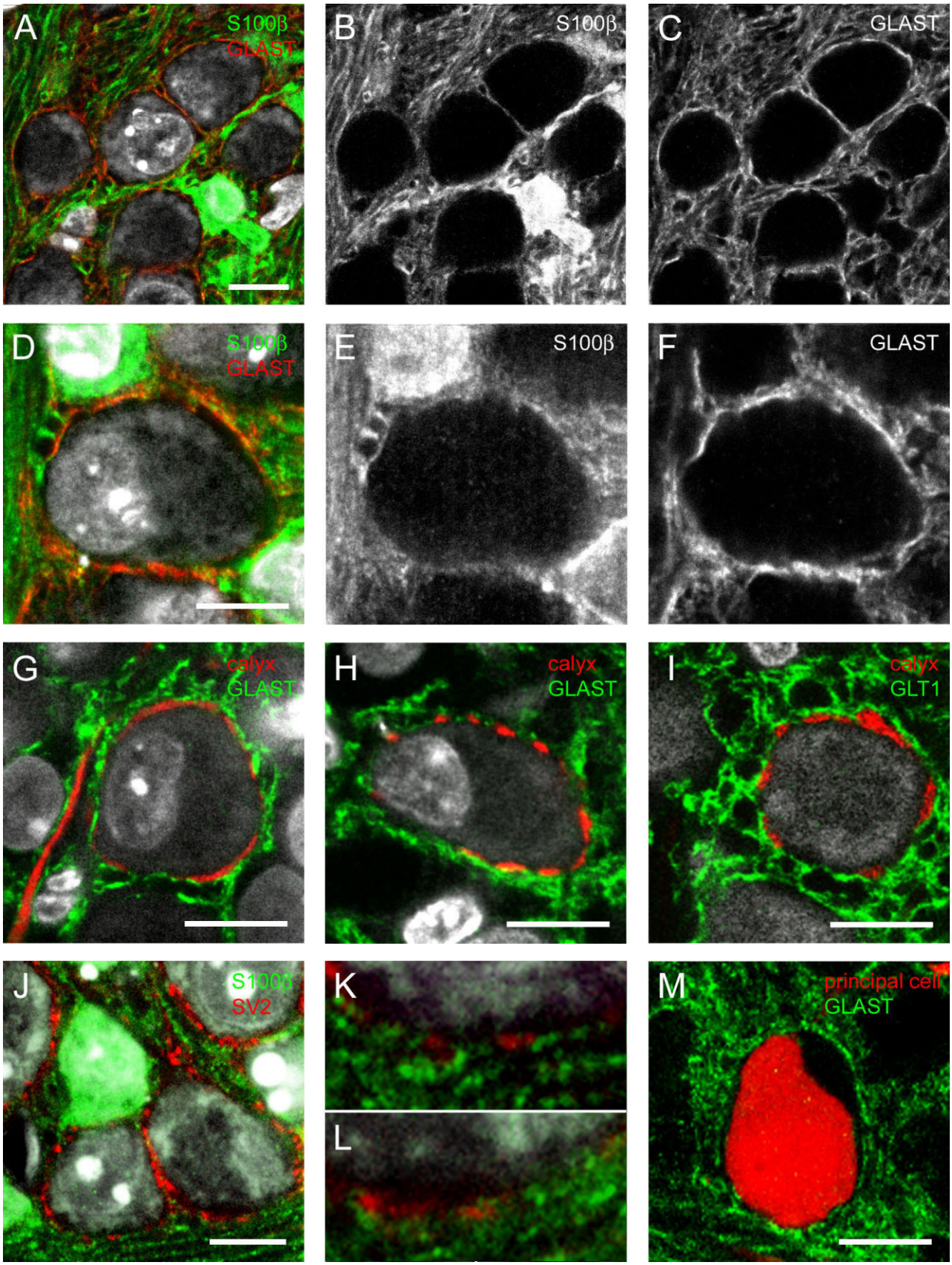
A
S100β
GLAST
B
S100β
C
GLAST
D
S100β
GLAST
E
S100β
F
GLAST
G
calyx
GLAST
H
calyx
GLAST
I
calyx
GLT1
J
S100β
SV2
K
L
M
principal cell
GLAST

Figure 7

and IIDs). The computations of ITDs and ILDs critically depend on temporal precision on a microsecond time scale (Goldberg and Brown, 1969; Caird and Klinke, 1983; Trussell, 1997; Oertel, 1999; Grothe, 2003; Pecka et al., 2008). Consistent with the high premium on temporal fidelity, the calyx of Held shows a number of specializations for temporal precision. The large size of the synapse as well as the direct synaptic contact to the soma of the electrically compact postsynaptic neuron are seen as such specializations (von Gersdorff and Borst, 2002). Several days before hearing onset, the presynaptic terminal covers about 40% of the surface area of the postsynaptic cell in a continuous fashion (Satzler et al., 2002). One problem with this closed morphology in combination with the large size of the calyx is the long diffusional pathways of released glutamate out of the synaptic cleft, before it can be taken up by transporters. A consequence of this impaired glutamate clearance is a higher probability of glutamate to rebind postsynaptic receptors, and thus prolonged synaptic events, i.e., synaptic currents with slow decay time constants. Before hearing onset, the postsynaptic cell contains AMPA receptor subunits that quickly desensitize in response to glutamate, such that receptor desensitization is a major mechanism that terminates synaptic events (Neher and Sakaba, 2001; Scheuss et al., 2002; Wong et al., 2003). However, in the first 2 weeks of postnatal development the AMPA receptors undergo a change in subunit composition. By hearing onset the GluR4 flop variant, the fastest variation of AMPA receptor subunits, is the dominant type (Koike-Tani et al., 2005). Receptor desensitization has only a minor influence on EPSC decay at this age (Taschenberger et al., 2002, 2005; Renden et al., 2005). The creation of diffusional exits in the presynaptic terminal, therefore, plays a crucial role in controlling the distance between release sites of transmitter and those sites where glutamate reuptake occurs, and thus has an effect on the decay of synaptic events.

Our data suggest that the fenestration occurs sequentially along the tonotopic axis, and that afferent activity plays a role in the establishment of this developmental gradient. Hearing onset in gerbils occurs at P12 (Woolf and Ryan, 1984), such that at P14, calyces would have experienced about 2 days of sound-evoked afferent activity. Therefore, it seems plausible that the particular activity patterns of high- versus low-frequency neurons might be responsible for the differential degree of fenestration observed at this age. Consistent with this hypothesis is the result that animals in which afferent activity had been eliminated before hearing onset do not show this gradient. However, note that best frequencies along the basilar membrane have been shown to change during development (Kossl et al., 2003; Russell et al., 2003), such that the input frequencies to particular single calyces might also change.

On the other hand, our data from P10 indicate that the fenestration process, although still at a very early stage, has nevertheless begun 2 days before hearing onset. It is therefore unlikely that sound-evoked activity could have influenced these early steps of fenestration. Spontaneous cochlear based afferent activity, as has been shown to occur in the developing auditory system before hearing onset (Lippe, 1994; Jones et al., 2001; Lu et al., 2007; Tritsch et al., 2007), is most likely the cause of the observed effect. Either different spontaneous activity patterns between high- and low-frequency areas might be responsible for the sequential fenestration, or the sequential development of other components along the pathway between inner ear and MNTB. Such sequential development has been shown, e.g., for hair cells, supporting cells, or spiral ganglion cells (Ruben, 1967; Souter et al., 1995, 1997), but have not been tested for in brainstem nuclei such as the MNTB. However, there is evidence from the avian auditory system suggesting that high-frequency areas of auditory brain stem nuclei start to function earlier than low-frequency areas of the same nucleus (Hackett et al., 1982; Jackson et al., 1982). It is therefore possible that high-frequency MNTB neurons receive electrical inputs from the cochlear nucleus before the corresponding low-frequency areas, and that the fenestration process is influenced by this activity.

Although a number of studies are available that describe calyx fenestration, none of these studies mentions differences based on the location along the tonotopic axis (Kandler and Friauf, 1993; Kil et al., 1995; Hoffpauir et al., 2006; Rodriguez-Contreras et al., 2008). The most likely reason for this discrepancy is that the older studies did not target specifically high- or low-frequency areas when analyzing the histological sections. Since in each section a variety of developmental stages can be observed even among neurons directly adjacent to each other, any tonotopy-based differences might easily be overlooked unless an explicit effort is made to separate between data from low- versus high-frequency areas.

Some previous studies present evidence supporting a role of afferent activity on the development of morphological and physiological properties of the calyx of Held, while other studies deny such a role. For example, Erazo-Fisher et al. (2007) report differences in postsynaptic currents recorded from control animals versus transgenic animals that were deprived of afferent activity during development. By contrast, Youssoufian et al. (2005, 2008) found no physiological or morphological consequences on the calyx of Held from congenital deafness. Although none of these studies discriminate between lateral and medial parts of the MNTB, our own findings are more consistent with the first study. While species or age differences, or the physiological hearing range of the experimental subjects, cannot be ruled out as one reason for these

Figure 7.
Occupation of diffusional exits by glial processes containing glutamate transporters. **A–C:** Colocalization of S100β, an astrocyte marker protein with GLAST. The images in B,C show that the labeling patterns of S100β and GLAST are very similar. **D–F:** MNTB principal neuron with adjacent astrocytes imaged at higher magnification. Colocalization between S100β and GLAST can be detected. Consistent with its cytosolic localization, S100β immunoreactivity can be observed in astrocyte somata as well as processes. GLAST, which is a transmembrane protein, appears to be localized in the plasma membrane of astrocytic processes, but not in the cytosol. **G,H:** Immunoreactivity for GLAST (green) at a weakly (G) and a highly (H) fenestrated calyx of Held (red). I: Immunoreactivity for GLT1 (green) in glial cells surrounding a highly fenestrated calyx of Held (red). Calyces (visualized via tracer injections in G–I) were immunonegative for both GLAST and GLT1. **J–L:** Double labelings of S100β and the synaptic vesicle protein SV2 (visualizing presynaptic terminals) show a similar result as seen in G–I, namely, the invasion by glial cells of the spaces between calyceal elements. Two regions of J are show in in K,L at higher magnification (lower left = K and lower right = L). **M:** Immunoreactivity for GLAST was absent in MNTB principal cells (red, labeled via retrograde tracing). Scale bars = 10 μm (in A,D also apply to B–C and E–F).

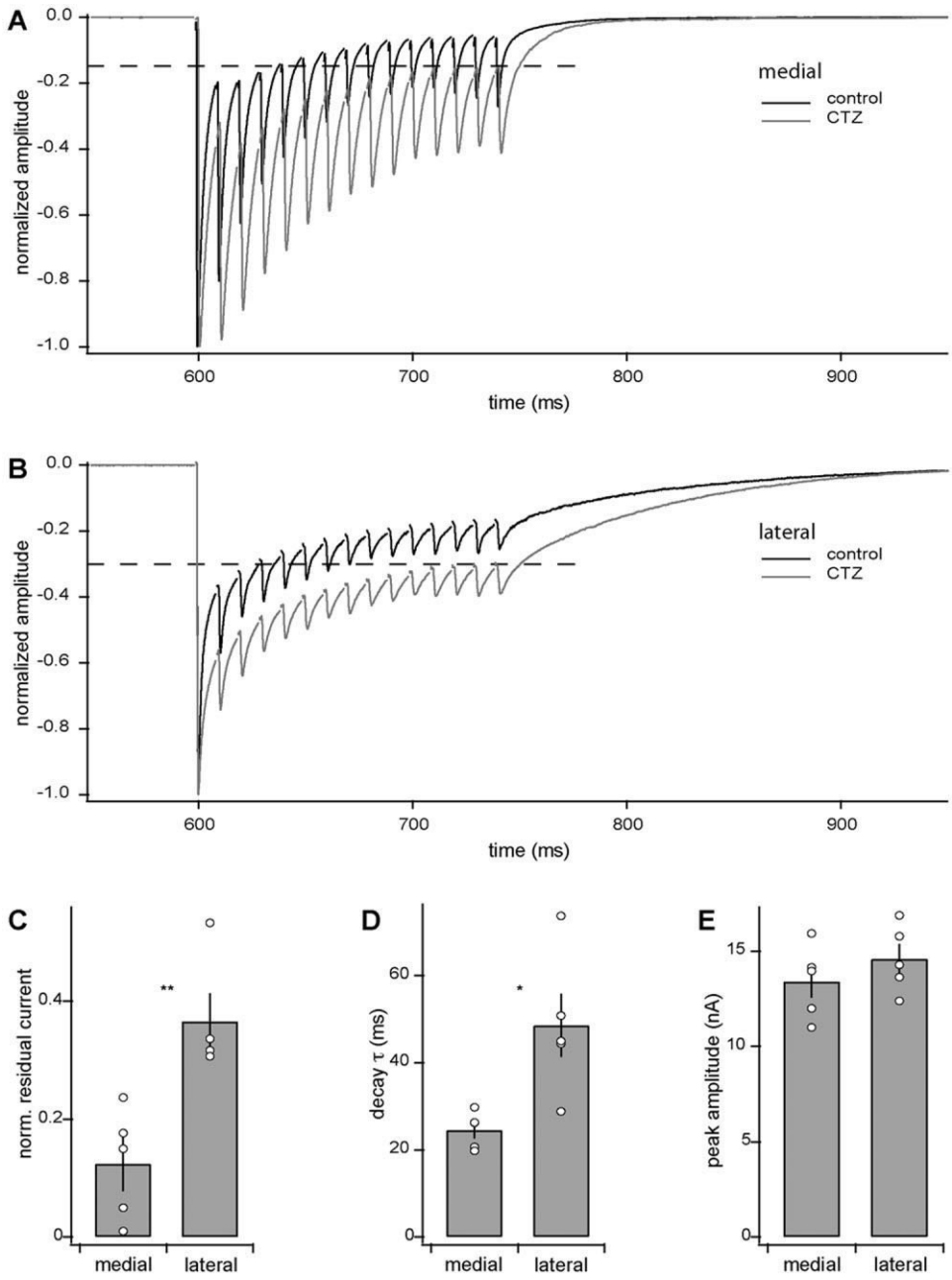

Figure 8.
Differences in glutamate clearance along the tonotopic axis of the MNTB at P14. **A,B:** EPSC trains of 15 pulses at 100 Hz recorded from principal cells located in the medial (A) and lateral (B) part of the MNTB in the absence (black) and presence (gray) of 100 μM CTZ. Traces are normalized to the amplitude of the first EPSC in the train. Dashed lines indicate the amplitude of the steady-state residual current. **C:** Values of normalized steady-state residual currents recorded from principal cells located medially (n = 5) and laterally (n = 5) in the MNTB. Open circles indicate values recorded from single neurons. The differences between the two groups are highly significant ($P = 0.004$). **D:** Differences in time constants describing the decay time course after the last EPSC in evoked trains. The differences between the two groups are statistically significant ($P = 0.013$). **E:** Peak amplitudes of EPSCs recorded from cells with a medial location in the MNTB were not significantly different from those recorded from cells located laterally in the nucleus.

discrepancies, the experimental method of removing afferent activity almost certainly has a major influence on the outcome of the experiments. For example, transgenic animals do not exhibit afferent activity from birth or even before, while on the other hand compensatory mechanisms (i.e., upregulation of other proteins to compensate for the loss of function of the manipulated protein) can never be ruled out, and have been shown to influence the outcome of experiments (van Brederode et al., 2001; Kopp-Scheinpflug et al., 2003). Cochlear removals are certainly very effective in removing afferent ac-

tivity, but should not be performed in animals before P9 or P10 due to degeneration problems, especially not on both ears (Russell and Moore, 1995; Vale and Sanes, 2002). Ototoxic drugs affect both ears and are relatively easy to perform, but can also not be performed in very young and small animals. Additionally, a common concern with ototoxic drugs is that complete deafness in all frequency bands is difficult to achieve, as apical hair cells are more resistant to ototoxic damage (Selimoglu, 2007). In the experiments reported here, similar effects for cochlear removal and ototoxic drugs were observed, suggesting that both methods yielded similar and acceptable results. Moreover, the results suggest that the specific drawbacks of each method, i.e., degeneration in case of cochlear removal and incomplete deafness in the case of the ototoxic drugs, were either absent in our case, or small enough to not compromise the outcome of the experiments.

Our data show a case where afferent activity influences the time course of development of a presynaptic terminal and plays a role in the establishment of a morphological gradient. Moreover, the morphological changes go along with changes in the properties of synaptic transmission supporting temporal fidelity, which in turn supports the functional role this circuit plays. Additionally, we show that glial processes occupy the windows created during the fenestration process, and thus respond to the morphological changes as well as presumably play a role in the processing of neural activity in the system.

ACKNOWLEDGMENTS

Otto Albrecht and Ludwig Feldmann performed the 3D reconstructions and blind analyses of the 5,664 calyces. Olga Alexandrova assisted with image evaluations, Matthias Starck and Bea Stiening provided valuable technical advice, and the members of the Division of Neurobiology at LMU contributed with helpful discussions and suggestions. Olga Alexandrova and Mario Wullimann gave helpful comments on an earlier version of the article. The monoclonal mouse SV2 antibody developed by Kathleen M. Buckley was obtained from the Developmental Studies Hybridoma Bank developed under the auspices of the NICHD and maintained by The University of Iowa, Department of Biological Sciences, Iowa City, IA 52242.

LITERATURE CITED

Awatramani GB, Turecek R, Trussell LO. 2004. Inhibitory control at a synaptic relay. J Neurosci 24:2643–2647.

Awatramani GB, Turecek R, Trussell LO. 2005. Staggered development of GABAergic and glycinergic transmission in the MNTB. J Neurophysiol 93:819–828.

Banks MI, Smith PH. 1992. Intracellular recordings from neurobiotin-labeled cells in brain slices of the rat medial nucleus of the trapezoid body. J Neurosci 12:2819–2837.

Bledsoe SC Jr, Snead CR, Helfert RH, Prasad V, Wenthold RJ, Altschuler RA. 1990. Immunocytochemical and lesion studies support the hypothesis that the projection from the medial nucleus of the trapezoid body to the lateral superior olive is glycinergic. Brain Res 517:189–194.

Brand A, Behrend O, Marquardt T, McAlpine D, Grothe B. 2002. Precise inhibition is essential for microsecond interaural time difference coding. Nature 417:543–547.

Buckley K, Kelly RB. 1985. Identification of a transmembrane glycoprotein specific for secretory vesicles of neural and endocrine cells. J Cell Biol 100:1284–1294.

Burger RM, Cramer KS, Pfeiffer JD, Rubel EW. 2005. Avian superior olivary nucleus provides divergent inhibitory input to parallel auditory pathways. J Comp Neurol 481:6–18.

Caird D, Klinke R. 1983. Processing of binaural stimuli by cat superior olivary complex neurons. Exp Brain Res 52:385–399.

Erazo-Fischer E, Striessnig J, Taschenberger H. 2007. The role of physiological afferent nerve activity during in vivo maturation of the calyx of Held synapse. J Neurosci 27:1725–1737.

Forsythe ID, Barnes-Davies M. 1993. The binaural auditory pathway: excitatory amino acid receptors mediate dual timecourse excitatory postsynaptic currents in the rat medial nucleus of the trapezoid body. Proc R Soc Lond B 251:151–157.

Futai K, Okada M, Matsuyama K, Takahashi T. 2001. High-fidelity transmission acquired via a developmental decrease in NMDA receptor expression at an auditory synapse. J Neurosci 21:3342–3349.

Gegelashvili G, Schousboe A. 1997. High affinity glutamate transporters: regulation of expression and activity. Mol Pharmacol 52:6–15.

Goldberg JM, Brown PB. 1969. Response of binaural neurons of dog superior olivary complex to dichotic tonal stimuli: some physiological mechanisms of sound localization. J Neurophysiol 32:613–636.

Grothe B. 2003. New roles for synaptic inhibition in sound localization. Nat Rev Neurosci 4:540–550.

Hackett JT, Jackson H, Rubel EW. 1982. Synaptic excitation of the second and third order auditory neurons in the avian brain stem. Neuroscience 7:1455–1469.

Heffner RS, Heffner HE. 1988. Sound localization and use of binaural cues by the gerbil (Meriones unguiculatus). Behav Neurosci 102:422–428.

Held H. 1891. Die centralen Bahnen des Nervus acusticus bei der Katze. Archiv für Anatomie und Physiologie — Anatomische Abteilung Year 1891:271–291.

Held H. 1892. Die Endigungsweise der sensiblen Nerven im Gehirn. Archiv für Anatomie und Physiologie — Anatomische Abteilung Year 1892: 33–39.

Hoffpauir BK, Grimes JL, Mathers PH, Spirou GA. 2006. Synaptogenesis of the calyx of Held: rapid onset of function and one-to-one morphological innervation. J Neurosci 26:5511–5523.

Ishikawa T, Takahashi T. 2001. Mechanisms underlying presynaptic facilitatory effect of cyclothiazide at the calyx of Held of juvenile rats. J Physiol 533(Pt 2):423–431.

Izumikawa M, Minoda R, Kawamoto K, Abrashkin KA, Swiderski DL, Dolan DF, Brough DE, Raphael Y. 2005. Auditory hair cell replacement and hearing improvement by Atoh1 gene therapy in deaf mammals. Nat Med 11:271–276.

Jackson H, Hackett JT, Rubel EW. 1982. Organization and development of brain stem auditory nuclei in the chick: ontogeny of postsynaptic responses. J Comp Neurol 210:80–86.

Jones TA, Jones SM, Paggett KC. 2001. Primordial rhythmic bursting in embryonic cochlear ganglion cells. J Neurosci 21:8129–8135.

Joris PX, Carney LH, Smith PH, Yin TC. 1994. Enhancement of neural synchronization in the anteroventral cochlear nucleus. I. Responses to tones at the characteristic frequency. J Neurophysiol 71:1022–1036.

Kandler K, Friauf E. 1993. Pre- and postnatal development of efferent connections of the cochlear nucleus in the rat. J Comp Neurol 328: 161–184.

Kil J, Kageyama GH, Semple MN, Kitzes LM. 1995. Development of ventral cochlear nucleus projections to the superior olivary complex in gerbil. J Comp Neurol 353:317–340.

Koike-Tani M, Saitoh N, Takahashi T. 2005. Mechanisms underlying developmental speeding in AMPA-EPSC decay time at the calyx of Held. J Neurosci 25:199–207.

Kopp-Scheinpflug C, Fuchs K, Lippe WR, Tempel BL, Rubsamen R. 2003. Decreased temporal precision of auditory signaling in Kcna1-null mice: an electrophysiological study in vivo. J Neurosci 23:9199–9207.

Kopp-Scheinpflug C, Tolnai S, Malmierca MS, Rubsamen R. 2008. The medial nucleus of the trapezoid body: comparative physiology. Neuroscience 154:160–170.

Kossl M, Foeller E, Drexl M, Vater M, Mora E, Coro F, Russell IJ. 2003. Postnatal development of cochlear function in the mustached bat, Pteronotus parnellii. J Neurophysiol 90:2261–2273.

Kuwabara N, Zook JM. 1991. Classification of the principal cells of the medial nucleus of the trapezoid body. J Comp Neurol 314:707–720.

Kuwabara N, DiCaprio RA, Zook JM. 1991. Afferents to the medial nucleus of the trapezoid body and their collateral projections. J Comp Neurol 314:684–706.

Lippe WR. 1994. Rhythmic spontaneous activity in the developing avian auditory system. J Neurosci 14(3 Pt 2):1486–1495.

Lu Y, Harris JA, Rubel EW. 2007. Development of spontaneous miniature

EPSCs in mouse AVCN neurons during a critical period of afferent-dependent neuron survival. J Neurophysiol 97:635–646.

Meinrenken CJ, Borst JG, Sakmann B. 2003. Local routes revisited: the space and time dependence of the Ca2+ signal for phasic transmitter release at the rat calyx of Held. J Physiol 547(Pt 3):665–689.

Moore MJ, Caspary DM. 1983. Strychnine blocks binaural inhibition in lateral superior olivary neurons. J Neurosci 3:237–242.

Morest DK. 1968a. The collateral system of the medial nucleus of the trapezoid body of the cat, its neuronal architecture and relation to the olivo-cochlear bundle. Brain Res 9:288–311.

Morest DK. 1968b. The growth of synaptic endings in the mammalian brain: a study of the calyces of the trapezoid body. Z Anat Entwicklungsgesch 127:201–220.

Neher E, Sakaba T. 2001. Combining deconvolution and noise analysis for the estimation of transmitter release rates at the calyx of held. J Neurosci 21:444–461.

Oertel D. 1999. The role of timing in the brain stem auditory nuclei of vertebrates. Annu Rev Physiol 61:497–519.

Pecka M, Brand A, Behrend O, Grothe B. 2008. Interaural time difference processing in the mammalian medial superior olive: the role of glycinergic inhibition. J Neurosci 28:6914–6925.

Renden R, Taschenberger H, Puente N, Rusakov DA, Duvoisin R, Wang LY, Lehre KP, von Gersdorff H. 2005. Glutamate transporter studies reveal the pruning of metabotropic glutamate receptors and absence of AMPA receptor desensitization at mature calyx of held synapses. J Neurosci 25:8482–8497.

Rodriguez-Contreras A, de Lange RP, Lucassen PJ, Borst JG. 2006. Branching of calyceal afferents during postnatal development in the rat auditory brainstem. J Comp Neurol 496:214–228.

Rodriguez-Contreras A, van Hoeve JS, Habets RL, Locher H, Borst JG. 2008. Dynamic development of the calyx of Held synapse. Proc Natl Acad Sci U S A 105:5603–5608.

Rowland KC, Irby NK, Spirou GA. 2000. Specialized synapse-associated structures within the calyx of Held. J Neurosci 20:9135–9144.

Ruben RJ. 1967. Development of the inner ear of the mouse: a radioautographic study of terminal mitoses. Acta Otolaryngol Suppl 220:221–244.

Russell FA, Moore DR. 1995. Afferent reorganisation within the superior olivary complex of the gerbil: development and induction by neonatal, unilateral cochlear removal. J Comp Neurol 352:607–625.

Russell IJ, Drexl M, Foeller E, Vater M, Kossl M. 2003. The development of a single frequency place in the mammalian cochlea: the cochlear resonance in the mustached bat Pteronotus parnellii. J Neurosci 23: 10971–10981.

Saint Marie RL, Luo L, Ryan AF. 1999. Effects of stimulus frequency and intensity on c-fos mRNA expression in the adult rat auditory brainstem. J Comp Neurol 404:258–270.

Sakaba T, Neher E. 2001. Quantitative relationship between transmitter release and calcium current at the calyx of Held synapse. J Neurosci 21:462–476.

Satzler K, Sohl LF, Bollmann JH, Borst JG, Frotscher M, Sakmann B, Lubke JH. 2002. Three-dimensional reconstruction of a calyx of Held and its postsynaptic principal neuron in the medial nucleus of the trapezoid body. J Neurosci 22:10567–10579.

Scheuss V, Schneggenburger R, Neher E. 2002. Separation of presynaptic and postsynaptic contributions to depression by covariance analysis of successive EPSCs at the calyx of Held synapse. J Neurosci 22:728–739.

Schneggenburger R, Forsythe ID. 2006. The calyx of Held. Cell Tissue Res 326:311–337.

Selimoglu E. 2007. Aminoglycoside-induced ototoxicity. Curr Pharm Des 13:119–126.

Smith PH, Joris PX, Carney LH, Yin TC. 1991. Projections of physiologically characterized globular bushy cell axons from the cochlear nucleus of the cat. J Comp Neurol 304:387–407.

Smith PH, Joris PX, Yin TC. 1998. Anatomy and physiology of principal cells of the medial nucleus of the trapezoid body (MNTB) of the cat. J Neurophysiol 79:3127–3142.

Souter M, Nevill G, Forge A. 1995. Postnatal development of membrane specialisations of gerbil outer hair cells. Hear Res 91:43–62.

Souter M, Nevill G, Forge A. 1997. Postnatal maturation of the organ of Corti in gerbils: morphology and physiological responses. J Comp Neurol 386:635–651.

Spangler KM, Warr WB, Henkel CK. 1985. The projections of principal cells of the medial nucleus of the trapezoid body in the cat. J Comp Neurol 238:249–262.

Spirou GA, Brownell WE, Zidanic M. 1990. Recordings from cat trapezoid body and HRP labeling of globular bushy cell axons. J Neurophysiol 63:1169–1190.

Taschenberger H, von Gersdorff H. 2000. Fine-tuning an auditory synapse for speed and fidelity: developmental changes in presynaptic waveform, EPSC kinetics, and synaptic plasticity. J Neurosci 20:9162–9173.

Taschenberger H, Leao RM, Rowland KC, Spirou GA, von Gersdorff H. 2002. Optimizing synaptic architecture and efficiency for high-frequency transmission. Neuron 36:1127–1143.

Taschenberger H, Scheuss V, Neher E. 2005. Release kinetics, quantal parameters and their modulation during short-term depression at a developing synapse in the rat CNS. J Physiol 568(Pt 2):513–537.

Tierney TS, Russell FA, Moore DR. 1997. Susceptibility of developing cochlear nucleus neurons to deafferentation-induced death abruptly ends just before the onset of hearing. J Comp Neurol 378:295–306.

Tritsch NX, Yi E, Gale JE, Glowatzki E, Bergles DE. 2007. The origin of spontaneous activity in the developing auditory system. Nature 450: 50–55.

Trussell LO. 1997. Cellular mechanisms for preservation of timing in central auditory pathways. Curr Opin Neurobiol 7:487–492.

Trussell LO. 1999. Synaptic mechanisms for coding timing in auditory neurons. Annu Rev Physiol 61:477–496.

Vale C, Sanes DH. 2002. The effect of bilateral deafness on excitatory and inhibitory synaptic strength in the inferior colliculus. Eur J Neurosci 16:2394–2404.

van Brederode JF, Rho JM, Cerne R, Tempel BL, Spain WJ. 2001. Evidence of altered inhibition in layer V pyramidal neurons from neocortex of Kcna1-null mice. Neuroscience 103:921–929.

von Gersdorff H, Borst JG. 2002. Short-term plasticity at the calyx of Held. Nat Rev Neurosci 3:53–64.

Warr WB. 1966. Fiber degeneration following lesions in the anterior ventral cochlear nucleus of the cat. Exp Neurol 14:453–474.

Warr WB. 1982. Parallel ascending pathways from the cochlear nucleus: neuroanatomical evidence of functional segregation. In: Neff WD, editor. Contributions to sensory physiology. New York: Academic Press. p 1–38.

Williams SM, Sullivan RK, Scott HL, Finkelstein DI, Colditz PB, Lingwood BE, Dodd PR, Pow DV. 2005. Glial glutamate transporter expression patterns in brains from multiple mammalian species. Glia 49:520–541.

Wimmer VC, Horstmann H, Groh A, Kuner T. 2006. Donut-like topology of synaptic vesicles with a central cluster of mitochondria wrapped into membrane protrusions: a novel structure-function module of the adult calyx of Held. J Neurosci 26:109–116.

Wong AY, Graham BP, Billups B, Forsythe ID. 2003. Distinguishing between presynaptic and postsynaptic mechanisms of short-term depression during action potential trains. J Neurosci 23:4868–4877.

Woolf NK, Ryan AF. 1984. The development of auditory function in the cochlea of the Mongolian gerbil. Hear Res 13:277–283.

Youssoufian M, Oleskevich S, Walmsley B. 2005. Development of a robust central auditory synapse in congenital deafness. J Neurophysiol 94: 3168–3180.

Youssoufian M, Couchman K, Shivdasani MN, Paolini AG, Walmsley B. 2008. Maturation of auditory brainstem projections and calyces in the congenitally deaf (dn/dn) mouse. J Comp Neurol 506:442–451.

Study 2

Author contributions:

All authors (M.C.F., O.A., L.C., D.A. and B.G.) contributed to designing the research. Anatomical experiments were performed and analyzed by M.C.F. and O.A. Simulations were performed by L.C. and D.A. M.C.F. prepared the figures. All authors (M.C.F., O.A., L.C., D.A. and B.G.) contributed to interpreting the data and writing the manuscript.

Tuning of myelinated axon properties to preserve temporal information

Marc C. Ford[1], Olga Alexandrova[1], Lee Cossell[2], David Attwell[2] and Benedikt Grothe[1]

[1]Division of Neurobiology, Department Biology II,

Ludwig-Maximilians-Universität Munich

[2]Department of Neuroscience, Physiology & Pharmacology, University College London

Correspondence to Benedikt Grothe, e-mail grothe@lmu.de

Abstract

Action potential timing is fundamental to information processing, but its determinants are incompletely understood. Here we report unexpected structural specializations of myelinated axons that help to preserve temporal information for sound localization. Myelination parameters of globular bushy cell axons deviate from the canonically assumed structure and specifically tune axon properties depending on their termination region in their target nucleus, and hence on the sound frequency they are tuned to. Low-frequency axons had a larger diameter than high-frequency axons, but, surprisingly, shorter internodes. This deviation from the generally assumed axonal structure helps to tune the conduction speed and timing of APs within the circuit. Moreover, along the distal part of these axons, internode length decreases and Ranvier node diameter increases progressively, which we show is essential to ensure precisely-timed depolarization of the giant calyx of Held. Thus, individual anatomical parameters of myelinated CNS axons can be tuned to optimize information processing.

Introduction

In the grey matter of the brain, neuronal dendrites and synapses have highly varying morphologies, which are adapted to particular information processing tasks (Stuart et al., 2007). In contrast, the white matter is generally assumed to be comprised of axons with a canonical structure defined by a ratio of internode length to myelin diameter of ~100 (Rushton, 1951) and a "g-ratio" of axon diameter to myelin diameter of ~0.75 (Peters et al., 1991). However, it would be surprising if myelinated CNS axons were as structurally invariant as is commonly assumed, because the shape and timing of action potentials plays a crucial role in synaptic transmission, information processing, rhythm generation and plasticity (Buzsáki et al., 2013; Caporale and Dan, 2008; Sabatini and Regehr, 1999; Usrey, 2002; Wang, 2010), and variation of any of the geometrical parameters of myelinated axons could be used to tune their conduction speed and action potential shape. For example, varying axon diameter at the node of Ranvier will alter the axial resistance and membrane capacitance (and possibly the number of voltage-gated Na^+ channels) at the node, varying internodal axon diameter will change axial current flow along the axon, while altering internode length will change the fraction of the axon which benefits from the capacitance-reducing effect of myelination. Indeed, in the peripheral nervous system, the internode length is reduced near synaptic terminals (at the neuromuscular junction) to increase the effective Na^+ current available to depolarize the terminals (Quick et al., 1979), while in the CNS the myelination pattern can vary significantly between similar neurons, possibly to tune conduction time (Tomassy et al., 2014).

A model system for a detailed morphometric analysis of single myelinated axons in vertebrates is the sound localization circuitry that processes spatial information with exquisite precision. For instance, it has been shown that, in the bird pathway processing interaural time differences (ITD), variation in axon morphology is used for adjusting action potential arrival times. There, thicker axons with longer internodes compensate for different axonal lengths (Seidl

et al., 2010, 2014). The analogous mammalian auditory brainstem circuits that process ITDs and interaural level differences (ILDs) have similar exceptional needs for temporal precision in action potential propagation, synaptic transmission, and postsynaptic integration (Carr and Soares, 2002). Both the ITD and ILD processing circuits contain a structure not present in birds, the medial nucleus of the trapezoid body (MNTB), which receives its excitatory inputs from the contralateral cochlear nucleus globular bushy cells (GBCs) via the giant calyx of Held synapses. MNTB neurons are themselves glycinergic and provide inhibition to the binaural comparator neurons in the medial and lateral superior olive (MSO, LSO, respectively). While the excitatory inputs from spherical bushy cells (SBCs) in the cochlear nucleus innervate MSO and LSO neurons directly (Fig. 1A), the inhibitory pathway includes the calyx of Held in the MNTB as an additional synapse. Despite the additional synaptic delay, recent experimental and theoretical data indicate an earlier arrival time for inhibitory than for excitatory input at the MSO (Brand et al., 2002; Roberts et al., 2013). Moreover, inhibitory and excitatory inputs arrive at about the same time at the LSO [reviewed in (Grothe et al., 2010)]. This suggests the involvement of structural adaptations for speeding up the conduction of inhibitory information in the binaural circuit. Moreover, action potentials in the GBC-MNTB-pathway are known to be particularly short (Taschenberger and von Gersdorff, 2000; Taschenberger et al., 2002), can propagate along axons at extremely high frequencies (>600 Hz: (Taschenberger and von Gersdorff, 2000; Wu and Kelly, 1993)) and are transmitted via the calyx of Held securely with short synaptic delays (Englitz et al., 2009).

Here we show that GBC myelinated axons, and in particular those of cells tuned to low sound frequencies that are involved in processing ITDs of only microseconds, significantly deviate from the canonically assumed structure, in a paradoxical way: low frequency fibers are thicker but exhibit a shorter intermodal length. Our simulations indicate that this makes action potential conduction particularly fast and precise. Furthermore, while it has been proposed that a long (20-40µm) heminode is necessary for depolarizing the giant calyx of Held presynaptic

terminal in juvenile animals (Leão et al., 2005), we found that the heminode at the adult calyx is much shorter than this. We found that the adult gerbil calyx lacks Na channel expression and is preceded by a long (4 to 30 micron) post-heminode region that is devoid of myelin (see (Leão et al., 2005)) and demonstrate a novel mechanism that promotes calyx depolarization. We show that the internode length decreases and the node diameter increases progressively towards the presynaptic terminal, and our detailed simulations predict that these gradations are crucial for precisely timed depolarization of the calyx of Held.

Results

Structural differences between SBC and GBC fibers

We first measured the internodal axon diameter and internode length in SBC fibers innervating the MSO and in GBC fibers innervating the MNTB. A combination of dye filling of axons (Fig. 1B) and immunohistochemical labeling of nodal and juxtaparanodal proteins allowed us to measure axon diameter, to unambiguously identify the position of nodes of Ranvier along axons (Fig. 1C), and to follow single axons with an identified termination site for up to 2200 µm. The internodal axon diameter of GBC axons was more than twice that of SBC axons (measured far from their synaptic terminals: SBC 1.35±0.03 µm at >500 µm from the terminals, GBC 2.87±0.05 µm at >700 µm from the terminals; $p<0.001$; Mann-Whitney test; Fig. 1D). The mean internode length in the thicker GBC fibers was also larger than in the thinner SBC fibers (SBC 164.8±12.4 µm, GBC 208.9±7.0 µm, $p=0.005$, t-test; Fig. 1E). Simulations presented below assess how this difference of parameters affects the conduction speed in the pathways bringing excitatory and inhibitory input to the MSO.

Structural parameters differ with the tonotopic identity of GBC fibers

The MNTB is a tonotopically organized nucleus with GBC axons conveying high sound frequencies targeting the medial region and those conveying low sound frequencies targeting the

lateral region (Guinan et al., 1972) (Fig. 2A). Tracing individual GBC axons to their calyx of Held terminals enabled us to categorize them, by their termination region in the MNTB, as providing input to the medial half of the nucleus (GBCmed, or high-frequency) or to the lateral half (GBClat, or low-frequency). In nine GBClat and eight GBCmed axons we determined internodal axon diameter, node of Ranvier diameter and internode length, three major structural determinants of the conduction speed of action potentials (Waxman, 1980) (Fig. 2B). Interestingly, we observed systematic differences in the two populations of GBC axons. GBClat axons had a significantly larger mean internodal axon diameter than GBCmed axons (GBClat 3.21±0.05 µm averaged over all positions, GBCmed 2.40±0.05 µm, $p<0.001$, Mann-Whitney test; Fig. 2B-D). The diameter of nodes of Ranvier was also larger in GBClat axons than in GBCmed axons (GBClat 1.91±0.04 µm, GBCmed 1.60±0.05 µm, $p<0.001$, t-test; Fig. 2E, F). However, despite the larger diameter of GBClat axons, the mean length of internodes located further than 700 µm away from the calyx (where internode length was constant, see below) was smaller in GBClat than in GBCmed axons (GBClat 195.7±8.5 µm, GBCmed 230.4±11.1 µm, $p=0.015$, t-test; Fig. 2G, H). This surprising finding contradicts the long-assumed notions (Rushton, 1951) that internode length is proportional to axon diameter, and that axons with similar function exhibit structural similarity.

This structural difference became even more apparent when the ratio of internode length to internodal axon diameter (L/d) was compared (Fig. 2I). GBCmed axons had, far from the calyx, a mean L/d ratio of ~100. In contrast, for GBClat axons the mean ratio was ~35% smaller (GBClat 64.9±3.1; GBCmed 99.6±5.67; $p<0.001$, Mann-Whitney test; Fig. 2J). Both of these values are lower than the canonical value of 133, which is predicted [for a g-ratio of 0.75 (Peters et al., 1991)] from Rushton's (Rushton, 1951) classical summary of the properties of PNS fibers as having a ratio of internode length to myelin outer diameter of ~100. These data suggest strongly that there are systematic differences in the structure of GBC axons that can be related to

the tonotopic organization, and thus to the function of these axons in the sound localization circuits processing interaural time and level differences.

Myelin thickness in GBC fibers

Another major structural determinant of action potential conduction velocity in myelinated axons is the thickness of the myelin sheath (Waxman, 1980). Increasing the number of myelin wraps lowers the capacitance along the internode, reducing the time required to charge the internodal membrane. This means that consecutive nodes of Ranvier reach threshold quicker and, therefore, the conduction velocity is increased. In addition, it increases the effective membrane resistance, thus reducing radial current leak between consecutive nodes of Ranvier. We determined myelin thickness from transmission electron micrographs of GBC fibers (Fig. 3A) in parasagittal ultrathin sections by measuring the axon perimeter and the fiber perimeter (Fig. 3B, C). The g-ratio was calculated by dividing the measured inner (axon) perimeter by the measured outer (myelin) perimeter (Michailov et al., 2004). As expected (Makinodan et al., 2012), g-ratio increased slightly with axon diameter, i.e. myelin thickness relative to axon diameter decreased at larger axon diameters (Fig. 3D). Estimated g-ratio values for the mean internodal axon diameter of GBCmed and GBClat axons were 0.748 and 0.764, respectively, which were used in our detailed computational axon model described below.

Spatial variation of anatomical parameters towards the calyx of Held

In addition to the variation of mean geometrical parameters between fibers with different tonotopic identity, we found a systematic variation of structural parameters along the distal part of all GBC fibers (Fig. 2E, G). From about 700 µm before reaching the heminode, the internode length decreased progressively from 195.7±8.5 µm to 53.5±0.2 µm at the last internode in GBClat fibers, and from 230.4±11.1 µm to 36.9±3.0 µm at the last internode in GBCmed fibers (Fig. 2G, Supplementary Fig. 1A). The observed decrease of internode lengths was not a secondary effect necessary to allow fiber branching (Carr and Konishi, 1990; Deschênes and Landry, 1980), as only 5 of the 17 analyzed GBC axons gave rise to a branch in their distal part. A gradation along

the axon was also found for node diameters (Fig. 2E, Supplementary Fig. 1B). On average, node diameter increased by 35% approaching the synaptic terminal in the most distally located eight nodes of Ranvier of GBClat fibers, and by 40% in the most distally located four nodes of GBCmed fibers. This increase in node diameter will decrease the nodal axial resistance and (for a fixed channel density per membrane area) increase the number of voltage-gated Na^+ channels per node which, together with the increased density of nodes associated with shorter internode lengths, could support an increased current flow down the axon to promote reliable action potential invasion into the giant calyx of Held. We test this idea in simulations presented below.

Morphometry of the pre-terminal axon segment

The myelinated part of GBC fibers was followed by a short unmyelinated pre-terminal axon segment that connected the last internode to the calyx of Held. Immunohistochemical staining revealed that it consisted of a sodium channel-rich heminode, directly adjacent to the last internode, and a sodium channel-free segment, which we refer to as the post-heminode (Fig. 4A-C). The heminode had a similar length in medially and laterally terminating fibers (2.13±0.13 µm in GBClat and 2.18±0.19 µm in GBCmed; Fig. 4D). In accordance with the differences in internodal axon and node diameters in GBClat and GBCmed fibers (Fig. 2C-F), the heminode diameter was significantly larger in GBClat fibers (GBClat 2.04±0.09 µm, GBCmed 1.60±0.15 µm, p=0.022, Mann-Whitney test, Fig. 4E). The diameter of the post-heminode was significantly larger than the heminode diameter in both GBClat (2.70±0.19 µm, p=0.007, paired t-test) and GBCmed axons (2.26±0.20 µm, p=0.002, paired t-test). The post-heminode ranged in length from 7 to 30 µm (mean 13.2±2.1 µm) in GBClat, and from 4 to 14 µm (10.7±1.3 µm) in GBCmed fibers (Fig. 4D). Consequently, it constitutes a large capacitance and has potentially strong effects on action potential invasion into the calyx of Held.

Dependence of simulated conduction velocity on L/d ratio in SBC, GBClat, and GBCmed axons

To explore how the morphological differences between SBC, GBClat and GBCmed axons affect action potential propagation we carried out detailed computer simulations (Bakiri et al., 2011) informed by the measured anatomical parameters for each axon type, as described in the Experimental Procedures and Supplementary Tables. The conduction velocity of the computed action potential far from the synaptic terminals was 4.4 m/s in SBC axons, 8.5 m/s in GBCmed axons and 11.3 m/s (33% faster) in GBClat axons that have a lower ratio of internode length to axon diameter (arrowed values in Fig. 5A). The lower velocity in SBC axons than in GBC axons correlates well with inhibitory information arriving before excitatory information at the MSO (Roberts et al., 2013) (Fig. 1A).

To estimate how much of the 33% increase in conduction velocity in GBClat axons (compared to GBCmed axons) was due to their smaller internode length to axon diameter (L/d) ratio, we systematically explored the effect of varying the internode length (without changing the axon diameter, node diameter, or g-ratio) in both populations of axon (Fig. 5A). At low internode lengths the conduction velocity decreases because a smaller fraction of the axon is myelinated, while at long internode lengths it decreases because of inefficient transfer of depolarization between nodes, giving an optimum value of L/d to maximize conduction velocity (Brill et al., 1977). Both lateral and medial GBC axons have an internode length greater than this optimum, which has been suggested to decrease energy use with little decrease of conduction velocity (Rushton, 1951), an idea we assess below. Increasing the internode length to increase L/d in GBClat axons from 64.9 to 99.6, the ratio we found in GBCmed axons (dashed arrow in Fig. 5A), decreased the conduction speed to 9.8 m/s. Thus, the smaller L/d ratio in GBClat fibers, which is closer to the simulated optimum (Fig. 5A), increases the conduction velocity by 15% (while 18% of the increase in speed of these axons is due to the larger internode and node diameters).

Dependence of simulated AP shape on L/d ratio in SBC, GBClat, and GBCmed axons

The presynaptic action potential waveform is a crucial determinant of the timing (synaptic delay) and strength of synaptic transmission (Boudkkazi et al., 2011; Sabatini and Regehr, 1999). In sound localization circuits, brief APs are not only crucial for keeping synaptic delays short and for preserving temporal information during synaptic transmission, but also support precise and reliable propagation of high-frequency AP trains up to 500-800 Hz as observed *in vivo* (Rhode and Smith, 1986; Spirou et al., 1990), a prerequisite for neurons tuned to low sound frequencies (<2000 Hz) to respond in a cycle by cycle manner to a specific phase of the sound wave (Joris et al., 1994). The simulated AP in GBClat fibers exhibited a more rapid rate of rise of the upstroke (1202 V/s), a shorter half-width (0.41 ms), and larger amplitude (101mV) than in GBCmed fibers (rate of rise 1039 V/s; half-width 0.44 ms; amplitude 94.1 mV; Fig. 5 B-D). Notably, this effect depended on the smaller L:d ratio in GBClat fibers because increasing the ratio to 99.6 decreased the rate of rise by 29 % to 859 V/s, increased the AP half-width by 14 % to 0.47 ms, and decreased the amplitude by 13 % to 87.8 mV. Briefer APs in GBClat fibers should allow for shorter intervals between action potentials and hence temporally more reliable responses to fast incoming signals (i.e. allowing the phase locking that is exhibited by low-frequency GBC fibers) (Joris et al., 1994), and a larger amplitude may increase the reliability (by increasing the safety factor) of AP propagation in these axons. Moreover, briefer APs have been shown to be associated with a smaller synaptic delay (Borst and Sakmann, 1999; Boudkkazi et al., 2011; Sabatini and Regehr, 1999), and increased fidelity of synaptic transmission (Taschenberger and von Gersdorff, 2000) which is fundamental to binaural processing of temporal information in sound localization circuits (Carr and Soares, 2002; Carr et al., 2001).

Effect of internode length and node diameter gradations on AP invasion into the calyx

To test the effect of the internode length and node diameter gradations toward the end of GBC axons on AP invasion into the calyx of Held, we simulated the end terminal as three

cylinders corresponding to the heminode, post-heminode and calyx (Fig. 4A, details of the parameters chosen are in the Experimental Procedures and Supplementary Tables). The dimensions of the heminode and post-heminode were taken from the anatomical observations above. The calyx of Held was modeled as an equivalent cylinder which represented the complex processes that make up the calyx (see Experimental Procedures) and had a total surface area of 1700 μm^2 (in the observed range (Grande and Wang, 2011)). Without any spatial gradation of internode length, node diameter, and internode diameter with distance from the synaptic terminal, for GBClat axons action potentials did not propagate successfully into the calyx (the maximum depolarization was 19.9 mV, Fig. 6A dark blue trace). After introducing the observed spatial gradation of internode length (shorter nearer the calyx), action potential propagation into the calyx was facilitated (the maximum depolarization was 31.4 mV, Fig. 6A light blue trace). A facilitation was achieved by introducing only the gradation of internode length, without introducing the gradation of internode and node diameter. However, additional introduction of the observed gradation of node diameter and internode diameter led to a more rapid entry of the action potential into the calyx (a 34 μs speeding of the action potential was observed with gradation of internode length only, versus a 51 μs speeding for all gradations included; delays were measured from the time for the action potential to pass -60 mV). The gradation of node diameter and internode diameter, when introduced alone, had little effect on the action potential waveforms (Fig. 6A, green and red traces). However, when the gradation of node diameter and internode length were introduced on top of that of the internode length, this led to a more rapid rate of rise of the action potential upstroke (maximum rate-of-rise: 96.7 V/s without any gradations, 126.0 V/s with gradation of internode length only, and 155.7 V/s with gradations of node diameter, internode diameter and internode length) and a larger action potential amplitude (52.3 mV, Fig 6A magenta trace).

The calyx shape varies considerably during development (Ford et al., 2009). We varied systematically the diameter of the processes of the simplified calyx while keeping the total calyx

surface area constant (by adjusting the process length), to examine how robustly the action potential invaded calyces of different shapes, and the role of the gradation of axonal properties in ensuring this invasion. The simulations revealed that gradations of internode length, and of nodal and internodal diameter, are essential for successful propagation of the AP into the GBClat terminal over a wide range of calyx geometries (Fig. 6B), as occurs experimentally (Taschenberger and von Gersdorff, 2000). Similar behavior was observed in simulations of GBCmed axons (Fig. 6A, B), except that the surface area of the calyx had to be reduced to 1250 μm^2 (also in the observed range (Grande and Wang, 2011)) in order for action potentials to depolarize the calyx beyond -40mV.

Discussion

We have identified several unusual morphological parameters of axons transmitting information to the MSO and LSO. First, the diameter and internode length of GBC axons, which transmit information that passes through an extra synapse in the MNTB and provide inhibition to the MSO and LSO (Fig. 1A), are larger than those of the SBC axons transmitting excitatory information. The resulting increase in transmission speed of the inhibitory information could explain why inhibitory information can arrive approximately simultaneously with the excitatory information in the LSO and even before excitatory information at the MSO (Grothe et al., 2010; Roberts et al., 2013) despite the additional synaptic delay in the MNTB. An analysis of the analogous ITD processing circuit in birds suggests that a different anatomical tuning mechanism occurs: differences of axon diameter and internode length may tune different length branches of the same myelinated axons to provide the required action potential arrival times (Seidl et al., 2010, 2014).

Secondly, the present study provides evidence that structural specializations in myelinated GBC axons that strongly deviate from the canonically assumed behavior can

additionally tune their conduction velocity, and thus the timing of action potentials. Specifically, we found systematic differences in the structure of GBC axons that correlate with their target region in the MNTB, and hence with their tonotopic identity. Lateral (low frequency) GBCs had a larger internodal axon diameter, but, paradoxically, a shorter internode length than medial (high frequency) GBCs. This result contradicts the principle of structural similarity of myelinated axons (Rushton, 1951). Our simulations predict that this difference in structure results in GBClat axons conducting action potentials 33% faster than GBCmed axons (Fig. 5A). About half of this increase in speed in GBClat compared to GCBmed axons is attributable to the lower L/d ratio in GBClat fibers. In addition, the lower L/d ratio increased the rate of rise and decreased the half-width of the action potential in GBClat axons, which is a prerequisite for temporally precise synaptic transmission at the calyx of Held. A first indication of differences of axon structure potentially related to tonotopic identity came from an investigation of peripheral auditory axons (Liberman and Oliver, 1984). In the light of our analysis of how individual structural parameters contribute to myelinated axon function in the CNS, it is likely that these PNS adaptations are also crucial for increasing the reliability and temporal precision of AP propagation in axons conveying low-frequency sound information for binaural processing.

It has been questioned whether the auditory circuits involved in temporal processing, which exhibit energy-demanding high frequency action potentials, are designed to use energy efficiently (Laughlin, 2001). Far from their synaptic terminals, SBC axons had a ratio of internode length to internodal axon diameter of 122, which is similar to the canonical value of 133 derived from peripheral axons (Rushton, 1951) by assuming a g-ratio of 0.75, while both GBC axon types had significantly lower values (GBCmed 99.6, GBClat 64.9) which increases their conduction speed (Fig. 5A). It is noteworthy that the ratio of internode length to internodal axon diameter in GBC and SBC axons is significantly higher than the value which maximizes conduction speed (Fig. 5A) – a situation which has been suggested to minimize energy consumption on pumping out the Na^+ that enters to generate the action potential (Rushton, 1951).

We assessed this by calculating (from our simulations) the Na^+ entering to generate an action potential for internode length to axon diameter ratios in Fig. 5A chosen to be either as observed experimentally or which would maximize the conduction speed. For SBC, GBCmed and GBClat axons, the observed values of L/d reduced the conduction speed by 28%, 22%, and 15% respectively (compared to the maximum velocities attainable), but reduced the energy needed for Na^+ pumping by a larger percentage (54%, 47% and 45% respectively).

Finally, we found unexpected gradations of geometrical parameters in CNS axons of the GBC-MNTB pathway which seem to be structurally and functionally analogous to those of PNS motorneurons close to the neuromuscular junction. We found that in GBCs the internode length, internodal axon diameter and node diameter all change systematically with distance from the synaptic terminal in the calyx of Held (Fig. 2). This spatial variation is crucial for ensuring rapid depolarization of the calyx of Held (Fig. 6A), which is reliable over a range of simulated calyx morphologies (Fig. 6B). Strikingly, in our simulations, for large calyces the shortening of internode length near the synaptic terminal (which has previously been suggested to promote synaptic depolarization in the PNS (Quick et al., 1979) and has been speculated to also exist in GBC fibers to promote depolarization of the long unmyelinated pre-terminal axon segment (Leão et al., 2005)) was not sufficient to ensure that a large and rapid depolarization occurred in the synaptic terminal, but additionally including the spatial variation of nodal and internodal axon diameter did ensure this. Interestingly, it has been proposed that 20-40 µm long Na_v-positive structures in the MNTB of young rats represent heminodes of GBC fibers, and that these putative heminodes might be necessary for depolarizing the giant calyx of Held presynaptic terminal (Leão et al., 2005). However, our labeling with Na_v, NFH, and K_v1 antibodies showed that the heminode in pre-calyceal segments of globular bushy cell axons of adult gerbils is only ~2 µm long. This indicates that the spatial variation of structural parameters, rather than a particularly long heminode, is the mechanism promoting precisely timed depolarization of the calyx.

The variation of the morphological parameters of myelinated axons that we report here thus plays a crucial role in the processing of temporal information for sound localization (as does the presence of myelin itself (Kim et al., 2013a, 2013b)). More generally, given that remodeling of the properties of myelinated axons can occur in adults (Young et al., 2013), our data highlight the fact that adjustment of parameters such as internode length, internodal axon diameter and node diameter can optimize information processing, and may contribute to the changes of white matter structure that contribute to learning (Scholz et al., 2009).

Experimental Procedures

All animal procedures were performed in accordance with the German guidelines for the care and use of laboratory animals as approved by the Regierung of Oberbayern (AZ 55.2-1-54-2531-105-10, Bavaria, Germany). Mongolian gerbils (*Meriones unguiculatus*) were housed in a vivarium with a normal light dark cycle (12 hours light/ 12 hours dark). Gerbils of both sexes, aged P25–30, were used for the anatomical experiments (in vitro axon tracing, immunohistochemistry, and electron microscopy).

***In vitro* axon tracing:**

Gerbils were deeply anaesthetized with pentobarbital (2 mg/kg body weight) and intracardially perfused with ice-cold Ringer's solution containing heparin. After decapitation, the brainstem was quickly removed from the skull under ice-cold dissecting aCSF comprising (in mM) 125 NaCl, 2.5 KCl, 1 $MgCl_2$, 0.1 $CaCl_2$, 25 glucose, 1.25 NaH_2PO_4, 25 $NaHCO_3$, 0.4 ascorbic acid, 3 myoinositol, 2 pyruvic acid (all chemicals from Sigma-Aldrich). For anterograde tracing of GBC axons, borosilicate micropipettes with a tip diameter of 10-15 µm were filled with a 10% solution of tetramethylrhodamine dextran (3000 MW; Invitrogen, La Jolla, CA) and visually guided to the anterior ventral cochlear nucleus (AVCN) in brainstem explants using a stereo microscope. Tracer was pressure injected (15 PSI) into the GBC area of the AVCN using a picospritzer (Picospritzer III, Parker, Cleveland, OH), followed by several electroporation pulse trains (modified from another study (Ford et al., 2009)). Pulses (50 ms) had an amplitude of 50 V and were applied at 10 Hz using an isolated pulse stimulator (A-M Systems). For anterograde tracing of SBC axons the brainstem was sectioned along the posterior-anterior axis until the outlines of the lateral superior olive (LSO) were clearly visible. Tracer was applied in the region of the medial limb of the LSO through pressure injections and electroporation as described above. SBC fibers (originating in the cochlear nucleus) pass through this region on their way to the contralateral MSO. This allowed us to label SBC axons without labeling GBC axons, and to

reduce the time needed for the tracer to diffuse within the axons to the contralateral MSO. Subsequently, the explants were transferred to a chamber with oxygenated incubating aCSF (the same as the dissecting aCSF described above except with 2 mM instead of 0.1 mM $CaCl_2$), and incubated for 2 hours at room temperature to allow for homogeneous distribution of the tracer in axons. Thereafter, the brainstems were immersion-fixed at room temperature overnight in 4% paraformaldehyde solution (PFA).

Immunohistochemistry:

Brainstems were sectioned coronally at 120 µm using a vibratome slicer. After rinsing in PBS, sections were transferred to a blocking solution containing 1% bovine serum albumin, 2% Triton X100, and 0.1% saponin in PBS. Multiple-immunofluorescence labeling was performed with the following primary antibodies (incubation time 2 days): ankyrin G (SantaCruz; USA; sc - 28561; rabbit polyclonal IgG; 1:500); Kv1.2 (NeuroMab; USA; 75-008 clone K14/16; Mouse IgG2b; 1:500); NFH (AbCam; UK; ab4680; chicken polyclonal IgY; 1:400); Pan Na_v (Sigma; Germany; S6936; rabbit polyclonal IgG; 1:300); MAP2 (Neuromics, USA, CH22103 chicken polyclonal, 1:1000). After incubation with secondary antibodies overnight, sections were rinsed 3 x 10 min in PBS, and coverslipped with Vectashield mounting medium.

Confocal microscopy:

Confocal optical sections were acquired with a Leica TCS SP5-2 confocal laser-scanning microscope (Leica Microsystems, Mannheim, Germany) equipped with HCX PL APO CS 20X / NA0.7, HCX PL APO Lambda Blue 63x / NA1.4 immersion oil, and HCX PL APO 63x / NA1.3 glycerol 37°C objectives. Fluorochromes were visualized with excitation wavelengths of 405 nm (emission filter 410-430 nm) for AMCA, 488 nm (emission filter 510–540 nm) for Alexa 488 and DyLight 488, 561 nm (emission filter 565–585 nm) for Cy3 and tetramethylrhodamine dextran, 594 nm (emission filter 605–625 nm) for Texas Red or DyLight 594 and 633 nm (emission filter 640–760 nm) for Nissl Deep Red and Cy5. For each optical section the images were collected sequentially for two to five fluorochromes. Stacks of 8-bit grayscale images were obtained with

axial distances of 290 nm between optical sections and pixel sizes of 120-1520 nm depending on the selected zoom factor and objective. To improve the signal-to-noise ratio, images were averaged from four successive scans. After stack acquisition, chromatic aberration induced Z shift between color channels was corrected for using a custom plugin written by Dr. Boris Joffe. RGB stacks, montages of RGB optical sections, and maximum-intensity projections were assembled using ImageJ 1.37k plugins and Adobe Photoshop 8.0.1 (Adobe Systems, San Jose, CA) software. For the morphometric analysis of traced GBC and SBC fibers, overlapping stacks of images were acquired from coronal brainstem slices (120 µm thick) at the level of the trapezoid body in the area spanning the MNTB and the contralateral tracer injection site (cochlear nucleus) (voxel size: 482 x 482 x 290 nm) and in the area between MSO and the contralateral injection site (medial limb of the lateral superior olive) (voxel size: 241 x 241 x 290 nm), respectively.

Identification of GBC and SBC axons:

GBC fibers were unambiguously identified as such from their prominent giant presynaptic endings (calyces of Held) which terminated in the contralateral MNTB. Based on their exact site of termination in the MNTB (in the medial or lateral half of the MNTB), GBC axons were classified as being either medially or laterally terminating. MNTB borders were determined using a counterstain (MAP2 or fluorescent Nissl stain). SBC fibers were identified as axons that that could be followed to the medial somatodendritic region of the MSO (the MSO contralateral to where tracer was applied in the medial limb of the LSO; see also section on *in vitro* axon tracing above). Some fibers formed varicosities in this region. Other fibers became very thin in the medial dendritic region and could not be followed any further, indicating that they terminated there. Since they were located in the middle of the slice (not on the surface), we can rule out that they were cut during the slicing procedure.

Morphometry:

Using the ImageJ 1.37k paint-brush tool, individual axons of GBCs and SBCs filled with tetrametylrhodamine dextran were manually labeled by following a single axon successively

through each optical section of the confocal image stack. Subsequently, the neighboring axons were digitally deleted. We refer to this method as digital extraction. The same axon was identified in the neighboring overlapping confocal image stacks and digitally extracted. This allowed us to follow single axons for up to ~ 2200 µm. Nodes of Ranvier were identified on the basis of immunohistochemical labeling of nodal and juxtaparanodal marker proteins (Ankyrin G and $K_v1.2$). Distances between nodes of Ranvier (i.e. internode lengths measured mid-node to mid-node) were measured in three dimensions in confocal image stacks using the ImageJ 1.37k Sync Measure 3D tool. Internodal axon diameter and node diameter measurements were made in two dimensions from maximum-intensity projections of confocal image stacks.

Electron microscopy:

Gerbils were deeply anaesthetized with pentobarbital (2 mg/kg body weight) and intracardially perfused with Ringer's solution. This was followed by perfusion with 2.5% glutaraldehyde plus 2% PFA in cacodylate buffer (CB). Subsequently the brainstem was removed from the skull and postfixed in the same fixative overnight at 4°C. After washing for 3 x 10 min in CB, brainstems were sectioned parasagittally at 200 µm using a vibratome slicer. Thereafter, a 1mm x 1 mm block containing the trapezoid body fibers was extracted using a razor blade. Tissue was then washed 4 times in CB, and postfixed in 1 % OsO_4 in CB for 1–2 hours. After washing and dehydrating in graded series of acetone, tissue was embedded in resin. Before ultrathin-sectioning, several semithin sections were cut for light microscopic investigation.

Statistics:

Data are represented as mean ± SEM. Tests for normal distribution and equal variance were performed using the Kolmogorov-Smirnov test and the Levene Median test, respectively. P values are from Student's two-tailed t-tests (for normally distributed data) or Mann-Whitney rank sum tests (for data that were not normally distributed). Tests were performed using SigmaStat 3.5 software. For multiple comparisons, p values were corrected using a procedure equivalent to the Holm-Bonferroni method (for N comparisons, the most significant p value is multiplied by N, the

2nd most significant by N-1, the 3rd most significant by N-2, etc.; corrected p values are significant if they are less than 0.05). Data presented in Fig. 2 C, E, G, and I were fit with linear or exponential functions using Igor Pro 5.02 (Wavemetrics).

Simulations:

The myelinated axon model of Halter & Clark (Halter and Clark, 1991) was implemented in MATLAB, modified to remove the periaxonal space in that model by setting its conductivity to zero, and adapted to the dimensions of GBClat, GBCmed and SBC axons. The values for the geometrical parameters are shown in Supplementary Tables 1, 2 and 3, and the values for the electrophysiological parameters are shown in Supplementary Table 4. The trans-myelin capacitance was calculated according to the equation $C_{my} = 2\pi L c_{my}/(\Sigma(1/r_i))$, where the r_i are the radii of the individual myelin membranes making up the sheath (assumed to occur at equally spaced radii between the axon radius and the outer radius of the sheath), L is the internode length and c_{my} is the specific capacitance/m^2 of a single membrane in the myelin. The trans-myelin conductance was calculated in a similar way. The differential equations of the model were derived and solved according to the method used in (Halter and Clark, 1991). For simulations examining the conduction velocity far from the calyx, 200 internodes were simulated with each internode being represented as 10 segments, an AP was initiated in the first node through brief current stimulation and the conduction speed was derived from the time needed for the AP to pass from the 71st to the 90th internode. The nodes of Ranvier contained inactivating Na^+ and low-threshold K^+ (K_{LT}) channels with Hodgkin-Huxley-like kinetics taken from (Rothman et al., 1993) and (Rothman and Manis, 2003), respectively, as well as a leak conductance. Explicitly, the equation governing current flow across the membrane in the node was:

$$-C_n\frac{dV}{dt} = G_{Na}(V - E_{Na}) + G_{K_{LT}}(V - E_K) + G_{Lkn}(V - E_{Lkn})$$

where C_n is the capacitance of the node ($C_n = \pi L_n d_n c_n$, where L_n is the length of the node, d_n is the diameter of the node and c_n is the specific capacitance of the nodal membrane), G_{Lkn} is the leak

conductance in the node ($G_{Lkn} = \pi L_n d_n g_{Lkn}$, where g_{Lkn} is the specific leak conductance of the nodal membrane), and V is the (time-varying) membrane potential in the node. E_{Na}, E_K and E_{Lkn} are the Na^+, K^+ and nodal leak reversal potentials, and

$$G_{Na} = \bar{G}_{Na} m^2 h$$

$$G_{K_{LT}} = \bar{G}_{K_{LT}} w^4 z$$

where $\bar{G}_{Na}$ and $\bar{G}_{K_{LT}}$ are the peak conductances of the Na^+ and K^+ currents in the node (derived from the specific conductances in a similar manner to G_{Lkn}) . The variables m, h, w and z are functions of membrane potential and time, and satisfy:

$$\frac{d\xi}{dt} = \alpha_\xi(V)(1-\xi) - \beta_\xi(V)\xi, \qquad \text{where } \xi = m, h, w, \text{or } z$$

and

$$\alpha_m(V) = \frac{0.36 * 3^{\frac{T-22}{10}} * (V+49)}{1 - \exp\left(-\frac{V+49}{3}\right)}$$

$$\beta_m(V) = \frac{-0.4 * 3^{\frac{T-22}{10}} * (V+58)}{1 - \exp\left(\frac{V+58}{20}\right)}$$

$$\alpha_h(V) = \frac{2.4 * 3^{\frac{T-22}{10}}}{1 + \exp\left(\frac{V+68}{3}\right)} + \frac{0.8 * 10^{\frac{T-22}{10}}}{1 + \exp(V+61.3)}$$

$$\beta_h(V) = \frac{3.6 * 3^{\frac{T-22}{10}}}{1 + \exp\left(-\frac{V+21}{10}\right)}$$

$$\alpha_w(V) = \frac{\left(1 + \exp\left(-\frac{V+48}{6}\right)\right)^{-\frac{1}{4}}}{100\left(6\exp\left(\frac{V+60}{6}\right) + 16\exp\left(-\frac{V+60}{45}\right)\right)^{-1} + 1.5}$$

$$\beta_w(V) = \frac{\left(1 - \left(1 + \exp\left(-\frac{V+48}{6}\right)\right)^{-\frac{1}{4}}\right)}{100\left(6\exp\left(\frac{V+60}{6}\right) + 16\exp\left(-\frac{V+60}{45}\right)\right)^{-1} + 1.5}$$

$$\alpha_z(V) = \frac{\left(0.5\left(1+\exp\left(\frac{V+71}{10}\right)\right)^{-1}+0.5\right)}{1000\left(\exp\left(\frac{V+60}{20}\right)+\exp\left(-\frac{V+60}{8}\right)\right)^{-1}+50}$$

$$\beta_z(V) = \frac{\left(0.5-0.5\left(1+\exp\left(\frac{V+71}{10}\right)\right)^{-1}\right)}{1000\left(\exp\left(\frac{V+60}{20}\right)+\exp\left(-\frac{V+60}{8}\right)\right)^{-1}+50}$$

where, for all these equations, V is in mV and the rate constants are in ms^{-1}. The Na^+ current kinetics were adjusted for temperature, T (in ˚C), as written in the equations above. The low-threshold K^+ current kinetics were defined at 22˚C and similarly adjusted for temperature using a Q_{10} value of 3.0.

For simulations examining action potential propagation into the calyx of Held, 50 internodes were simulated and action potentials were again initiated in the first node of Ranvier. The end terminal was simulated by extending the last node by three compartments corresponding to the heminode, post-heminode (represented as 10 segments) and calyx. The morphometric parameters for the heminode and post-heminode were taken from this paper (Supplementary Table 3). The heminode contained the inactivating Na^+, low-threshold K^+ and leak channels as described above for the nodes of Ranvier. The post-heminode was taken to be a capacitor without conductance. The calyx was represented as a single cylinder (divided into 50 equal serial segments), equivalent to 5 smaller cylinders representing the main processes of the calyx structure, with a surface area of 1700µm^2 or 1250 µm^2 (see main text), consistent with published values (Grande and Wang, 2011). When investigating the effect of altering calyx geometry, the radius of these smaller cylinders was varied, with corresponding alterations in their length to keep the surface area constant. A single cylinder of *A* µm diameter and *L* µm length can be shown to be equivalent to N parallel cylinder "processes" each with diameter $A / N^{2/3}$ µm and length $L / N^{1/3}$ µm. Therefore, a simulated calyx equivalent cylinder of 10 µm diameter and 54.1 µm length (giving a surface area of 1700 µm^2) represents 5 parallel cylinders of diameter 3.42 µm and

length 31.6 µm. The calyx contained high-threshold K^+ (K_{HT}) and hyperpolarization-activated cation (I_h) conductances with Hodgkin-Huxley-like kinetics taken from (Rothman and Manis, 2003). It also contained a calcium conductance taken from (Borst and Sakmann, 1998). Explicitly, the equation governing current flow across the membrane in the calyx was:

$$-C_c\frac{dV}{dt} = G_{Ca}(V - E_{Ca}) + G_{K_{HT}}(V - E_K) + G_h(V - E_h) + G_{Lkc}(V - E_{Lkc})$$

where C_c is the capacitance of the calyx, G_{Lkc} is the leak conductance in the calyx, E_{Ca} and E_h are the reversal potentials of the calcium and I_h currents and,

$$G_{Ca} = \bar{G}_{Ca}s^2$$

$$G_{K_{HT}} = 0.85\bar{G}_{K_{HT}}n^2 + 0.15\bar{G}_{K_{HT}}p$$

$$G_h = \bar{G}_h r$$

where $\bar{G}_{Ca}$, $\bar{G}_{K_{HT}}$, and $\bar{G}_h$ are the peak conductances (conductance values were taken from (Spirou et al., 2008), but $\bar{G}_h$ was reduced 10-fold to increase the input resistance of the calyx to make it more similar to published values (Forsythe measured a value of 388±228MΩ (Forsythe, 1994); in the model, GBClat and GBCmed calyces had input resistances of 240MΩ and 325MΩ, respectively), and s, n, p, and r are functions of membrane potential and time which satisfy:

$$\frac{d\xi}{dt} = \alpha_\xi(V)(1 - \xi) - \beta_\xi(V)\xi, \qquad \text{where } \xi = s, n, p, \text{or } r$$

and

$$\alpha_s(V) = 1.78\exp\left(\frac{V}{23.3}\right)$$

$$\beta_s(V) = 0.14\exp\left(-\frac{V}{15}\right)$$

$$\alpha_n(V) = \frac{\left(1 + \exp\left(-\frac{V+15}{5}\right)\right)^{-\frac{1}{2}}}{100\left(11\exp\left(\frac{V+60}{24}\right) + 21\exp\left(-\frac{V+60}{23}\right)\right)^{-1} + 0.7}$$

$$\beta_n(V) = \frac{1 - \left(1 + \exp\left(-\frac{V+15}{5}\right)\right)^{-\frac{1}{2}}}{100\left(11\exp\left(\frac{V+60}{24}\right) + 21\exp\left(-\frac{V+60}{23}\right)\right)^{-1} + 0.7}$$

$$\alpha_p(V) = \frac{\left(1 + \exp\left(-\frac{V+23}{6}\right)\right)^{-1}}{100\left(4\exp\left(\frac{V+60}{32}\right) + 5\exp\left(-\frac{V+60}{22}\right)\right)^{-1} + 5}$$

$$\beta_p(V) = \frac{1 - \left(1 + \exp\left(-\frac{V+23}{6}\right)\right)^{-1}}{100\left(4\exp\left(\frac{V+60}{32}\right) + 5\exp\left(-\frac{V+60}{22}\right)\right)^{-1} + 5}$$

$$\alpha_r(V) = \frac{\left(1 + \exp\left(\frac{V+76}{7}\right)\right)^{-1}}{10^5\left(237\exp\left(\frac{V+60}{12}\right) + 17\exp\left(-\frac{V+60}{14}\right)\right)^{-1} + 25}$$

$$\beta_r(V) = \frac{1 - \left(1 + \exp\left(\frac{V+76}{7}\right)\right)^{-1}}{10^5\left(237\exp\left(\frac{V+60}{12}\right) + 17\exp\left(-\frac{V+60}{14}\right)\right)^{-1} + 25}$$

For all of these equations V is in mV and the rate constants are in ms^{-1}. The Ca^{2+} current kinetics were defined at 24˚C, and the high-threshold K^+ and I_h current kinetics were defined at 22˚C. All were adjusted for temperature with a Q_{10} value of 3.0.

References

Bakiri, Y., Káradóttir, R., Cossell, L., and Attwell, D. (2011). Morphological and electrical properties of oligodendrocytes in the white matter of the corpus callosum and cerebellum. J. Physiol. *589*, 559–573.

Borst, J.G., and Sakmann, B. (1998). Calcium current during a single action potential in a large presynaptic terminal of the rat brainstem. J. Physiol. *506 (Pt 1)*, 143–157.

Borst, J.G., and Sakmann, B. (1999). Effect of changes in action potential shape on calcium currents and transmitter release in a calyx-type synapse of the rat auditory brainstem. Philos. Trans. R. Soc. Lond. B. Biol. Sci. *354*, 347–355.

Boudkkazi, S., Fronzaroli-Molinieres, L., and Debanne, D. (2011). Presynaptic action potential waveform determines cortical synaptic latency. J. Physiol. *589*, 1117–1131.

Brand, A., Behrend, O., Marquardt, T., McAlpine, D., and Grothe, B. (2002). Precise inhibition is essential for microsecond interaural time difference coding. Nature *417*, 543–547.

Brill, M.H., Waxman, S.G., Moore, J.W., and Joyner, R.W. (1977). Conduction velocity and spike configuration in myelinated fibres: computed dependence on internode distance. J. Neurol. Neurosurg. Psychiatry *40*, 769–774.

Buzsáki, G., Logothetis, N., and Singer, W. (2013). Scaling brain size, keeping timing: evolutionary preservation of brain rhythms. Neuron *80*, 751–764.

Caporale, N., and Dan, Y. (2008). Spike timing-dependent plasticity: a Hebbian learning rule. Annu. Rev. Neurosci. *31*, 25–46.

Carr, C.E., and Konishi, M. (1990). A circuit for detection of interaural time differences in the brain stem of the barn owl. J. Neurosci. *10*, 3227–3246.

Carr, C.E., and Soares, D. (2002). Evolutionary convergence and shared computational principles in the auditory system. Brain. Behav. Evol. *59*, 294–311.

Carr, C.E., Soares, D., Parameshwaran, S., and Perney, T. (2001). Evolution and development of time coding systems. Curr. Opin. Neurobiol. *11*, 727–733.

Deschênes, M., and Landry, P. (1980). Axonal branch diameter and spacing of nodes in the terminal arborization of identified thalamic and cortical neurons. Brain Res. *191*, 538–544.

Englitz, B., Tolnai, S., Typlt, M., Jost, J., and Rübsamen, R. (2009). Reliability of synaptic transmission at the synapses of Held in vivo under acoustic stimulation. PloS One *4*, e7014.

Ford, M.C., Grothe, B., and Klug, A. (2009). Fenestration of the calyx of Held occurs sequentially along the tonotopic axis, is influenced by afferent activity, and facilitates glutamate clearance. J. Comp. Neurol. *514*, 92–106.

Forsythe, I.D. (1994). Direct patch recording from identified presynaptic terminals mediating glutamatergic EPSCs in the rat CNS, in vitro. J. Physiol. *479 (Pt 3)*, 381–387.

Grande, G., and Wang, L.-Y. (2011). Morphological and functional continuum underlying heterogeneity in the spiking fidelity at the calyx of Held synapse in vitro. J. Neurosci. *31*, 13386–13399.

Grothe, B., Pecka, M., and McAlpine, D. (2010). Mechanisms of sound localization in mammals. Physiol. Rev. *90*, 983–1012.

Guinan, J., Guinan, S., and Norris, B. (1972). Single auditory units in superior olivary complex .2. Locations of unit categories and tonotopic organization. Int. J. Neurosci. *4*, 147–166.

Halter, J.A., and Clark, J.W., Jr (1991). A distributed-parameter model of the myelinated nerve fiber. J. Theor. Biol. *148*, 345–382.

Joris, P.X., Carney, L.H., Smith, P.H., and Yin, T.C. (1994). Enhancement of neural synchronization in the anteroventral cochlear nucleus. I. Responses to tones at the characteristic frequency. J. Neurophysiol. *71*, 1022–1036.

Kim, J.H., Renden, R., and Gersdorff, H. von (2013a). Dysmyelination of auditory afferent axons increases the jitter of action potential timing during high-frequency firing. J. Neurosci. *33*, 9402–9407.

Kim, S.E., Turkington, K., Kushmerick, C., and Kim, J.H. (2013b). Central dysmyelination reduces the temporal fidelity of synaptic transmission and the reliability of postsynaptic firing during high-frequency stimulation. J. Neurophysiol.

Laughlin, S.B. (2001). Energy as a constraint on the coding and processing of sensory information. Curr. Opin. Neurobiol. *11*, 475–480.

Leão, R.M., Kushmerick, C., Pinaud, R., Renden, R., Li, G.-L., Taschenberger, H., Spirou, G., Levinson, S.R., and von Gersdorff, H. (2005). Presynaptic Na+ channels: locus, development, and recovery from inactivation at a high-fidelity synapse. J. Neurosci. Off. J. Soc. Neurosci. *25*, 3724–3738.

Liberman, M.C., and Oliver, M.E. (1984). Morphometry of intracellularly labeled neurons of the auditory nerve: correlations with functional properties. J. Comp. Neurol. *223*, 163–176.

Makinodan, M., Rosen, K.M., Ito, S., and Corfas, G. (2012). A critical period for social experience-dependent oligodendrocyte maturation and myelination. Science *337*, 1357–1360.

Michailov, G.V., Sereda, M.W., Brinkmann, B.G., Fischer, T.M., Haug, B., Birchmeier, C., Role, L., Lai, C., Schwab, M.H., and Nave, K.-A. (2004). Axonal neuregulin-1 regulates myelin sheath thickness. Science *304*, 700–703.

Peters, A., Palay, L.S., and Webster, H. deF. (1991). The fine structure of the nervous system: neurons and their supporting cells (Oxford University Press).

Quick, D.C., Kennedy, W.R., and Donaldson, L. (1979). Dimensions of myelinated nerve fibers near the motor and sensory terminals in cat tenuissimus muscles. Neuroscience *4*, 1089–1096.

Rhode, W.S., and Smith, P.H. (1986). Encoding timing and intensity in the ventral cochlear nucleus of the cat. J. Neurophysiol. *56*, 261–286.

Roberts, M.T., Seeman, S.C., and Golding, N.L. (2013). A mechanistic understanding of the role of feedforward inhibition in the mammalian sound localization circuitry. Neuron *78*, 923–935.

Rothman, J.S., and Manis, P.B. (2003). The roles potassium currents play in regulating the electrical activity of ventral cochlear nucleus neurons. J. Neurophysiol. *89*, 3097–3113.

Rothman, J.S., Young, E.D., and Manis, P.B. (1993). Convergence of auditory nerve fibers onto bushy cells in the ventral cochlear nucleus: implications of a computational model. J. Neurophysiol. *70*, 2562–2583.

Rushton, W.A.H. (1951). A theory of the effects of fibre size in medullated nerve. J. Physiol. *115*, 101–122.

Sabatini, B.L., and Regehr, W.G. (1999). Timing of synaptic transmission. Annu. Rev. Physiol. *61*, 521–542.

Scholz, J., Klein, M.C., Behrens, T.E.J., and Johansen-Berg, H. (2009). Training induces changes in white-matter architecture. Nat. Neurosci. *12*, 1370–1371.

Seidl, A.H., Rubel, E.W., and Harris, D.M. (2010). Mechanisms for adjusting interaural time differences to achieve binaural coincidence detection. J. Neurosci. *30*, 70–80.

Seidl, A.H., Rubel, E.W., and Barría, A. (2014). Differential Conduction Velocity Regulation in Ipsilateral and Contralateral Collaterals Innervating Brainstem Coincidence Detector Neurons. J. Neurosci. *34*, 4914–4919.

Spirou, G.A., Brownell, W.E., and Zidanic, M. (1990). Recordings from cat trapezoid body and HRP labeling of globular bushy cell axons. J. Neurophysiol. *63*, 1169–1190.

Spirou, G.A., Chirila, F.V., von Gersdorff, H., and Manis, P.B. (2008). Heterogeneous Ca2+ influx along the adult calyx of held: a structural and computational study. Neuroscience *154*, 171–185.

Stuart, G., Spruston, N., and Hausser, M. (2007). Dendrites, 2nd edition (Oxford University Press).

Taschenberger, H., and von Gersdorff, H. (2000). Fine-tuning an auditory synapse for speed and fidelity: developmental changes in presynaptic waveform, EPSC kinetics, and synaptic plasticity. J. Neurosci. Off. J. Soc. Neurosci. *20*, 9162–9173.

Taschenberger, H., Leão, R.M., Rowland, K.C., Spirou, G.A., and von Gersdorff, H. (2002). Optimizing synaptic architecture and efficiency for high-frequency transmission. Neuron *36*, 1127–1143.

Tomassy, G.S., Berger, D.R., Chen, H.-H., Kasthuri, N., Hayworth, K.J., Vercelli, A., Seung, H.S., Lichtman, J.W., and Arlotta, P. (2014). Distinct Profiles of Myelin Distribution Along Single Axons of Pyramidal Neurons in the Neocortex. Science *344*, 319–324.

Usrey, W.M. (2002). The role of spike timing for thalamocortical processing. Curr. Opin. Neurobiol. *12*, 411–417.

Wang, X.-J. (2010). Neurophysiological and computational principles of cortical rhythms in cognition. Physiol. Rev. *90*, 1195–1268.

Waxman, S.G. (1980). Determinants of conduction velocity in myelinated nerve fibers. Muscle Nerve *3*, 141–150.

Wu, S.H., and Kelly, J.B. (1993). Response of neurons in the lateral superior olive and medial nucleus of the trapezoid body to repetitive stimulation: intracellular and extracellular recordings from mouse brain slice. Hear. Res. *68*, 189–201.

Young, K.M., Psachoulia, K., Tripathi, R.B., Dunn, S.-J., Cossell, L., Attwell, D., Tohyama, K., and Richardson, W.D. (2013). Oligodendrocyte dynamics in the healthy adult CNS: evidence for myelin remodeling. Neuron *77*, 873–885.

Acknowledgements:

Supported by the DFG (SFB 870 TP B02&B13, IRTG 1373), Wellcome Trust and UK Medical Research Council. Lee Cossell was in the 4 year PhD in Neuroscience at UCL. We thank Silvia Dobler for her contribution to EM tissue processing and Gerhard Wanner for his technical expertise with the transmission electron microscope. We thank Tom Mrsic-Flogel, Julia Harris, and Elisabeth Engl for comments on the manuscript.

Author contributions:

All authors (M.C.F., O.A., L.C., D.A. and B.G.) contributed to designing the research. Anatomical experiments were performed and analyzed by M.C.F. and O.A. Simulations were performed by L.C. and D.A. All authors (M.C.F., O.A., L.C., D.A. and B.G.) contributed to interpreting the data and writing the paper.

Competing financial interests:

The authors declare no competing financial interests.

Figure Legends

Figure 1 Afferent inputs to coincidence detection neurons of the MSO and LSO.

(**A**) Simplified schematic of the mammalian ITD- and ILD-detection circuit. (**B**) Aligned projections of confocal image stacks from transverse brain stem slices at the level of the trapezoid body. GBC axons were anterogradely traced with tetramethylrhodamine dextran. Three individual fibers are highlighted in color. (**C**) Magnification of a GBC axon segment (red) including two nodes of Ranvier (arrowheads). The position of juxtaparanodal immunolabeled K_v 1.2 channels is shown in green. (**D**) Mean internodal axon diameter is significantly larger in GBC axons than in SBC axons. (**E**) Mean internode length is larger in GBC axons than in SBC axons. For GBC and SBC axons mean INL was calculated from internodes located >700 µm away from the heminode, and from internodes located >500 µm away from the MSO, respectively. Data in (**D**) and (**E**) are represented as mean ± SEM.

Figure 2 Structural parameters of GBC axons vary systematically with their termination region in the MNTB and, hence, their tonotopic identity.

(**A**) Schematic of the tonotopically organized MNTB with GBC axons terminating in the lateral low frequency region (GBClat; dark blue) and in the medial high frequency region (GBCmed; light blue). (**B**) Schematic of a myelinated axon segment illustrating the structural parameters analyzed. (**C**, **E**, **G**) Internodal axon diameter, node diameter, and internode length plotted as functions of distance from the heminode. In GBCmed and GBClat axons, node diameter increases (**E**) whereas internode length decreases (**G**) closer to the synaptic terminals (see also Supplementary Figure 1). The x-value of each data point represents the position of the center of each internode or node along the axon. (**D**, **F**) Internodal axon diameter and node diameter are larger in GBClat than in GBCmed axons (averaged over all positions). (**H**) For >700 µm upstream of the heminode (dashed line in **G**) internode length is significantly larger in GBCmed

than in GBClat axons. (**I**) L/d ratio in GBCmed and GBClat axons plotted against distance from heminode. (**J**) For internodes >700 µm away from the heminode (dashed line in **I**), L/d ratio is larger in GBCmed than in GBClat axons. Numbers on bars are of internodes or nodes in 9 GBClat and 8 GBCmed axons. Data in (**D**, **F**, **H**, **J**) are represented as mean ± SEM.

Figure 3 Myelin thickness in GBC fibers.

(**A**) Transmission electron micrograph of a GBC axon. (**B**) Schematic cross section of a myelinated axon illustrating the measured parameters. (**C**) Outer (fibre) perimeter plotted against inner (axon) perimeter. For calculating g-ratios, perimeter measurements were preferred to diameter measurements because the latter can lead to quite variable results, depending on where diameters are measured. (**D**) G-ratios (inner perimeter/outer perimeter) from 32 individual fibres plotted as a function of axon diameter. Estimated g-ratio values for the mean internodal axon diameter of GBCmed and GBClat axons (0.748 and 0.764) were obtained via interpolation using the line of best fit.

Figure 4 Morphometry of the pre-terminal segment of GBC axons.

(**A**) Schematic of the terminal part of a GBC axon (gray) illustrating the measured parameters. Red segments indicate the position of sodium channels at the last node of Ranvier and the heminode. PN denotes paranode. Green rectangles indicate the position of juxtaparanodal $K_v1.2$ channels and the green open box indicates the position of pre-calyceal $K_v1.2$ channels. (**B**) Maximum-intensity projection of confocal images displaying axons (blue, neurofilament heavy chain) in the MNTB. Arrowheads indicate nodes of Ranvier stained with an anti-pan-Na_v antibody (red). $K_v1.2$ channels are shown in green. (**C**) Distal part of a GBC axon (blue) after digital extraction from the surrounding image. The last node of Ranvier (arrowhead) and the heminode (arrow) are labeled with an anti-pan-Na_v antibody (red). Juxtaparanodal and pre-calyceal $K_v1.2$ channels are shown in green. (**D**) Heminode length and post-heminode length do

not differ between GBCmed and GBClat axons. (**E**) The heminode diameter is larger in GBClat than in GBCmed axons. In GBCmed and GBClat axons the post-heminode diameter is larger than that of the heminode. Data in (**D**) and (**E**) are represented as mean ± SEM.

Figure 5 Computer simulations exploring the effect of morphological parameters on action potential propagation in SBC and GBC axons.

(**A**) Dependence of conduction velocity on L/d ratio in GBClat, GBCmed and SBC axons. For GBClat, GBCmed and SBC axons the internodal diameters were fixed at 3.06, 2.40 and 1.35 µm respectively, and the nodal diameters were fixed at 1.68, 1.50, and 0.85 µm. At low L/d ratios the conduction velocity decreases because a smaller fraction of the axon is myelinated, while at long internode lengths it decreases because of inefficient transfer of depolarization between nodes. Solid arrows indicate the experimentally determined L/d ratios. Dashed arrow shows extra simulated L/d ratio for GBClat. (**B-D**) Dependence of the maximum rate-of-rise (**B**), half-width (**C**) and amplitude (**D**) of the simulated axonal AP on L/d ratios in GBCmed and GBClat fibers. Vertical lines indicate the experimentally observed L/d ratios in GBCmed and GBClat fibers.

Figure 6 Computer simulations exploring the effect of morphological parameters on action potential invasion into the calyx of Held.

(**A**) Propagation of APs into the GBClat (left) and GBCmed (right) axon terminals is facilitated by including experimentally observed gradations of the axon and myelin parameters. The membrane potential waveform in the calyx has a shorter delay, larger amplitude and faster rate of rise when gradations of node diameter, internode diameter and internode length are included. (**B**) Action potential propagation into the calyx of GBClat (left) and GBCmed (right) axons occurs over a wider range of calyx geometries when experimentally observed gradations of the axon anatomy are included. When the diameter of the calyx processes was varied, whilst retaining the same calyx membrane surface area (thus altering the longitudinal resistance into the calyx

processes, but retaining the same conductance and capacitance across the calyx membrane) it was found that graded properties of the axon toward the end of the presynaptic axon allowed propagation of the action potential into the synaptic terminal over a wider range of calyx dimensions. Dotted line indicates calyx process diameter for which the membrane potential waveforms are shown in (**A**). Calyx surface area was 1700 μm^2 for GBClat and 1250 μm^2 for GBCmed.

Figures

Figure 1

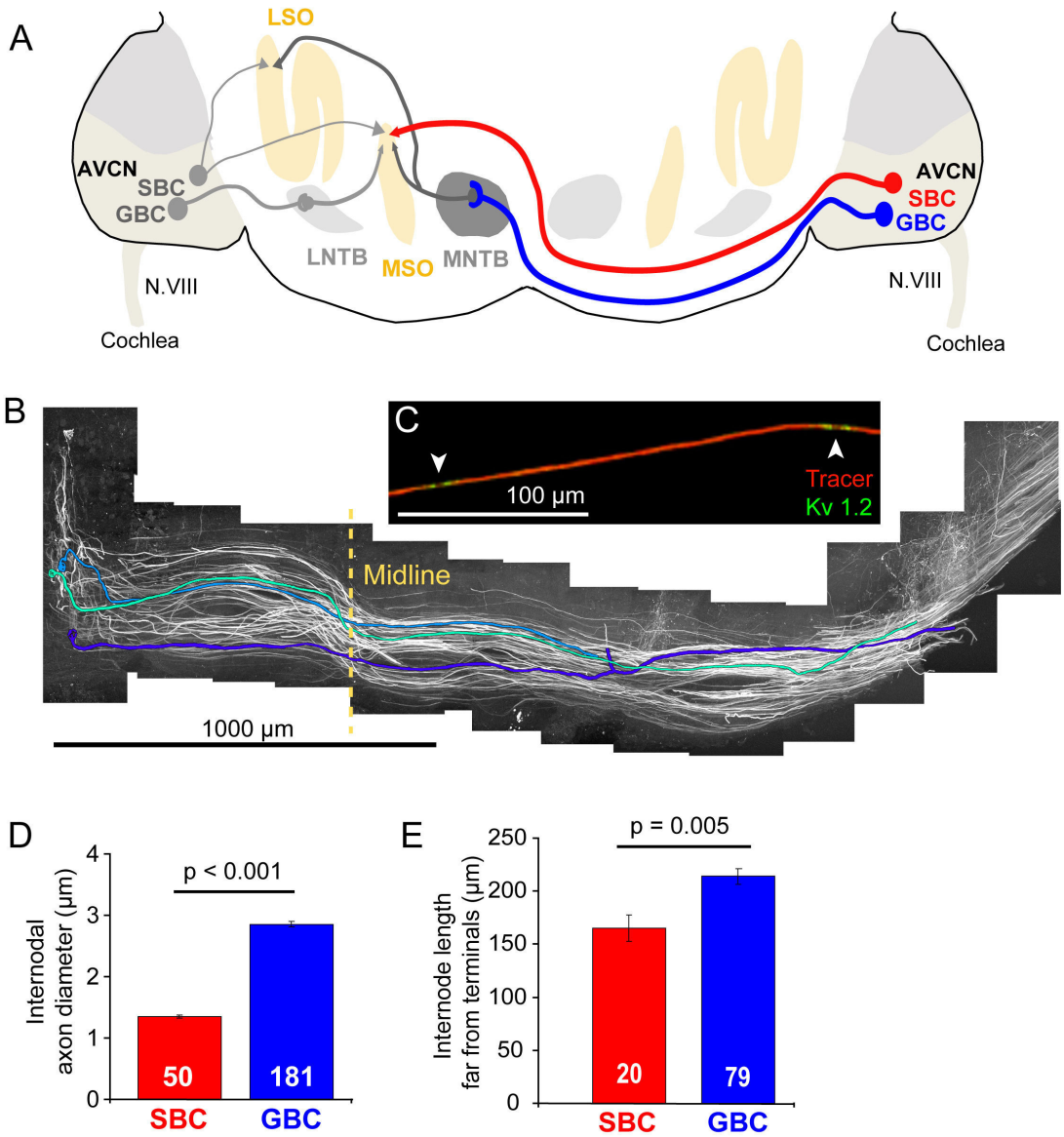

Figure 2

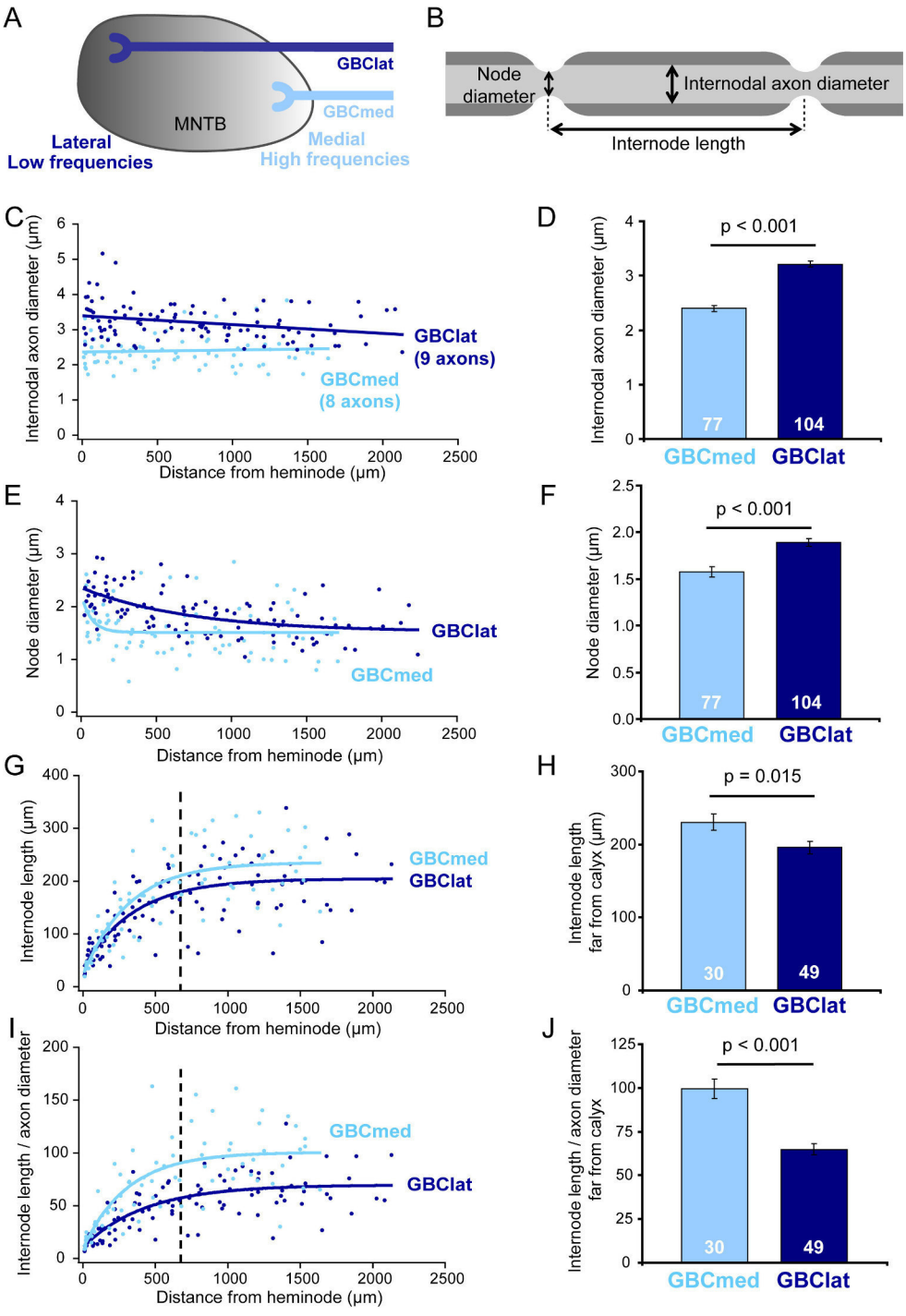
A
GBClat
GBCmed
MNTB
Lateral
Low frequencies
Medial
High frequencies
B
Node diameter
Internodal axon diameter
Internode length
C
Internodal axon diameter (µm)
GBClat (9 axons)
GBCmed (8 axons)
Distance from heminode (µm)
D
p < 0.001
Internodal axon diameter (µm)
77
104
GBCmed
GBClat
E
Node diameter (µm)
GBClat
GBCmed
Distance from heminode (µm)
F
p < 0.001
Node diameter (µm)
77
104
GBCmed
GBClat
G
Internode length (µm)
GBCmed
GBClat
Distance from heminode (µm)
H
p = 0.015
Internode length far from calyx (µm)
30
49
GBCmed
GBClat
I
Internode length / axon diameter
GBCmed
GBClat
Distance from heminode (µm)
J
p < 0.001
Internode length / axon diameter far from calyx
30
49
GBCmed
GBClat

Figure 3

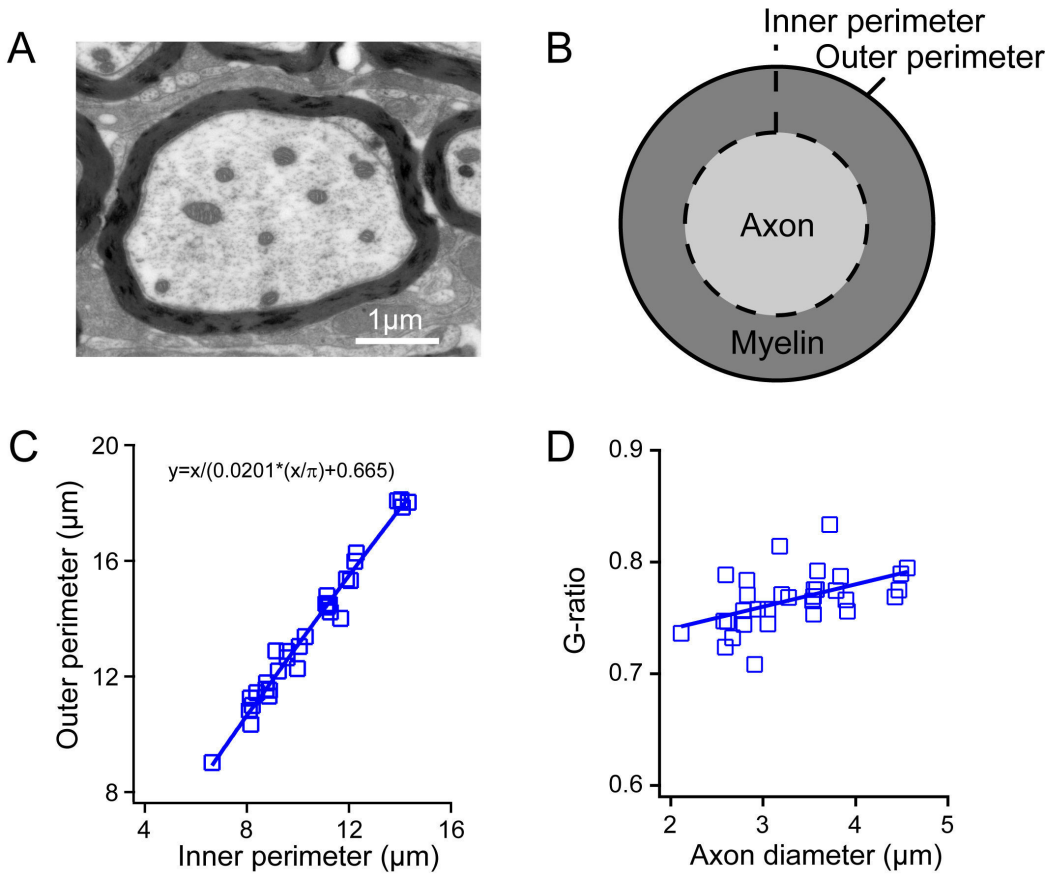
A
1μm
B
Inner perimeter
Outer perimeter
Axon
Myelin
C
y=x/(0.0201*(x/π)+0.665)
Outer perimeter (μm)
Inner perimeter (μm)
D
G-ratio
Axon diameter (μm)

Figure 4

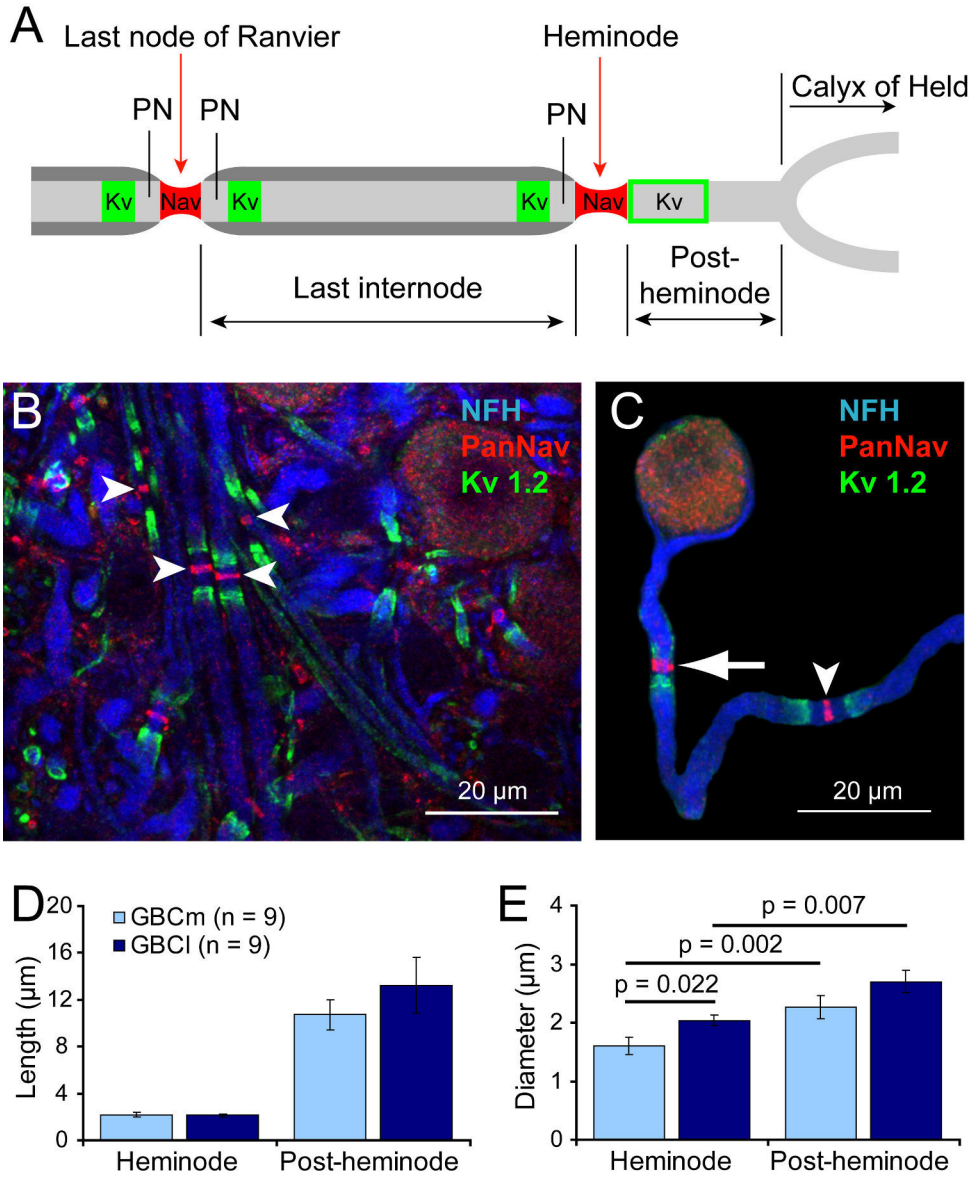
A
Last node of Ranvier
Heminode
Calyx of Held
PN
PN
PN
Kv
Nav
Kv
Kv
Nav
Kv
Last internode
Post-
heminode
B
NFH
PanNav
Kv 1.2
20 µm
C
NFH
PanNav
Kv 1.2
20 µm
D
GBCm (n = 9)
GBCl (n = 9)
Length (µm)
20
16
12
8
4
0
Heminode
Post-heminode
E
Diameter (µm)
4
3
2
1
0
p = 0.007
p = 0.002
p = 0.022
Heminode
Post-heminode

Figure 5

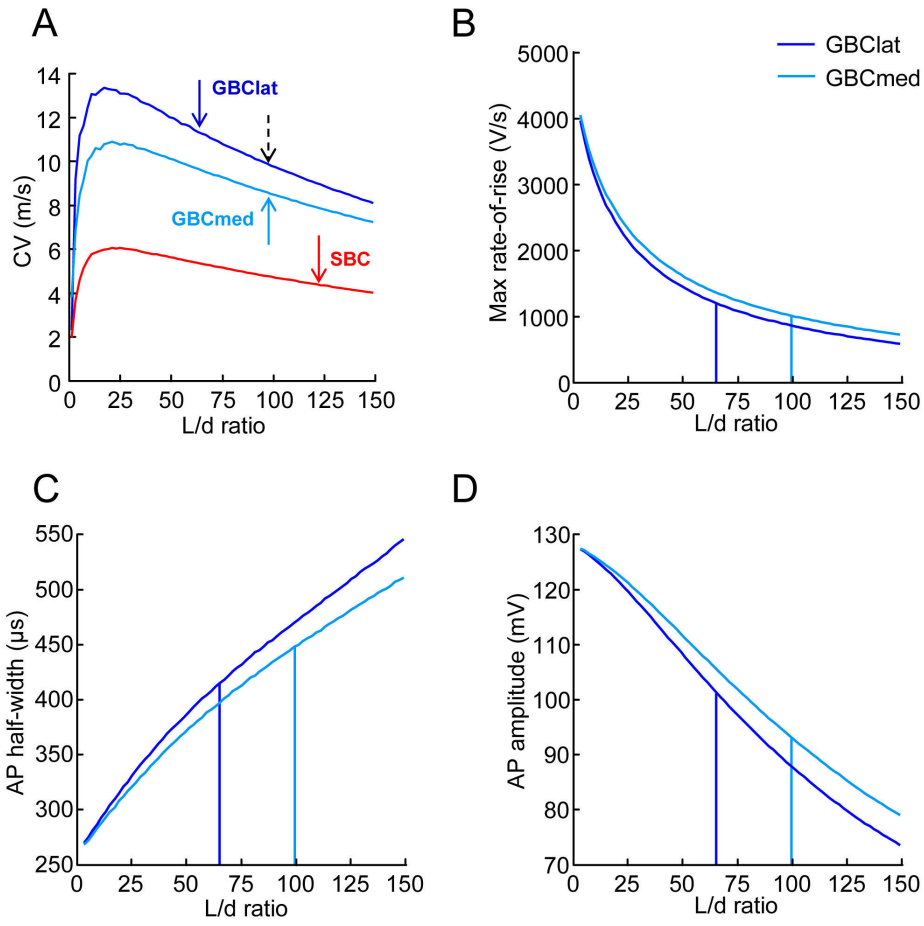
A
CV (m/s)
GBClat
GBCmed
SBC
L/d ratio
B
Max rate-of-rise (V/s)
GBClat
GBCmed
L/d ratio
C
AP half-width (µs)
L/d ratio
D
AP amplitude (mV)
L/d ratio

Figure 6

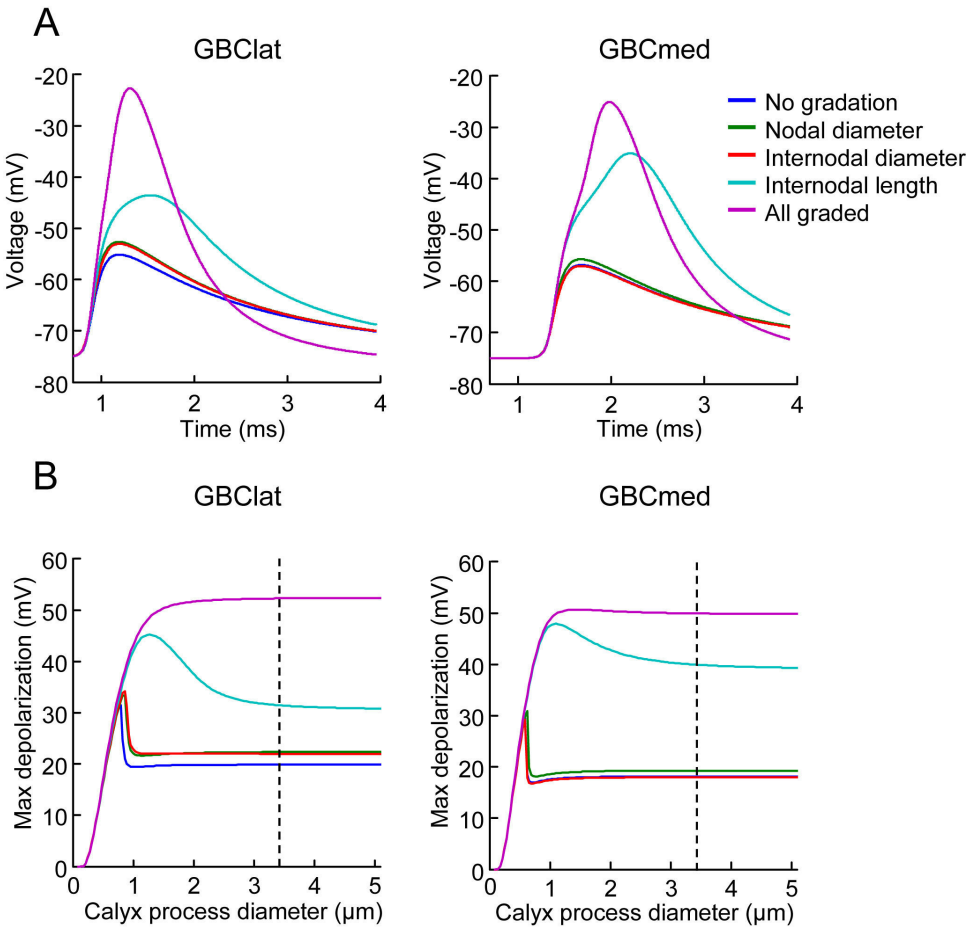
A
GBClat
GBCmed
Voltage (mV)
Time (ms)
No gradation
Nodal diameter
Internodal diameter
Internodal length
All graded
B
GBClat
GBCmed
Max depolarization (mV)
Calyx process diameter (µm)

Supplementary Information

Tuning of myelinated axon properties to preserve temporal information

Marc C. Ford, Olga Alexandrova, Lee Cossell, David Attwell and Benedikt Grothe

Supplementary Figure

Supplementary figure 1

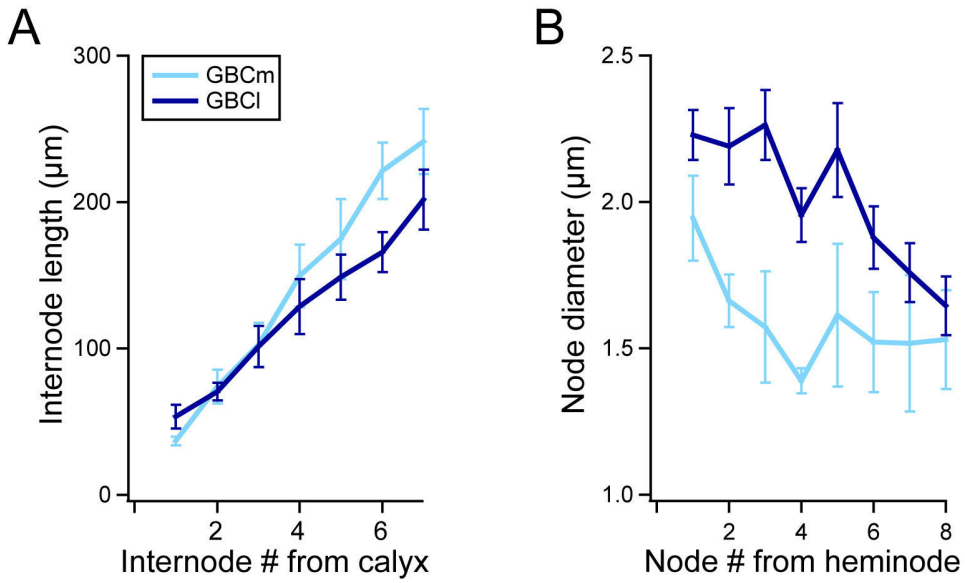

Supplementary Figure Legends

Supplementary Figure 1 Internode lengths and node diameters are graded in the distal part of GBC fibres.

(**A**) In GBCmed fibres the mean internode length decreases progressively from 242±22 µm (7^{th} internode from calyx) to 36.9±3.0 µm (last internode; $p<0.001$; Mann-Whitney rank sum test). A comparable decrease in mean internode length from 202±20 µm (7^{th} internode from calyx) to 53.5±8.3 µm (last internode) was found in GBClat fibers ($p<0.001$; Student's t-test). (**B**) In GBCmed fibers the mean diameter of nodes of Ranvier increases from 1.39±0.04 µm (4^{th} node from calyx) to 1.95±0.15 µm (last node; $p=0.002$). A similar increase in node of Ranvier mean diameter from 1.65±0.10 µm (8^{th} node from calyx) to 2.23±0.09 µm (last node) was found in GBClat fibers ($p<0.001$).

Supplementary Table 1. Geometrical parameters of GBClat, GBCmed and SBC axons along the part of the axon distant from the calyx.

Parameter	Value	Unit
Internode axon diameter		
GBC lateral	3.06	µm
GBC medial	2.41	µm
SBC	1.35	µm
Internodal myelin diameter		
GBC lateral	4.01	µm
GBC medial	3.20	µm
SBC	1.77	µm
Node diameter		
GBC lateral	1.68	µm
GBC medial	1.50	µm
SBC	0.85	µm
Internode length		
GBC lateral	197.7	µm
GBC medial	238.6	µm
SBC	163.8	µm
Node length	1	µm
Number of myelin layers		
GBC lateral	31	
GBC medial	26	
SBC	14	

Supplementary Table 2. Graded geometrical parameters of GBC axons near calyx.

Parameter	GBClat value	GBCmed value	Unit
Internode length			
1st (internode from calyx)	53.5	36.9	µm
2nd	70.7	73.7	µm
3rd	101.5	102.4	µm
4th	128.5	149.5	µm
5th	148.6	174.7	µm
6th	166.0	221.2	µm
Internode axon diameter			
1st (internode from calyx)	3.44	2.38	µm
2nd	3.62	2.47	µm
3rd	3.34	2.31	µm
4th	3.17	2.38	µm
5th	3.28	2.19	µm
6th	3.22	2.53	µm
Node diameter			
1st (node from calyx)	2.23	1.95	µm
2nd	2.19	1.66	µm
3rd	2.26	1.57	µm
4th	1.95	1.39	µm
5th	2.18	1.61	µm
6th	1.88	1.52	µm

Supplementary Table 3. Geometrical parameters of GBC axon terminals.

Parameter	GBClat value	GBCmed value	Unit
Heminode			
Diameter	2.04	1.60	µm
Length	2.13	2.18	µm
Postheminode			
Diameter	2.70	2.26	µm
Length	13.22	10.71	µm

Supplementary Table 4. Electrophysiological parameters of the model.

Parameter	Explanation	Value	Unit	Source
T	Temperature	37	˚C	
g_{Na}	Nodal peak Na^+ conductance	588	mS/cm^2	1
g_{KLT}	Nodal peak low-threshold K^+ conductance	40	mS/cm^2	2
g_{Lkn}	Nodal leak conductance	1.76	mS/cm^2	Adjusted to set V_{rest}
g_{Ca}	Calyx peak Ca^{2+} conductance	3	mS/cm^2	2
g_{KHT}	Calyx peak high-threshold K^+ conductance	20	mS/cm^2	2
g_h	Calyx peak I_h conductance	0.095	mS/cm^2	2†
g_{Lkc}	Calyx leak conductance	0.094	mS/cm^2	Adjusted to set V_{rest}
g_{Lki}	Internode axon leak conductance	0.1	mS/cm^2	3
g_{my}	Myelin membrane conductance	1	mS/cm^2	3
c	Membrane capacitance (includes node, c_n, internode axon, c_i, myelin, c_{my}, and calyx, c_c, membrane)	1	$\mu F/cm^2$	4
ρ_{ax}	Axoplasmic resistivity	70	Ω cm	3
V_{rest}	Resting membrane potential	−75	mV	5
E_{Lkn}	Nodal leak reversal potential	−72	mV	Adjusted to set V_{rest}
E_{Lkc}	Calyx leak reversal potential	−90	mV	Set to E_K
E_{Lki}	Internode axon leak reversal potential	−75	mV	Set to V_{rest}
E_{Na}	Na^+ reversal potential	+55	mV	6
E_K	K^+ reversal potential	−90	mV	7
E_{Ca}	Ca^{2+} reversal potential	+43.5	mV	8
E_h	I_h reversal potential	−43	mV	9

† Reduced 10-fold to increase the input resistance of the calyx.

Supplementary references

1. Lorincz, A. & Nusser, Z. Molecular identity of dendritic voltage-gated sodium channels. *Science* **328,** 906–909 (2010).
2. Spirou, G. A., Chirila, F. V., von Gersdorff, H. & Manis, P. B. Heterogeneous Ca2+ influx along the adult calyx of held: a structural and computational study. *Neuroscience* **154,** 171–185 (2008).
3. Richardson, A. G., McIntyre, C. C. & Grill, W. M. Modelling the effects of electric fields on nerve fibres: influence of the myelin sheath. *Med. Biol. Eng. Comput.* **38,** 438–446 (2000).
4. Hodgkin, A. L. & Huxley, A. F. A quantitative description of membrane current and its application to conduction and excitation in nerve. *J. Physiol.* **117,** 500–544 (1952).
5. Huang, H. & Trussell, L. O. KCNQ5 channels control resting properties and release probability of a synapse. *Nat. Neurosci.* **14,** 840–847 (2011).
6. Rothman, J. S., Young, E. D. & Manis, P. B. Convergence of auditory nerve fibers onto bushy cells in the ventral cochlear nucleus: implications of a computational model. *J. Neurophysiol.* **70,** 2562–2583 (1993).
7. McIntyre, C. C., Richardson, A. G. & Grill, W. M. Modeling the excitability of mammalian nerve fibers: influence of afterpotentials on the recovery cycle. *J. Neurophysiol.* **87,** 995–1006 (2002).
8. Borst, J. G. & Sakmann, B. Calcium current during a single action potential in a large presynaptic terminal of the rat brainstem. *J. Physiol.* **506 (Pt 1),** 143–157 (1998).
9. Rothman, J. S. & Manis, P. B. The Roles Potassium Currents Play in Regulating the Electrical Activity of Ventral Cochlear Nucleus Neurons. *J. Neurophysiol.* **89,** 3097–3113 (2003).

Study 3

Author contributions:

S.L. and C.L. designed the simulations; M.C.F designed the tracer experiments; M.C.F. and O.A. designed the immunohistochemical experiments; F.F. designed the physiological experiments; S.L. performed the simulations; M.C.F. and O.A. performed the anatomical experiments; F.H. and F.F. performed the physiological experiments; S.L. analysed the simulations; M.C.F and O.A. analysed the anatomical data; F.H. and F.F. analysed the physiological data; M.C.F. prepared figure 2, S.L. prepared the other figures; M.C.F wrote the sections concerning the anatomical data, F.F wrote the section concerning the physiological data, S.L. and C.L. wrote the other sections of the manuscript; S.L., M.C.F., F.F., B.G., and C.L. revised the manuscript.

Systems/Circuits

Action Potential Generation in an Anatomically Constrained Model of Medial Superior Olive Axons

Simon Lehnert,[1] Marc C. Ford,[1,2] Olga Alexandrova,[1] Franziska Hellmundt,[1,2] Felix Felmy,[1,3] Benedikt Grothe,[1] and Christian Leibold[1]

[1]Department Biology II, [2]Graduate School of Systemic Neurosciences, and [3]Department Biology I, BioImaging Zentrum, Ludwig-Maximilians-Universität München, D-82152 Planegg-Martinsried, Germany

Neurons in the medial superior olive (MSO) encode interaural time differences (ITDs) with sustained firing rates of >100 Hz. They are able to generate such high firing rates for several hundred milliseconds despite their extremely low-input resistances of only few megaohms and high synaptic conductances *in vivo*. The biophysical mechanisms by which these leaky neurons maintain their excitability are not understood. Since action potentials (APs) are usually assumed to be generated in the axon initial segment (AIS), we analyzed anatomical data of proximal MSO axons in Mongolian gerbils and found that the axon diameter is <1 μm and the internode length is ~100 μm. Using a morphologically constrained computational model of the MSO axon, we show that these thin axons facilitate the excitability of the AIS. However, for ongoing high rates of synaptic inputs the model generates a substantial fraction of APs in its nodes of Ranvier. These distally initiated APs are mediated by a spatial gradient of sodium channel inactivation and a strong somatic current sink. The model also predicts that distal AP initiation increases the dynamic range of the rate code for ITDs.

Key words: **action potential; axon; coincidence detection; interaural time difference; sound localization**

Introduction

The generation of action potentials (APs) is widely assumed to take place in the axon initial segment (AIS). Evidence for this assumption stems predominantly from cortical pyramidal neurons and cerebellar Purkinje neurons using simultaneous somatic and axonal whole-cell recordings (Stuart and Sakmann, 1994; Stuart et al., 1997; Kole et al., 2007; Shu et al., 2007) and voltage-sensitive dye imaging (Palmer and Stuart, 2006; Foust et al., 2010; Palmer et al., 2010; Popovic et al., 2011). At rest, these neurons have relatively high input resistances of 10–200 MΩ, allowing them to integrate synaptic inputs over several milliseconds. Thus, during depolarizing stimuli, the soma generally serves as a strong and temporarily stable current source for the AIS. In neurons with very low input resistances of 2–5 MΩ, the mechanisms of AP initiation have not yet been studied in such great detail. In those cells, the membrane time constants are too short to allow the soma to serve as a temporarily stable current source. Conversely, the soma might even act as a current sink to the AP generating zone and therefore increases the AP threshold at the AIS.

In the present study, we investigated AP generation in neurons of very low input resistance, the principal cells of the medial superior olive (MSO). These neurons have membrane time constants in the range of only a few hundreds of microseconds and input resistances as low as 5 MΩ (Scott et al., 2005; Couchman et al., 2010). The MSO is a binaural nucleus in the ascending auditory pathway. MSO neurons encode the azimuthal position of low-frequency sounds via differences in the time of arrival at the two ears by their firing rate (Goldberg and Brown, 1969; Yin and Chan, 1990; Fitzpatrick et al., 1997; Brand et al., 2002) with a precision of only a few tens of microseconds. This exquisite temporal precision of binaural coincidence detection is partly achieved by the fast membrane time constants of neurons resulting from the high expression of low-voltage-activated potassium channels and hyperpolarization-activated cation channels (Svirskis et al., 2002; Koch et al., 2004; Scott et al., 2005; Mathews et al., 2010; Baumann et al., 2013), both of which are already open at rest. Despite the resulting low input resistance, these neurons can fire at high rates of ~100 Hz and more. The mechanisms by which this is possible are still unresolved.

In this article, we address the question of how AP generation is accomplished in leaky neurons using a computational model of MSO neurons with axonal morphology based on new detailed morphometric data. Our simulations show that, despite the leaky soma, the AIS remains electrotonically isolated and retains its ability to generate APs. However, we also identified conditions under which the APs are initiated at the nodes of Ranvier. This distal initiation of APs increases the dynamic range of the rate code of interaural time differences (ITDs).

Received Sept. 20, 2013; revised March 5, 2014; accepted March 8, 2014.

Author contributions: S.L., M.C.F., O.A., F.F., B.G., and C.L. designed research; S.L., M.C.F., O.A., F.H., and F.F. performed research; S.L., M.C.F., O.A., F.H., and F.F. analyzed data; S.L., M.C.F., F.F., B.G., and C.L. wrote the paper.

This work was supported by the German Research Foundation via the Collaborative Research Center 870 and the Elisabeth und Helmut Uhl Stiftung.

The authors declare no competing financial interests.

Correspondence should be addressed to Christian Leibold, Computational Neuroscience, Department Biology II, Ludwig-Maximilians-University Munich, Grosshaderner Strasse 2, D-82152 Planegg-Martinsried, Germany. E-mail: leibold@bio.lmu.de.

DOI:10.1523/JNEUROSCI.4038-13.2014

 0270-6474/14/345370-15$15.00/0

Materials and Methods

General

All experiments were performed according to institutional guidelines, and national and regional laws; it was approved by the Regierung von Oberbayern (AZ55.2–1-54–2531-105–10). All results are given as the mean ± SEM.

Retrograde labeling of MSO cells

Mongolian gerbils (*Meriones unguiculatus*) of either sex [$n = 4$; postnatal day 29 (P29) to P31] were anesthetized with pentobarbital (2 mg/kg body weight) and intracardially perfused with ice-cold Ringer's solution containing 0.1% heparin. After decapitation, the brainstem was removed from the skull under ice-cold dissection solution comprising the following (in mM): 125 NaCl, 2.5 KCl, 1 $MgCl_2$, 0.1 $CaCl_2$, 25 glucose, 1.25 NaH_2PO_4, 25 $NaHCO_3$, 0.4 ascorbic acid, 3 *myo*-inositol, and 2 pyruvic acid (all chemicals were from Sigma-Aldrich). For retrograde labeling of MSO cells, the brainstem was sectioned along the posterior–anterior axis until the MSO, lateral superior olive, and superior paraolivary nucleus (SPN) were clearly visible. Borosilicate glass micropipettes with a tip diameter of 10–15 μm were filled with a 10% solution of tetramethylrhodamine dextran (3000 molecular weight; Invitrogen) and visually guided to the SPN. Cells were labeled by applying 2–4 electroporation pulse trains (50 ms, 50 V, 10 Hz; modified from previous studies; Ford et al., 2009). Subsequently, the explants were transferred to a chamber containing oxygenated incubation solution (same as incubation solution, but containing 2 mM instead of 0.1 mM $CaCl_2$) and incubated at room temperature for 90 min. Thereafter, brainstems were immersion fixed at room temperature overnight in 4% paraformaldehyde solution.

Immunohistochemistry

Brainstems were sectioned transversally (80–120 μm slice thickness), rinsed in PBS, and transferred to blocking solution containing 1% bovine serum albumin, 2% Triton X-100, and 0.1% saponin in PBS. Multiple-immunofluorescence labeling was performed with the following primary antibodies: ankyrin G (sc-28561; rabbit; 1:500; Santa Cruz Biotechnology), Kv1.2 (75-008 clone K14/16; mouse; 1:500; NeuroMab), microtubule-associated protein 2 (CH22103; chicken polyclonal; 1:1000; Neuromics), and myelin basic protein (ab7349; rat monoclonal; 1:20; abcam). The incubation time (4°C) for primary antibodies was 3 d. After incubation with secondary antibodies (1–2 d; 4°C) and rinsing in PBS, sections were mounted with Vectashield mounting medium.

Confocal microscopy

Confocal images were acquired with a TCS SP5-2 confocal laser-scanning microscope (Leica Microsystems) equipped with HCX PL APO 63×/numerical aperture 1.3 glycerol objective. Fluorochromes were excited at 405, 488, 561, 594, and 633 nm for aminoethylcoumarin acetate, DyLight488, tetramethylrhodamine dextran, Alexa Fluor 594, and DyLight649, respectively. The emission filters for these fluorochromes were set to (in the same order) 410–460, 510–550, 565–585, 605–625, and 640–760 nm. For each optical section the images were collected sequentially for four to five fluorochromes. Stacks of 8-bit grayscale images were obtained with axial distances of 290 nm between optical sections and a pixel size of 120.4 nm. To obtain an improved signal-to-noise ratio, each section image was averaged from five successive scans. After stack acquisition, the Z chromatic shift between color channels was corrected. RGB stacks, montages of RGB optical sections, and maximum-intensity projections were assembled into tables by using ImageJ 1.37k plugins and Photoshop version 8.0.1 (Adobe Systems) software.

Morphometry

Morphometric measurements were made from overlapping image stacks of MSO principal cells. Using the ImageJ 1.37k paint-brush tool, individual axons of MSO cells filled with tetrametylrhodamine dextran were manually labeled by following single axons subsequently through each optical section of the confocal stack (Werthat et al., 2008; for dendrites, see Couchman et al., 2010). Afterward, the neighboring axons were digitally deleted. We refer to this method as digital extraction. The same axon was identified in the neighboring overlapping confocal stacks and digitally extracted. AISs and nodes of Ranvier were identified on the basis ankyrin G/Kv1.2 antibody staining. AIS and internode lengths were measured in three dimensions in confocal stack images using the ImageJ 1.37k Sync Measure 3D tool. AIS and internodal axon diameters were measured at the positions defined by ankyrin G and Kv1.2 labeling (see Fig. 2*B*) in maximum-intensity projections of image stacks based on tetrametylrhodamine dextran labeling. The mean diameter of the first internode was averaged from measurements at several (10–29) different positions between the outer borders of the juxtaparanodes (see Fig. 2*B*, K3 and K6).

Electrophysiology

Experimental procedures were as described in Couchman et al. (2010). In brief, Mongolian gerbils of either sex of P60–P80 were anesthetized with isoflurane. Brains were removed after decapitation, and 110-μm-thick horizontal brainstem slices were taken with a VT1200S vibratome (Leica) in dissection solution containing the following (in mM): 50 sucrose, 25 NaCl, 27 $NaHCO_3$, 2.5 KCl, 1.25 NaH_2PO_4, 3 $MgCl_2$, 0.1 $CaCl_2$, 25 glucose, 0.4 ascorbic acid, 3 myo-inositol, and 2 Na-pyruvate, pH 7.4 when bubbled with 95% O_2 and 5% CO_2. Slices were incubated in recording solution (same as slice solution but with 125 mM NaCl, no sucrose, and 2 mM $CaCl_2$ and 1 mM $MgCl_2$) at 36°C for 45 min, bubbled with 5% CO_2 and 95% O_2.

Incubated slices were placed into a recoding chamber attached to a BX51WI microscope (Olympus) equipped with a custom-made gradient contrast illumination and continuously perfused with recording solution kept at 34–36°C by a Warner Instruments heating system. MSO neurons were visualized at 60× magnification with a Retiga 2000 DC camera (Till Photonics/FEI Munich). Current-clamp whole-cell recordings were performed using an EPC10/2 amplifier (HEKA Elektronik) on visually identified MSO neurons with electrode resistances of ~3 MΩ. Access resistance was estimated in voltage-clamp after break in and was bridge balanced to 100% in current-clamp mode. The internal recording solution consisted of the following (in mM): 145 K-gluconate, 4.5 KCl, 15 HEPES, 2 Mg-ATP, 2 K-ATP, 0.3 Na_2-GTP, 7.5 Na_2-phosphocreatine, 5 K-EGTA, pH 7.2. The liquid junction potential was corrected on-line with an estimated value of 17 mV.

Computational modeling

Based on the morphometric analysis, a multicompartmental model was created to study the generation of APs in MSO principal cells. The model consists of one large somatic compartment that combines the somatic and dendritic membrane surface (Ashida et al., 2007). The model focuses on the axonal morphology, since APs are generally assumed to be generated there. The axon model consisted of an unmyelinated AIS followed by an extensive myelinated part that was periodically interrupted by 21 nodes of Ranvier. Figure 1*A* shows a schematic drawing of the first segments of the model up to the fourth node of Ranvier (R4). The AIS was further subdivided into a tapering part (tAIS) and a constant part (cAIS), resembling the actual geometry of the AIS. The voltages of the compartments followed a Hodgkin–Huxley-type equation as follows:

$$C_m \frac{dV}{dt} = -(I_{Na} + I_{KHT} + I_{KLT} + I_h + I_{lk} + I_{syn} + I_{axial} + I_{ext}),$$

where I_{ext} is the external current, and the ohmic transmembrane currents are as follows:

$$I_x(V) = g_x a_x^m b_x^n (V - E_x).$$

Here, C_m is the membrane capacitance, g_x is respective peak conductances, a_x and b_x are the gating variables, and m and n are the respective cooperativities. The dynamics of the gating variables are modeled according to first-order kinetics, as follows:

$$\frac{da}{dt} = \frac{a_\infty - a}{\tau_a} \text{ and } \frac{db}{dt} = \frac{b_\infty - b}{\tau_b}$$

where a_∞ and b_∞ are the steady-state activation functions, and τ_a and τ_b are the voltage-dependent time constants.

The axial current for the ith compartment is defined as follows:

$$I^{i}_{\text{axial}} = \frac{V_{i-1} - V_i}{R^{i-1,\,i}_{\text{axial}}} + \frac{V_{i+1} - V_i}{R^{i+1,\,i}_{\text{axial}}},$$

in which R_{axial} denotes the axial resistance between the ith compartment and its respective neighboring compartments. The axial resistance results from the geometry of the axonal segment (diameter and length) as well as the specific axial resistivity of 100 Ωcm, which is in the range of usually assumed values (Mainen et al., 1995; Mainen and Sejnowski, 1996; Shu et al., 2007).

The specific model for the sodium channel was taken from Scott et al. (2010) with a reversal potential for sodium of 69 mV and a modified conductance density in the axon of 4 nS/μm^2 to fit the firing threshold of our current-clamp measurements (see Fig. 4). We chose the somatic sodium conductance density to be 0.2 nS/μm^2, a value 20-fold smaller than that in the axon and reflecting the low sodium channel density found in MSO principal cell somata (Scott et al., 2010). The high-threshold potassium channel was modeled according to Rothman and Manis (2003) without a slow activation variable and only at the soma since it had only little effect in the axon. The low-threshold potassium channel (KLT) was modeled according to (Mathews et al., 2010) and was present in the soma and all unmyelinated axonal compartments. The potassium reversal potential was set to −90 mV. The hyperpolarization-activated cation channel gives rise to a somatic hyperpolarization (h)-activated cation current (I_h), which was modeled using the kinetics measured in dorsal MSO neurons (Baumann et al., 2013), with a reversal potential of −35 mV. The resting potential of −68 mV and the somatic input resistance of 5 MΩ were set by adjusting the peak conductances of KLT and h current. The somatic surface was set to 8750 μm^2, such that we get a somatodendritic capacitance of 70 pF (Rautenberg et al., 2009), assuming a specific capacitance of 0.8 μF/cm^2 (Gentet et al., 2000; Shu et al., 2007). As a consequence, the somatic membrane time constant is 350 μs, which closely resembles the measured membrane time constants *in vitro* (Scott et al., 2005; Couchman et al., 2010). The specific myelin conductance per lamella was set to 0.1 μF/cm^2 (McIntyre et al., 2002, 2004). Together with a g-ratio of 0.7 and an assumed myelin periodicity of 16 nm (Agrawal et al., 2009), our standard model exhibits nine myelin lamellae. Thus, we obtain a specific capacitance of the myelin sheath of 0.0111 μF/cm^2, similar to the value of 0.01 μF/cm^2 used in Kuba et al. (2006) for axons of nucleus laminaris (NL) neurons. Some computational studies of axons use specific capacitances per lamella that are significantly higher; however, they compensate for this by a larger number of myelin lamellae. Using a substantially larger myelin capacitance (e.g., three times or higher) would cause propagation failures of generated APs in our model, a result that would contradict the secure propagation of APs known from MSO principal neurons (Scott et al., 2007). This matching of an experimental finding argues in favor of our parameter choice. The validity of the parameter choice is further supported by our physiological measurements of firing thresholds for onset-like responses in Figure 4.

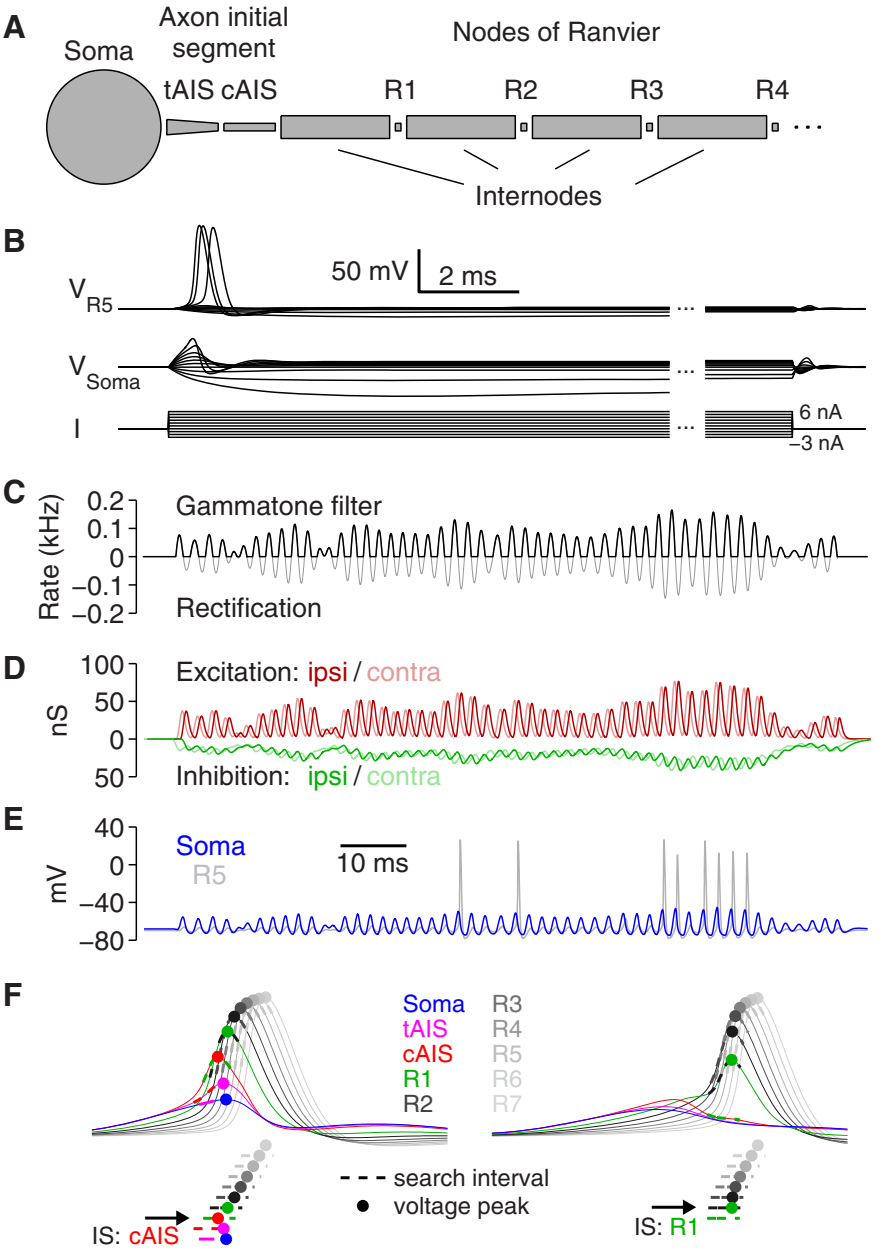

Figure 1. Computational model. ***A***, Schematic drawing of the first segments from the soma to R4 of the MSO model neuron. The AIS is subdivided into two compartments: the tAIS and the cAIS. ***B***, Voltage response in different compartments (top, R5; middle, soma) to current injections at the soma (bottom). ***C***, ***D***, The input conductances were obtained from noise that is filtered by a gammatone filter with a center frequency of 500 Hz (gray) and half-wave rectified (***C***, black). The trace from ***C*** is transformed into conductance inputs by convolution with excitatory (ipsilateral, dark red; contralateral, light red) and inhibitory (ipsilateral, green; contralateral, light green) synaptic kernels (***D***; see Materials and Methods). ***E***, Voltage responses of the soma (blue) and R5 (light gray) of the model when driven with the conductance trains depicted in ***D***. ***F***, The AP initiating segment (IS, black arrow) is derived from the voltage traces at the individual compartments (color coded segments: blue, soma; pink, tAIS; red, cAIS; green, R1; dark gray to light gray, R2–R7). Example traces show a cAIS-generated (left) and an R1-generated (right) AP. Dashed traces indicate the search intervals of duration L that are defined by the voltage peak (dot) of the downstream segment (see Materials and Methods). The voltage peak that occurs earliest in time defines the SIS.

A detailed account of the geometrical and electrical features of the model is given in Tables 1 and 2, respectively.

In response to somatic current injections, the neuron model exhibits typical onset behavior (Fig. 1*B*; i.e., it fires only one AP; Scott et al., 2005; Couchman et al., 2010) at the onset of the depolarizing pulse. The AP amplitude at the soma resembles physiologically measured values of ~10 mV (Scott et al., 2005; Couchman et al., 2010), whereas, at the nodes of Ranvier, the APs exhibit usual amplitude values of ~100 mV.

Table 1. Geometrical parameters of the model

Parameters	Values
Soma/somatodendritic compartment	
Area	8750 μm^2
Axon initial segment (tapering part)	
Length	10 μm
Large diameter	1.64 μm
Small diameter	0.66 μm
Axon initial segment (constant part)	
Length	10 μm
Diameter	0.66 μm
Internodes	
Length	100 μm
Inner diameter	0.66 μm
Outer diameter	0.948 μm (corresponding to a g-ratio of 0.7),
Myelin lamellae	9 (corresponding to a myelin periodicity of 16 nm)*
Node(s) of ranvier	
Length	1 μm
Diameter	0.66 μm

*From Agrawal et al. (2009).

Table 2. Maximum conductances of voltage-gated channels

Channels	Soma	tAIS	cAIS	Internodes	Nodes
gNa	0.2	4	4	0	4
gKHT	0.1	0	0	0	0
gKLT	1.55	1.55	1.55	0	1.55
gh	0.02	0.02	0.02	0	0
glk	0.0005	0.0005	0.0005	0.0002	0.05

Data are in nS/μm^2.

Since ongoing synaptic bombardment under *in vivo* conditions increases the leakiness of the neuron, we decided to study AP generation using a temporally extended naturalistic stimulus that resembles the periodicity of a cochlear channel with a specific center frequency. Our stimuli were generated using bandpass-filtered white noise $n(t)$ (Fig. 1*C*) that was linearly filtered (convolved) with a gammatone kernel, as follows:

$$f(t) = t^4 e^{-t\gamma} \cos(t\omega_c),$$

with $\gamma\ (\omega_c) = 24.7(4.37 \times \omega_c/(2\pi)+1)$ in kilohertz (Glasberg and Moore, 1990) and the center frequency $\omega_c/(2\pi)$ in kilohertz. The filter output was half-wave rectified and normalized to yield a spike probability function with a mean AP rate R (200 Hz) during the stimulus length l = 300 ms. The resulting input train was then multiplied with a factor S, which we call the stimulus intensity, and afterward convolved with double-exponential functions G_{exc} and G_{inh}, which we created to resemble electrophysiologically measured synaptic kinetics for excitatory and inhibitory synaptic activity (Couchman et al., 2010):

$$G_{exc}(t) = g_{exc} \frac{(1 - e^{-t/1.0})^{1.3}\ e^{-t/0.27}}{\max\left((1 - e^{-t/1.0})^{1.3}\ e^{-t/0.27}\right)} \text{ and}$$

$$G_{inh}(t) = g_{inh} \frac{(1 - e^{-t/0.4})\ e^{-t/1.6}}{\max\left((1 - e^{-t/0.4})\ e^{-t/1.6}\right)}.$$

Here, g_{exc} = 37 nS and g_{inh} = 57 nS are the peak conductances of single fibers (Couchman et al., 2010), and time t is considered in milliseconds. Examples for such synaptic conductance trains are shown in Figure 1*D*. Unless mentioned otherwise, we used two inhibitory inputs based on the same stimulus wave form; one advances the excitatory inputs by 0.6 ms and one lags them by 0.11 ms (see Impact of distal AP initiation on ITD coding; Leibold, 2010). Apart from the simulations in which the inhibitory inputs are essential (see Figs. 5*M*, 8), all simulations were performed with only excitatory inputs activated.

Neuron model with dendrites

To test the robustness of our findings in a model with dendrites, we performed simulations (see Fig. 8) in a model variant in which two identical dendrites (five compartments each) were added to the soma. Excitatory synapses were placed at the dendrites (ipsilateral inputs at the lateral dendrite, contralateral inputs at the medial dendrite), and inhibitory synapses were restricted to the soma (Kapfer et al., 2002). The parameters of the dendritic model were chosen such that the basic characteristics at the soma (input resistance, resting potential, capacitance, and EPSP kinetics) matched that of the model with a single somatodendritic compartment and hence the physiological data from Scott et al. (2005) and Couchman et al. (2010). Most importantly, the length of each of the dendrites was 200 μm, with a constant diameter of 5 μm. The somatic surface was reduced to 2467 μm^2, such that the total cell surface remained at 8750 μm^2, which is equal to the model with only one somatodendritic compartment. The geometrical length of the dendritic compartments appears slightly longer than that observed in MSO neurons (Rautenberg et al., 2009), since we did not take into account branching of dendrites but had to match the overall cell surface for comparability.

In the dendritic compartments, sodium channels were omitted (Scott et al., 2010), and thus the sodium density of the remaining somatic compartment was scaled up such that the total sodium conductance matched that of the simpler model with only one somatodendritic compartment. The conductance of the low-threshold potassium channels decayed exponentially along the dendrites with a length constant of 74 μm (Mathews et al., 2010). The peak conductance at the somatic compartment was thereby identical to that of the simpler model. The conductance of the h current was chosen to follow the same gradient along the dendrite to keep the local balance of the two channels. Finally, the input resistance and resting potential of the model with dendrites were matched to those of the simpler model by adjusting the peak conductances of the h current and the passive leak current.

Analysis of simulations

In our simulations, APs during ongoing stimulation were often not detectable in the soma (Fig. 1*E*). However, at more distal locations in the axon, the amplitude and kinetic differences of subthreshold responses and APs are much larger, and, thus, at the more distal axonal compartments these two cases are very easy to separate by a simple amplitude threshold.

Initiating segment. Since the MSO model is described by a system of coupled differential equations, the generation of an AP necessarily requires the interplay of all compartments. The question of where an AP is generated thus can only be answered by a phenomenological criterion. This phenomenological AP-initiating segment was identified as follows (Fig. 1*F*). First, a stimulus evoked AP was defined by a voltage threshold criterion in R7 at which AP and no AP events are clearly separable. Second, we inspected the voltage trace at the axonal nodes of Ranvier and the AIS going from distal to proximal, and identified the segment-specific AP times via the voltage peaks (above −50 mV) that occurred within a certain time interval of duration L around the voltage peak in the (previous) downstream node. The duration L of this time interval is determined by $L = 5.33\ \lambda$, where λ is the impulse conduction time from node to node for a strong current stimulus delivered at rest, which elicits a clear AIS AP. The window is asymmetrically aligned to the previous voltage peak such that the preceding part is three times longer than the part following the voltage peak. The factor 5.33 allows for a slower AP propagation of the AIS and near-threshold stimuli. Within the set of all detected voltage peaks, the earliest in time defines the AP initiation segment. This algorithm has been tested against a variety of simple threshold and phase space criteria, and has proven to give more reliable results for different axonal morphologies and different input parameters, even for extremely fast voltage deflections.

In simulations in which we tested higher somatic input resistances (see Fig. 5*L*), the somatic AP was strongly influencing the voltage trace in the AIS, which made it difficult to identify a clear AIS voltage peak. We therefore identified the AIS AP as the first drop of the voltage derivative below 50 V/s, identifying a shoulder in the voltage deflection.

In few cases (see Fig. 6) during orthodromic propagation does the AP amplitude initially decrease before increasing again in the more distal

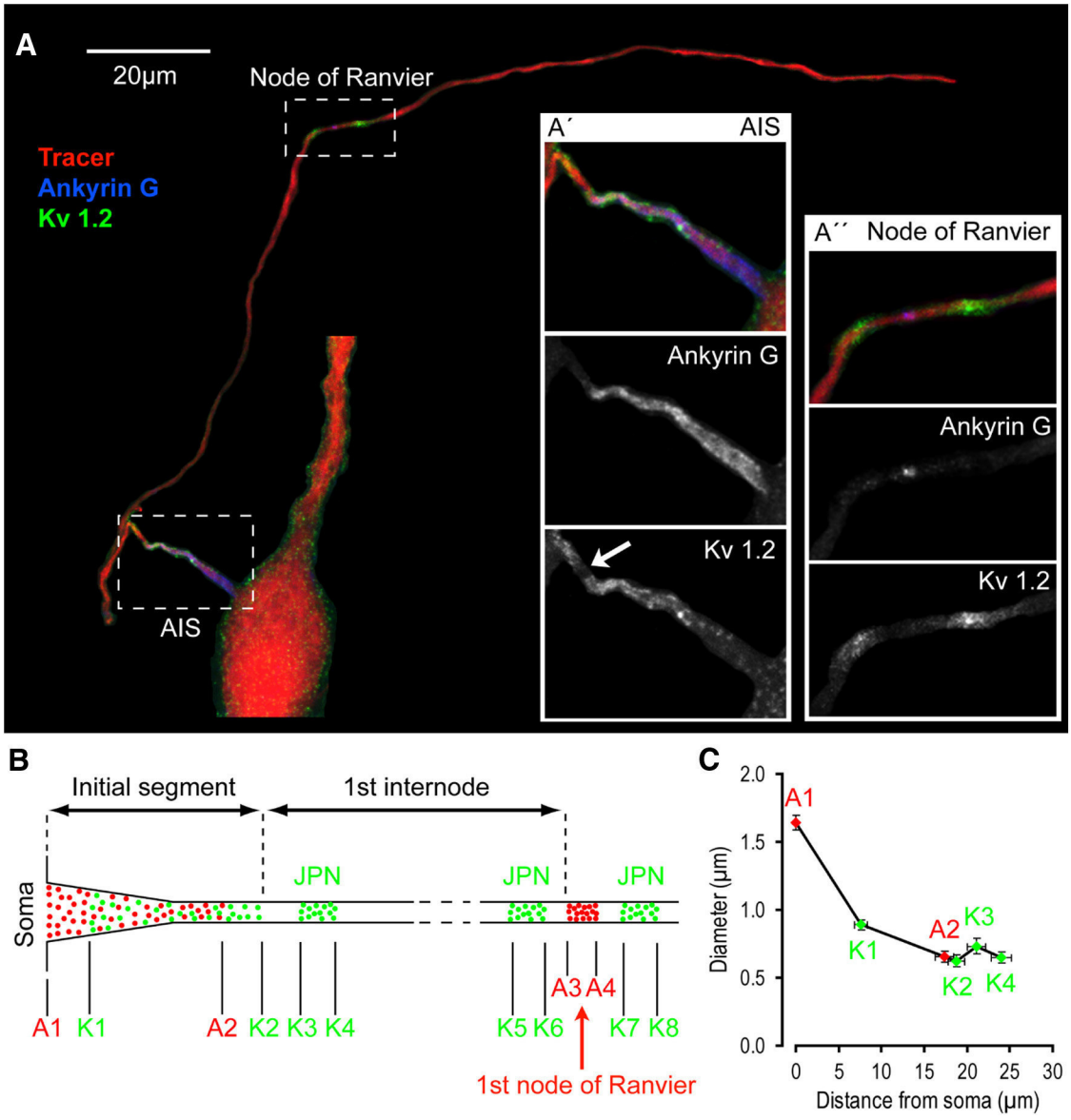

Figure 2. Morphometry of the AIS and first internodal segments in MSO neurons. ***A***, Retrogradely labeled MSO neuron after digital extraction from the surrounding area. Insets ***A′*** and ***A″*** show magnifications of the AIS and first node of Ranvier, respectively. ***B***, Schematic of the proximal axon segment comprising the AIS, the first internode, and the first node of Ranvier, illustrating the positions where measurements were made. Red and green dots indicate the distribution of ankyrin G and Kv1.2 immunolabeling in the AIS and axon. A1–A4 and K1–K8 indicate the borders of ankyrin G- and Kv1.2-positive domains, respectively. JPN, Juxtaparanodes. ***C***, Mean diameter of the AIS at various positions plotted as a function of the mean distance from the soma. Diameter and distance measurements were made at the positions indicated in ***B***. Error bars show the SEM.

axonal segments. Such APs were also labeled as being distally initiated, even though they would have been an AIS AP according to the time-window criterion.

Relative slope during ongoing conductance trains. To identify the input features that are most predictive for spiking, we placed particular emphasis on current amplitude and the relative current slope (derivative divided by amplitude). We chose relative slope because the derivative of any oscillating function linearly scales with the amplitude of the input, and, thus, without such normalization, dependencies on slopes are confounded by amplitude effects. To determine the relative derivative of the input current in Figure 7, *G* and *H*, we normalized by the amplitude of a high-pass-filtered version (fourth-order Butterworth filter with a cutoff of one-third of the stimulation frequency) of the input current rather than by the actual amplitude itself. This was necessary to obtain the actual local relative slope for each cycle and not a distorted value caused by the temporal summation of the input currents of high-frequency stimuli.

ITD coding

To assess how well the responses of the model neuron resolve an ITD τ, we computed the Fisher information $I(\tau)$, assuming a Gaussian distribution of AP counts. From at least 90 repetitions of a 300 ms stimulus, we obtained the mean AP count (tuning curve) $\mu(\tau)$ and its variance $\nu(\tau)$, and calculated the Fisher information as follows:

$$I(\tau) = \frac{\mu'(\tau)^2}{\nu(\tau)} + \frac{1}{2}\left(\frac{\nu'(\tau)}{\nu(\tau)}\right)^2$$

Results

Morphometry of the AIS and proximal axon

Using a combination of retrograde tracing of MSO neurons and immunohistochemical labeling of ankyrin G and Kv1.2 channels, a detailed morphometric analysis of the AIS and proximal axon of

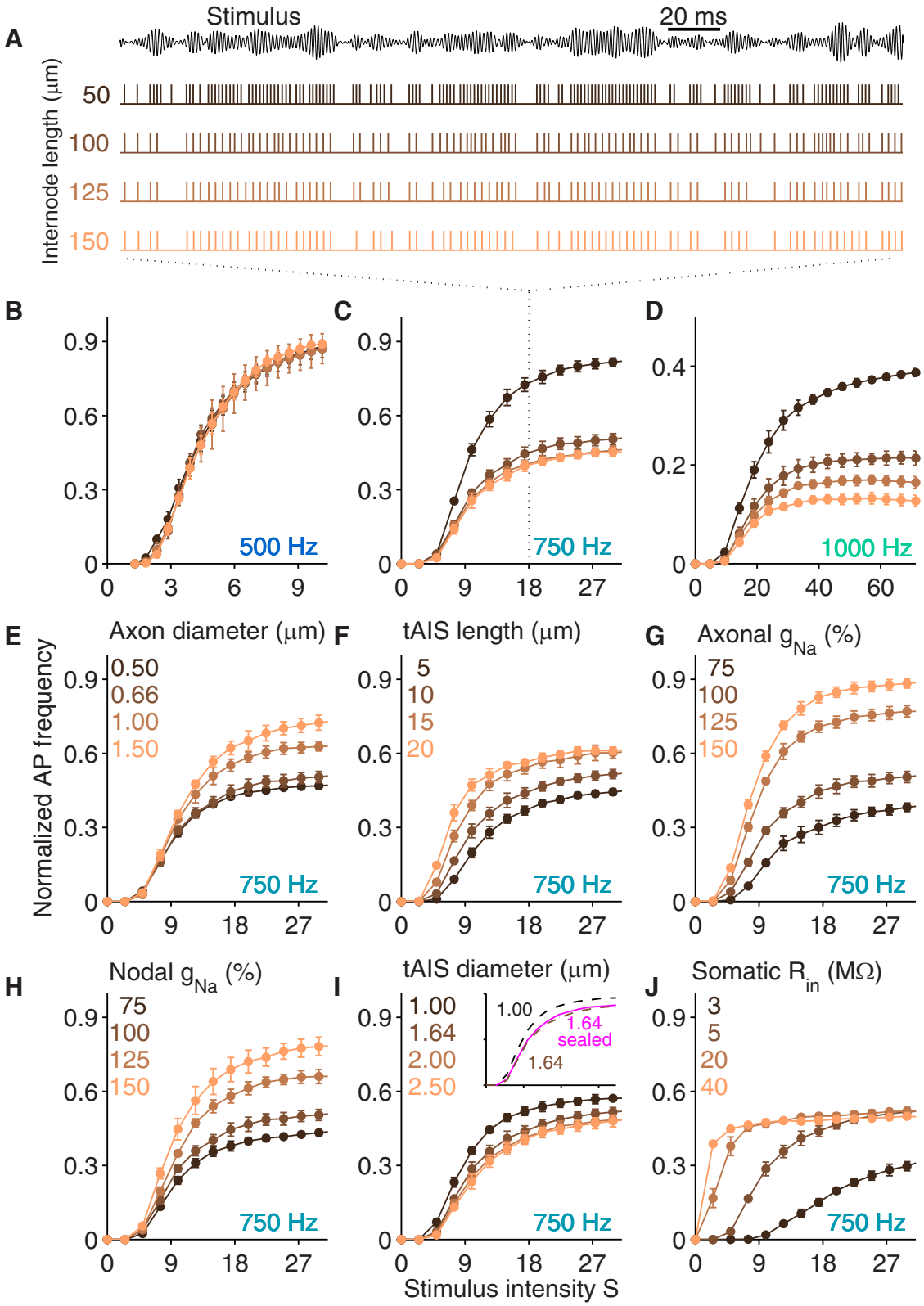

Figure 3. Input/output functions of the model. ***A***, Spike trains were simulated for bandpass stimuli (top trace) of duration 300 ms. The four spike trains are derived from the same (frozen noise) stimulus with a center frequency of 750 Hz and intensity $S = 18$ (as indicated by dotted lines) and internode lengths as indicated by colors. ***B–J***, Graphs depict firing probabilities for different (color-coded) morphological parameters and sodium conductances and for increasing stimulus intensities *S* (see Materials and Methods). Parameters that were varied are internode length (color coded) and center frequency (***B–D***), axonal diameter (***E***), length of the AIS tapering part (***F***), peak sodium conductance in all unmyelinated parts of the axon (***G***), peak sodium conductance in the nodes of Ranvier (***H***), proximal diameter of the AIS tapering part (***I***), and somatic input resistance (***J***). Inset in ***I*** compares relative AP frequencies of two control traces (with different tAIS diameter) from ***I*** to a model where all subthreshold transmembrane conductances were removed from the tAIS (pink trace, sealed).

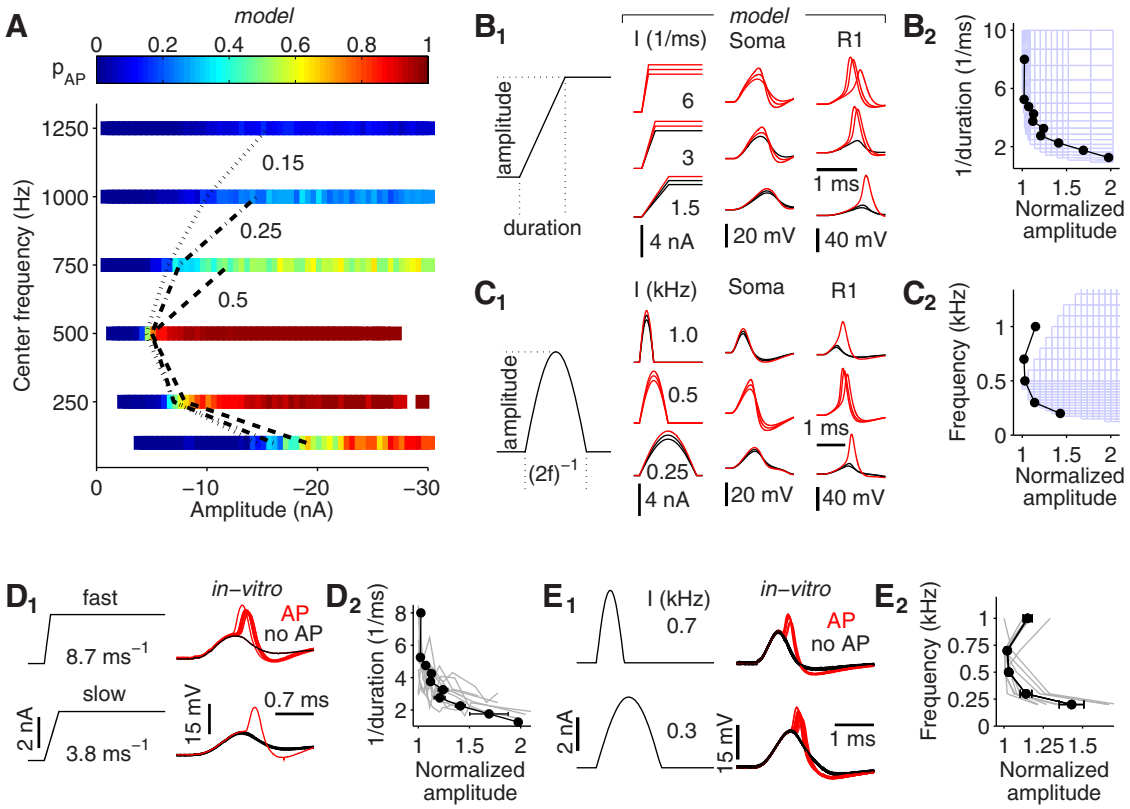

Figure 4. Frequency-dependent AP threshold. ***A***, Firing probability (color coded) of the model cell as a function of center frequency and cycle amplitude for ongoing inputs. Iso-probability contours are shown for firing probabilities of 15% (dotted trace), 25% (dot-dashed trace), and 50% (dashed trace). ***B*$_1$**, Ramp stimulus (left) and raw data of the simulation for three different ramp durations (right). Black and red traces indicate subthreshold and AP responses, respectively. ***B*$_2$**, Light blue mesh shows parameter region that evoked an AP response. *In vitro* threshold is overlaid as a black line (see ***D***). ***C***, same as ***B***, for half-wave-rectified sine stimuli. ***D***, ***E***, *In vitro* results. ***D*$_1$**, Stimuli (left) and current-clamp traces (right) for the ramp stimulus experiment. ***D*$_2$**, Threshold curves from individual neurons (gray traces) and their average (black, $n = 12$, same as in ***B*$_2$**). ***E***, same as ***D***, but for half-wave-rectified sine stimuli *in vitro* ($n = 8$). The data of ***B***–***E*** were normalized to the smallest amplitude that elicited an AP response in the specific cell. Error bars show the SEM.

12 MSO neurons was performed (Fig. 2*A*). Our immunostainings revealed that the AIS consisted of a 17.3 ± 1.1-μm-long ankyrin G-positive domain emerging directly from the soma and a 11.2 ± 0.6-μm-long Kv1.2-positive domain starting at 7.6 ± 0.7 μm distal from the soma in the labeled axons (Fig. 2*A*,*B*). Diameter measurements indicated that the AIS consisted of the tAIS and the cAIS. On average, the diameter of the AIS decreased from 1.6 ± 0.1 μm at the soma (position A1) to 0.6 ± 0.1 μm at the position K2, as defined in Figure 2, *B* and *C*. The length of the AIS (measured from A1 to K2; Fig. 2*B*) ranged from 14.0 to 24.0 μm (18.8 ± 1.0 μm). Adjacent to the AIS was a 2.3 ± 0.2-μm-long segment devoid of ankyrin G and Kv1.2 labeling, which we interpret as the paranodal (or para-AIS) region, where myelin is anchored to the axon (Duflocq et al., 2011; Fig. 2*A*′, arrow). The paranodal region was followed by a 2.9 ± 0.5-μm-long Kv1.2-positive domain representing the juxtaparanode (or juxtapara-AIS). The first node of Ranvier was identified based on its typical arrangement of two juxtaparanodal Kv1.2-positive domains that were separated from the nodal ankyrin G domain through unlabeled paranodes (Fig. 2*A*′). The length of the first internode ranged from ~50 to ~150 μm (100.4 ± 9.1 μm), and its mean diameter (Fig. 2*B*,*C*, measured at several positions between the two juxtaparanodal borders K3 and K6) was 0.7 ± 0.1 μm. These axonal parameters were used to constrain a computational model of the MSO neuron (Table 1).

Input–output functions

We first determined how the AP frequency of our computational neuron model is influenced by the parameters that we assumed to be most crucial for axonal excitability (AP threshold), i.e., the morphological parameters internode length, axonal diameter, proximal diameter, and tAIS length; and the electrical properties density of sodium channels in the unmyelinated axonal segments and somatic input resistance (Fig. 3). We tested how much the influence of these excitability parameters on AP probability depended on the center frequency of the bandpass stimuli (see Materials and Methods) and found that for center frequencies of ≤500 Hz all of the axonal parameters had little influence on spiking probability (Fig. 3*A*–*D*, example of internode length). For higher stimulus frequencies, the axonal parameters had distinct influences on the input–output functions. As we increased the internode length, the spiking probability generally decreased (Fig. 3*A*–*D*), which can be attributed to a reduction of the axial current flow. Geometrical alterations that increase the axonal sodium conductance (while keeping the channel density constant) mostly result in an increase of the firing rate. This increase could be observed in simulations with altered axonal diameter [keeping a constant ratio of 0.7 between the inner (axon) and outer (myelin) diameter of the internode]. The firing rate also increased with axonal diameter (Fig. 3*E*), reflecting the corresponding increase of the number of sodium channels. Also an increase of the length of the tAIS led to a higher AIS sodium

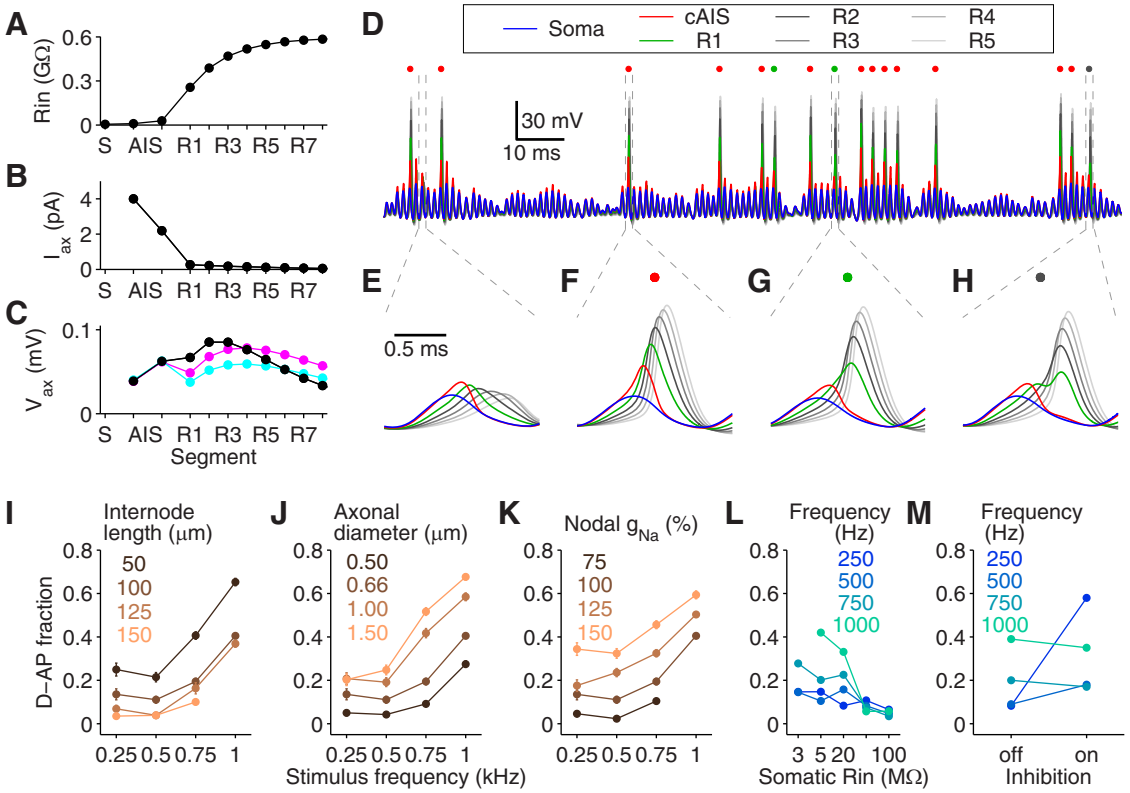

Figure 5. Distal AP initiation. ***A–C***, Local input resistance (***A***), axial current (***B***), and V_{ax} (***C***) in the different model compartments for the standard parameters (black traces), the model with shorter internode lengths of 50 μm (magenta traces), and thicker axonal diameter of 1.5 μm (cyan traces). ***D***, Exemplary voltage traces in different compartments (colors as indicated). Filled colored circles show the AP-initiating segment for each suprathreshold response (see legend). ***E–H***, Example events (from ***D***) for subthreshold response (***E***), and evoked APs generated in the AIS (***F***), R1 (***G***), and R2 (***H***). ***I–K***, Fraction of distally initiated APs (D-AP; for a fixed AP probability of 15%), with varying internode length (***I***), axonal diameter (***J***), and sodium conductance in the nodes of Ranvier (***K***). ***L***, Fraction of distally initiated APs for different somatic input resistances. ***M***, Fraction of distally initiated APs without and with inhibition for several input frequencies.

conductance and an increasing firing probability (Fig. 3*F*). In line with these findings, a direct increase in the sodium conductance in unmyelinated axonal compartments (Fig. 3*G*,*H*) also facilitated AP probabilities. However, a different effect was observed when the proximal diameter of the tAIS was decreased, which also decreased the amount of sodium conductance but, interestingly, increased AP frequency (Fig. 3*I*). This indicates that in addition to the total local sodium conductance excitability of the axon also profits from an increased electrotonic isolation from the leak currents in the soma. This interpretation was corroborated by the following two additional sets of simulations: (1) an increase of the tAIS input resistance by removing all tAIS subthreshold conductances from the equation had almost no effect on firing probability (Fig. 3*I*, inset); and (2) increasing the somatic input resistance (by multiplicative scaling of the peak conductances of KLT channel and h current, keeping a constant resting potential) strongly enhanced AP frequency (Fig. 3*J*). The MSO soma thus acts as a strong current sink for the AIS, and, hence, the axon excitability crucially depends on rather small changes of the somatic current reaching the axon.

Frequency-dependent threshold

Since the firing probabilities strongly depended on the center frequency of the inputs (Fig. 3), we performed a more systematic analysis of the frequency dependence of excitability of our computational neuron model and corroborated these data by *in vitro* measurements of MSO cells. The frequency dependence of MSO firing probability in the model was determined for a large range of bandpass stimuli with center frequencies ranging from 100 to 1250 Hz and varying stimulation intensities (Fig. 4*A*). This allows the assessment of the firing thresholds of MSO neurons with respect to both the shape (frequency content) and the amplitude of the input currents. The lowest current thresholds were observed at ~500 Hz. For higher as well as lower input frequencies, more excitatory drive was necessary to reach a certain firing probability.

To better understand the dependence of AP initiation on the input kinetics, we simulated two onset stimulation paradigms using brief current stimuli applied at rest. First, we applied a ramp stimulus for which we could independently vary amplitude and ramp duration (Fig. 4B_1). The ramp duration was assumed to serve as a proxy for stimulus shape (frequency) during the ongoing bandpass stimulation. The firing probabilities (Fig. 4B_2) obtained with these stimuli very well explained the behavior observed for low-frequency bandpass inputs, which effectively implements a slope threshold (Golding and Oertel, 2012); that is, the neuron fires in response to a specific speed of membrane depolarization that is rather independent of amplitude. Such behavior has been previously described in octopus cells (Ferragamo and Oertel, 2002), in the vestibular pathway (Beraneck et al., 2007) and the MSO (Jercog et al., 2010), and is generally attributed to the fast kinetics of the KLT channels, which are further opening only for slow stimuli and cannot generate such additional leaks for fast-rising stimuli. The high-frequency behavior of our threshold profile, however, could not be modeled using the simple ramp stimuli. We therefore also applied half-wave-rectified sine waves (Fig. 4C_1). Here again, both the low- and the high-frequency increase of threshold amplitudes was observed

(Fig. 4C_2). Thus, the threshold amplitude for high frequencies crucially depends on the duration of the stimulus. This indicated that the high-frequency part of the threshold curve reflects the limit imposed by the charging of the membrane capacitor for regimes in which the membrane voltage rises too quickly to open the low-threshold potassium channels (Jercog et al., 2010). These modeling results were verified physiologically using whole-cell current-clamp recordings using the same stimuli as in the model (see Materials and Methods). From the recorded data obtained with the ramp stimuli, the AP probability was fitted by a sigmoid for each ramp duration as a function of the amplitude using at least 10 consecutive trials. The amplitude at which the fit was at 50% AP probability was defined as the threshold. The physiologically obtained threshold curves qualitatively matched the modeling results for the ramp-current stimuli (Fig. 4B_2, superimposed black trace, *D*) with less firing for slow-input ramps and secure responses for faster ramps. For the half-wave-rectified sine stimuli, threshold amplitudes were obtained by manual testing (Fig. 4C_2, superimposed black trace, *E*) and also qualitatively matched the simulations with the lowest firing threshold for medium frequencies and less firing for low and high frequencies. From these simulations and experiments, we concluded that the threshold behavior observed during ongoing stimulation is functionally very similar to that in onset-like stimulus paradigms with single current pulses.

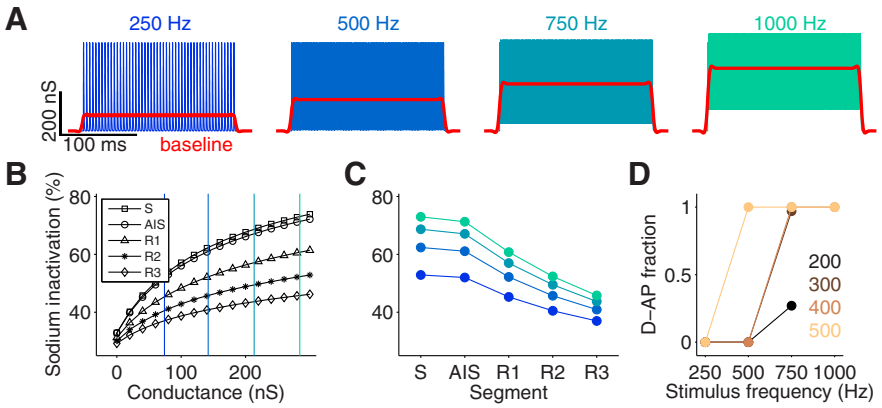

Figure 6. High input frequencies cause sodium channel inactivation in the somatic and proximal axonal membranes. ***A***, Periodic synaptic conductances with a peak value of 400 nS for center frequencies of 250, 500, 750, and 1000 Hz. Red traces are obtained by low-pass filtering the voltage traces (cutoff frequency, 100 Hz). ***B***, Steady-state sodium channel inactivation measured in different model compartments for increasing excitatory conductances. ***C***, Steady-state sodium channel inactivation for traces (color coded) in ***A*** in different compartments. ***D***, Fraction of distally initiated APs (D-APs) for input traces in ***A*** with different conductance peak values (color coded; in nS).

Site of AP initiation

Although AP initiation might be functionally similar under onset and ongoing stimulus conditions, the underlying mechanisms may be different, since, owing to the temporal summation of the inputs, the ongoing stimulation sets the cell membrane into a state that is very different from resting conditions (e.g., because of steady-state activation of channels and changes in input resistance). We therefore investigated AP initiation during ongoing stimulation in greater detail. In particular, we were interested in the contributions of the different cellular (somatic and axonal) compartments to the generation of APs.

A first assessment of the local excitability of the model neuron was derived from local input resistance measurements, using small hyperpolarizing current pulses (amplitude, −100 pA for 300 ms) that were consecutively injected into the soma, the cAIS, and the nodes of Ranvier of our model at rest (Fig. 5*A*, black trace). Here, the input resistance was derived from the peak of the voltage responses and not the steady-state component to obtain a measure for the instantaneous susceptibility of the local membrane. In our model, the peak conductance parameters were chosen such that the somatic input resistance was fixed at 5 MΩ (Scott et al., 2005; Couchman et al., 2010). With the standard parameter settings (Tables 1 and 2), the AIS had two (tAIS, 9.7 MΩ) to six times (cAIS, 28.5 MΩ) the input resistance of the soma. Further distally in the axon, the R1 showed a 50-fold increase of input resistance (256.5 MΩ). We next applied a current pulse of 1 nA at the soma while at the same time extracting the peak of the axial current in the respective axonal segments (Fig. 5*B*, black trace). The portion of this current that spread from the soma into the AIS was only 0.4% (4 pA), with further attenuation at the R1 (0.3 pA). Multiplying the axial current by the local input resistance yields a measure that can be interpreted as the axonally mediated voltage amplitude (V_{ax}). This voltage amplitude was further used as an estimate for the local excitability. The axially mediated voltage amplitude was maximal at the second and third nodes of Ranvier (Fig. 5*C*, black trace). Thus, in contrast to the classical model of AP initiation at the AIS, the second and third nodes appear to be more excitable, indicating that the more distal compartments play an important role in axon excitability in leaky neurons.

A detailed analysis of AP times in the individual compartments revealed that the site of AP initiation was indeed not restricted to the AIS (Fig. 5*D–H*). Although many APs were initiated in the AIS (Fig. 5*F*,*I–K*), 5–60% (depending on input conditions) of the APs first crossed the detection threshold (see Materials and Methods) at the first (Fig. 5*G*) or even the second (Fig. 5*H*) node of Ranvier, while the AIS showed a response similar to the subthreshold case (Fig. 5*E*). The amplitudes of the somatic and AIS APs were relatively small, independent of where they were generated, and underwent subsequent amplification by the nodes of Ranvier as they orthodromically propagated along the axon (Fig. 5*F–H*).

To further elucidate the mechanisms of this distal AP initiation, we quantified its occurrence under our naturalistic ongoing input paradigm for different morphological parameters. For purely excitatory inputs, the fraction of distally initiated APs over AIS APs increased with stimulus frequency (Fig. 5*I–L*). For shorter internodes (Fig. 5*I*) and thicker axonal diameter (Fig. 5*J*), more distal APs were observed. This is because the resulting increased axial conductance allows the stimulus-evoked potential to propagate further along the axon and is also illustrated by the peak of the V_{ax} located at more distal regions of the axon in both conditions (Fig. 5*C*, cyan and magenta traces). Consistently, a higher nodal sodium conductance increased the fraction of distally initiated APs as well, because APs could be more easily initiated at the nodes (Fig. 5*K*).

A major factor influencing distal AP initiation for inputs at all center frequencies is the somatic input resistance. The prevalence of distal AP initiation is strongly reduced with the increase of input resistance of the soma (Fig. 5*L*). Hence, distal spiking

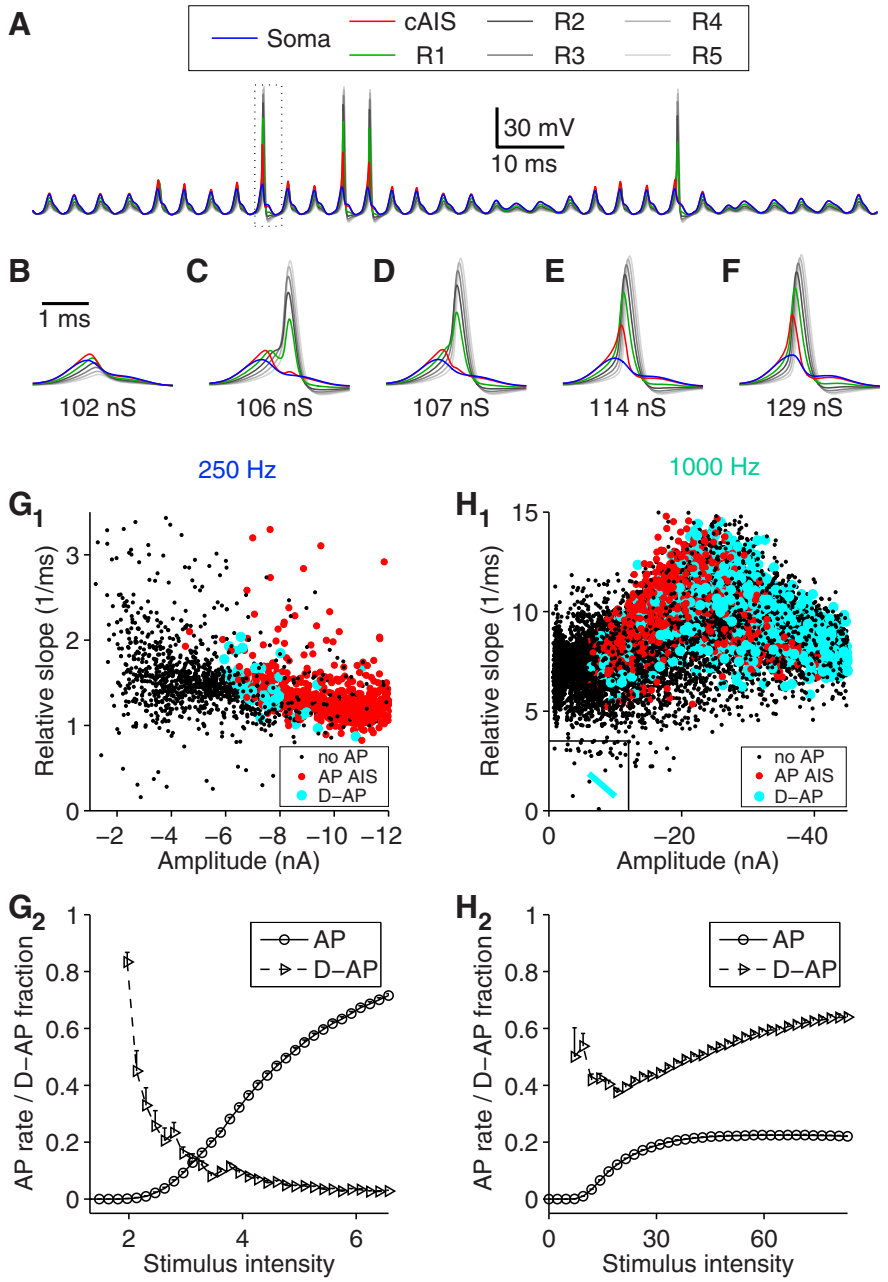

Figure 7. Function of distal AP initiation. ***A***, Example voltage traces for a stimulus with center frequency 250 Hz. The box indicates a cycle that was further investigated for different excitatory peak conductance values. ***B–F***, The selected stimulus cycle evolves from a subthreshold response (***B***), via a distally initiated AP (***C***, ***D***), to an AP initiated in the AIS (***E***, ***F***). G_1, Model responses to input trains with a center frequency of 250 Hz generate a broad range of cycle amplitudes and relative derivatives (see Materials and Methods). Each dot corresponds to a cycle within the input train. Black, Subthreshold response; red, AP response initiated in the AIS; cyan, AP response initiated in a node of Ranvier (D-AP). G_2, Firing rate and fraction of distally initiated APs for increasing excitatory synaptic conductances and an input with 250 Hz center frequency. H_1, Same as G_1 for an input with a center frequency of 1000 Hz. The cyan line in the box is a linear fit to the distally initiated APs from G_1. H_2, Same as G_2 but for inputs with 1000 Hz center frequency.

should be particularly prevalent in leaky neurons that receive fast-fluctuating inputs such as in the MSO.

Since MSO neurons not only receive excitatory inputs but also strong phase-locked inhibitory inputs via the medial and lateral trapezoid body, we also performed simulations with excitatory and inhibitory inputs. In these simulations, the frequency dependence of the site of AP initiation is less clear (Fig. 5*M*). On the one hand, the fraction of distally initiated APs also increased with frequency for center frequencies of >500 Hz. On the other hand, for a low center frequency of 250 Hz, inhibition also generated large amounts of distal AP initiation. This already indicates that distal AP initiation may result from a variety of different mechanisms, particularly also those that add to the somatic current sink.

Distal AP initiation for high-frequency inputs

The steady-state approach to axonal excitability (Fig. 5*A–C*) disregards contributions from the dynamics of the ion channels. To understand whether such dynamic properties of the neuron model also contribute to distal AP initiation, we used strictly periodic synaptic (conductance) input trains of different frequencies (Fig. 6*A*). Temporal summation of the synaptic inputs generated a conductance plateau that increased with frequency as revealed by low-pass filtering (Fig. 6*A*, second-order Butterworth low-pass filter with a cutoff frequency of 100 Hz, red traces). We then applied these average conductance values as a constant conductance to the cell and measured the corresponding steady-state sodium channel inactivation at the soma, the AIS, and the first three nodes of Ranvier (Fig. 6*B*). This revealed that a larger average conductance generally caused more sodium channel inactivation. Moreover, the conductance level was highest at the soma and decreases along the axon. Thus, a regime of a high-frequency input generates a persistent depolarization of the membrane with a larger fraction of inactivated sodium channels at the proximal axonal membranes than at the distal segments (Fig. 6*C*). As a result, this leads to a larger fraction of distal AP initiation with increased input frequency (Fig. 6*D*).

Influence of distal AP initiation on the firing threshold

To understand the functional relevance of distal AP initiation, we next investigated which input properties are particularly amenable to evoke distal APs during ongoing stimulation (Fig. 2*B–D*). We therefore repeatedly stimulated the neuron model with identical input trains for consecutively increasing mean synaptic conductances. Figure 7*A–F* shows an exemplary stimulus cycle for which, with increasing conductance, the voltage profile along the axon transitions from a completely subthreshold response (Fig. 7*B*) over an AP being initiated at the nodes of Ranvier (Fig. 7*C*,*D*) to an AP generated at the AIS (Fig. 7*E*,*F*). From these examples, it seemed that distal AP initiation is particularly prevalent at the AP threshold.

To further evaluate the threshold property of distal AP initiation, we ran the simulations using excitatory bandpass inputs of

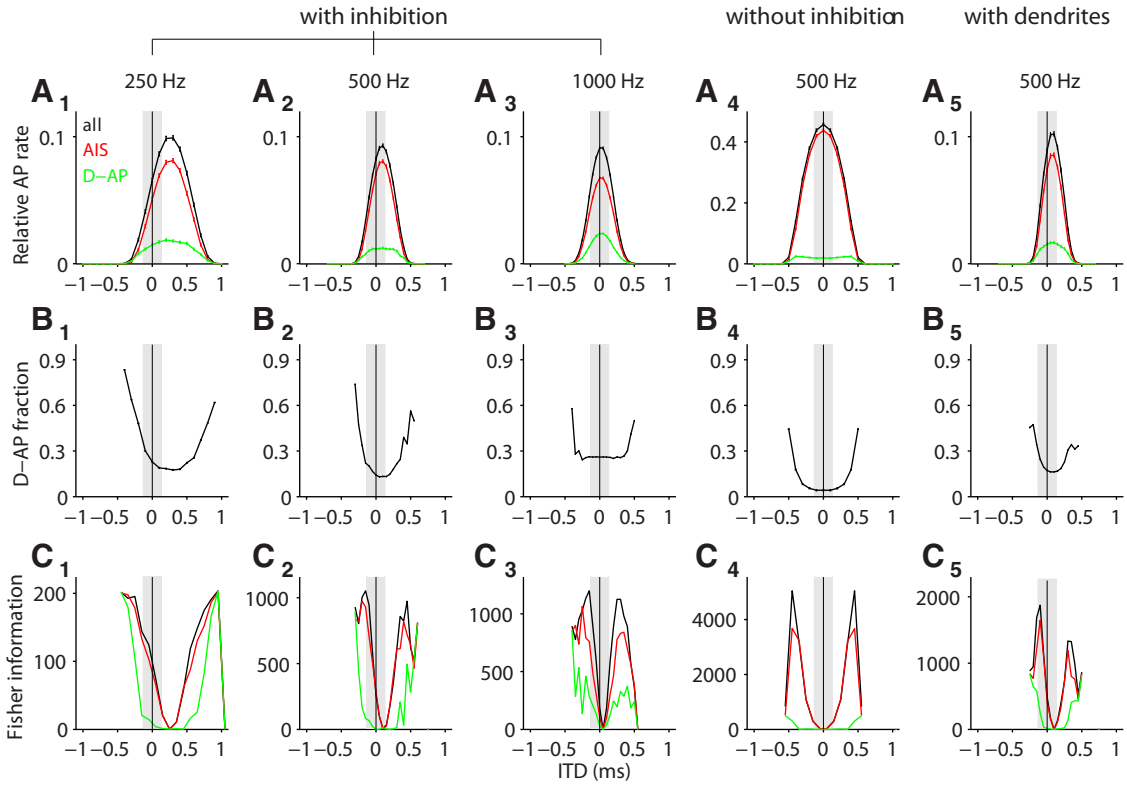

Figure 8. Representation of auditory space. ***A***, ITD tuning curves (more specifically noise delay functions; black) for input trains of 250, 500, and 1000 Hz center frequency, a purely excitatory model, and a model with dendrites (both receiving input with 500 Hz center frequency). Tuning curves without distally initiated APs are depicted in red, and tuning curves with only distally initiated APs are depicted in green. Gray bar indicates the physiological range of ITDs for gerbils. ***B***, Fraction of distally initiated APs (D-APs) of the tuning curves from ***A***. ***C***, Fisher information (in kHz^2, stimulus duration 300 ms) of the tuning curves (and the respective distal and AIS parts) from ***A***.

different center frequencies and amplitudes. For a low-frequency input with a center frequency of 250 Hz, the rate of distally initiated APs was highest right at the border between no APs and AIS APs (Fig. 7G_1,G_2). The orientation of this border was diagonal in amplitude–frequency space and qualitatively matched the AP boundaries from Figure 4 (Fig. 7G_1). For 1000 Hz, the distribution of AIS APs and distally initiated APs is different (Fig. 7H_1,H_2). There, the boundary between AP firing and no firing was approximately vertical, indicating that the cell effectively implemented an amplitude threshold being insensitive to the slope of the input current (Fig. 7H_1). Moreover, for 1000 Hz center frequency, distal AP initiation could no longer be seen as a threshold effect. In fact, after an initial dip for low amplitudes, the overall fraction of distally initiated spikes rose with input amplitude (Fig. 7H), which is in line with the dependence of the fraction of distally initiated APs on sodium inactivation from Figure 6.

In conclusion, distal AP initiation seems to have two effects. (1) If the sodium channels were only slightly inactivated, the cell is able to fire in response to smaller stimulus amplitudes than without distal initiation of APs. (2) If the sodium channels are largely inactivated (as in the case of temporally summed high-frequency input), distal AP initiation allows the cell to keep up high firing rates for high-frequency stimuli with large stimulus amplitudes.

Impact of distal AP initiation on ITD coding

The above findings have important consequences for the firing behavior of MSO cells *in vivo*. We simulated ITD tuning functions using our ongoing input paradigm with synaptic conductances derived from bandpass-filtered noise. Mimicking phase-locked auditory activity from the two ears, we split up the synaptic inputs into two channels with distinct temporal disparity for the putative ipsilateral and contralateral excitatory synapses, which, disregarding possible additional cochlear and transmission delays, we interpret as an ITD. We assumed that the cell also received phase-locked inhibitory input from both ears (from the medial and lateral nuclei of the trapezoid body) and used the inhibitory synapses to generate a maximum shift in best ITD (Brand et al., 2002; Leibold and van Hemmen, 2005; Pecka et al., 2008; Leibold, 2010). For bandpass input with a center frequency of 250 and 500 Hz, the contralateral inhibition was advanced compared with excitation by 0.8 ms, whereas the ipsilateral inhibition was delayed with respect to excitation by 0.11 ms. For these low center frequencies of the input, the model generated a rate code of ITD (Fig. 8A_1,A_2) in which firing at low rates was relatively more supported by distally initiated APs (Fig. 8B_1,B_2). This becomes obvious if one computes Fisher information as a means to assess the ITD resolution of the neuronal responses (Fig. 8C). Fisher information (resolution) is particularly high at the slopes of the tuning curves. In line with the high fractions of distally initiated APs at low firing rates (Fig. 8B), distally initiated APs also contribute a particularly large amount of information at these low rate regimes. Although, for the present definition of ITDs, these low rate parts are largely outside the physiological range (Fig. 8, gray bars), they might still become physiologically relevant if additional bilaterally asymmetric cochlear, axonal, or cellular delays exist that shift the tuning curves in parallel to the ITD axis.

To achieve the maximal peak shift for bandpass input with a center frequency of 1000 Hz, we set the contralateral inhibition to lead the excitation by 0.5 ms. The situation was very similar to

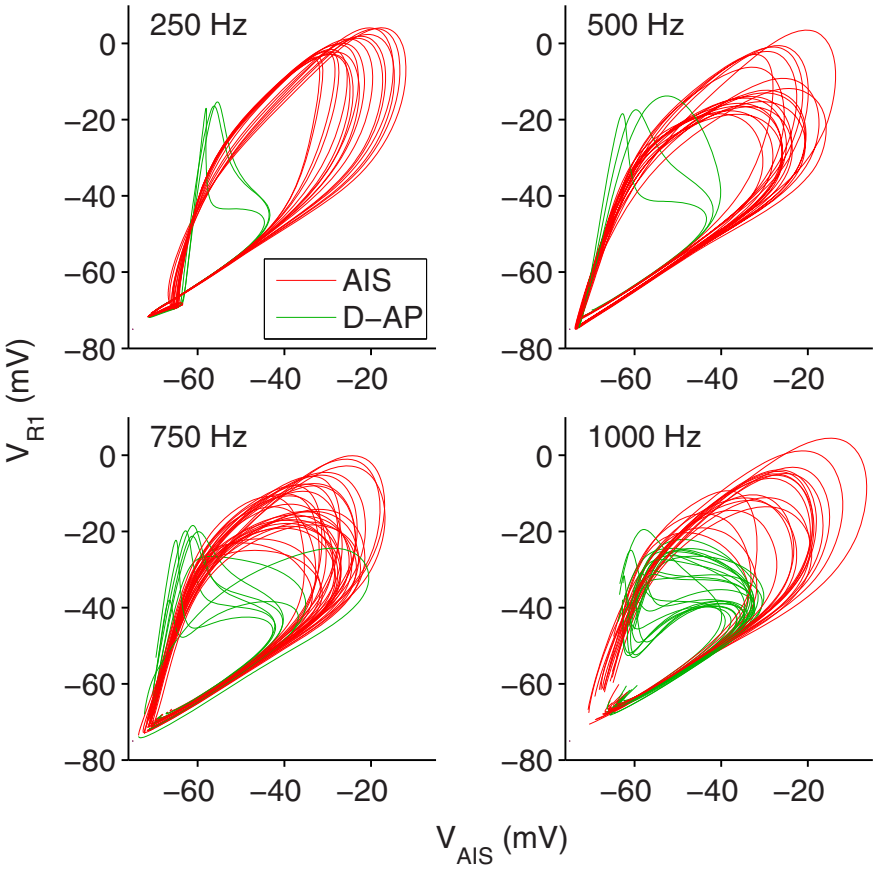

Figure 9. Is there a discrete site of AP initiation? AIS voltage vs voltage at the first node of Ranvier during AP firing for inputs with different center frequencies (as indicated). Red traces are APs identified as AIS APs by the algorithm described in Figure 1*F*. Green traces are APs classified as distally initiated (D-AP).

those for the two lower center frequencies, only that the best ITD, in contrast to *in vivo* findings (Brand et al., 2002), was close to the midline (Fig. 8A_3), and the code was mediated by distal AP initiation to an even larger extent (Fig. 8B_3). Also Fisher information was particularly high for distally initiated APs, even within the physiological range without any additional asymmetric delays (Fig. 8C_3). Thus, the realistically slow decaying inhibition (exponential decay with a time constant of 1.6 ms; Magnusson et al., 2005; Couchman et al., 2010) could well account for the observed peak shifts of low-frequency cells in gerbils, whereas it (at least alone) does not do so for frequencies of ~1 kHz and beyond (Pecka et al., 2008).

As a control, we ran the simulations without inhibitory inputs (Fig. 8A_4,B_4,C_4) which resulted in a best delay of zero. In this case, distally initiated APs were less prevalent. We thus conclude that distal AP initiation is an important mode of AP generation, particularly in the high-frequency channels but also in low-frequency channels with phase-locked inhibition.

In a final set of simulations, we tested how robust our findings are in a model that includes dendrites (Fig. 8A_5,B_5,C_5). MSO neurons typically have two dendrites, a lateral one receives ipsilateral excitatory input fibers and a medial one targeted by contralateral excitatory input fibers. We adjusted the model such that all basic physiological properties matched those of the simpler model and, hence, the published electrophysiological data (Scott et al., 2005; Couchman et al., 2010). The tuning curves and distal AP fractions from this extended model were almost identical to that of the simpler model. We thus conclude that the additional dendritic current sinks do not influence the excitability of the neuron beyond their contribution to the basic physiological parameters (input resistance, resting potential, and EPSP shape).

Discussion

In this study, we used naturalistic synaptic conductance trains to investigate AP initiation in a model of binaural coincidence detector neurons in the MSO, featuring a detailed axonal morphology. Modeling as well as electrophysiology showed that MSO cells incorporate temporal filtering properties such that they were easiest to excite for an input frequency of ~500 Hz. In contrast to current theories, the site of AP generation was not restricted to the AIS but varied depending on the spectral composition of the input. Further distally initiated APs (at the nodes of Ranvier) occurred close to the AP threshold in low-frequency channels, particularly in the presence of inhibition, as well as for strong stimulation in the high-frequency channels. Mechanistically, distal AP initiation at low frequencies was mediated by a strong somatic current sink, whereas for high frequencies it resulted from a stronger sodium channel inactivation in the AIS than in the distal axon. Importantly, in both cases, the ability of the neuron to generate APs in more distal axonal segments increased the dynamic range of firing rates. Distal AP initiation thereby facilitates the resolution of the rate code of ITDs in the cell (Skottun, 1998).

Our model simulations show that AP initiation cannot be viewed to generally occur at one specific site, but rather the proximal axonal segments act as a whole during this process. This is because the axial transport of charge particularly strongly determines the excitability of neighboring axonal segments (Baranauskas et al., 2013). To support the idea of distributed AP generation on a phenomenological level, we compared the trajectories of AIS APs and distally initiated APs plotting AIS voltage against voltage at the first node of Ranvier (Fig. 9). Although, on average, we see a clear distinction between the trajectories of the AIS and distally initiated APs, for higher stimulus frequencies the two sorts of trajectories form a continuum. This means that for some APs it is valid to assign a single site of initiation, but for others (Fig. 9, close to the border between red and green traces) it is rather difficult. A further argument in favor of spatially distributed AP generation is that the distribution of AP initiation sites in our model also depends on stimulus frequency, with high frequencies giving rise to more distal spiking (Fig. 5*I*). This finding is consistent with previous reports about layer 5 pyramidal neurons revealing that the first node of Ranvier facilitates high-frequency (>100 Hz) burst firing and reduces the somatic AP threshold by 5 mV (Kole, 2011). In summary, these results suggest that for high-frequency inputs, AP initiation of MSO cells indeed results from a spatially distributed and collective mechanism,

whereas for low-frequency inputs APs are rather generated at a distinct site.

Our computational model explains the small AP amplitudes observed *in vivo* (Yin and Chan, 1990) and *in vitro* (Scott et al., 2007; Couchman et al., 2010). However, the specific choice of parameters is crucial to further justify the model results. Whereas most of the parameters are closely tied to the existing MSO literature and the new morphometric data presented in this article, specifically the sodium conductances have not yet been determined experimentally in MSO axons. We have set the axonal sodium conductance density such that the firing threshold (70–110 nS) for a single excitatory synaptic conductance stimulus fits our current-clamp measurements (Couchman et al., 2010). Moreover, the axonal sodium conductance density of 4 nS/μm^2 used in the model lies within the range of values reported for cortical pyramidal neuron AISs (2.5 nS/μm^2, Kole et al., 2008) and has been used in several other studies (7.5 nS/μm^2, Shu et al., 2007; 4.5 nS/μm^2, Spirou et al., 2008). In our standard parameter set, we decided to use the same sodium channel density for all unmyelinated axonal compartments (the AIS and the nodes of Ranvier). This simplification rather leads to an underestimation of distal AP initiation (Fig. 5*K*). Assuming a higher sodium channel density in the nodes of Ranvier than in the axon initial segment, as shown by immunogold electron microscopy in cortical pyramidal cells (Lorincz and Nusser, 2010), relatively decreases the excitability of the AIS, thereby increasing the fraction of distally initiated APs.

In the analog ITD circuitry of birds, axonal processing has also been shown to be functionally important (Kuba et al., 2006; Ashida et al., 2007). In NL cells receiving phase-locked inputs up to 3 kHz, the AP initiation zone (clustering of sodium channels) of the AIS is located substantially more distal compared with the low-frequency neurons (Kuba et al., 2006). This finding is in line with the present observation of AP initiation moving to more distal parts of the axon for high-frequency stimuli. Compared with MSO principal neurons, which we suggest to have a dynamically changing site of AP initiation, in NL neurons the site of AP initiation seems rather hardwired, which is also supported by a partial myelination of the initial segment (Carr and Boudreau, 1993).

The mechanisms underlying ITD tuning of MSO principal neurons are highly debated (Grothe et al., 2010; Roberts et al., 2013; van der Heijden et al., 2013). Traditionally, ITD processing was thought to rely exclusively on the coincidence detection of excitatory inputs and neuronal ITD representation on the neurons that respond most at their best ITD. This best ITD is determined by the difference of internal delay lines between the ears and the coincidence detector neuron (Jeffress, 1948). While in the bird systems this concept still seems to constitute the core mechanism underlying ITD maps (Ashida and Carr, 2011), the situation in mammals is less clear. In brainstem and midbrain, the best ITDs change with stimulus frequency inconsistently with the assumption of a solely temporal conduction delay (i.e., they exhibit a so-called characteristic phase; Yin and Chan 1990, Agapiou and McAlpine, 2008, Siveke et al., 2012). Furthermore, blockade of glycinergic transmission *in vivo* shifted the best ITD of MSO neurons toward zero (Brand et al., 2002), hence arguing for a distinct effect of inhibitory inputs on the timing and shape of the excitatory potentials (Brand et al., 2002; Pecka et al., 2008) and providing a putative explanation for the frequency-dependent best ITDs (Leibold, 2010). Although it has been assumed that, given its slow kinetics, inhibition alone cannot account for a substantial shift of the best ITD (Jercog et al., 2010; Day and Semple, 2011; Roberts et al., 2013), our present modeling results show that inhibition has the potential to generate shifts as large as the physiological ITD range of gerbils (~130 μs), at least for frequencies <500 Hz. This, of course, does not exclude further mechanisms like cochlear or axonal delays (Schroeder, 1977; Shamma et al., 1989; Joris et al., 2006; Day and Semple, 2011) and morphological (Zhou et al., 2005; but see Rautenberg et al., 2009) or physiological (Jercog et al., 2010; but see Roberts et al., 2013) asymmetries. A further argument against a contribution of fast inhibition to the shift of best ITDs stems from recent *in vivo* whole-cell recordings (van der Heijden et al., 2013), which state a lack of obvious hyperpolarizing IPSPs. Because of the slow inhibitory time constant, our simulations show that during an ongoing stimulus IPSPs indeed do not show up as isolated potentials (Fig. 1*D*) but nevertheless influence the phase of the monaurally induced oscillations sufficiently to induce a shift of best ITDs (even for 1 kHz, although not much).

Beyond the auditory brainstem, fast and leaky cell membranes have also been reported in cortical pyramidal cells during massive synaptic bombardment such as in high-conductance states [Paré et al., 1998 (who reported input resistances as low as 4 MΩ)] and sharp wave ripple events (Bähner et al., 2011). Under both conditions, the cells show extensive spiking activity *in vivo* (Csicsvari et al., 1999; Steriade, 2001). It is thus tempting to speculate that distal AP initiation contributes to firing as well by allowing the somatic current sink to decouple from the axonal AP-generating zones in a context-dependent manner (Vladimirov et al., 2013).

References

Agapiou JP, McAlpine D (2008) Low-frequency envelope sensitivity produces asymmetric binaural tuning curves. J Neurophysiol 100:2381–2396. CrossRef Medline

Agrawal D, Hawk R, Avila RL, Inouye H, Kirschner DA (2009) Internodal myelination during development quantitated using x-ray diffraction. J Struct Biol 168:521–526. CrossRef Medline

Ashida G, Carr CE (2011) Sound localization: Jeffress and beyond. Curr Opin Neurobiol 21:745–751. CrossRef Medline

Ashida G, Abe K, Funabiki K, Konishi M (2007) Passive soma facilitates submillisecond coincidence detection in the owl's auditory system. J Neurophysiol 97:2267–2282. CrossRef Medline

Bähner F, Weiss EK, Birke G, Maier N, Schmitz D, Rudolph U, Frotscher M, Traub RD, Both M, Draguhn A (2011) Cellular correlate of assembly formation in oscillating hippocampal networks in vitro. Proc Natl Acad Sci U S A 108:E607–616. CrossRef Medline

Baranauskas G, David Y, Fleidervish IA (2013) Spatial mismatch between the Na+ flux and spike initiation in axon initial segment. Proc Natl Acad Sci U S A 110:4051–4056. CrossRef Medline

Baumann VJ, Lehnert S, Leibold C, Koch U (2013) Tonotopic organization of the hyperpolarization-activated current (Ih) in the mammalian medial superior olive. Front Neural Circuits 7:117. CrossRef Medline

Beraneck M, Pfanzelt S, Vassias I, Rohregger M, Vibert N, Vidal PP, Moore LE, Straka H (2007) Differential intrinsic response dynamics determine synaptic signal processing in frog vestibular neurons. J Neurosci 27:4283–4296. CrossRef Medline

Brand A, Behrend O, Marquardt T, McAlpine D, Grothe B (2002) Precise inhibition is essential for microsecond interaural time difference coding. Nature 417:543–547. CrossRef Medline

Carr CE, Boudreau RE (1993) An axon with a myelinated initial segment in the bird auditory system. Brain Res 628:330–334. CrossRef Medline

Couchman K, Grothe B, Felmy F (2010) Medial superior olivary neurons receive surprisingly few excitatory and inhibitory inputs with balanced strength and short-term dynamics. J Neurosci 30:17111–17121. CrossRef Medline

Csicsvari J, Hirase H, Czurkó A, Mamiya A, Buzsáki G (1999) Oscillatory coupling of hippocampal pyramidal cells and interneurons in the behaving Rat. J Neurosci 19:274–287. Medline

Day ML, Semple MN (2011) Frequency-dependent interaural delays in the

medial superior olive: implications for interaural cochlear delays. J Neurophysiol 106:1985–1999. CrossRef Medline

Duflocq A, Chareyre F, Giovannini M, Couraud F, Davenne M (2011) Characterization of the axon initial segment (AIS) of motor neurons and identification of a para-AIS and a juxtapara-AIS, organized by protein 4.1B. BMC Biol 9:66. CrossRef Medline

Ferragamo MJ, Oertel D (2002) Octopus cells of the mammalian ventral cochlear nucleus sense the rate of depolarization. J Neurophysiol 87: 2262–2270. CrossRef Medline

Fitzpatrick DC, Batra R, Stanford TR, Kuwada S (1997) A neuronal population code for sound localization. Nature 388:871–874. CrossRef Medline

Ford MC, Grothe B, Klug A (2009) Fenestration of the calyx of Held occurs sequentially along the tonotopic axis, is influenced by afferent activity, and facilitates glutamate clearance. J Comp Neurol 514:92–106. CrossRef Medline

Foust A, Popovic M, Zecevic D, McCormick DA (2010) Action potentials initiate in the axon initial segment and propagate through axon collaterals reliably in cerebellar Purkinje neurons. J Neurosci 30:6891–6902. CrossRef Medline

Gentet LJ, Stuart GJ, Clements JD (2000) Direct measurement of specific membrane capacitance in neurons. Biophys J 79:314–320. CrossRef Medline

Glasberg BR, Moore BC (1990) Derivation of auditory filter shapes from notched-noise data. Hear Res 47:103–138. CrossRef Medline

Goldberg JM, Brown PB (1969) Response of binaural neurons of dog superior olivary complex to dichotic tonal stimuli: some physiological mechanisms of sound localization. J Neurophysiol 32:613–636. Medline

Golding NL, Oertel D (2012) Synaptic integration in dendrites: exceptional need for speed. J Physiol 590:5563–5569. CrossRef Medline

Grothe B, Pecka M, McAlpine D (2010) Mechanisms of sound localization in mammals. Physiol Rev 90:983–1012. CrossRef Medline

Jeffress LA (1948) A place theory of sound localization. J Comp Physiol Psychol 41:35–39. CrossRef Medline

Jercog PE, Svirskis G, Kotak VC, Sanes DH, Rinzel J (2010) Asymmetric excitatory synaptic dynamics underlie interaural time difference processing in the auditory system. PLoS Biol 8:e1000406. CrossRef Medline

Joris PX, Van de Sande B, Louage DH, van der Heijden M (2006) Binaural and cochlear disparities. Proc Natl Acad Sci U S A 103:12917–12922. CrossRef Medline

Kapfer C, Seidl AH, Schweizer H, Grothe B (2002) Experience-dependent refinement of inhibitory inputs to auditory coincidence-detector neurons. Nat Neurosci 5:247–253. CrossRef Medline

Koch U, Braun M, Kapfer C, Grothe B (2004) Distribution of HCN1 and HCN2 in rat auditory brainstem nuclei. Eur J Neurosci 20:79–91. CrossRef Medline

Kole MH (2011) First node of Ranvier facilitates high-frequency burst encoding. Neuron 71:671–682. CrossRef Medline

Kole MH, Letzkus JJ, Stuart GJ (2007) Axon initial segment Kv1 channels control axonal action potential waveform and synaptic efficacy. Neuron 55:633–647. CrossRef Medline

Kole MH, Ilschner SU, Kampa BM, Williams SR, Ruben PC, Stuart GJ (2008) Action potential generation requires a high sodium channel density in the axon initial segment. Nat Neurosci 11:178–186. CrossRef Medline

Kuba H, Ishii TM, Ohmori H (2006) Axonal site of spike initiation enhances auditory coincidence detection. Nature 444:1069–1072. CrossRef Medline

Leibold C (2010) Influence of inhibitory synaptic kinetics on the interaural time difference sensitivity in a linear model of binaural coincidence detection. J Acoust Soc Am 127:931–942. CrossRef Medline

Leibold C, van Hemmen JL (2005) Spiking neurons learning phase delays: how mammals may develop auditory time-difference sensitivity. Phys Rev Lett 94:168102. CrossRef Medline

Lorincz A, Nusser Z (2010) Molecular identity of dendritic voltage-gated sodium channels. Science 328:906–909. CrossRef Medline

Magnusson AK, Kapfer C, Grothe B, Koch U (2005) Maturation of glycinergic inhibition in the gerbil medial superior olive after hearing onset. J Physiol 568:497–512. CrossRef Medline

Mainen ZF, Sejnowski TJ (1996) Influence of dendritic structure on firing pattern in model neocortical neurons. Nature 382:363–366. CrossRef Medline

Mainen ZF, Joerges J, Huguenard JR, Sejnowski TJ (1995) A model of spike initiation in neocortical pyramidal neurons. Neuron 15:1427–1439. CrossRef Medline

Mathews PJ, Jercog PE, Rinzel J, Scott LL, Golding NL (2010) Control of submillisecond synaptic timing in binaural coincidence detectors by K(v)1 channels. Nat Neurosci 13:601–609. CrossRef Medline

McIntyre CC, Richardson AG, Grill WM (2002) Modeling the excitability of mammalian nerve fibers: influence of afterpotentials on the recovery cycle. J Neurophysiol 87:995–1006. Medline

McIntyre CC, Grill WM, Sherman DL, Thakor NV (2004) Cellular effects of deep brain stimulation: model-based analysis of activation and inhibition. J Neurophysiol 91:1457–1469. CrossRef Medline

Palmer LM, Stuart GJ (2006) Site of action potential initiation in layer 5 pyramidal neurons. J Neurosci 26:1854–1863. CrossRef Medline

Palmer LM, Clark BA, Gründemann J, Roth A, Stuart GJ, Häusser M (2010) Initiation of simple and complex spikes in cerebellar Purkinje cells. J Physiol 588:1709–1717. CrossRef Medline

Paré D, Shink E, Gaudreau H, Destexhe A, Lang EJ (1998) Impact of spontaneous synaptic activity on the resting properties of cat neocortical pyramidal neurons In vivo. J Neurophysiol 79:1450–1460. Medline

Pecka M, Brand A, Behrend O, Grothe B (2008) Interaural time difference processing in the mammalian medial superior olive: the role of glycinergic inhibition. J Neurosci 28:6914–6925. CrossRef Medline

Popovic MA, Foust AJ, McCormick DA, Zecevic D (2011) The spatiotemporal characteristics of action potential initiation in layer 5 pyramidal neurons: a voltage imaging study. J Physiol 589:4167–4187. CrossRef Medline

Rautenberg PL, Grothe B, Felmy F (2009) Quantification of the three-dimensional morphology of coincidence detector neurons in the medial superior olive of gerbils during late postnatal development. J Comp Neurol 517:385–396. CrossRef Medline

Roberts MT, Seeman SC, Golding NL (2013) A mechanistic understanding of the role of feedforward inhibition in the mammalian sound localization circuitry. Neuron 78:923–935. CrossRef Medline

Rothman JS, Manis PB (2003) The roles potassium currents play in regulating the electrical activity of ventral cochlear nucleus neurons. J Neurophysiol 89:3097–3113. CrossRef Medline

Schroeder MR (1977) New viewpoints in binaural interactions. In: Psychophysics and physiology of hearing (Evans EF, Wilson JP, eds), pp 455–467. New York: Academic.

Scott LL, Mathews PJ, Golding NL (2005) Posthearing developmental refinement of temporal processing in principal neurons of the medial superior olive. J Neurosci 25:7887–7895. CrossRef Medline

Scott LL, Hage TA, Golding NL (2007) Weak action potential backpropagation is associated with high-frequency axonal firing capability in principal neurons of the gerbil medial superior olive. J Physiol 583:647–661. CrossRef Medline

Scott LL, Mathews PJ, Golding NL (2010) Perisomatic voltage-gated sodium channels actively maintain linear synaptic integration in principal neurons of the medial superior olive. J Neurosci 30:2039–2050. CrossRef Medline

Shamma SA, Shen NM, Gopalaswamy P (1989) Stereausis: binaural processing without neural delays. J Acoust Soc Am 86:989–1006. CrossRef Medline

Shu Y, Duque A, Yu Y, Haider B, McCormick DA (2007) Properties of action-potential initiation in neocortical pyramidal cells: evidence from whole cell axon recordings. J Neurophysiol 97:746–760. CrossRef Medline

Siveke I, Leibold C, Schiller E, Grothe B (2012) Adaptation of binaural processing in the adult brainstem induced by ambient noise. J Neurosci 32: 462–473. Medline

Skottun BC (1998) Sound location and neurons. Nature 393:531. CrossRef Medline

Spirou GA, Chirila FV, von Gersdorff H, Manis PB (2008) Heterogeneous Ca2+ influx along the adult calyx of held: a structural and computational study. Neuroscience 154:171–185. CrossRef Medline

Steriade M (2001) Impact of network activities on neuronal properties in corticothalamic systems. J Neurophysiol 86:1–39. Medline

Stuart GJ, Sakmann B (1994) Active propagation of somatic action poten-

tials into neocortical pyramidal cell dendrites. Nature 367:69–72. CrossRef Medline

Stuart G, Schiller J, Sakmann B (1997) Action potential initiation and propagation in rat neocortical pyramidal neurons. J Physiol 505:617–632. CrossRef Medline

Svirskis G, Kotak V, Sanes DH, Rinzel J (2002) Enhancement of signal-to-noise ratio and phase locking for small inputs by a low-threshold outward current in auditory neurons. J Neurosci 22:11019–11025. Medline

van der Heijden M, Lorteije JA, Plauška A, Roberts MT, Golding NL, Borst JG (2013) Directional hearing by linear summation of binaural inputs at the medial superior olive. Neuron 78:936–948. CrossRef Medline

Vladimirov N, Tu Y, Traub RD (2013) Synaptic gating at axonal branches, and sharp-wave ripples with replay: a simulation study. Eur J Neurosci 38:3435–3447. CrossRef Medline

Werthat F, Alexandrova O, Grothe B, Koch U (2008) Experience-dependent refinement of the inhibitory axons projecting to the medial superior olive. Dev Neurobiol 68:1454–1462. CrossRef Medline

Yin TC, Chan JC (1990) Interaural time sensitivity in medial superior olive of cat. J Neurophysiol 64:465–488. Medline

Zhou Y, Carney LH, Colburn HS (2005) A model for interaural time difference sensitivity in the medial superior olive: interaction of excitatory and inhibitory synaptic inputs, channel dynamics, and cellular morphology. J Neurosci 25:3046–3058. CrossRef Medline

Study 4

Author contributions:

A.S. performed the *in vivo* experiments, analyzed the data and wrote the relevant parts of the manuscript. M.H.M. performed the *in vitro* experiments, analyzed the data and wrote the relevant parts of the manuscript. A.L. performed the psychophysical experiments, analyzed the data and wrote the relevant parts of the manuscript. M.C.F. designed and performed the fiber tracing experiments, analyzed the data, prepared figure 6 a-g, and wrote the parts of the manuscript concerning the anatomical experiments. M.C.F and O.A. designed the immunohistochemistry experiments. O.A. performed the immunohistochemistry experiments and confocal microscopy, analyzed the data and wrote the relevant parts of the methods section. F.F. supervised the *in vitro* electrophysiology experiments. M.P. supervised the adaptation (*in vivo* and psychophysical) experiments and wrote parts of the manuscript. I.S. and B.G. supervised the project and wrote the manuscript. All authors revised the manuscript.

nature neuroscience

Adaptation in sound localization: from $GABA_B$ receptor–mediated synaptic modulation to perception

Annette Stange[1], Michael H Myoga[1], Andrea Lingner[1,2], Marc C Ford[1,3], Olga Alexandrova[1], Felix Felmy[1,3,4], Michael Pecka[1], Ida Siveke[1] & Benedikt Grothe[1–3]

Across all sensory modalities, the effect of context-dependent neural adaptation can be observed at every level, from receptors to perception. Nonetheless, it has long been assumed that the processing of interaural time differences, which is the primary cue for sound localization, is nonadaptive, as its outputs are mapped directly onto a hard-wired representation of space. Here we present evidence derived from *in vitro* and *in vivo* experiments in gerbils indicating that the coincidence-detector neurons in the medial superior olive modulate their sensitivity to interaural time differences through a rapid, $GABA_B$ receptor–mediated feedback mechanism. We show that this mechanism provides a gain control in the form of output normalization, which influences the neuronal population code of auditory space. Furthermore, psychophysical tests showed that the paradigm used to evoke neuronal $GABA_B$ receptor–mediated adaptation causes the perceptual shift in sound localization in humans that was expected on the basis of our physiological results in gerbils.

Neuronal adaptation is a key feature of signal processing, which allows organisms to adjust the parameters of signal detection to sharpen the most relevant characteristics of a stimulus in a given context. Normalization is a general mechanism for adaptation that is used across sensory modalities, and the term 'divisive normalization' refers to a computational process that matches the sensitivity of a neuron to the mean strength of its input[1]. In the auditory system, sound localization exhibits neuronal adaptation according to recent stimulus history. This adaptation is conventionally thought to take place at higher levels of the auditory pathway and not at the initial site of binaural processing, the superior olivary complex[2–5]. However, recent studies on human psychoacoustics have indicated that binaural adaptation might occur early in the binaural system[6]. Furthermore, it has been shown that the processing of differences in level between the two ears (interaural level differences) in the auditory brainstem is subject to adaptation through a gain-control mechanism that is mediated by retrograde $GABA_B$ receptor signaling[7,8]. However, the importance of such early adaptation mechanisms in the perception of sound locations by interaural time differences (ITDs) remains unclear.

In the present study we investigated adaptation in the gerbil medial superior olive (MSO), the initial site of ITD processing. Neurons of the MSO show very stereotyped connectivity: each cell receives both excitatory and inhibitory inputs from either side (**Fig. 1a**). The spiking rate of MSO cells is in turn highly dependent on differences in the arrival time of these inputs, which allows for neuronal sensitivity to ITDs with microsecond resolution[9]. The excitatory MSO inputs are glutamatergic, whereas the inhibitory inputs are glycinergic[10–15]. Rather surprisingly, recent *in vitro* studies have established that both excitatory and inhibitory inputs to the MSO can be modulated by $GABA_B$ receptor activation[16,17]. However, the source of such GABAergic transmission is unclear, as is the putative function of $GABA_B$ receptor–mediated inhibition in the MSO in the intact brain. We designed the present study to clarify these issues and provide coherent data based on *in vitro* and *in vivo* electrophysiology and pharmacology, as well as neuronal fiber tracing, which indicated the operation of $GABA_B$ receptor–mediated adaptation in the gerbil MSO that is likely implemented through a disynaptic feedback loop. We found that this feedback circuit allows for frequency-specific and activity-dependent normalization of MSO responses. Moreover, because this normalization is independently performed in each brain hemisphere, it has a discernible effect on the neuronal population coding of sound-source locations. We also show that the observed changes in the population code generated by $GABA_B$ receptor–mediated adaptation can be correlated with predictable shifts in localization percepts in human subjects.

RESULTS

Effects of $GABA_B$ receptor modulation *in vivo*

Because *in vitro* experiments have shown that inputs to the MSO are modulated by $GABA_B$ receptor–mediated inhibition, we wished to test its relevance *in vivo*. We therefore determined the effects of GABA, the $GABA_B$ receptor agonist baclofen and the $GABA_B$ receptor antagonist CGP on the firing rate of neurons in the MSO recorded extracellularly in anesthetized Mongolian gerbils (**Fig. 1b**). Single MSO neurons showed a significantly decreased firing rate after iontophoretic application of either GABA or baclofen (**Fig. 1c**,**e**;

[1]Division of Neurobiology, Department Biologie II, Ludwig-Maximilians-Universität München, Planegg-Martinsried, Germany. [2]German Center for Vertigo and Balance Disorders (IFB), University Hospital Munich-Großhadern, Munich, Germany. [3]Graduate School of Systemic Neurosciences (GSN-LMU), Ludwig-Maximilians-Universität München, Planegg-Martinsried, Germany. [4]BioImaging Zentrum (Biz), Ludwig-Maximilians-Universität München, Planegg-Martinsried, Germany. Correspondence should be addressed to B.G. (grothe@lmu.de).

Received 20 May; accepted 17 September; published online 20 October 2013; doi:10.1038/nn.3548

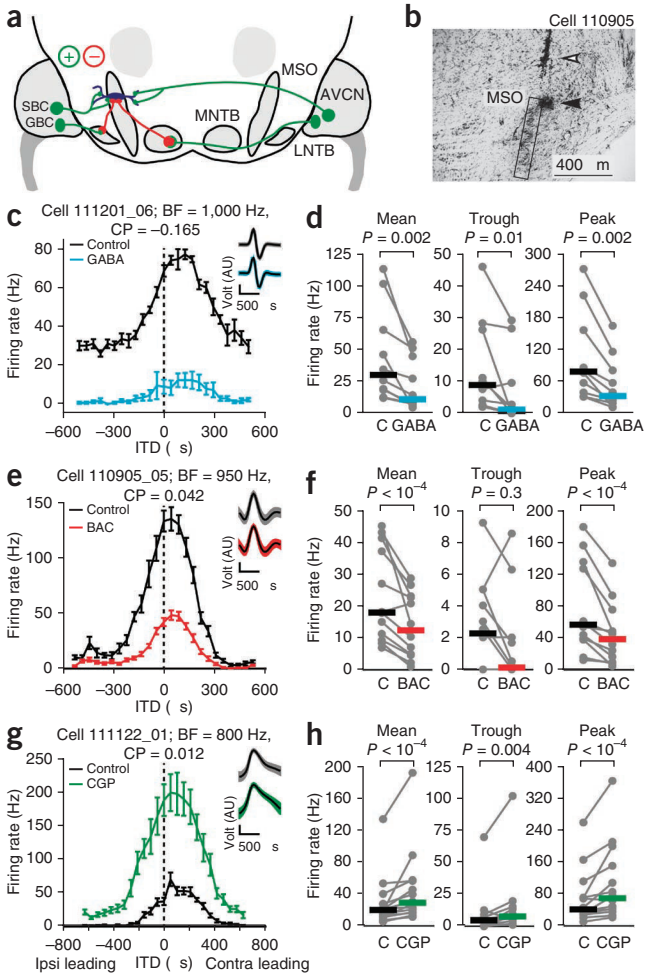

Figure 1 $GABA_B$ receptor–dependent modulation of neuronal responses in the MSO *in vivo*. (**a**) Schematic drawing of the excitatory and inhibitory inputs to a principal cell (blue) in the MSO. SBC, spherical bushy cell; GBC, globular bushy cell; MNTB, medial nucleus of the trapezoid body; LNTB, lateral nucleus of the trapezoid body; AVCN, anterior ventral cochlear nucleus. (**b**) The recording site of the neuron shown in **e** labeled by injection of horseradish peroxidase (HRP). The HRP staining is clearly visible in the dorsal region of the characteristic MSO cell band (boxed). The filled arrowhead marks the recording site, and the open arrowhead marks the visible electrode trace. (**c**,**e**,**g**) Representative responses to different ITDs in the absence (black) or presence of GABA (blue; **c**), the $GABA_B$ receptor agonist baclofen (BAC) (red; **e**) or the $GABA_B$ receptor antagonist CGP (green; **g**). Error bars, s.e.m. The insets on the right show voltage traces of action potentials in the recorded neuron. The black traces indicate the mean action potential waveform, and the colored envelopes indicate the standard error for the entire recording session. BF, best frequency; CP, characteristic phase; AU, arbitrary units; ipsi, ipsilateral; contra, contralateral. (**d**,**f**,**h**) The mean firing rates averaged over all measured ITDs (left), the firing rate at the ITD of minimum response (trough; middle) and the firing rate at the ITD of maximum response (peak; right) are plotted for each cell (gray dots) during control conditions (C) and during drug application. The population medians (colored bars) are shown before (C) and after application of GABA (**d**; $n = 10$), BAC (**f**; $n = 12$) or CGP (**h**; $n = 14$). Significance was assessed using Wilcoxon's signed rank test. The color codes in **a** and **c**–**h** are not related.

$P < 10^{-5}$). This decrease was also evident at the population level (**Fig. 1d**,**f**; GABA reduced the mean firing rate averaged over all ITDs tested from 30 to 11 Hz, $P = 0.002$; baclofen reduced the mean firing rate from 18 to 12 Hz, $P < 10^{-4}$). This decrease in the response rate was also present at the minima (troughs) and maxima (peaks) of the individual ITD functions. Conversely, the $GABA_B$ receptor antagonist CGP significantly increased the firing rate for individual MSO neurons and the population of MSO neurons tested (**Fig. 1g**,**h**; from 20 to 29 Hz, $P < 10^{-4}$). Again, we found this increase in the response rate at the minima and maxima of the individual ITD functions (**Fig. 1h**).

Having thus established that $GABA_B$ receptors modulate the firing rate of MSO neurons *in vivo*, we investigated their specific effects on ITD sensitivity. We analyzed the following three parameters that characterize ITD tuning functions: (i) the total modulation depth, (ii) the half width and (iii) the best interaural phase difference (IPD), which corresponds to the best ITD (maximum of the ITD function) normalized to the cycle length of the neuron's best frequency (**Fig. 2a**,**b**). Surprisingly, local activation of $GABA_B$ receptors by application of baclofen, although sometimes markedly changing the absolute response rate, had rather small and nonsignificant effects on the modulation depth and half width of the ITD function (**Fig. 2c**,**d**). Blocking $GABA_B$ receptors with CGP significantly decreased the modulation depth of the ITD function (**Fig. 2c**; from 93% to 89%, $P = 0.02$) while also significantly increasing its half width (**Fig. 2d**; from 0.35 to 0.37 cycles, $P = 0.005$). However, neither the agonist nor the antagonist of $GABA_B$ receptor–mediated inhibition had any effect on the best IPD of the neurons tested (**Fig. 2e**). These *in vivo* results suggest that $GABA_B$ receptor activation does not alter the balance of excitation and inhibition, which has been shown to be crucial for adjusting ITD sensitivity[18].

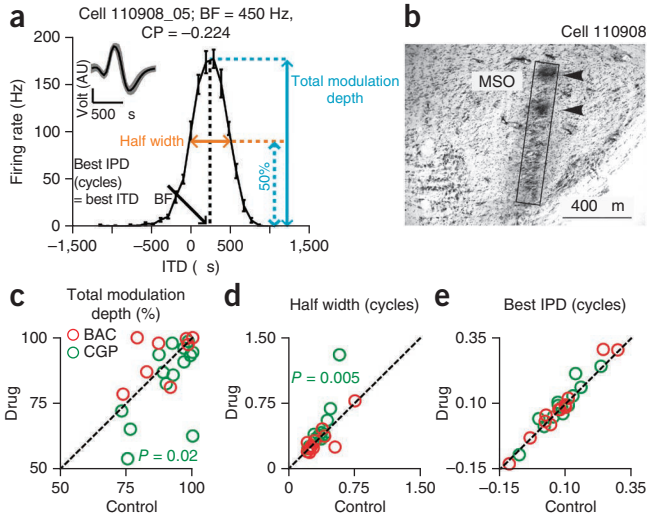

Figure 2 $GABA_B$ receptor–mediated modulation of ITD sensitivity in the MSO. (**a**) Three characteristic parameters of ITD functions are shown for the representative cell: total modulation depth, half width and best IPD. Error bars and gray envelope, s.e.m. (**b**) Two HRP injection sites that were labeled before and after recording the cell in **a**. The two HRP injections are marked by filled symbols in the dorsal and more medial region of the MSO cell band (boxed). (**c**–**e**) The characteristic parameters of ITD sensitivity of each cell determined in the absence (control) and presence of the drug ($n = 26$). The red circles indicate the measured parameters of each cell before and after activation of $GABA_B$ receptors by BAC, and the green circles indicate the data points before and after blocking $GABA_B$ receptors by CGP. Significance was assessed using Wilcoxon's signed rank test. The dashed diagonal lines indicate unity.

Effects of $GABA_B$ receptor activation *in vitro*

In light of recent *in vitro* studies[16,17], the maintenance of the best IPD during the activation of $GABA_B$ receptors is somewhat unexpected.

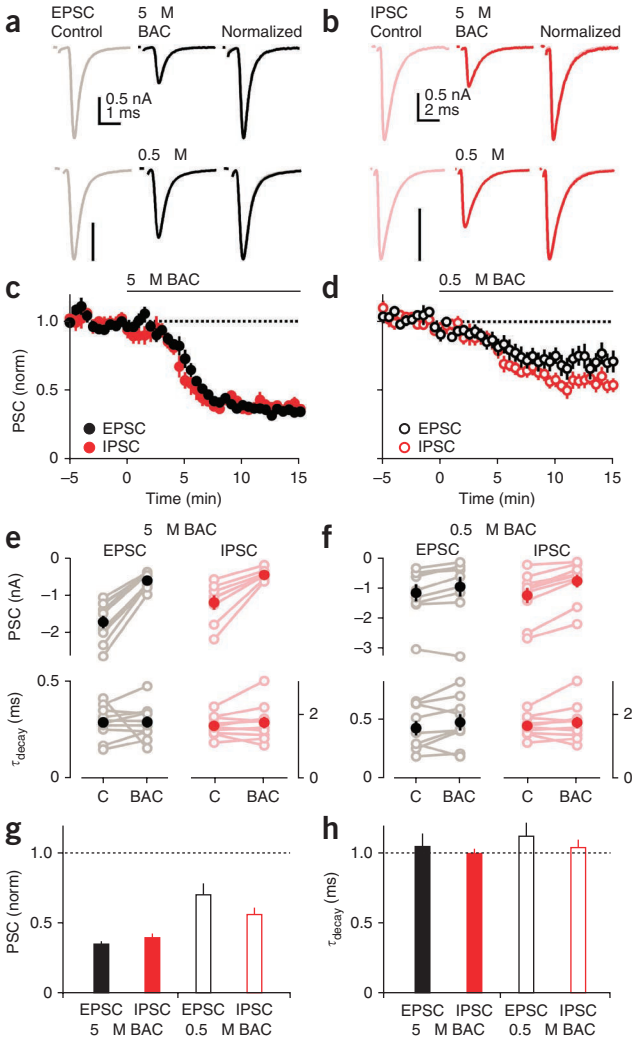

Figure 3 $GABA_B$ receptor–mediated modulation of basal synaptic strength measured *in vitro* in acute brain slices. (**a**) Representative traces of single pulses of glutamatergic EPSC inputs before (left) and after (middle) application of BAC and then normalized to control conditions (right). Two concentrations of BAC (5 μM (top) and 0.5 μM (bottom; scale bar, 0.5 nA)) were tested. (**b**) The effect of BAC on glycinergic IPSCs is shown as in **a**. (**c**,**d**) Time course showing the effects of application of 5 μM (**c**) or 0.5 μM (**d**) BAC on the normalized (norm) amplitude of EPSCs (black) and IPSCs (red). (**e**) Effect of 5 μM BAC on EPSC (left) and IPSC (right) amplitudes (top; EPSCs reduced to 35.4 ± 1.3% (mean ± s.e.m.); $n = 10$; IPSCs reduced to 54.0 ± 4.4%, $n = 12$) and decay kinetics (bottom; EPSC: $\tau_{decay} = 0.29 \pm 0.02$ ms (mean ± s.e.m.) compared to 0.29 ± 0.02 ms; IPSC: $\tau_{decay} = 1.40 \pm 0.08$ ms compared to 1.39 ± 0.09 ms). (**f**) Effect of 0.5 μM BAC on EPSC (left) and IPSC (right) amplitudes (top; EPSCs reduced to 69.8 ± 6.2%; $n = 11$; IPSCs reduced to 39.8 ± 2.6%, $n = 8$) and decay kinetics (bottom). (**g**,**h**) Summary of the effects of BAC on current amplitudes ($P = 0.021$; **g**) and decay kinetics (**h**). Error bars, s.e.m.

The *in vitro* studies indicated that $GABA_B$ receptors are expressed at both glutamatergic and glycinergic inputs to MSO neurons, and they affect these inputs differentially. Such differential modulation would be expected to change the balance of inhibition and excitation and should therefore alter the best IPD of the MSO cells, which is in contrast to our *in vivo* results (**Fig. 2e**). However, the *in vitro* studies were done on younger (around postnatal day (P) 20) gerbils and used quite different concentrations of baclofen. To test whether these age and concentration differences might account for the discrepancies, we performed whole-cell voltage-clamp experiments on MSO neurons obtained from adult (P60–P90) gerbils that were similar to those used in our *in vivo* studies. Furthermore, we used a physiologically relevant calcium concentration (1.2 mM) and different doses of baclofen to investigate the $GABA_B$ sensitivity of glutamatergic and glycinergic synapses (**Fig. 3**). At a saturating concentration (5 μM) of baclofen, excitatory postsynaptic currents (EPSCs) and inhibitory postsynaptic currents (IPSCs) were both substantially inhibited (**Fig. 3a**,**b**). On average, the magnitudes of both the EPSCs and IPSCs were similarly reduced to about one-third of those seen under control conditions (**Fig. 3c**,**e**,**g**; $P = 0.066$). However, an intermediate concentration (0.5 μM) of baclofen inhibited EPSCs to a lesser extent than IPSCs (**Fig. 3a**,**b**,**d**,**f**,**g**; $P = 0.021$). Recent findings have suggested an age-dependent effect of $GABA_B$ receptor activation on IPSC decay kinetics[16]. This may be important for the manner in which MSO neurons integrate their synaptic inputs. When we normalized and superimposed traces from before and after baclofen application (**Fig. 3a**,**b**), we observed no detectable change in the kinetics of either the EPSCs or IPSCs (**Fig. 3e**,**f**,**h**).

Overall, and in accord with previous results, our *in vitro* findings suggest that in adult animals, glutamatergic synapses are less sensitive to $GABA_B$ receptor signaling than glycinergic synapses (**Fig. 3g**), but only in the presence of nonsaturating concentrations of baclofen. When higher concentrations of the agonist are used, the effective reduction is similar for both input types.

Stimulus-induced adaptation in the MSO

Because the *in vivo* and *in vitro* data reported above show that $GABA_B$ receptor–mediated inhibition does not change ITD sensitivity *per se*, it may have a more general function in adapting the response characteristics of MSO cells in an activity-dependent manner. A similar function of $GABA_B$-mediated modulation during the processing of interaural intensity differences in the lateral superior olive has been recently described[8]. Whether such adaptation also takes place in the MSO is unknown. We therefore tested for neuronal adaptation to preceding adapter stimuli in the MSO (**Fig. 4a**,**b**). We found that the neuronal responses to test tones presented 500 ms after adapter signals of the same frequency were indeed markedly influenced by the prior adapter, as was clear from the spike raster plot (**Fig. 4c**), as well as the average responses of single neurons (**Fig. 4d**). In general, the adapter reduced the firing rate evoked by the following test tone. The degree of suppression was highly dependent on the nature of the adapter condition and affected the response to test tones at all ITDs (**Fig. 4d**,**e**). However, we found the greatest suppressive effect of the adapter for test tones presented at positive ITDs (bin+) (**Fig. 4d**). We therefore focused on this test-tone ITD in our further analysis of the effects of different adapter conditions. First, we tested whether the frequency of the adapter is important for its efficacy at driving suppression (**Fig. 4e**). In contrast to adapters presented at the cell's best frequency, we found that adapters presented at twice the cell's best frequency (2BF), which did not activate the specific MSO neurons tested, failed to induce significant ($P = 0.15$) adaptation. This failure was independent of the binaural condition (ipsilateral: 0; contralateral: −0.11; 2BF: −0.08; **Fig. 4e**). Second, we presented adapters at the neuron's best frequency and tested whether the binaural nature of the adapter matters and found the strongest adaptation when the adapter was presented binaurally at an ITD favored by the MSO (bin−: −0.13, $P = 0.03$; bin+: −0.32, $P < 10^{-5}$; **Fig. 4e**). As MSO neurons that respond to the same frequency tend to have similar best ITDs[12,19], this adapter

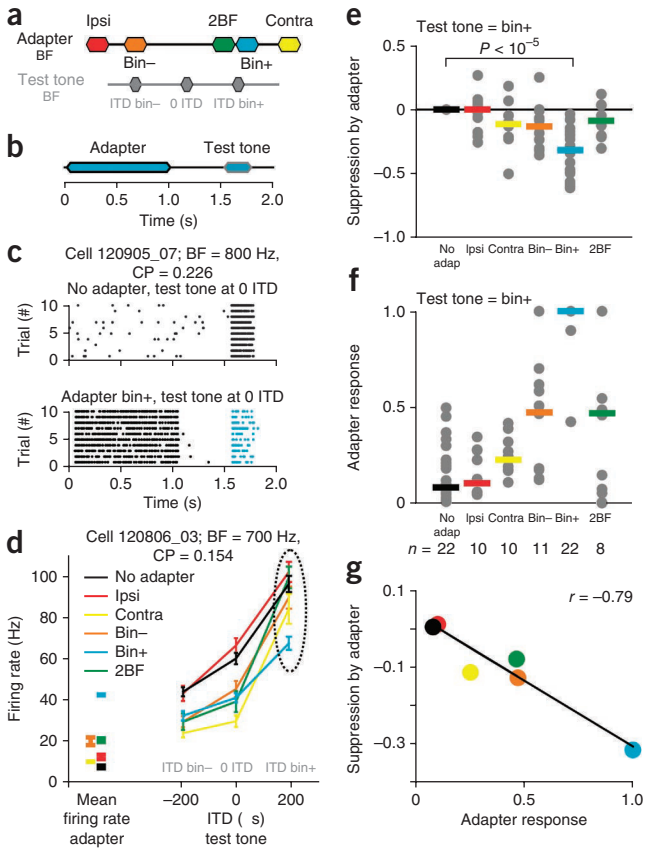

Figure 4 Prior stimuli induce adaptation in the MSO. (**a**,**b**) Schematics depicting the experimental design. (**a**) In each recording, an adapter stimulus is presented monaurally to the ipsilateral (ipsi; red) or contralateral (contra; yellow) ear and binaurally at a negative ITD (bin–; orange), a positive ITD (bin+; blue) and at a twice the best frequency of the given neuron (2BF; green). The color code shown in **a** applies to **d**–**g**. (**b**) The adapter was presented for 1 s, and then the test tone was presented after a 500-ms pause. (**c**) Raster plots showing responses to the test tone (0 ITD) without the adapter (top) and after the bin+ adapter (blue; bottom). There was a robust response to the adapter stimulus. Each tick mark represents an action potential, and each line represents one (of ten total) stimulus repetition. (**d**) Representative mean response of an MSO cell to the adapters (left) and test tones (right). The dotted circle indicates the response to the bin+ test tone, which was used for further analysis in **e**–**g**. Error bars, s.e.m. (**e**) The degree of suppression of the response to the test tone by the adapters, which was calculated by dividing the response to the test tone by the response to the test tone without adapter (no adap), is plotted for each cell in gray. The colored bars represent the median suppression. Significance was assessed using Wilcoxon's signed rank test. (**f**) The response to the adapter normalized to the maximal response is plotted for each adapter condition. (**g**) Correlation between the adapter response (shown in **f**) and the degree of suppression (shown in **e**). The black line indicates a linear regression fit.

configuration should cause maximal activation of the local population of MSO neurons. Moreover, the fact that the source of the adaptation is apparently ITD sensitive itself suggests that it is downstream of the MSO, indicating a population-based feedback mechanism.

To test this idea, we investigated the dependence of adaptation on the actual firing rate of MSO neurons when presented with the adapter. The normalized firing rates observed for all adapters except the monaural adapter showed significant responses compared to the no-adapter condition (**Fig. 4f**; no adapter: 0.08; ipsilateral: 0.1; contralateral: 0.22; bin–: 0.47, $P = 0.007$; bin+: 1, $P < 10^{-5}$; 2BF: 0.47, $P = 0.008$). When we plotted the median suppression induced by the adapter against the median firing rate evoked by the different adapters, we observed a high level of correlation between these two parameters (**Fig. 4g**). Thus, adaptation to the preceding stimulation indeed depends on the firing rate of MSO cells themselves and is induced mainly by high firing rates to binaural stimulations. Furthermore, this result indicates that the observed adaptation cannot be induced by monaural MSO input but must involve some feedback mechanism(s).

To test the hypothesis that $GABA_B$ receptors mediate this feedback adaptation, we combined the adaptation experiments with drug application in a subpopulation of neurons (**Fig. 5**; $n = 11$). Here we used the bin+ adapter condition, which induced the largest effect, and compared this condition to the no-adapter condition before (control) and after blocking $GABA_B$ receptor–mediated inhibition (by application of CGP). As the test-tone condition, we used the bin– stimulation. In contrast to the bin+ ITD, bin– ITDs induced more moderate response rates in MSO neurons (**Fig. 4f**). Using this test tone offered the possibility to investigate decreases and increases in the response rates without saturating the responses. This is of particular importance during the application of CGP, because CGP strongly increases the response rates of the MSO neurons (see below and **Fig. 1g**,**h**). In all MSO neurons tested, application of CGP increased the neuronal responses to the test tone alone, as well as to the adapter itself (**Fig. 5a**; control and no adapter: 0.039, CGP and no adapter: 0.056; $P = 0.042$; control and bin+: 0.79, CGP and bin+: 1; $P < 10^{-4}$).

To investigate the effect of $GABA_B$ receptor–mediated inhibition on stimulus-dependent adaptation of the test-tone response, we next compared the suppression induced by the adapter in presence and absence of CGP. Notably, the suppression induced by the adapter was significantly reduced during blockade of $GABA_B$ receptors with CGP (**Fig. 5b**; control: −0.45; CGP: −0.30; $P = 0.042$).

This decreased suppression by CGP application after an increased response to the adapter is of particular importance. As shown in **Figure 4g**, the neuronal response to the different adapters strongly indicates that suppression increases proportionally with the response rate to the adapter. It follows that if blocking $GABA_B$ receptor–mediated inhibition with CGP would have no effect on the adaptation, one would expect an even further suppression of the response to the test tone induced by the increased response resulting from CGP. However, the opposite is the case. The reasoning is illustrated in **Figure 5c**, which shows the data of **Figure 4g**, the associated regression line and the predicted suppression by the adapter after CGP application as a hypothetical value (magenta dot). Again, despite CGP increasing the response to the adapter, we found a markedly reduced suppression to the test stimulus. This suppression was significantly different from the extrapolated hypothetical value (estimated hypothetical suppression: −1.28; measured suppression: −0.86; $P < 10^{-4}$). Together with the directly measured decrease of adapter-induced suppression (**Fig. 5b**), the difference between the predicted and observed suppression (**Fig. 5c**) strongly indicates that CGP not only increased the firing rate of MSO neurons but also reduced the adapter-induced suppression. Together these findings provide evidence for sound-induced GABA release for adaptation. But what is the source of this GABA, and where is it located?

A potential source of GABAergic MSO input

Direct synaptic inputs to the MSO are all either glutamatergic or glycinergic, and the MSO output is glutamatergic and projects to the auditory midbrain[14,18,20]. However, a potential source of bilaterally

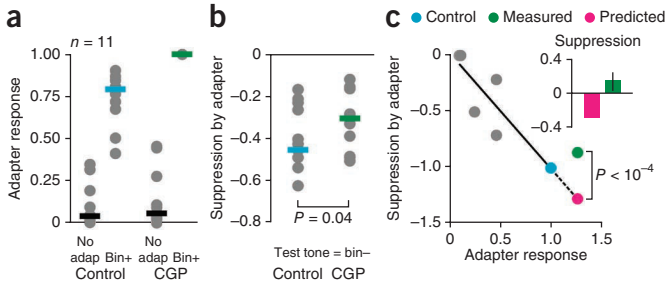

Figure 5 Blocking $GABA_B$ receptor–mediated inhibition decreases the stimulus-induced adaptation in the MSO. (**a**) The response to the adapter normalized to the maximal response is plotted for each condition. The response of each cell tested is plotted in gray, and the colored bars represent the median adapter response. (**b**) The degree of suppression of the response to the test tone at bin– due to the bin+ adapter presentation, which was estimated by dividing the adapted response to the test tone by the response to the test tone without the adapter. This was performed separately for the control condition (left) and blockade of $GABA_B$ receptors with application of CGP (right). The suppression of each cell is plotted in gray, and the colored bars represent the median population suppression. (**c**) Correlation between the adapter response (shown in **a**) and the degree of suppression (shown in **b**). The adapter response and the suppression by the adapter were normalized to the maximally adapting condition (bin+). The gray dots represent the values for different adapter conditions replotted from **Figure 4g**, including the regression line. The magenta dot represents the estimated, hypothetical suppression expected if the suppression depends only on the response rate and blocking $GABA_B$ receptor–mediated inhibition with CGP has no effect on the suppression. The green dot shows the measured value. The inset highlights the difference between the estimated and the measured suppression after CGP application. Error bars, s.e.m. Significance was assessed using Wilcoxon's signed rank test.

modulated GABAergic input to the MSO is the superior periolivary nucleus (SPN), which contains a substantial population of GABAergic neurons[21] and is located just dorsomedially to the MSO. Moreover, collateral inputs to SPN neurons from the MSO have been reported[22], but the function of this connection has never been studied. The question thus arises of whether the SPN projects back to the MSO to provide GABAergic feedback. We examined this possibility by focally applying a fluorescent dextran tracer in the SPN *in vitro*. Fiber tracing revealed projections to the ipsilateral MSO (**Fig. 6a–c,f**). Subsequent immunohistochemistry confirmed that some of these labeled fibers were also GAD65 positive, with varicosities of dextran-filled fibers targeted to the somata and dendrites of MSO neurons. To exclude the possibility of en passant labeling of descending projections from other possible sources (for example, the inferior colliculus), we also applied the tracer focally to the MSO. This resulted in retrograde labeling of GAD67-positive neurons in the SPN, suggesting that at least a subpopulation of GABAergic neurons in the SPN project to the MSO (**Fig. 6d,e**). SPN neurons are rather heterogeneous in their electrophysiological profile, but some show sustained firing patterns in response to pure tones[23–25]. We thus investigated the possibility that these neurons are driven by MSO inputs. First we combined our MSO tracer injections with VGLUT immunostaining, which revealed that the MSO projections to the SPN were in fact glutamatergic (**Fig. 6g**). We then recorded five histologically confirmed SPN cells that we encountered when searching for ITD-sensitive MSO neurons. These neurons responded with sustained discharges, were excited by both ears, as described earlier for the gerbil SPN[23,26], and exhibited ITD sensitivity that was most likely inherited from the MSO (**Fig. 6h,i**). We do not know what response type the SPN neurons that project to the MSO are, but such cell types would clearly allow for the kind of adaptive control described above (with the bin+ condition having the strongest effect). Although we cannot exclude that other nuclei are involved, we could not identify any other source of a binaural, GABAergic input that was coherent with the dependency on the ITD of the adaptation effects described above.

Taken together, the results of these tracing experiments in combination with our physiological findings strongly indicate that MSO and SPN neurons form a negative feedback loop that provides $GABA_B$ receptor–mediated adaptive control of ITD sensitivity in the MSO.

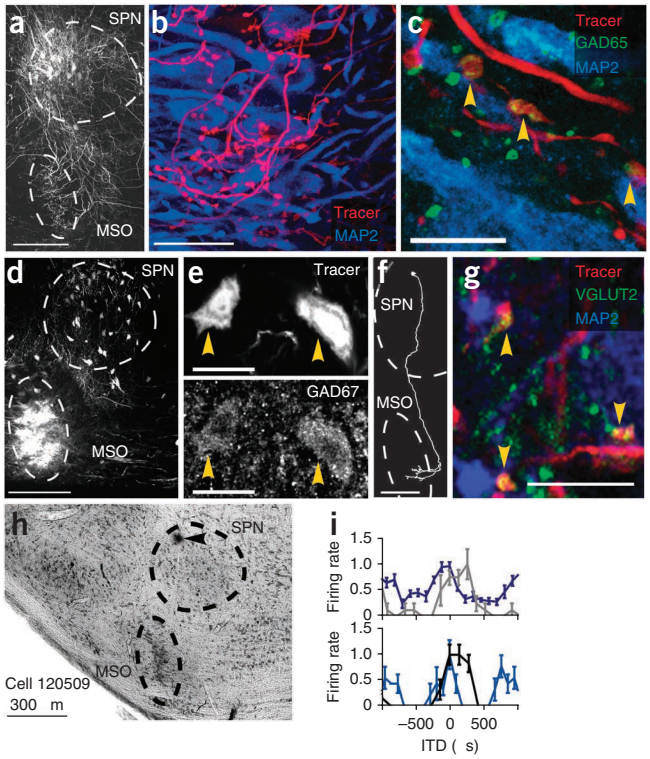

Figure 6 The SPN provides GABAergic input to the MSO. (**a–c**) Focal application of fluorescent dextran tracer to the SPN results in anterograde labeling of projections to the MSO. (**a**) Maximum projection of confocal images showing projections from the SPN to the MSO (both areas outlined by dashed circles). (**b**) Magnification of an area within the MSO showing fibers and varicosities labeled by tracer injection in the SPN (red) and MAP2-stained MSO cells (blue). (**c**) Dextran tracer injected as in **a** combined with GAD65 staining (green). Arrowheads indicate tracer-labeled varicosities that are GAD65 positive. (**d**) Maximum projection showing retrograde labeling of SPN somata after tracer application in the MSO. (**e**) Higher magnification of the SPN neurons (top) that are positive for GAD67 (bottom). Arrowheads indicate tracer-labeled GAD67-positive neurons. (**f**) A complete fiber from a single SPN cell to the MSO in a 200-µm slice. (**g**) Tracer that was focally applied in the MSO as in **d**; the SPN was also stained for MAP2 (blue) and VGLUT2 (green) to mark glutamatergic terminals. Arrowheads indicate VGLUT2-positive varicosities of traced MSO collaterals to the SPN (red). (**h**) Image showing the recording site of the neuron recorded in **i** (upper graph, blue). Recording sites in the SPN were labeled by subsequent injection of HRP. The arrowhead in the lateral region of the SPN marks the HRP injection. (**i**) Functions of ITD-sensitive neurons in the SPN are shown (dark blue: cell 120509_04; CP = –0.09; gray: cell 120802_01, CP = –0.09; light blue: cell 120509_05, CP = –0.07; black: cell 120801_02, CP = 0.1). The firing rate was normalized to the maximal rate. Error bars, s.e.m. Scale bars, 200 µm (**a**,**d**); 20 µm (**b**,**e**); 10 µm (**c**,**g**); 100 µm (**f**). In the merged images (**b**,**c**,**g**), the individual color channels were adjusted.

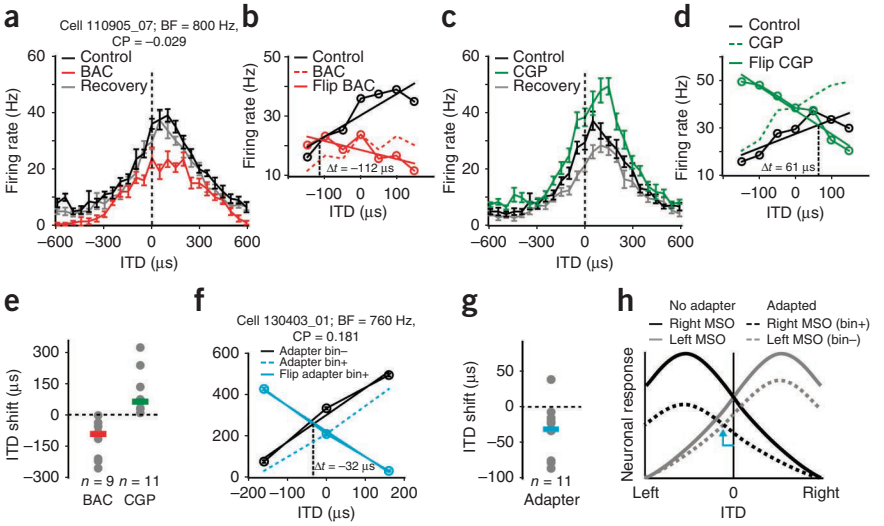

Figure 7 $GABA_B$ receptor modulation and acoustic adaptation change the MSO population code. (**a**,**c**) Neuronal responses of the same cell to different ITDs presented before (black), during (color) and after (gray) activating (**a**) or blocking (**c**) $GABA_B$ receptors. Error bars, s.e.m. (**b**,**d**) Magnification of the important (physiologically relevant) range of ITDs from **a** and **c**. Black indicates the control condition, and red (BAC) and green (CGP) indicate the drug conditions. The dashed lines indicate the actual recording from the cell, and the solid lines indicate its inferred counterpart in the opposite MSO (the flipped version of the former; flip BAC or CGP). The ITD of the intercept of the linear fits to the control and flipped versions is indicated as a dashed black line. (**e**) The calculated intercept is shown for application of BAC (left) and CGP (right). The colored bars represent the median ITD shift. (**f**) Responses to the bin– and the bin+ adapter conditions are shown as in **b** and **d**. (**g**) The calculated intercept is shown between the bin– and bin+ adapter conditions. The colored bar represents the median ITD shift. (**h**) A theoretical scenario is schematized for the shift in the population code (blue arrow) on the basis of the output of the left and right MSOs.

Effects on the population code

Knowing that the neuronal processing of ITDs can be modulated by $GABA_B$ receptor–mediated adaptation through a feedback mechanism at the single-neuron level, the question emerges of how this relates to ITD coding on the systems level. Theoretical studies have suggested that the highest information content of neuronal responses resides at the steepest slopes, where the highest changes in firing rates appear[27]. *In vivo* MSO studies have shown that in most neurons, this point is located around zero ITD. Furthermore, the ITD functions of the ipsilateral and contralateral MSO populations theoretically intersect at this point, which is compatible with the highest ITD resolution being straight ahead. To evaluate the consequences on the basis of the changed responses of two differently adapted MSOs, we symmetrically flipped the ITD sensitivity functions for the different experimental conditions (either during drug application or after a preceding adapter) and compared this flipped response to the response recorded under control conditions. The intercept obtained from the flipped and nonflipped response functions should correspond to the point of intersection of the two differently adapted populations (left and right MSO output). The location of the point of interception should shift because of the adaptation we observed in the MSO. As mentioned above, application of baclofen and CGP changed the firing rate of MSO neurons in opposite directions (**Fig. 7a**,**c**). Focusing on a narrower range of ITDs around the midline showed that the intercept of the control as compared to the symmetrically flipped test condition was indeed shifted (**Fig. 7b**,**d**). The $GABA_B$ receptor agonist baclofen shifted the intercept to a negative ITD, whereas the $GABA_B$ receptor antagonist CGP moved the point of intersection to a positive ITD. These shifts to negative ITDs (−92 µs, $P < 0.004$) and positive ITDs (62 µs, $P < 10^{-4}$) were apparent in all MSO neurons (**Fig. 7e**).

To achieve an estimation of the effect of a real adapter on the population response, we used the adapter condition (bin+) for one MSO and compared its output to the hypothetical contralateral MSO under the bin– condition to mimic the effect in the opposite MSO. Because of the flipping, the bin+ adapter now corresponds to negative ITDs. The intercept of the bin– condition with the flipped bin+ condition was shifted significantly to negative ITDs (**Fig. 7f**,**g**, median: −32 µs, $P = 0.025$). Thus, the adaptation led to a change of the population response with an intercept shifted toward the ITD of the adapter stimulus. Furthermore, the negative shift compares well to the condition during baclofen application (**Fig. 7e**,**h**), which indicates that the $GABA_B$ receptor–mediated inhibition is at least sufficient to explain the adaptation of ITD sensitivity in the MSO. Together these results raise the question of whether such a shift at the level of initial ITD processing is also manifest at the level of perception and, hence, whether such an adapter would cause an according shift of the perceived midline.

Sound-induced adaptation in human perception

The adaptation we observed in the MSO *in vivo* predicts shifts in ITD sensitivity at a perceptual level. Interestingly, human psychoacoustic studies have suggested[6,28] that adapters can affect our spatial perception in a manner that is compatible with a change in the balance of activity between two populations of ITD-coding neurons. We therefore tested sound-source perception in humans using a similar approach as has been used in previous studies[6,29], but we modified the adapter paradigm to match the stimuli used in our *in vivo* experiments in gerbils (**Fig. 4**). We asked listeners to report the perceived position of a test tone presented with or without a preceding adapter. Human listeners were able to reliably determine the perceived intracranial position of test tones using a scheme presented on a computer screen (**Fig. 8a**). Mean position scores increased linearly with test-tone ITDs presented from −454 µs (left) to +454 µs (right). The mean position score for one listener is shown in **Figure 8b**, which depicts the perceived position of test tones both for the no-adapter (black line) and adapter (red line) conditions. When an adapter of the same frequency preceded the test tone, the mean position scores (red line) of test tones were shifted to higher values, most prominently in the hemisphere to which the adapter was presented. Thus, for human listeners, the perceived 'midline' shifted toward the ear at which the adapter was presented, which resulted in a more 'rightward' perception of the test tones. This systematic perceptual shift became particularly apparent when we plotted the difference score as a function of test-tone positions for all four human listeners (**Fig. 8c**). All human listeners perceived test tones presented to the left hemisphere as coming from a position to the right of their true source. Because the adaptation described above is frequency dependent, we tested the effect of adapter frequency on the perceptual shift by presenting the adapter

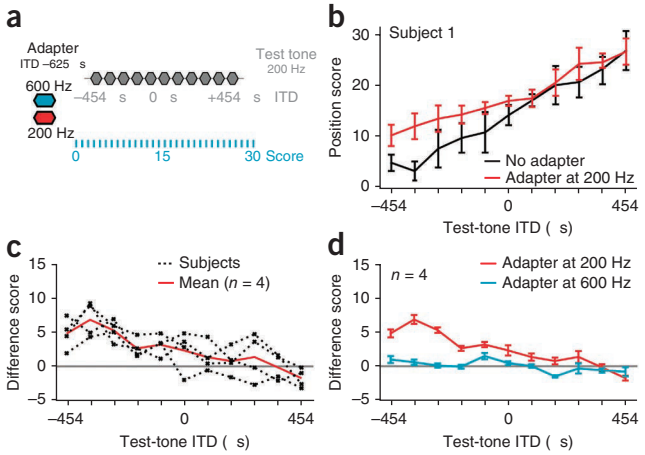

Figure 8 Adaptation to prior stimuli in human ITD-based sound lateralization. (**a**) Schematic depicting the experimental design. (**b**) Psychophysical results for subject 1 are shown. The perceived position of test tones, i.e., the position score (no dimension), is plotted as a function of the ITD for the test tone presented. Error bars, s.d. (**c**) Individual and mean difference scores (black dashed and red solid lines, respectively) are plotted as a function of the test-tone ITD. A positive difference indicates a shift in perception away from the adapter. (**d**) Mean difference scores for the two different adapter conditions: adapter presented with the same stimulus frequency as the test tone (red) or adapter presented with a frequency different from the test tone (blue). Error bars, s.e.m.

tone with a different frequency than the test tone (**Fig. 8d**). The resulting data revealed that the perceptual shift of test tones induced by an adapter could be completely abolished if the adapter had a different frequency (**Fig. 8d**).

These psychophysical data are in agreement with the hypothesis drawn from the *in vivo* recordings and also suggest that the intercept of the neuronal responses of the 'two' MSO populations is indeed a meaningful electrophysiological measure for the population coding of ITD sensitivity.

DISCUSSION

In the present study we have shown that neuronal adaptation has a prominent role in the initial processing of ITDs, which is the dominant cue for human sound localization[9] and takes place in the MSO. Data obtained from *in vitro* and *in vivo* electrophysiological, pharmacological and fiber-tracing experiments revealed a $GABA_B$ receptor–mediated process of adaptation in the gerbil MSO, which is probably implemented through a disynaptic feedback loop. We found that this feedback circuit allowed for the frequency-specific and activity-dependent normalization of MSO responses. Because this normalization was differentially performed in each brain hemisphere, it had substantial effects on the neuronal population coding of sound-source locations. Moreover, we show that these changes in the population code generated by $GABA_B$ receptor–mediated adaptation could be correlated with the localization percepts of human listeners.

Our findings indicate that the ITD-sensitive output of the MSO directly activates feedback from GABAergic neurons in the SPN on the same side of the brainstem. Presynaptic $GABA_B$ receptors in the MSO cause downscaling of the ITD-sensitive responses in a sound frequency– and activity–dependent manner: the downscaling was strongest for binaural stimuli favoring the contralateral ear, which MSO neurons generally prefer[12,30,31]. For example, a stimulus located to the right will reduce the level of activity in the left MSO to a greater extent than that in the right MSO because of stronger activation of the GABAergic feedback to the former. Hence, the balance between the outputs of the two MSOs is changed, and the population code for sound location is altered[19]. The change in the MSO population responses correlates with the altered localization percept we found in human subjects when we tested them with a similar stimulation paradigm and also corroborates a phenomenon described previously[6,29]. In accordance with our predictions based on MSO activity patterns, prior exposure to an adapter stimulus causes a pronounced shift of perceived sound locations away from the adapter location[6,28]. Thus, the adaptation mechanism described here may facilitate spatial segregation of two sound sources and is compatible with increased spatial resolution at an adapter location[32].

The nervous system exploits numerous mechanisms to induce response adaptation at both the cellular and network levels[33,34]. These mechanisms operate on various timescales and seem to serve different functional purposes. For example, rapid response adaptation in the auditory nerve[35,36] and cochlear nucleus[37] adjusts neuronal activity for the optimal detection of changes in the acoustic stimulus and preserves reliable coding of the fine structure of the stimulus, which is a prerequisite for accurate binaural processing[30,38]. Such monaural adaptations allow the MSO to remain sensitive to binaural coincidence detection (i.e., spatial position) over a wide range of intensity combinations[39]. The $GABA_B$ receptor–mediated gain control described here should contribute to this effect by suppressing the response to unfavorable ITDs. Furthermore, the gain control guarantees optimal coding by adjusting the firing rate of the MSO neurons, especially in the most sensitive range of ITDs around the midline.

However, monaural gain control does not seem to be the critical function of $GABA_B$ receptor–mediated adaptation in the MSO. The fact that the major driving force, as we have shown here, is the MSO activity itself, together with our evidence for a feedback circuit through the SPN, indicate that the main purpose of this circuit is an adaptation of the neuronal representation of sound location itself. Interestingly, the particular design of this adaptation circuit conforms to a general pattern of neuronal processing that is seen in sensory systems, namely divisive normalization[1]. Divisive normalization refers to the computation of the ratio between the response of an individual neuron (here a single MSO neuron) and the response of a pool of neurons (here the SPN) in order to match the sensitivity of a neuron to the mean input strength. In particular, we found normalization of the MSO output through the SPN to be highly frequency specific, i.e., MSO activity was differentially controlled according to the spectral composition of the stimulus. Although divisive normalization in the mammalian brain is typically associated with cortical processing[40–42], our findings imply that MSO neurons use GABAergic SPN feedback to normalize their ITD-sensitive response gain at the level of the brainstem. Together with recent findings from the lateral superior olive, which is responsible for the processing of interaural level differences[9], these findings indicate that normalization mechanisms that operate in the brainstem account for some prominent downstream neuronal adaptation effects[2,5,43].

METHODS

Methods and any associated references are available in the online version of the paper.

Note: Any Supplementary Information and Source Data files are available in the online version of the paper.

ACKNOWLEDGMENTS

The *in vivo* experiments and anatomical studies were funded by Deutsche Forschungsgemeinschaft (DFG) grant DFG-SFB870 TP-B02, the *in vitro* recordings were funded by DFG-SFB870 TP-B01 and the Alexander von Humboldt Foundation, and the psychophysical study was funded by the Bundesministerium für Bildung und Forschung (BMBF)-funded German Center for Vertigo and Balance Disorders (IFB). We thank T. Jennings and H. Gleiss for help with stimulus programming and P. Hardy for helpful suggestions concerning the text.

AUTHOR CONTRIBUTIONS

A.S. performed the *in vivo* experiments, analyzed the data and wrote the relevant parts of the manuscript. M.H.M. performed the *in vitro* experiments, analyzed the data and wrote the relevant parts of the manuscript. A.L. performed the psychophysical experiments, analyzed the data and wrote the relevant parts of the manuscript. M.C.F. performed the fiber tracing experiments, analyzed the data and wrote the relevant parts of the manuscript. O.A. performed the immunohistochemistry experiments and confocal microscopy, analyzed the data and wrote the relevant parts of the manuscript. F.F. supervised the *in vitro* experiments. M.P. supervised the adaptation (*in vivo* and psychophysical) experiments and wrote parts of the manuscript. I.S. and B.G. supervised the project and wrote the manuscript.

COMPETING FINANCIAL INTERESTS

The authors declare no competing financial interests.

1. Carandini, M. & Heeger, D.J. Normalization as a canonical neural computation. *Nat. Rev. Neurosci.* **13**, 51–62 (2012).
2. Maier, J.K. *et al.* Adaptive coding is constrained to midline locations in a spatial listening task. *J. Neurophysiol.* **108**, 1856–1868 (2012).
3. Ingham, N.J. & McAlpine, D. Spike-frequency adaptation in the inferior colliculus. *J. Neurophysiol.* **91**, 632–645 (2004).
4. Sanes, D.H., Malone, B.J. & Semple, M.N. Role of synaptic inhibition in processing of dynamic binaural level stimuli. *J. Neurosci.* **18**, 794–803 (1998).
5. Dahmen, J.C., Keating, P., Nodal, F.R., Schulz, A.L. & King, A.J. Adaptation to stimulus statistics in the perception and neural representation of auditory space. *Neuron* **66**, 937–948 (2010).
6. Phillips, D.P. & Hall, S.E. Psychophysical evidence for adaptation of central auditory processors for interaural differences in time and level. *Hear. Res.* **202**, 188–199 (2005).
7. Park, T.J., Brand, A., Koch, U., Ikebuchi, M. & Grothe, B. Dynamic changes in level influence spatial coding in the lateral superior olive. *Hear. Res.* **238**, 58–67 (2008).
8. Magnusson, A.K., Park, T.J., Pecka, M., Grothe, B. & Koch, U. Retrograde GABA signaling adjusts sound localization by balancing excitation and inhibition in the brainstem. *Neuron* **59**, 125–137 (2008).
9. Wightman, F.L. & Kistler, D.J. The dominant role of low-frequency interaural time differences in sound localization. *J. Acoust. Soc. Am.* **91**, 1648–1661 (1992).
10. Grothe, B. & Sanes, D.H. Synaptic inhibition influences the temporal coding properties of medial superior olivary neurons: an *in vitro* study. *J. Neurosci.* **14**, 1701–1709 (1994).
11. Magnusson, A.K., Kapfer, C., Grothe, B. & Koch, U. Maturation of glycinergic inhibition in the gerbil medial superior olive after hearing onset. *J. Physiol.* (*Lond.*) **568**, 497–512 (2005).
12. Pecka, M., Brand, A., Behrend, O. & Grothe, B. Interaural time difference processing in the mammalian medial superior olive: the role of glycinergic inhibition. *J. Neurosci.* **28**, 6914–6925 (2008).
13. Brand, A., Behrend, O., Marquardt, T., McAlpine, D. & Grothe, B. Precise inhibition is essential for microsecond interaural time difference coding. *Nature* **417**, 543–547 (2002).
14. Couchman, K., Grothe, B. & Felmy, F. Functional localization of neurotransmitter receptors and synaptic inputs to mature neurons of the medial superior olive. *J. Neurophysiol.* **107**, 1186–1198 (2012).
15. Smith, A.J., Owens, S. & Forsythe, I.D. Characterisation of inhibitory and excitatory postsynaptic currents of the rat medial superior olive. *J. Physiol.* (*Lond.*) **529**, 681–698 (2000).
16. Fischl, M.J., Combs, T.D., Klug, A., Grothe, B. & Burger, R.M. Modulation of synaptic input by GABAB receptors improves coincidence detection for computation of sound location. *J. Physiol.* (*Lond.*) **590**, 3047–3066 (2012).
17. Hassfurth, B., Grothe, B. & Koch, U. The mammalian interaural time difference detection circuit is differentially controlled by GABAB receptors during development. *J. Neurosci.* **30**, 9715–9727 (2010).
18. Grothe, B. New roles for synaptic inhibition in sound localization. *Nat. Rev. Neurosci.* **4**, 540–550 (2003).
19. McAlpine, D. & Grothe, B. Sound localization and delay lines—do mammals fit the model? *Trends Neurosci.* **26**, 347–350 (2003).
20. Ito, T. & Oliver, D.L. Origins of glutamatergic terminals in the inferior colliculus identified by retrograde transport and expression of VGLUT1 and VGLUT2 genes. *Front. Neuroanat.* **4**, 135 (2010).
21. Roberts, R.C. & Ribak, C.E. GABAergic neurons and axon terminals in the brainstem auditory nuclei of the gerbil. *J. Comp. Neurol.* **258**, 267–280 (1987).
22. Kuwabara, N. & Zook, J.M. Local collateral projections from the medial superior olive to the superior paraolivary nucleus in the gerbil. *Brain Res.* **846**, 59–71 (1999).
23. Behrend, O., Brand, A., Kapfer, C. & Grothe, B. Auditory response properties in the superior paraolivary nucleus of the gerbil. *J. Neurophysiol.* **87**, 2915–2928 (2002).
24. Kopp-Scheinpflug, C. *et al.* The sound of silence: ionic mechanisms encoding sound termination. *Neuron* **71**, 911–925 (2011).
25. Felix, R.A., Fridberger, A., Leijon, S., Berrebi, A.S. & Magnusson, A.K. Sound rhythms are encoded by postinhibitory rebound spiking in the superior paraolivary nucleus. *J. Neurosci.* **31**, 12566–12578 (2011).
26. Dehmel, S., Kopp-Scheinpflug, C., Dorrscheidt, G.J. & Rubsamen, R. Electrophysiological characterization of the superior paraolivary nucleus in the Mongolian gerbil. *Hear. Res.* **172**, 18–36 (2002).
27. Grothe, B., Pecka, M. & McAlpine, D. Mechanisms of sound localization in mammals. *Physiol. Rev.* **90**, 983–1012 (2010).
28. Vigneault-MacLean, B.K., Hall, S.E. & Phillips, D.P. The effects of lateralized adaptors on lateral position judgements of tones within and across frequency channels. *Hear. Res.* **224**, 93–100 (2007).
29. Kashino, M. & Nishida, S. Adaptation in the processing of interaural time differences revealed by the auditory localization aftereffect. *J. Acoust. Soc. Am.* **103**, 3597–3604 (1998).
30. Goldberg, J.M. & Brown, P.B. Response of binaural neurons of dog superior olivary complex to dichotic tonal stimuli: some physiological mechanisms of sound localization. *J. Neurophysiol.* **32**, 613–636 (1969).
31. Yin, T.C. & Chan, J.C. Interaural time sensitivity in medial superior olive of cat. *J. Neurophysiol.* **64**, 465–488 (1990).
32. Getzmann, S. Spatial discrimination of sound sources in the horizontal plane following an adapter sound. *Hear. Res.* **191**, 14–20 (2004).
33. Wark, B., Lundstrom, B.N. & Fairhall, A. Sensory adaptation. *Curr. Opin. Neurobiol.* **17**, 423–429 (2007).
34. Robinson, B.L. & McAlpine, D. Gain control mechanisms in the auditory pathway. *Curr. Opin. Neurobiol.* **19**, 402–407 (2009).
35. Wen, B., Wang, G.I., Dean, I. & Delgutte, B. Dynamic range adaptation to sound level statistics in the auditory nerve. *J. Neurosci.* **29**, 13797–13808 (2009).
36. Wen, B., Wang, G.I., Dean, I. & Delgutte, B. Time course of dynamic range adaptation in the auditory nerve. *J. Neurophysiol.* **108**, 69–82 (2012).
37. May, B.J. & Sachs, M.B. Dynamic range of neural rate responses in the ventral cochlear nucleus of awake cats. *J. Neurophysiol.* **68**, 1589–1602 (1992).
38. Park, T.J., Grothe, B., Pollak, G.D., Schuller, G. & Koch, U. Neural delays shape selectivity to interaural intensity differences in the lateral superior olive. *J. Neurosci.* **16**, 6554–6566 (1996).
39. Pecka, M., Siveke, I., Grothe, B. & Lesica, N.A. Enhancement of ITD coding within the initial stages of the auditory pathway. *J. Neurophysiol.* **103**, 38–46 (2010).
40. Heeger, D.J. Normalization of cell responses in cat striate cortex. *Vis. Neurosci.* **9**, 181–197 (1992).
41. Carandini, M., Heeger, D.J. & Movshon, J.A. Linearity and normalization in simple cells of the macaque primary visual cortex. *J. Neurosci.* **17**, 8621–8644 (1997).
42. Pouille, F., Marin-Burgin, A., Adesnik, H., Atallah, B.V. & Scanziani, M. Input normalization by global feedforward inhibition expands cortical dynamic range. *Nat. Neurosci.* **12**, 1577–1585 (2009).
43. Rabinowitz, N.C., Willmore, B.D.B., Schnupp, J.W.H. & King, A.J. Contrast gain control in auditory cortex. *Neuron* **70**, 1178–1191 (2011).

ONLINE METHODS

Ethical approval for animal experiments. All experiments were approved in accordance with the stipulations of the German law (Tierschutzgesetz) governing animal welfare (AZ 55.2-1-54.2531.8-211-10).

***In vivo* electrophysiology.** Details of all procedures used for anesthesia, surgical operations, acoustic stimulus delivery, stimulus calibration and recording techniques have been published previously[44,45]. Electrophysiological recordings were performed on adult (2- to 5-month-old) Mongolian gerbils (*Meriones unguiculatus*) of both sexes. A craniotomy was performed caudal to the posterior aspect of the transverse sinus, and the underlying cerebellum was partially aspirated to expose the floor of the fourth ventricle. Single-unit responses were recorded extracellularly with glass electrodes (5–15 MΩ; Harvard Apparatus, Kent, UK) filled with 2% HRP dissolved in 10% NaCl. Visual inspection of the impulse amplitude and shape during the experiment and offline spike cluster analysis (Brainware, Jan Schnupp, Tucker-Davis Technologies) enabled secure identification of action potentials from single neurons. To mark recording sites, HRP was iontophoretically ejected (HV-TR 150, NPI) from the recording electrode using a current of 1 µA applied for 3 min. In a few cases, no distinct HRP staining was found, and the recording site was localized on the basis of the track of the recording electrode.

Acoustic stimuli. To search for auditory responses, binaurally uncorrelated noise bursts were presented. When a neuron was encountered, its threshold (lowest sound intensity eliciting spikes) and best frequency (the frequency eliciting the most spikes at the preferred ITD) were determined using binaural pure tones of equal sound pressure level delivered to both ears. Stimuli were presented in randomized order with stimulus duration of 200 ms, plus 5 ms cosine rise-fall times. To determine the effects of $GABA_B$ receptor activation and blockade on ITD sensitivity, neurons were tested before, during and after iontophoretic drug application using pure tones at the best frequency with a range of ITDs equivalent to at least one cycle of the best frequency (25 steps). Each data point was based on at least ten stimulus repetitions. Sound intensity was set to 20 dB above the threshold.

During adaptation experiments, neurons were stimulated with a 1-s adapter signal consisting of a train of 20 50-ms tone pips, followed by a test tone (220 ms) at the best frequency, including linear rise-fall times of 10 ms. The adapter signal and test tone were separated by a 500-ms pause. The test tone was presented randomly with the following three ITDs: −0.125/best frequency (bin−), 0, and +0.125/best frequency (bin+). The following six different adapter conditions were tested: (i) a control stimulus without adapter, (ii,iii) ipsilateral and contralateral monaural adapters at the best frequency, (iv,v) two binaural adapters at the best frequency (ITD at −0.125/best frequency and +0.125/best frequency named bin− and bin+, respectively) and (vi) a binaural adapter at twice the best frequency (ITD at +0.125/best frequency, named 2BF) (**Fig. 4a**). Each adapter condition was repeated 20 times with a pause of 45 s between each condition.

Pharmacology. Five-barrel glass electrodes were used for the iontophoretic application of drugs. Barrels were backfilled with baclofen ((R)-4-amino-3-(4-chlorophenyl)butanoic acid; 50 mM, pH 2.8;), CGP 55845 ((2*S*)-3-[[(1*S*)-1-(3,4-dichlorophenyl)ethyl]amino-2hydroxypropyl](phenyl-methyl)phosphinic acid hydrochloride; 5 or 10 mM, pH 2.6 or 3.6) or GABA (4-aminobutyric acid; 500 mM, pH 3.8) (chemicals from Tocris Bioscience). The center barrel was filled with 1 M NaCl for current balancing. Retention and ejection currents were applied using a Neurophore BH-2 system and IP-2 current pumps (Harvard Apparatus). Baclofen, CGP and GABA were retained with a current of −20 nA and ejected with a current of between +60 nA and +120 nA. In the majority of cells, the effects of the drugs on the neuronal responses were recorded not during but immediately after applying the ejecting current.

Data analyses and statistics. We recorded 59 histologically confirmed single neurons in the MSO and 5 neurons in the SPN with best frequency <1.5 kHz. Only neurons that showed statistically significant ITD sensitivity (see below) were included in this study. Most of the neurons (52/59) showed a characteristic phase between −0.25 and +0.25 (indicating net excitatory input from the two ears, estimated as described previously[46]).

Data were analyzed offline using Matlab 7.0 (MathWorks). In general, average single-cell responses are presented as the mean ± s.e.m., and the averages for populations of neurons are shown as the medians. Accordingly, rate changes at the single-cell level were tested for significance using Student's two-tailed, one-sample paired *t* test ($P < 0.05$), and population-level significance was assessed using Wilcoxon's signed rank test ($P < 0.05$).

The mean number of spikes over all measured ITDs and repetitions as well as the firing rate at the trough and the peak of the ITD functions were calculated for stimulations during control and drug applications of each cell separately. To characterize ITD sensitivity, three parameters were further analyzed: (i) the best IPD (representing the ITD that evoked the highest spike rate normalized to the cycle length of the neuron's best frequency), (ii) the total modulation depth (the difference between the maximal and minimal average spike rates normalized to the maximal spike rate) and (iii) the absolute half width (width of the ITD tuning at the 50% response level). The last two parameters were determined from a Gaussian fit to the ITD function. Best ITDs were calculated using vector analysis[30,47]. Significant best ITDs were scored using the Rayleigh test for uniformity[48] ($P < 0.05$).

To investigate the effect of the adapter on the response to the test tone, responses to the adapter and test tone were analyzed separately. Responses to the adapters were normalized to the maximal firing rate. Suppression of the response to the test tone was quantified in terms of a decrease in response compared to the response to the test tone without the adapter, meaning the suppression of the response to the test tone without adapter was set to zero. Regression lines were obtained using a linear robust fit (Matlab 7.0).

Responses to different ITDs after drug application or during adapter presentation were analyzed with respect to shifts in the azimuthal midline compared to the control, or bin− condition. Therefore, mean spike rates in response to ITDs in the range of ±0.125/best frequency (seven ITDs for the drug and three ITDs for the adaptation experiments) were fitted using a linear fit. Then the mean response and linear fit of the test condition (drug or bin+ adapter) were inverted around zero (midline) ITD. The intercept of the flipped test condition with the linear fit of the control or bin− condition was then measured as a shift in ITD. Seven neurons were discarded because their control ITD functions peaked near 0 ITD or at negative ITDs and thus the intercept of the ITD functions could not be defined.

***In vitro* electrophysiology.** Mongolian gerbils of both sexes at P60–P90 were used. Tissue preparation and recording conditions were as described previously[49], except for the following alterations. All experiments were performed in perfused saline (1 ml per min and bubbled with 95% O_2 and 5% CO_2) with a reduced (1.2 mM) external $CaCl_2$ concentration at 35 ± 1 °C. Visually identified MSO neurons were voltage clamped at −60 mV using an EPC10/2 amplifier (HEKA Elektronik) with borosilicate glass electrodes with resistances of 2–3 MΩ, and series resistance was compensated to a residual of 1.5–2 MΩ. The internal solution contained the following (in mM): 130 Cs-gluconate, 20 tetraethylammonium (TEA)-Cl, 15 Cs-4-(2-hydroxyethyl)-1-piperazineethanesulfonic acid (HEPES), 5 Cs-ethylene glycol tetraacetic acid (EGTA), 5 QX-314 [N-(2,6-dimethylphenylcarbamoylmethyl) triethylammonium chloride], 5 Na_2-phosphocreatine, 3 Mg-ATP, 0.3 Na_2-GTP, 0.05 Alexa Fluor 568 (Invitrogen) and 0.01 4-ethylphenylamino-1,2-dimethyl-6-methylaminopyrimidinium chloride (ZD 7288, Biotrend), adjusted to pH 7.25 and 320 mOsm.

Synaptic inputs were stimulated with borosilicate glass electrodes (resistances of 3–4 MΩ) filled with saline and placed in the vicinity (50–150 µm) of the recorded neuron. Axons were shocked with brief (0.2 ms) pulses of 10–50 V generated by a Model 2100 Isolated Pulse Stimulator (A-M Systems). The stimulus voltage was adjusted such that putative single fibers were activated, as indicated by all-or-none threshold responses and less than 25% amplitude jitter. Stimuli were delivered every 7 s.

***In vitro* pharmacology.** All experiments were performed in the presence of 10 µM 3-((R)-2-carboxypiperazin-4-yl)-propyl-1-phosphonic acid (R-CPP) and 10 µM 6-imino-3-(4-methoxyphenyl)-1(6H)-pyridazinebutanoic acid hydrobromide (SR 95531) to block NMDA receptors and $GABA_A$ receptors, respectively. Glutamatergic and glycinergic inputs were isolated with 0.5 µM strychnine and 20 µM 6,7-dinitroquinoxaline-2,3-dione (DNQX), respectively.

Baclofen ((R)-4-amino-3-(4-chlorophenyl)butanoic acid) was applied at 5 or 0.5 µM to activate $GABA_B$ receptors. All drugs were obtained from Biotrend, with the exception of baclofen, which was purchased from Sigma. Unless otherwise noted, all other chemicals were also from Sigma.

Analyses of *in vitro* data. Data were acquired at 100 kHz and filtered at 4–8 kHz using a three-pole Bessel filter on the EPC10/2 amplifier. All analyses were performed offline using Igor Pro (Wavemetrics). The representative traces shown in the figures were each selected from an average of 15–45 trials. Other averages are presented as the mean ± s.e.m. after testing for normal distribution (Kolmogorov-Smirnov test, $P < 0.05$). Student's *t* test was used to determine statistical significance ($P < 0.05$) where indicated.

Fiber tracing. Mongolian gerbils ($n = 19$, P30–P32) of both sexes were anesthetized with pentobarbital (2 mg per kg body weight) and intracardially perfused with ice-cold Ringer solution containing heparin. After decapitation, the brainstem was removed from the skull under ice-cold dissection artificial cerebrospinal fluid (dACSF) comprising the following (in mM): 125 NaCl, 2.5 KCl, 1 $MgCl_2$, 0.1 $CaCl_2$, 25 glucose, 1.25 NaH_2PO_4, 25 $NaHCO_3$, 0.4 ascorbic acid, 3 *myo*-inositol and 2 pyruvic acid (all chemicals were from Sigma-Aldrich). For anterograde tracing of SPN fibers ($n = 11$), the brainstem was sectioned along the posterior-anterior axis until the MSO, lateral superior olive and SPN were clearly visible. Borosilicate glass micropipettes with a tip diameter of 10–15 µm were filled with a 10% solution of tetramethylrhodamine dextran (3,000 molecular weight (MW); Invitrogen) and visually guided to the SPN. Cells were labeled by applying two to four electroporation pulse trains (50 ms, 50 V, 10 Hz; modified from previous studies[50]). For retrograde tracing of SPN projections to the MSO ($n = 8$), the cerebellum was removed, and the brainstem was cut along the ventral-dorsal axis until both MSOs were clearly visible. Tracer was focally applied in the MSO by electroporation as described above. Subsequently, the explants were transferred to a chamber containing oxygenated incubation ACSF (similar to the dACSF described above but containing 2 mM instead of 0.1 mM $CaCl_2$) and incubated at room temperature for 30–90 min. For anterograde tracing of SPN to MSO projections, a short incubation time (30 min) sufficed to label GABAergic inputs in the MSO. Longer incubation times resulted in additional (retrograde) labeling of MSO cells. Thereafter, brainstems were immersion fixed at room temperature overnight in 4% paraformaldehyde solution.

Immunohistochemistry and confocal microscopy. Brainstems were sectioned coronally (70–200 µm slice thickness), rinsed in PBS and transferred to blocking solution containing 1% bovine serum albumin, 2% Triton X-100 and 0.1% saponin in PBS. Double-immunofluorescence labeling was performed with primary antibodies to the followings: GAD67 (Abcam, ab26116 mouse monoclonal, 1:1,000), GAD65 (Millipore, MAB 351R mouse monoclonal, 1:500), MAP2 (Neuromics, CH22103 chicken polyclonal, 1:1,000) and VGLUT2 (Millipore, AB2251 guinea pig polyclonal, 1:2,000). After incubation with secondary antibodies and rinsing in PBS, sections were mounted with Vectashield mounting medium. Confocal optical sections were acquired with a Leica TCS SP5-2 confocal laser-scanning microscope (Leica Microsystems) using HCX PL APO Lambda Blue 63× numerical aperture (NA) 1.4 immersion oil and HCX PL APO 63× NA 1.3 glycerol objectives. Fluorophores were visualized using a 405-nm diode laser (emission filter: 410–430 nm) for aminoethylcoumarin acetate (AMCA), the 488-nm line of an argon laser (emission filter: 510–540 nm) for Alexa Fluor 488 and a 561-nm diode-pumped solid-state laser (emission filter: 565–585 nm) for tetramethylrhodamine dextran. For each optical section, the images for two or three fluorophores were collected sequentially. Stacks of eight-bit grayscale images were obtained with axial distances of 0.3–3 µm between optical sections and pixel sizes of 481–120 nm, depending on the selected zoom factor and objective. To obtain an improved signal-to-noise ratio, each section image was averaged from four successive scans. After stack acquisition, the *Z* chromatic shift between color channels was corrected. RGB stacks, montages of RGB optical sections and maximum-intensity projections were assembled into tables using ImageJ 1.37k plugins and Adobe Photoshop 8.0.1 (Adobe Systems, San Jose, CA) software. For three-dimensional reconstructions, we used the ImageJ 1.37k paint-brush tool to manually label individual axons. Subsequently, the neighboring axons were digitally deleted. The same axon was identified in the neighboring overlapping confocal image stacks.

Psychophysics. All experiments were approved in accordance with the ethical board of the Ludwig-Maximilians-Universität medical center, project number 359-07. Four human listeners (two male and two female, aged 24–31 years) participated in this study. All subjects had experience with psychoacoustic tasks and showed normal audiograms between 250 and 8,000 Hz. The subjects were seated in a double-walled, sound-attenuated chamber (Industrial Acoustics Company GmbH) and wore circumaural earphones (HDA 200, Sennheiser Electronic GmbH & Co. KG,).

All stimuli were generated in Matlab at a sampling rate of 44.1 kHz and were digital-to-analog (D/A) converted (MOTU, UltraLite-mk3) before being presented to the listeners. The stimulus paradigm was a 1-s adapter sequence consisting of 20 50-ms tone pips followed by a 220-ms test tone (including linear rise-fall times of 10 ms) and was similar to that used in the *in vivo* adaptation experiments. The adapter and test tone were separated by a 500-ms pause. The test tone was presented at 200 Hz and at 11 different ITDs ranging from −454 µs to 454 µs in steps of approximately 90 µs. The following three different adapter conditions were presented: (i) a control stimulus without adapter (no adapter), (ii) an adapter with a frequency matching that of the test tone (adapter at 200 Hz) or (iii) an adapter with a different frequency (adapter at 600 Hz). All stimuli were presented at 80 dB.

Subjects were asked to determine the perceived intracranial position of a test tone by pressing 1 of 31 linearly arranged buttons (score values from 0 (far left) to 30 (far right); **Fig. 7a**) displayed on a computer screen. One trial consisted of one of the three adapter conditions. After each trial, listeners reported the perceived position without a time limit. The next trial started 500 ms after answering. The full set of adapter conditions (330 trials with 10 trials per test-tone ITD and adapter condition) was presented in three sessions. In the first session the no-adapter condition was presented, in the second session the adapter stimulus was presented with the matched frequency (200 Hz), and in the third session the adapter with the unmatched frequency (600 Hz) was presented. Within one session, the intracranial positions of the stimuli were presented randomly.

For each subject, scores were averaged over all trials for each adapter condition. A difference score was calculated by subtracting the position scores of the no-adapter condition from the position scores of either the 200 or 600 Hz condition. This was done separately for each listener and test-tone ITD. The average position score for each subject is presented as the mean ± s.d., and the mean difference score is presented as the mean ± s.e.m.

44. Khouri, L., Lesica, N.A. & Grothe, B. Impaired auditory temporal selectivity in the inferior colliculus of aged mongolian gerbils. *J. Neurosci.* **31**, 9958–9970 (2011).
45. Siveke, I., Leibold, C., Schiller, E. & Grothe, B. Adaptation of binaural processing in the adult brainstem induced by ambient noise. *J. Neurosci.* **32**, 462–473 (2012).
46. Siveke, I., Pecka, M., Seidl, A.H., Baudoux, S. & Grothe, B. Binaural response properties of low-frequency neurons in the gerbil dorsal nucleus of the lateral lemniscus. *J. Neurophysiol.* **96**, 1425–1440 (2006).
47. Kuwada, S. & Yin, T.C. Binaural interaction in low-frequency neurons in inferior colliculus of the cat. I. Effects of long interaural delays, intensity, and repetition rate on interaural delay function. *J. Neurophysiol.* **50**, 981–999 (1983).
48. Mardia, K. *Statistics of Directional Data* (Academic, London, 1972).
49. Couchman, K., Grothe, B. & Felmy, F. Medial superior olivary neurons receive surprisingly few excitatory and inhibitory inputs with balanced strength and short-term dynamics. *J. Neurosci.* **30**, 17111–17121 (2010).
50. Ford, M.C., Grothe, B. & Klug, A. Fenestration of the calyx of Held occurs sequentially along the tonotopic axis, is influenced by afferent activity, and facilitates glutamate clearance. *J. Comp. Neurol.* **514**, 92–106 (2009).

doi:10.1038/nn.3548

3 General Discussion

Structure-function relations at the calyx of Held

During postnatal development the calyx of Held presynaptic terminal undergoes considerable morphological changes (Kandler and Friauf, 1993; Kil et al., 1995). The transformation from a spoon-shaped, closed morphology to a highly fenestrated structure has been proposed to improve high-fidelity synaptic transmission at this synapse (Taschenberger et al., 2002). The goal of the first study (Ford et al., 2009) was to investigate these morphological changes and their impact on temporal fidelity.

The role of cochlea-generated activity in the morphological maturation of the calyx

We were able to demonstrate that the fenestration process does not occur simultaneously in all calyces. Calyces located medially in the MNTB, which are transmitting high-frequency sound information after hearing onset, fenestrate significantly earlier than calyces located laterally in the MNTB which transmit low-frequency sound information. This finding indicates that a temporary developmental gradient along the mediolateral tonotopic axis (Guinan et al., 1972) is established around the time of hearing onset in Mongolian gerbils.

At present, it is unclear why morphological maturation of medially located calyces is happening earlier and whether this plays a functional role in the development of the circuit. An analysis of the distribution of large perisomatic clusters of vesicular glutamate transporters in the MNTB indicates that, during development, medially located MNTB neurons form synaptic contacts more rapid than laterally located MNTB neurons (Rodríguez-Contreras et al., 2008). This suggests that selection of synaptic partners and synapse formation may occur earlier in the medial MNTB, which probably results in earlier morphological maturation (fenestration) of medially located calyces of Held.

However, it is also possible that patterned pre-hearing activity contributes to the formation of the developmental gradient. Before hearing onset spontaneous activity is generated by immature auditory hair cells in the cochlea (Tritsch et al., 2007; Johnson et al., 2011). The pattern of spontaneous activity varies depending on the position along the length of the cochlea from base to apex, with basal hair cells showing higher firing rates and more sustained discharges compared to apical hair cells, which show lower mean firing rates and bursting activity (Johnson et al., 2011, 2012). Hence, medially and laterally terminating calyces may receive significantly different spontaneous activity patterns before hearing onset.

Patterned spontaneous activity before hearing onset has been reported for MNTB cells in mice, rats, and gerbils (Sonntag et al., 2009; Tritsch et al., 2010; Clause et al., 2014), but it has not been correlated with the cells' locations in the nucleus. Histologically confirmed *in vivo* recordings of presynaptic activity in pre-hearing animals would be necessary to identify possible differences in the pattern of spontaneous activity received by calyces of Held along the mediolateral axis of the MNTB.

Consistent with a potential role of spontaneous activity, we found that the developmental gradient was not present in animals that were unilaterally cochlear ablated or administered ototoxic drugs. These procedures are commonly used to remove or significantly decrease cochlea-generated spontaneous and sound evoked activity. Interestingly, calyces located in the medial part of the MNTB appeared more fenestrated in animals that were deprived of activity originating in the cochlea compared to control animals. This indicates that cochlea-generated activity influences the fenestration process, but also that it is not necessary for the fenestration process *per se* to occur. The finding that calyx fenestration still occurs in the absence of cochlea-generated activity is in line with findings in congenitally deaf mice and mice with unilateral conductive hearing loss (Youssoufian et al., 2008; Grande et al., 2014).

It has been reported that in the congenitally deaf *dn/dn* mouse calyces did not appear to be different from those in control animals (Youssoufian et al., 2008). However, in that study only two age groups were examined, one pre-hearing group aged between P5 and P8, and one post-hearing group aged between P20 and P22. In our study, an effect of afferent activity on calyx morphology became apparent by comparing the

developmental state of calyces along the tonotopic axis around the time of hearing onset in control animals with that in sensory deprived animals. In age groups similar to those investigated by Youssoufian and colleagues, no gradient was apparent in gerbils. Thus it is possible that a developmental gradient comparable to that found in the gerbil also exists in mice. In addition, since the frequency range experienced by mice is much smaller and missing the low-frequency portion compared to that experienced by Mongolian gerbils (Ryan, 1976; Radziwon et al., 2009), it may be more difficult to detect possible developmental differences in calyx morphology along the tonotopic axis of the MNTB in mice, and hence possible differences between control and sensory deprived animals.

Finally, it should be noted that we cannot rule out compensatory mechanisms that restore spontaneous activity in animals that were cochlear ablated or administered ototoxic drugs. Indeed, compensatory mechanisms have been described in other systems after removal of spontaneous activity [reviewed in (Blankenship and Feller, 2010)]. Such mechanisms may overcompensate for the removal of spontaneous activity and may lack potentially important information carried in the burst pattern of cochlea-generated activity.

Functional implications of calyx fenestration

Our immunohistochemical staining revealed that astrocytic processes containing the glutamate transporters GLAST and GLT1 occupy the newly created diffusional exits in the calyx and thus could augment fast reuptake of neurotransmitter. In line with this idea, our physiological data show a faster decay time course of postsynaptic currents as well as a lower amount of residual current accumulating during synaptic stimulation at 100 Hz, suggesting that glutamate clearance is indeed faster at calyces located medially in the MNTB which are more fenestrated than those located laterally in the MNTB.

Astroglial synapse invasion has been shown to modulate the synaptic strength through glutamate uptake at hippocampal excitatory synapses (Pannasch et al., 2014). In contrast, at the calyx of Held glial glutamate transporters have been reported to play a minor role in transmitter clearance from the synaptic cleft in older

animals. Instead, facilitated transmitter diffusion at morphologically mature calyces may be the major mechanism terminating synaptic events (Renden et al., 2005). This raises the question why astrocytic process containing GLT1 and GLAST invade the newly created diffusional exits. It has been speculated that glutamate transporters may restrict glutamate diffusion and prevent spillover to neighboring synapses in the MNTB (Renden et al., 2005). Moreover, an important function of astrocytes is to sequester synaptically released glutamate and to convert it into glutamine (Sibson et al., 2001). It has been shown recently that astrocytes adjacent to the calyx of Held rapidly release glutamine in response to activation of their glutamate transporters (Uwechue et al., 2012). The same group has further demonstrated that extracellular glutamine, which is a precursor for glutamate, activates presynaptic glutamine transporters in the calyx. This supply of glutamine for generation of presynaptic glutamate helps to sustain synaptic transmission at the calyx of Held (Billups et al., 2013).

It is thus possible that the closer distance of astrocytic glutamate transporters to the sites where glutamate is released from the calyx facilitates glutamate reuptake and leads to a faster supply of glutamine by astrocytes. Moreover, it may help to keep local glutamine levels high at the sites where presynaptic transporters mediate uptake of glutamine into the calyx. It is likely that, as a result of the fenestration process, the surface to volume ratio is increased at the finger-like calyx processes, which may increase the efficiency of glutamine uptake into the calyx. Further analysis of the subcellular distribution and proximity of glutamine transporters in astrocytes and calyces are necessary to gain further understanding of the interplay between astrocytes and the morphologically matured presynaptic terminal. Taken together, the morphological changes and the invasion of diffusional exits by processes of perisynaptic astrocytes could contribute to sustain synaptic transmission at high rates at the calyx of Held.

To conclude, differences in calyx morphology along the tonotopic axis of the MNTB around hearing onset go along with physiological differences and should be considered in *in vitro* studies.

Structure-function relations in bushy cell fibers

The goal of the second study was to perform a detailed morphometric analysis of the structure of spherical and globular bushy cell axons that provide well-timed excitatory and inhibitory input to the coincidence detector neurons of the MSO, and to assess how the individual structural parameters contribute to the high temporal fidelity of the circuit. In particular, we were interested in answering the question of how conduction velocity is tuned in the inhibitory GBC-MNTB pathway, which has been shown to be particularly fast despite the additional synapse in the MNTB (Grothe and Sanes, 1994; Roberts et al., 2013).

The mammalian ITD processing circuit represents an ideal model system for studying structure-function relations in myelinated axons because the sensitivity of MSO neurons to microsecond differences in the time of arrival of sound at the two ears is likely to critically depend on well timed inputs (Grothe et al., 2010; Seidl, 2013; Myoga et al., 2014), which suggests that conduction time in these fibers is well tuned. We used anterograde labeling of axons in combination with immunohistochemical staining of nodal and juxtaparanodal marker proteins to determine the internodal axon diameter, the node of Ranvier diameter, and the length of internodal segments, which are important determinants of conduction speed in myelinated axons (Waxman, 1980), in bushy cell fibers. In addition we determined the myelin thickness of bushy cell fibers using transmission electron microscopy.

We found that, on average, the diameter of GBC axons was more than twice the diameter of SBC axons and the internode length in GBC axons was larger than that found in SBC axons, which is in line with Rushton's observations of thicker axons having larger internodes than thinner axons (Rushton, 1951). Unexpectedly, the population of GBC fibers was not structurally homogeneous. GBC fibers transmitting low-frequency sound information, which terminate laterally in the tonotopically organized MNTB, were larger in diameter and had an anomalous internode length to axon diameter ratio that is 35% smaller than the value found in axons transmitting high-frequency sound information which target cells medially in the MNTB. Using a multi-compartment computational model of the myelinated axon we estimate that the shorter internode lengths, together with the larger diameter of laterally terminating

GBC axons, increase the action potential conduction speed by ~36% as compared to medially terminating GBC axons, which helps to explain why the inhibitory input can arrive before the excitatory input at the MSO (Grothe and Sanes, 1994; Roberts et al., 2013). The striking deviation of GBC axon geometry from the canonically assumed axon structure may serve different functions in GBC fibers as explained in the following paragraphs.

It has been speculated that the structure of myelinated axons may be tuned by evolution to provide the highest conduction velocity (i.e. internodes exhibit an optimal length and myelin thickness with respect to maximizing conduction velocity) (Rushton, 1951; Debanne et al., 2011). However, Huxley and Stämpfli speculated that the length of internodes may be greater than the length (theoretical value) which would maximize the conduction velocity (optimal values), and that this situation should result in decreased energy expenditure (Huxley and Stampfli, 1949). Our morphometric data obtained from GBC axons indicate that axons are not tuned to reach the highest conduction velocity but rather to achieve a particular arrival time at the target nucleus. Moreover, the geometry of bushy cell fibers is probably tuned to reduce their energy demand. Our simulations predict that the measured internode length to axon diameter ratios in SBC, GBCmed and GBClat fibers are larger than those which would maximize conduction velocity. Notably, the mean internode length to axon diameter ratio in GBClat axons (measured far from the calyx of Held terminal) was closer to the simulated optimum for maximizing conduction velocity than the measured internode length in GBCmed fibers. This indicates that, due to the shorter internode lengths, which are associated with a larger number of nodes of Ranvier, and the larger axon diameter, GBClat fibers may be energetically more demanding than GBCmed fibers. It has been reported that MSO neurons are energetically more costly than other SOC nuclei (Trattner et al., 2013). Taken together, the exceptionally high demands for temporal precision in binaural processing of low-frequency sound information in the ITD-detection circuit may be associated with high energy expenditure.

Myelination of GBC fibers may not only contribute to tuning action potential conduction time, but also to the preservation of the temporal information carried by phase-locked action potentials. Action potentials in sound localization circuits are very brief, which may help to keep synaptic delays short (Sabatini and Regehr, 1999;

Boudkkazi et al., 2011) and possibly aids reliable conduction of temporal information at high firing rates.

The short duration of action potentials in the sound localization circuits is usually assumed to be due to the fast activation kinetics of sodium channels (Leão et al., 2005) and the high expression of high-voltage-activated K_v3-type potassium channels which lead to a fast repolarization of the action potential (Johnston et al., 2010). However, our detailed computer simulations suggest that myelination may also play a role in shaping axonal action potential waveforms. In particular, we found that the half-width of the simulated action potential is reduced when the internode length to axon diameter ratio is decreased in GBC fibers. In line with this finding, the reduction in action potential half-width observed during postnatal development at the calyx of Held (Taschenberger and von Gersdorff, 2000) may in part be attributable to an increase in myelination of GBC fibers during this period (Kim et al., 2013a).

However, in a recent study comparing presynaptic action potential waveforms in calyces of Held in Long-Evans shaker (LES) rats with those measured in control rats, the action potential half-width was reported to be similar on average in both strains (Kim et al., 2013a), even though compaction of myelin is not happening in LES rats due to a lack of myelin basic protein (Kwiecien et al., 1998). Notably, the variability was much larger for action potentials in LES rats. It is conceivable that in shaker rats compensatory mechanisms lead to similar action potential shapes, probably by changing axon geometry or ion channel densities in the axonal membrane. Indeed, in LES rats axonal diameters are decreased in the spinal cord (Smith et al., 2013), and our simulations suggest that the action potential half-width is shorter in thinner axons than in thicker axons that are otherwise structurally similar. Further experiments are needed to test if GBC axon geometry in LES rats differs from control rats. Moreover, as myelin helps to cluster ion channels in the axonal membrane (Rasband and Trimmer, 2001), it is likely that differences between LES and control rats are not only attributable to the lack of compact myelin.

Another major finding of this study is that in all GBC fibers the internode length decreases progressively towards the calyx of Held. Our computer simulations suggest that these gradations aid impedance matching at the giant presynaptic terminal (Leão et al., 2005) and thus could contribute to the reliable and precise transmission of information demonstrated experimentally at this synapse. In line with

this idea, the fidelity of presynaptic action potential timing and synaptic transmission is decreased in the GBC-MNTB pathway in Long-Evans shaker rats (Kim et al., 2013a, 2013b), as indicated by an increase of presynaptic action potential jitter and synaptic failures at high stimulation rates as compared to control animals.

A decrease of internode lengths in distal axon segments has been reported for neocortical axons and nucleus magnocellularis axons innervating nucleus laminaris (Deschênes and Landry, 1980; Carr and Konishi, 1990). These internode length gradations are likely a result of extensive fiber branching, as there is usually a node at every branch point in myelinated axons. Our finding of internode gradation towards the calyx of Held is not a secondary effect related to fiber branching, but is more comparable to the gradations reported to exist close to the neuromuscular junction (Quick et al., 1979). This suggests that evolutionary pressures have led to analogous structural adaptations in the central and peripheral nervous system of mammals that help to depolarize large presynaptic terminals like the calyx of Held and the neuromuscular junction.

In fact, myelin itself seems to provide a strong selective advantage as it has arisen several times independently during evolution in annelids, crustacean, and in vertebrates, albeit the implementation varies (Hartline and Colman, 2007). Along this line, the question arises whether internode length gradations similar to those found in mammals can also be found in other taxa, e.g. in the axons that give rise to giant synaptic endings in the chick ciliary ganglion (Paysan et al., 2000) or to the giant synapse in the electrosensory system of *Gymnarchus* (Matsushita and Kawasaki, 2004). An existence of similar internode length gradations in birds and weakly electric fish may represent a striking example of convergent evolution.

Action potential initiation in MSO neurons

MSO neurons are highly specialized coincidence detector neurons that can encode ITDs in the range of microseconds. These neurons have a remarkably low input resistance of only ~ 5 MOhms and very short time constants of only a few hundred microseconds (Scott et al., 2005; Couchman et al., 2010). The low input resistance and short membrane time constants are attributable to the expression of low-voltage-

activated potassium channels and hyperpolarization-activated cyclic nucleotide-gated channels which are already activated at the resting membrane potential (Scott et al., 2005; Baumann et al., 2013). While these biophysical specializations help to achieve the temporal precision necessary for binaural coincidence detection, they also constitute a serious problem because the leaky soma might act as a current sink and could thus hamper action potential generation in the axon initial segment, in particular when synaptic conductances are high.

In the third study (Lehnert et al., 2014) we investigated the mechanisms that enable MSO neurons to generate action potentials at high rates despite their low input resistance. We performed a detailed morphometric analysis of the axon initial segment and proximal axon segments of MSO neurons and found that the axon is less than 1 µm in diameter. Our computer simulations show that the thin axons of MSO neurons facilitate action potential initiation in the axon initial segment. Moreover, the model suggests that, under conditions of high synaptic input rates, action potentials are also generated in the nodes of Ranvier. The expansion of the spike initiation area to nodes of Ranvier in the proximal axon is caused by spatial gradient of sodium channel inactivation and a somatic current sink.

Similarly, a recent study showed that hippocampal dentate granule cells can rapidly adapt their ability to initiate spikes, depending on ongoing synaptic activity, by expanding the area where action potentials are initiated away from the soma (Scott et al., 2014). Corresponding with our findings, the reason for the broadening of the spike-initiating zone was distance dependent sodium channel inactivation caused by somatic depolarization.

In contrast to dentate granule cells and MSO neurons, in which the site of action potential generation changes dynamically, nucleus laminaris neurons of the analogous avian ITD-detection circuit use a more hardwired mechanism for ensuring action potential generation. There, the length of the AIS and the position of sodium channels vary as a function of the best frequency of the cells. In neurons tuned to high (2.5-3.3 kHz) and middle (1.0-2.5 kHz) sound frequencies sodium channels are clustered in short segments that are located 20-50µm away from the soma whereas in neurons tuned to low (0.4-1.0 kHz) sound frequencies they are clustered in longer segments which are located closer to the soma (Kuba et al., 2006). Computer simulations indicate that this differential arrangement reduces the threshold for action

potential generation and improves the ITD sensitivity of the coincidence detector neurons. Especially in high-frequency neurons the electrotonically more isolated, distal site of spike initiation reduced the extent of sodium channel inactivation and improved the detection of ITDs at high synaptic input rates (Kuba et al., 2006). In conclusion, axonal spike initiation in birds and mammals, although differentially implemented, improves ITD sensitivity of binaural coincidence detector neurons.

The biophysical specializations of mature MSO neurons which enable them to process temporal information with very high precision restrict action potential invasion of the somatodendritic compartment (Scott et al., 2005, 2007). Notably, a restricted backpropagation into the soma and dendrites may be disadvantageous during the developmental period when experience dependent circuit refinement occurs (Kapfer et al., 2002; Werthat et al., 2008) since refinement may depend on the relative timing between backpropagating action potentials and synaptic events. For instance, a refinement of the distribution of glycinergic inhibitory inputs on MSO neurons has been shown to be dependent on normal binaural experience during postnatal development (Kapfer et al., 2002). Accordingly, a later study showed that developmental refinement of the axonal arborization pattern in MNTB principal cell axons innervating the MSO depends on normal acoustic experience (Werthat et al., 2008). Exposing animals to omnidirectional white noise, a procedure that reduces binaural timing information, impaired the spatial refinement of inhibitory inputs and the pruning of MNTB axonal arbors. Moreover, a theoretical study suggested that a spike timing dependent developmental mechanism may refine ITD sensitivity (Gerstner et al., 1996).

Thus, it would be of great interest to test whether active mechanisms exist in younger animals that promote action potential backpropagation into the somatodendritic compartment, which might be necessary for possible spike timing-dependent plasticity. For instance, it has been shown that two opposed gradients of the voltage-activated sodium channels $Na_v1.2$ and $Na_v1.6$ exist in axon initial segments of layer 5 pyramidal neurons of the prefrontal and somatosensory cortex. This differential distribution of high- and low-threshold voltage-activated sodium channels promotes backpropagation of action potentials into the somatodendritic compartment of the cell and thus may play a crucial role in spike timing-dependent plasticity (Hu et al., 2009).

Further experiments are needed to test if similar adaptations also exist in MSO neurons during the period when experience dependent circuit refinement occurs.

GABAergig feedback mechanisms in mammalian sound localization circuits: structure-function relations

The fourth study (Stange et al., 2013) demonstrated that, *in vivo*, the ITD sensitivity of MSO neurons is modulated via a $GABA_B$ receptor dependent mechanism. GABAergic modulation of excitatory and inhibitory MSO inputs has been previously demonstrated *in vitro* (Hassfurth et al., 2010; Fischl et al., 2012), however the functional significance of this modulation for sound source localization *in vivo* and the source providing GABA were unclear (Grothe and Koch, 2011).

Our anterograde and retrograde fiber tracing experiments suggest that a subpopulation of SPN neurons sends GABAergic projections to the MSO. Using anterograde and retrograde tracing we were also able to corroborate the earlier finding that MSO neurons send collateral projections to the SPN in the gerbil (Kuwabara and Zook, 1999). Using immunohistochemical stainings we were able to show that the projections to the SPN are glutamatergic. Taken together, our anatomical data strongly indicate that a disynaptic feedback loop via the SPN is involved in GABAergic modulation of MSO inputs.

Similarly, the processing of ILDs in the LSO has been recently described to be adjusted through GABAergic feedback by balancing excitatory and inhibitory inputs (Magnusson et al., 2008). However, the implementation of the feedback mechanism underlying the activation of presynaptic $GABA_B$ receptors seems to be fundamentally different to that proposed for the MSO. In LSO neurons spiking activity results in retrograde release of GABA in a calcium dependent manner which modulates presynaptic transmitter release from excitatory and inhibitory inputs to the LSO via a $GABA_B$ receptor-dependent mechanism. The proposed mechanism of calcium dependent retrograde release of GABA from LSO neurons is supported by a more recent *in vitro* study which showed that the density of high-voltage-activated calcium currents is upregulated during postnatal development and, using two-photon calcium imaging, revealed that dendritic calcium influx occurs in response to action potential

trains evoked through somatic current injections (Ford et al., 2010), conceivably through high-voltage-activated calcium channels.

Why do the MSO and LSO circuits employ two fundamentally different mechanisms for providing GABAergic feedback to the presynaptic inputs (retrograde release of GABA from LSO neurons vs. disynaptic feedback loop)? While retrograde release of GABA from LSO neurons provides a fast and direct mechanism for providing transmitter for GABAergic modulation of presynaptic inputs, this mechanism may not have evolved in the MSO because it could hamper coincidence detection of excitatory and inhibitory inputs as explained below.

Experimental and theoretical data suggest that in MSO neurons spikes are initiated at the axon initial segment or proximal axon (Scott et al., 2005, 2007; Lehnert et al., 2014). Due to the high expression of low-voltage-activated potassium channels action potentials are strongly attenuated as they backpropagate into the soma and dendrites (Scott et al., 2007). It has been speculated that this restricted invasion of the somatodendritic compartment of MSO neurons may be important for minimizing interference with synaptic integration at high input rates (Scott et al., 2007). Thus, the biophysical properties of MSO neurons which enable them to perform coincidence detection in the microsecond range may be incompatible with a retrograde release mechanism similar to the one proposed for the LSO.

It remains to be determined which SPN cells project back to the MSO. Retrograde prelabeling studies revealed that several cell types in the SPN receive collateral projections from the MSO which are likely to be tonotopic (Kuwabara and Zook, 1999). A large number of these SPN cells projects to the ipsilateral inferior colliculus, and a small number projects to the cochlear nucleus. The study also reported a population of SPN cells that received MSO inputs but neither projected to the inferior colliculus, nor to the cochlear nucleus. It may represent the subpopulation projecting to the MSO, although it can not be ruled out that those SPN cells projecting to the inferior colliculus or the cochlear nucleus also send collaterals to the MSO. Furthermore, it is unknown whether these SPN cells solely serve to convert glutamatergic input from the MSO into GABAergic output, or if they receive other inputs in addition to the collateral inputs from MSO axons, which would allow for additional context-dependent modulation.

Trans-synaptic tracing using modified rabies virus (Rancz et al., 2011) may allow shedding light on these open questions. The approach reported by Rancz and colleagues combines *in vivo* whole-cell recordings with retrograde, monosynaptic tracing of the neuron's presynaptic inputs. If this method could be successfully applied in the brainstem of Mongolian gerbils, it may allow tracing the anatomical connectivity of single SPN cells that have been electrophysiologically characterized. Thus, it may be possible to label neurons that are presynaptically connected to the SPN cell from which recordings have been obtained, which would not only allow to determine the number of MSO neurons innervating an SPN cell but also to trace possible inputs from other nuclei. As the SPN cell is also labeled through this approach, it would be possible to trace its axon and determine whether the GABAergic projections to the MSO are tonotopic, as suggested by the lack of modulation of single MSO cells via off-best frequency adapter sounds (Stange et al., 2013). If this approach turns out to be not feasible, one could try to combine *in vivo* cell-attached recordings from SPN neurons with subsequent single cell electroporation (Kitamura et al., 2008) to deliver the DNA vectors necessary for tracing the inputs.

In summary, due to their tonotopic organization and the numerous specializations that preserve temporal information, the initial stages of binaural processing in the auditory brainstem represent an ideal model system for studying structure-function relations in neural circuits.

References

Attwell D, Gibb A (2005) Neuroenergetics and the kinetic design of excitatory synapses. Nat Rev Neurosci 6:841–849.

Bakiri Y, Káradóttir R, Cossell L, Attwell D (2011) Morphological and electrical properties of oligodendrocytes in the white matter of the corpus callosum and cerebellum. J Physiol 589:559–573.

Baumann VJ, Lehnert S, Leibold C, Koch U (2013) Tonotopic organization of the hyperpolarization-activated current (Ih) in the mammalian medial superior olive. Front Neural Circuits 7:117.

Billups D, Marx M-C, Mela I, Billups B (2013) Inducible presynaptic glutamine transport supports glutamatergic transmission at the calyx of Held synapse. J Neurosci Off J Soc Neurosci 33:17429–17434.

Blankenship AG, Feller MB (2010) Mechanisms underlying spontaneous patterned activity in developing neural circuits. Nat Rev Neurosci 11:18–29.

Borst JGG, Soria van Hoeve J (2012) The calyx of held synapse: from model synapse to auditory relay. Annu Rev Physiol 74:199–224.

Borst JG, Sakmann B (1996) Calcium influx and transmitter release in a fast CNS synapse. Nature 383:431–434.

Borst JG, Sakmann B (1998) Calcium current during a single action potential in a large presynaptic terminal of the rat brainstem. J Physiol 506 (Pt 1):143–157.

Boudkkazi S, Fronzaroli-Molinieres L, Debanne D (2011) Presynaptic action potential waveform determines cortical synaptic latency. J Physiol 589:1117–1131.

Brand A, Behrend O, Marquardt T, McAlpine D, Grothe B (2002) Precise inhibition is essential for microsecond interaural time difference coding. Nature 417:543–547.

Brill MH, Waxman SG, Moore JW, Joyner RW (1977) Conduction velocity and spike configuration in myelinated fibres: computed dependence on internode distance. J Neurol Neurosurg Psychiatry 40:769–774.

Caicedo A, Eybalin M (1999) Glutamate receptor phenotypes in the auditory brainstem and mid-brain of the developing rat. Eur J Neurosci 11:51–74.

Cant NB, Casseday JH (1986) Projections from the anteroventral cochlear nucleus to the lateral and medial superior olivary nuclei. J Comp Neurol 247:457–476.

Carr CE, Konishi M (1990) A circuit for detection of interaural time differences in the brain stem of the barn owl. J Neurosci 10:3227–3246.

Carr CE, Macleod KM (2010) Microseconds matter. PLoS Biol 8:e1000405.

Carr CE, Soares D (2002) Evolutionary convergence and shared computational principles in the auditory system. Brain Behav Evol 59:294–311.

Carr CE, Soares D, Parameshwaran S, Perney T (2001) Evolution and development of time coding systems. Curr Opin Neurobiol 11:727–733.

Cathala L, Holderith NB, Nusser Z, DiGregorio DA, Cull-Candy SG (2005) Changes in synaptic structure underlie the developmental speeding of AMPA receptor-mediated EPSCs. Nat Neurosci 8:1310–1318.

Clause A, Kim G, Sonntag M, Weisz CJC, Vetter DE, Rűbsamen R, Kandler K (2014) The precise temporal pattern of prehearing spontaneous activity is necessary for tonotopic map refinement. Neuron 82:822–835.

Couchman K, Grothe B, Felmy F (2010) Medial superior olivary neurons receive surprisingly few excitatory and inhibitory inputs with balanced strength and short-term dynamics. J Neurosci Off J Soc Neurosci 30:17111–17121.

Debanne D, Campanac E, Bialowas A, Carlier E, Alcaraz G (2011) Axon Physiology. Physiol Rev 91:555–602.

Deschênes M, Landry P (1980) Axonal branch diameter and spacing of nodes in the terminal arborization of identified thalamic and cortical neurons. Brain Res 191:538–544.

Dondzillo A, Sätzler K, Horstmann H, Altrock WD, Gundelfinger ED, Kuner T (2010) Targeted three-dimensional immunohistochemistry reveals localization of presynaptic proteins Bassoon and Piccolo in the rat calyx of Held before and after the onset of hearing. J Comp Neurol 518:1008–1029.

Dreyer A, Delgutte B (2006) Phase locking of auditory-nerve fibers to the envelopes of high-frequency sounds: implications for sound localization. J Neurophysiol 96:2327–2341.

Elezgarai I, Díez J, Puente N, Azkue JJ, Benítez R, Bilbao A, Knöpfel T, Doñate-Oliver F, Grandes P (2003) Subcellular localization of the voltage-dependent potassium channel Kv3.1b in postnatal and adult rat medial nucleus of the trapezoid body. Neuroscience 118:889–898.

Fischl MJ, Combs TD, Klug A, Grothe B, Burger RM (2012) Modulation of synaptic input by GABAB receptors improves coincidence detection for computation of sound location. J Physiol 590:3047–3066.

Ford MC, Grothe B, Klug A (2009) Fenestration of the calyx of Held occurs sequentially along the tonotopic axis, is influenced by afferent activity, and facilitates glutamate clearance. J Comp Neurol 514:92–106.

Ford MC, Grothe B, Koch U (2010) Development of voltage gated calcium channels in the lateral superior olive of the Mongolian gerbil. Soc Neurosci Abstr Viewer Itiner Plan 40.

Forsythe ID, Barnes-Davies M (1993) The binaural auditory pathway: excitatory amino acid receptors mediate dual timecourse excitatory postsynaptic currents in the rat medial nucleus of the trapezoid body. Proc Biol Sci 251:151–157.

Foust A, Popovic M, Zecevic D, McCormick DA (2010) Action potentials initiate in the axon initial segment and propagate through axon collaterals reliably in cerebellar Purkinje neurons. J Neurosci Off J Soc Neurosci 30:6891–6902.

Futai K, Okada M, Matsuyama K, Takahashi T (2001) High-fidelity transmission acquired via a developmental decrease in NMDA receptor expression at an auditory synapse. J Neurosci Off J Soc Neurosci 21:3342–3349.

Galambos R, Davis H (1943) The Response of Single Auditory-Nerve Fibers to Acoustic Stimulation. J Neurophysiol 6:39–57.

Gegelashvili G, Schousboe A (1998) Cellular distribution and kinetic properties of high-affinity glutamate transporters. Brain Res Bull 45:233–238.

Gerstner W, Kempter R, van Hemmen JL, Wagner H (1996) A neuronal learning rule for sub-millisecond temporal coding. Nature 383:76–81.

Glendenning KK, Hutson KA, Nudo RJ, Masterton RB (1985) Acoustic chiasm II: Anatomical basis of binaurality in lateral superior olive of cat. J Comp Neurol 232:261–285.

Goldberg JM, Brown PB (1968) Functional organization of the dog superior olivary complex: an anatomical and electrophysiological study. J Neurophysiol 31:639–656.

Goldman L, Albus JS (1968) Computation of impulse conduction in myelinated fibers; theoretical basis of the velocity-diameter relation. Biophys J 8:596–607.

Grande G, Negandhi J, Harrison RV, Wang L-Y (2014) Remodelling at the calyx of Held-MNTB synapse in mice developing with unilateral conductive hearing loss. J Physiol 592:1581–1600.

Grothe B (2003) New roles for synaptic inhibition in sound localization. Nat Rev Neurosci 4:540–550.

Grothe B, Koch U (2011) Dynamics of binaural processing in the mammalian sound localization pathway--the role of GABA(B) receptors. Hear Res 279:43–50.

Grothe B, Pecka M, McAlpine D (2010) Mechanisms of sound localization in mammals. Physiol Rev 90:983–1012.

Grothe B, Sanes DH (1993) Bilateral inhibition by glycinergic afferents in the medial superior olive. J Neurophysiol 69:1192–1196.

Grothe B, Sanes DH (1994) Synaptic inhibition influences the temporal coding properties of medial superior olivary neurons: an in vitro study. J Neurosci Off J Soc Neurosci 14:1701–1709.

Guinan J, Guinan S, Norris B (1972) Single auditory units in superior olivary complex .2. Locations of unit categories and tonotopic organization. Int J Neurosci 4:147–166.

Guinan JJ Jr, Li RY (1990) Signal processing in brainstem auditory neurons which receive giant endings (calyces of Held) in the medial nucleus of the trapezoid body of the cat. Hear Res 49:321–334.

Hartline DK, Colman DR (2007) Rapid conduction and the evolution of giant axons and myelinated fibers. Curr Biol CB 17:R29–R35.

Hassfurth B, Grothe B, Koch U (2010) The mammalian interaural time difference detection circuit is differentially controlled by GABAB receptors during development. J Neurosci Off J Soc Neurosci 30:9715–9727.

Held H (1893) Die centrale Gehörleitung. Arch Anat Physiol Anat Abt 17:201–248.

Henning GB (1974) Detectability of interaural delay in high-frequency complex waveforms. J Acoust Soc Am 55:84–90.

Hursh JB (1939) Conduction Velocity and Diameter of Nerve Fibers. Am J Physiol -- Leg Content 127:131–139.

Hu W, Tian C, Li T, Yang M, Hou H, Shu Y (2009) Distinct contributions of Na(v)1.6 and Na(v)1.2 in action potential initiation and backpropagation. Nat Neurosci 12:996–1002.

Huxley AF, Stampfli R (1949) Evidence for saltatory conduction in peripheral myelinated nerve fibres. J Physiol 108:315–339.

Johnson SL, Eckrich T, Kuhn S, Zampini V, Franz C, Ranatunga KM, Roberts TP, Masetto S, Knipper M, Kros CJ, Marcotti W (2011) Position-dependent patterning of spontaneous action potentials in immature cochlear inner hair cells. Nat Neurosci 14:711–717.

Johnson SL, Kennedy HJ, Holley MC, Fettiplace R, Marcotti W (2012) The resting transducer current drives spontaneous activity in prehearing mammalian cochlear inner hair cells. J Neurosci Off J Soc Neurosci 32:10479–10483.

Johnston J, Forsythe ID, Kopp-Scheinpflug C (2010) Going native: voltage-gated potassium channels controlling neuronal excitability. J Physiol 588:3187–3200.

Joris PX, Carney LH, Smith PH, Yin TC (1994) Enhancement of neural synchronization in the anteroventral cochlear nucleus. I. Responses to tones at the characteristic frequency. J Neurophysiol 71:1022–1036.

Joshi I, Shokralla S, Titis P, Wang L-Y (2004) The role of AMPA receptor gating in the development of high-fidelity neurotransmission at the calyx of Held synapse. J Neurosci Off J Soc Neurosci 24:183–196.

Joshi I, Wang L-Y (2002) Developmental profiles of glutamate receptors and synaptic transmission at a single synapse in the mouse auditory brainstem. J Physiol 540:861–873.

Kandler K, Clause A, Noh J (2009) Tonotopic reorganization of developing auditory brainstem circuits. Nat Neurosci 12:711–717.

Kandler K, Friauf E (1993) Pre- and postnatal development of efferent connections of the cochlear nucleus in the rat. J Comp Neurol 328:161–184.

Kapfer C, Seidl AH, Schweizer H, Grothe B (2002) Experience-dependent refinement of inhibitory inputs to auditory coincidence-detector neurons. Nat Neurosci 5:247–253.

Kil J, Kageyama GH, Semple MN, Kitzes LM (1995) Development of ventral cochlear nucleus projections to the superior olivary complex in gerbil. J Comp Neurol 353:317–340.

Kim JH, Renden R, Gersdorff H von (2013a) Dysmyelination of auditory afferent axons increases the jitter of action potential timing during high-frequency firing. J Neurosci 33:9402–9407.

Kim SE, Turkington K, Kushmerick C, Kim JH (2013b) Central dysmyelination reduces the temporal fidelity of synaptic transmission and the reliability of postsynaptic firing during high-frequency stimulation. J Neurophysiol.

Kiss A, Majorossy K (1983) Neuron morphology and synaptic architecture in the medial superior olivary nucleus. Light- and electron microscope studies in the cat. Exp Brain Res 52:315–327.

Kitamura K, Judkewitz B, Kano M, Denk W, Häusser M (2008) Targeted patch-clamp recordings and single-cell electroporation of unlabeled neurons in vivo. Nat Methods 5:61–67.

Koike-Tani M, Saitoh N, Takahashi T (2005) Mechanisms underlying developmental speeding in AMPA-EPSC decay time at the calyx of Held. J Neurosci Off J Soc Neurosci 25:199–207.

Kole MHP, Ilschner SU, Kampa BM, Williams SR, Ruben PC, Stuart GJ (2008) Action potential generation requires a high sodium channel density in the axon initial segment. Nat Neurosci 11:178–186.

Kole MHP, Stuart GJ (2008) Is action potential threshold lowest in the axon? Nat Neurosci 11:1253–1255.

Kole MHP, Stuart GJ (2012) Signal processing in the axon initial segment. Neuron 73:235–247.

Kopp-Scheinpflug C, Tolnai S, Malmierca MS, Rübsamen R (2008) The medial nucleus of the trapezoid body: comparative physiology. Neuroscience 154:160–170.

Kuba H, Ishii TM, Ohmori H (2006) Axonal site of spike initiation enhances auditory coincidence detection. Nature 444:1069–1072.

Kuwabara N, Zook JM (1992) Projections to the medial superior olive from the medial and lateral nuclei of the trapezoid body in rodents and bats. J Comp Neurol 324:522–538.

Kuwabara N, Zook JM (1999) Local collateral projections from the medial superior olive to the superior paraolivary nucleus in the gerbil. Brain Res 846:59–71.

Kwiecien JM, O'Connor LT, Goetz BD, Delaney KH, Fletch AL, Duncan ID (1998) Morphological and morphometric studies of the dysmyelinating mutant, the Long Evans shaker rat. J Neurocytol 27:581–591.

Leakey DM, Sayers BM, Cherry C (1958) Binaural Fusion of Low□ and High□Frequency Sounds. J Acoust Soc Am 30:222–222.

Leão RM, Kushmerick C, Pinaud R, Renden R, Li G-L, Taschenberger H, Spirou G, Levinson SR, von Gersdorff H (2005) Presynaptic Na+ channels: locus, development, and recovery from inactivation at a high-fidelity synapse. J Neurosci Off J Soc Neurosci 25:3724–3738.

Lehnert S, Ford MC, Alexandrova O, Hellmundt F, Felmy F, Grothe B, Leibold C (2014) Action potential generation in an anatomically constrained model of medial superior olive axons. J Neurosci Off J Soc Neurosci 34:5370–5384.

Lesica NA, Lingner A, Grothe B (2010) Population coding of interaural time differences in gerbils and barn owls. J Neurosci Off J Soc Neurosci 30:11696–11702.

Lindsey BG (1975) Fine structure and distribution of axon terminals from cochlear nucleus on neurons in the medial superior olivary nucleus of the cat. J Comp Neurol 160:81–103.

Lorincz A, Nusser Z (2010) Molecular identity of dendritic voltage-gated sodium channels. Science 328:906–909.

Lorteije JAM, Rusu SI, Kushmerick C, Borst JGG (2009) Reliability and precision of the mouse calyx of Held synapse. J Neurosci Off J Soc Neurosci 29:13770–13784.

Magnusson AK, Park TJ, Pecka M, Grothe B, Koch U (2008) Retrograde GABA signaling adjusts sound localization by balancing excitation and inhibition in the brainstem. Neuron 59:125–137.

Maki K, Furukawa S (2005) Acoustical cues for sound localization by the Mongolian gerbil, Meriones unguiculatus. J Acoust Soc Am 118:872–886.

Makinodan M, Rosen KM, Ito S, Corfas G (2012) A critical period for social experience-dependent oligodendrocyte maturation and myelination. Science 337:1357–1360.

Mann ZF, Kelley MW (2011) Development of tonotopy in the auditory periphery. Hear Res 276:2–15.

Matsushita A, Kawasaki M (2004) Unitary giant synapses embracing a single neuron at the convergent site of time-coding pathways of an electric fish, Gymnarchus niloticus. J Comp Neurol 472:140–155.

McFadden D, Pasanen EG (1976) Lateralization of high frequencies based on interaural time differences. J Acoust Soc Am 59:634–639.

Mills A (1958) On the Minimum Audible Angle. J Acoust Soc Am 30:237–246.

Moore MJ, Caspary DM (1983) Strychnine blocks binaural inhibition in lateral superior olivary neurons. J Neurosci Off J Soc Neurosci 3:237–242.

Morest DK (1968) The growth of synaptic endings in the mammalian brain: a study of the calyces of the trapezoid body. Z Für Anat Entwicklungsgeschichte 127:201–220.

Myoga MH, Lehnert S, Leibold C, Felmy F, Grothe B (2014) Glycinergic inhibition tunes coincidence detection in the auditory brainstem. Nat Commun 5:3790.

Nakamura PA, Cramer KS (2011) Formation and maturation of the calyx of Held. Hear Res 276:70–78.

Nakamura Y, Takahashi T (2007) Developmental changes in potassium currents at the rat calyx of Held presynaptic terminal. J Physiol 581:1101–1112.

Otis TS, Wu YC, Trussell LO (1996) Delayed clearance of transmitter and the role of glutamate transporters at synapses with multiple release sites. J Neurosci Off J Soc Neurosci 16:1634–1644.

Paintal AS (1965) Effects of temperature on conduction in single vagal and saphenous myelinated nerve fibres of the cat. J Physiol 180:20–49.

Pannasch U, Freche D, Dallérac G, Ghézali G, Escartin C, Ezan P, Cohen-Salmon M, Benchenane K, Abudara V, Dufour A, Lübke JHR, Déglon N, Knott G, Holcman D, Rouach N (2014) Connexin 30 sets synaptic strength by controlling astroglial synapse invasion. Nat Neurosci 17:549–558.

Paysan J, Conroy WG, Coggan JS, Berg DK (2000) The neurofilament infrastructure of a developing presynaptic calyx. J Comp Neurol 425:284–294.

Pecka M, Brand A, Behrend O, Grothe B (2008) Interaural time difference processing in the mammalian medial superior olive: the role of glycinergic inhibition. J Neurosci Off J Soc Neurosci 28:6914–6925.

Perkins RE (1973) An electron microscopic study of synaptic organization in the medial superior olive of normal and experimental chinchillas. J Comp Neurol 148:387–415.

Portfors CV, von Gersdorff H (2013) Macrocircuits for sound localization use leaky coincidence detectors and specialized synapses. Neuron 78:755–757.

Quick DC, Kennedy WR, Donaldson L (1979) Dimensions of myelinated nerve fibers near the motor and sensory terminals in cat tenuissimus muscles. Neuroscience 4:1089–1096.

Radziwon KE, June KM, Stolzberg DJ, Xu-Friedman MA, Salvi RJ, Dent ML (2009) Behaviorally measured audiograms and gap detection thresholds in CBA/CaJ mice. J Comp Physiol A Neuroethol Sens Neural Behav Physiol 195:961–969.

Rancz EA, Franks KM, Schwarz MK, Pichler B, Schaefer AT, Margrie TW (2011) Transfection via whole-cell recording in vivo: bridging single-cell physiology, genetics and connectomics. Nat Neurosci 14:527–532.

Rasband MN, Trimmer JS (2001) Developmental clustering of ion channels at and near the node of Ranvier. Dev Biol 236:5–16.

Renden R, Taschenberger H, Puente N, Rusakov DA, Duvoisin R, Wang L-Y, Lehre KP, von Gersdorff H (2005) Glutamate transporter studies reveal the pruning of metabotropic glutamate receptors and absence of AMPA receptor desensitization at mature calyx of held synapses. J Neurosci Off J Soc Neurosci 25:8482–8497.

Ritchie JM (1982) On the relation between fibre diameter and conduction velocity in myelinated nerve fibres. Proc R Soc Lond Ser B Contain Pap Biol Character R Soc G B 217:29–35.

Roberts MT, Seeman SC, Golding NL (2013) A mechanistic understanding of the role of feedforward inhibition in the mammalian sound localization circuitry. Neuron 78:923–935.

Roberts RC, Ribak CE (1987) GABAergic neurons and axon terminals in the brainstem auditory nuclei of the gerbil. J Comp Neurol 258:267–280.

Rodríguez-Contreras A, van Hoeve JSS, Habets RLP, Locher H, Borst JGG (2008) Dynamic development of the calyx of Held synapse. Proc Natl Acad Sci U S A 105:5603–5608.

Rose JE, Brugge JF, Anderson DJ, Hind JE (1967) Phase-locked response to low-frequency tones in single auditory nerve fibers of the squirrel monkey. J Neurophysiol 30:769–793.

Rowland KC, Irby NK, Spirou GA (2000) Specialized synapse-associated structures within the calyx of Held. J Neurosci Off J Soc Neurosci 20:9135–9144.

Rushton WAH (1951) A theory of the effects of fibre size in medullated nerve. J Physiol 115:101–122.

Ryan A (1976) Hearing sensitivity of the mongolian gerbil, Meriones unguiculatis. J Acoust Soc Am 59:1222–1226.

Sabatini BL, Regehr WG (1999) Timing of synaptic transmission. Annu Rev Physiol 61:521–542.

Sanes DH, Geary WA, Wooten GF, Rubel EW (1987) Quantitative distribution of the glycine receptor in the auditory brain stem of the gerbil. J Neurosci Off J Soc Neurosci 7:3793–3802.

Sätzler K, Söhl LF, Bollmann JH, Borst JGG, Frotscher M, Sakmann B, Lübke JHR (2002) Three-dimensional reconstruction of a calyx of Held and its postsynaptic principal neuron in the medial nucleus of the trapezoid body. J Neurosci Off J Soc Neurosci 22:10567–10579.

Scott LL, Hage TA, Golding NL (2007) Weak action potential backpropagation is associated with high-frequency axonal firing capability in principal neurons of the gerbil medial superior olive. J Physiol 583:647–661.

Scott LL, Mathews PJ, Golding NL (2005) Posthearing developmental refinement of temporal processing in principal neurons of the medial superior olive. J Neurosci Off J Soc Neurosci 25:7887–7895.

Scott RS, Henneberger C, Padmashri R, Anders S, Jensen TP, Rusakov DA (2014) Neuronal adaptation involves rapid expansion of the action potential initiation site. Nat Commun 5:3817.

Seidl AH (2013) Regulation of conduction time along axons. Neuroscience.

Seidl AH, Rubel EW, Barría A (2014) Differential Conduction Velocity Regulation in Ipsilateral and Contralateral Collaterals Innervating Brainstem Coincidence Detector Neurons. J Neurosci 34:4914–4919.

Seidl AH, Rubel EW, Harris DM (2010) Mechanisms for adjusting interaural time differences to achieve binaural coincidence detection. J Neurosci 30:70–80.

Sibson NR, Mason GF, Shen J, Cline GW, Herskovits AZ, Wall JE, Behar KL, Rothman DL, Shulman RG (2001) In vivo (13)C NMR measurement of neurotransmitter glutamate cycling, anaplerosis and TCA cycle flux in rat brain during. J Neurochem 76:975–989.

Smith CM, Cooksey E, Duncan ID (2013) Myelin Loss Does Not Lead to Axonal Degeneration in a Long-Lived Model of Chronic Demyelination. J Neurosci 33:2718–2727.

Smith PH, Joris PX, Yin TC (1993) Projections of physiologically characterized spherical bushy cell axons from the cochlear nucleus of the cat: evidence for delay lines to the medial superior olive. J Comp Neurol 331:245–260.

Sonntag M, Englitz B, Kopp-Scheinpflug C, Rübsamen R (2009) Early postnatal development of spontaneous and acoustically evoked discharge activity of principal cells of the medial nucleus of the trapezoid body: an in vivo study in mice. J Neurosci Off J Soc Neurosci 29:9510–9520.

Spangler KM, Warr WB, Henkel CK (1985) The projections of principal cells of the medial nucleus of the trapezoid body in the cat. J Comp Neurol 238:249–262.

Spirou GA, Brownell WE, Zidanic M (1990) Recordings from cat trapezoid body and HRP labeling of globular bushy cell axons. J Neurophysiol 63:1169–1190.

Stange A, Myoga MH, Lingner A, Ford MC, Alexandrova O, Felmy F, Pecka M, Siveke I, Grothe B (2013) Adaptation in sound localization: from GABA(B) receptor-mediated synaptic modulation to perception. Nat Neurosci 16:1840–1847.

Stotler WA (1953) An experimental study of the cells and connections of the superior olivary complex of the cat. J Comp Neurol 98:401–431.

Stuart GJ, Sakmann B (1994) Active propagation of somatic action potentials into neocortical pyramidal cell dendrites. Nature 367:69–72.

Taschenberger H, Leão RM, Rowland KC, Spirou GA, von Gersdorff H (2002) Optimizing synaptic architecture and efficiency for high-frequency transmission. Neuron 36:1127–1143.

Taschenberger H, von Gersdorff H (2000) Fine-tuning an auditory synapse for speed and fidelity: developmental changes in presynaptic waveform, EPSC kinetics, and synaptic plasticity. J Neurosci Off J Soc Neurosci 20:9162–9173.

Trattner B, Gravot CM, Grothe B, Kunz L (2013) Metabolic Maturation of Auditory Neurones in the Superior Olivary Complex. PloS One 8:e67351.

Tritsch NX, Rodríguez-Contreras A, Crins TTH, Wang HC, Borst JGG, Bergles DE (2010) Calcium action potentials in hair cells pattern auditory neuron activity before hearing onset. Nat Neurosci 13:1050–1052.

Tritsch NX, Yi E, Gale JE, Glowatzki E, Bergles DE (2007) The origin of spontaneous activity in the developing auditory system. Nature 450:50–55.

Trussell LO (1997) Cellular mechanisms for preservation of timing in central auditory pathways. Curr Opin Neurobiol 7:487–492.

Trussell LO (1999) Synaptic mechanisms for coding timing in auditory neurons. Annu Rev Physiol 61:477–496.

Turecek R, Trussell LO (2000) Control of synaptic depression by glutamate transporters. J Neurosci Off J Soc Neurosci 20:2054–2063.

Uwechue NM, Marx M-C, Chevy Q, Billups B (2012) Activation of glutamate transport evokes rapid glutamine release from perisynaptic astrocytes. J Physiol 590:2317–2331.

Von Gersdorff H, Borst JGG (2002) Short-term plasticity at the calyx of held. Nat Rev Neurosci 3:53–64.

Waxman SG (1980) Determinants of conduction velocity in myelinated nerve fibers. Muscle Nerve 3:141–150.

Werthat F, Alexandrova O, Grothe B, Koch U (2008) Experience-dependent refinement of the inhibitory axons projecting to the medial superior olive. Dev Neurobiol 68:1454–1462.

Wimmer VC, Horstmann H, Groh A, Kuner T (2006) Donut-like topology of synaptic vesicles with a central cluster of mitochondria wrapped into membrane protrusions: a novel structure-function module of the adult calyx of Held. J Neurosci Off J Soc Neurosci 26:109–116.

Wu SH, Kelly JB (1993) Response of neurons in the lateral superior olive and medial nucleus of the trapezoid body to repetitive stimulation: intracellular and extracellular recordings from mouse brain slice. Hear Res 68:189–201.

Youssoufian M, Couchman K, Shivdasani MN, Paolini AG, Walmsley B (2008) Maturation of auditory brainstem projections and calyces in the congenitally deaf (dn/dn) mouse. J Comp Neurol 506:442–451.

List of abbreviations

AIS	Axon initial segment
AMPA	α-amino-3-hydroxy-5-methyl-4-isoxazolepropionic acid
EPSP	Excitatory postsynaptic potential
GABA	Gamma-Aminobutyric acid
GBC	Globular bushy cell
GLAST	Glutamate/aspartate transporter
GLT1	Glutamate transporter 1
ITD	Interaural time difference
ILD	Interaural level difference
LES	Long-Evans shaker
LNTB	Lateral nucleus of the trapezoid body
LSO	Lateral superior olive
MNTB	Medial nucleus of the trapezoid body
MSO	Medial superior olive
NMDA	N-Methyl-D-aspartate
SBC	Spherical bushy cell
SPN	Superior paraolivary nucleus

Acknowledgements

I would like to express my sincere gratitude to everyone who supported me during this dissertation.

Firstly, I thank my supervisor Prof. Dr. Benedikt Grothe for intellectual guidance and support during this dissertation, especially for always finding the time to thoroughly discuss data despite his very busy schedule and for teaching me how to interpret data in a larger systems neuroscience context.

I thank Prof. Dr. Achim Klug for supervising the first study and for arousing my interest in auditory systems neuroscience and neuron-glial interactions.

I am grateful to Dr. Olga Alexandrova for countless methodological discussions and her collaboration on several projects.

I am grateful to Prof. Dr. David Attwell for an intellectually very stimulating collaboration and for encouraging me to apply for the Marie Curie Fellowship.

Also, I thank Dr. Lee Cossell for collaborating on study 2.

I thank Prof. Dr. Ursula Koch for supervising another project which is not included in this thesis and Prof. Dr. Veronica Egger for her collaboration on that project.

I thank Prof. Dr. Christian Leibold and Simon Lehnert for inviting me to collaborate on the third study presented in this thesis.

I thank Otto Albrecht and Ludwig Feldmann for performing the blinded analysis of calyx morphology.

I am grateful to Dr. Michael Pecka for many interesting discussions on sound localization circuits and for proofreading the introduction and discussion of this thesis.

I thank Dr. Todd Jennings for proofreading the introduction of this thesis.

I thank Prof. Dr. Gerhard Wanner for enabling me to use the electron microscope.

I thank Prof. Dr. Dierk Reiff and Dr. Hartmann Harz for helpful discussions and being members of my thesis advisory committee.

I thank everyone in Prof. Grothe's lab for helpful discussions during lab meetings, progress reports, and whenever I asked for it.

Finally, I thank the whole GSN team for providing an intellectually stimulating environment in which PhD and Master students of different scientific background can interact.

Eidesstattliche Versicherung/Affidavit

Hiermit versichere ich an Eides statt, dass ich die vorliegende Dissertation *Structure-function relations in mammalian sound localization circuits* selbstständig angefertigt habe, mich außer der angegebenen keiner weiteren Hilfsmittel bedient und alle Erkenntnisse, die aus dem Schrifttum ganz oder annähernd übernommen sind, als solche kenntlich gemacht und nach ihrer Herkunft unter Bezeichnung der Fundstelle einzeln nachgewiesen habe.

I hereby confirm that the dissertation *Structure-function relations in mammalian sound localization circuits* is the result of my own work and that I have only used sources or materials listed and specified in the dissertation.

München, den

Munich, date Unterschrift signature

Author contributions

Study 1:

M.C.F. and A.K. designed the research, M.C.F. performed the experiments; M.C.F. analysed the data [blinded analysis of calyx morphology (assignment of calyces to one of five morphology categories) was performed by two student assistants]. M.C.F. prepared all figures; M.C.F. and A.K. wrote the manuscript; M.C.F., B.G., and A.K. revised the manuscript.

Study 2:

All authors (M.C.F., O.A., L.C., D.A. and B.G.) contributed to designing the research. Anatomical experiments were performed and analyzed by M.C.F. and O.A. Simulations were performed by L.C. and D.A. M.C.F. prepared the figures. All authors (M.C.F., O.A., L.C., D.A. and B.G.) contributed to interpreting the data and writing the manuscript.

Study 3:

S.L. and C.L. designed the simulations; M.C.F designed the tracer experiments; M.C.F. and O.A. designed the immunohistochemical experiments; F.F. designed the physiological experiments; S.L. performed the simulations; M.C.F. and O.A. performed the anatomical experiments; F.H. and F.F. performed the physiological experiments; S.L. analysed the simulations; M.C.F and O.A. analysed the anatomical data; F.H. and F.F. analysed the physiological data; M.C.F. prepared figure 2, S.L. prepared the other figures; M.C.F wrote the sections concerning the anatomical data, F.F wrote the section concerning the physiological data, S.L. and C.L. wrote the other sections of the manuscript; S.L., M.C.F., F.F., B.G., and C.L. revised the manuscript.

Study 4:

A.S. performed the *in vivo* experiments, analyzed the data and wrote the relevant parts of the manuscript. M.H.M. performed the *in vitro* experiments, analyzed the data and wrote the relevant parts of the manuscript. A.L. performed the psychophysical experiments, analyzed the data and wrote the relevant parts of the manuscript. M.C.F. designed and performed the fiber tracing experiments, analyzed the data, prepared figure 6 a-g, and wrote the parts of the manuscript concerning the anatomical experiments. M.C.F and O.A. designed the immunohistochemistry experiments. O.A. performed the immunohistochemistry experiments and confocal microscopy, analyzed the data and wrote the relevant parts of the methods section. F.F. supervised the *in vitro* electrophysiology experiments. M.P. supervised the adaptation (*in vivo* and psychophysical) experiments and wrote parts of the manuscript. I.S. and B.G. supervised the project and wrote the manuscript. All authors revised the manuscript.